Effectively Cornering New Physics at Colliders and Beyond

Wrishik Naskar
School of Physics & Astronomy, College of Science & Engineering

A dissertation submitted in fulfillment of the requirements for the degree of
Doctor of Philosophy

Abstract

The Standard Model has achieved remarkable success, yet growing empirical and theoretical tensions point to the need for new physics at the TeV scale. As collider experiments enter a precision era, even small deviations from Standard Model predictions can provide crucial clues about the underlying structure of fundamental interactions. This thesis explores these possibilities through both model-dependent studies and the effective field theory approach. Multi-Higgs production is used to probe extended scalar sectors, offering insight into the nature of electroweak symmetry breaking and the dynamics of possible phase transitions. Electroweak-scale triplet models are examined through collider signatures and flavour constraints, presenting a realistic mechanism for radiative neutrino mass generation. In the top-quark sector, momentum-dependent width effects are implemented in a gauge-consistent way, leading to more accurate predictions for SMEFT constraints. To address the challenge of high-multiplicity final states, machine learning techniques, including graph neural networks, are applied to identify hidden correlations and enhance signal sensitivity. Together, these studies sharpen existing bounds and provide complementary strategies to guide future experimental efforts at the High-Luminosity LHC and beyond.

Declaration

The content of this thesis is my own work except where explicit attribution to others is made. Chapter 1 introduces the thesis. Chapter 2 provides a description of the underlying important concepts in particle physics to the reader. The remaining chapters are based on the following publications:

- Chapter 3:
  "BSM patterns in scalar-sector coupling modifiers" [1] written in collaboration with Prof. Christoph Englert and Dr. Dave Sutherland, and "Double and triple Higgs boson production to probe the electroweak phase transition" [2] written in collaboration with Dr. Lisa Biermann, Dr. Christoph Borschensky, Prof. Christoph Englert, and Prof. Margarete Mühlleitner.
  Fig. 3.1 was generated by Prof. Christoph Englert. The calculations in Secs. 3.2.1 and 3.2.4 were carried out independently by Dr. Dave Sutherland and myself, and later cross-checked for consistency. The loop-level singlet analysis (Sec. 3.2.2) and the dilaton-mixing scenario (Sec. 3.2.3) were performed by Prof. Christoph Englert. The parameter scans presented in Sec. 3.3.1, which make use of `ScannerS`, `HiggsTools`, and `BSMPT`, were performed by Dr. Lisa Biermann and Dr. Christoph Borschensky.

- Chapter 4:
  "Resurrecting the LHC discovery potential in the extended type-II seesaw model" [3] written in collaboration with Dr. Upalaparna Banerjee and Prof. Christoph Englert.

- Chapter 5:
  "Impact of new physics on momentum dependent widths and propagators" [4] written in collaboration with Prof. Christoph Englert and Prof. Michael Spannowsky.

- Chapter 6:
  "BSM reach of four-top production at the LHC" [5] written in collaboration with Dr. Anisha, Dr. Oliver Atkinson, Dr. Akanksha Bhardwaj, Prof. Christoph Englert, and Dr. Panagiotis Stylianou.
  Figs. 6.1 to 6.3 were generated by Dr. Akanksha Bhardwaj and myself, and Fig. 6.7 was prepared by Dr. Akanksha Bhardwaj. Fig. 6.4 was produced jointly by Dr. Panagiotis Stylianou, Dr. Akanksha Bhardwaj, and myself. The foundation of the Graph Neural Network code was developed by Dr. Panagiotis Stylianou and Dr. Akanksha Bhardwaj for a previous project; I subsequently adapted, extended, and optimised it for the specific requirements of our four-top analysis. The parameter scans for the 2HDM presented in Sec. 6.2.3, which utilised `2HDecay` and `HiggsBounds`, were carried out by Dr. Oliver Atkinson. Fig. 6.10 was produced by Dr. Oliver Atkinson and myself.

Beyond the work presented in this thesis, I have also contributed to additional collaborative publications during my PhD [6–9], and community efforts like the Early Career Researchers' Input to the European Strategy for Particle Physics Update. While these are not included as thesis chapters, they have formed an important part of my broader research experience.

Wrishik Naskar

Acknowledgements

This is easily my favourite part of the thesis. I have been looking forward to writing it ever since I began. My PhD journey has been nothing short of incredible: memorable, life-changing, and without a doubt the best experience of my life so far. I want to take this chance to acknowledge everyone who made it even better.

First and foremost, I have to thank my Doktorvater, Prof. Christoph Englert. Christoph, I honestly do not think I can ever put into words how amazing a supervisor you have been. Everything that made this PhD so rewarding stems from working with you. I used to think of a PhD as a daunting, long, and frustrating endeavour, but I could not have been more wrong. Thank you for choosing me as your student, for constantly pushing me to become a better researcher, for making the journey so enjoyable with your amazing and politically incorrect sense of humour, and for inspiring all of us every single day with your incredible work ethic. I am especially grateful for your patience and for always being available whenever I got stuck, no matter how big or small the problem. You made me fall in love with particle physics, and that excitement has never faded from day one to now. I promise to keep striving as a researcher and to be a padawan you are proud of.

I would like to thank the outstanding collaborators I have had the privilege to work with, who made research engaging and smooth: Prof. Joydeep Chakrabortty (for first getting me interested in particle physics), Prof. Michael Spannowsky, Prof. Margarete Mühlleitner, Prof. Ben Allanach, Dr. Rodrigo Alonso, Dr. Dave Sutherland, Dr. Sophie Renner, Dr. Anisha, Dr. Akanksha Bhardwaj, Dr. Oliver Atkinson, Dr. Panagiotis Stylianou, Dr. Upalaparna Banerjee, Dr. Shakeel Ur Rahaman, Dr. Vishal Ngairangbam, Dr. Lisa Biermann, Dr. Christoph Borschensky, and Christiane Mayer.

I also gratefully acknowledge the support of the School of Physics and Astronomy's administrative staff, especially Jill Borland and Karen Law, for handling formalities and travel logistics so smoothly. I am also thankful to the University of Glasgow

College of Science and Engineering for awarding me my PhD fellowship and for additional support through the Lord Kelvin Travel Fund.

I feel incredibly fortunate to have been part of the Glasgow PPT group, a nurturing and intellectually stimulating environment that helped me grow tremendously. I am especially grateful to my second supervisor, Dave Sutherland, for always being available to answer questions, and for his patience, insight, and unwavering support across projects. I also want to thank Sophie Renner, who brought so much life to the group, not only through initiatives like our Friday meetings and watching the BSM forum, but also by encouraging me to value the social side of academic life through networking, and by inspiring me with her commitment to causes she cares deeply about. And of course, Glasgow PPT would not be the same without Dr. David Miller and Dr. Chris Bouchard. Their humour, and our legendary pub and lunch chats about teaching allocations and $B \to \pi$, will be sorely missed. I also want to thank Prof. Christine Davies, Dr. Judd Harrison, and Dr. Brian Colquhoun for being such important and valued members of the group. Huge thanks to Akanksha, Anisha, Panos, and Oliver for making the transition from Master's to PhD so smooth. I am deeply grateful for their consistent support and generosity during those early days. I am very grateful to Olmo and Mario for always being available with guidance and advice, especially during the postdoc application season, and the rest of my PhD cohort: Logan (my gluten-free DnD lad), Kerr (the best conference buddy), and Alastair. And thanks to the Glasgow PPE group for our regular pub nights and Friday doughnut sessions! A special mention to Jay Howarth: I'd have written a page about you, but alas, the margins are too small!

The biggest shoutout, of course, goes to my amazing lads: Ben and Graeme. I honestly do not know if I would have enjoyed working as much without you two. Graeme, your insane dedication day after day kept me motivated. Ben, I really admired the way you tried to learn from other groups and brought those ideas into ours, like the "Schwartz Club." You both helped create the kind of group dynamic I had always dreamed of. Every day, I tried to be a good role model for you, and it makes me genuinely happy when others say we are annoyingly close. I will miss you the most. You are going to be amazing researchers, and I cannot wait to see your work, attend your talks, and of course, meet you for our summer trip to Germany in 2026. (Yes, this paragraph was originally a page long. I tried my best to condense it.)

I am grateful to have met so many incredible people at conferences. You have all been truly inspiring. Special thanks to Sid, Malina, Michael, and Eugenia for our

continued meetups; to Marion, for inspiring me with her incredible work ethic; and to my generational BFF, Tim. Finally to my role model in almost every aspect, Mia West, for inspiring me with the phenomenal physics she does, for always lending an ear when I needed one, and for being a constant source of kindness and encouragement. I am excited to keep seeing you all at conferences and to hopefully collaborate in the future.

I also feel incredibly fortunate to have had the opportunity to teach during my PhD, as teaching is something I genuinely enjoy. I especially loved working in the computational labs and supervising group projects, which were both rewarding and fun. A special shoutout to my first ever group from Relativistic Stars: Marc, Olivia, and Andie, who made the experience one of the most enjoyable and memorable parts of my PhD.

Thanks to all my friends who made this journey even more joyful. To my first-year gang: Aurys, Théo (mon frère d'une autre mère), Amelia, Adam, Hasret, and Aleks. To the legendary Bad Mintz Bantz crew: Dwayne (thanks for being a 'father' figure, and introducing me to Koko House, I cannot wait for Hamburg), Chris/Cairis (thanks for letting me win by being lazy), the wee lassie and powerkraut: Celine, for keeping me grounded with a punch but always lending an ear for rants and gossip. Ardiana (Trauma team!), thank you for always showing up for badminton and being an amazing doubles partner, I only wish others were as committed. To my chaotic badminton singles gang: Thejas (massive thanks to you for improving my game, and for taking me to the best food places in Glasgow!), Ryan, and Dev, I am definitely going to be rubbish at playing Dwayne without you. To Jonathan, thanks for being an unofficial older brother and completing my racket-sport experience (who cares about table tennis anyway?). I was also incredibly fortunate have one of my closest friends from my school live close by, GG and Neha: thank you for being amazing friends: for our continued meetups over the years, the long drives, the gossip sessions, and the most delicious home-cooked Indian food every time I visited. I would also like to acknowledge Samkit and Athmika, I've had a lot of fun at our hangouts and board game sessions, and I'll definitely miss you! I've missed plenty of names here, but if you've ever seen me smiling with you, know that you'll be missed.

A massive, massive thanks to Katie. I absolutely adore our dynamic. Our wholesome hangouts were some of the best parts of these years, and definitely some of my core memories. You are one of the most wonderful people I have met, and I cannot thank you enough for being there when I needed a shoulder to cry on.

To the amazing members of the University badminton club, thanks for all the great games and memories, and finally, Glasgow Ultimate, even though I am terrible, you have been the most welcoming and brilliant group I have met. Special shoutout to 'The King', the BUX club, and DDD!

I gratefully acknowledge my viva committee: David Miller, Chris Bouchard, and especially Dr. Jessica Turner for the smooth experience, the amazing discussions, and their fruitful suggestions to improve and perfect this thesis. I am also really thankful to my dear friends who spent a lot of their time proofreading this thesis: Ben, Graeme, and Tim, thanks so much!

Finally, I want to thank my incredibly supportive parents, my family, and my friends all over the world. You may be miles away, but you are always close to my heart.

Contents

Chapter 1.

Introduction

"Somewhere, something incredible is waiting to be known."
— Carl Sagan

The Standard Model (SM) of particle physics stands as one of the most successful and predictive frameworks in all of science. By unifying electroweak and strong interactions within a single quantum field theory, it has withstood decades of experimental scrutiny. Its crowning achievement came in 2012, when the ATLAS [10] and CMS [11] collaborations observed a 125 GeV Higgs boson, completing the SM particle spectrum and confirming the mechanism of electroweak symmetry breaking. That discovery, however, also marked a turning point: the SM seemed complete, but new questions were left unanswered. Why has no further structure emerged at accessible energies?

Over the past decade, the Large Hadron Collider (LHC) has extended experimental sensitivity into the multi-TeV regime, steadily improving precision measurements and setting stringent bounds on possible deviations from SM predictions. As Run 3 proceeds and the High-Luminosity LHC (HL-LHC) approaches, the field finds itself in a moment of quiet tension: the SM works, but it is not enough. Meanwhile, talks and studies for next-generation colliders are already underway, promising even greater reach in Higgs physics, top quark studies, and rare processes.

The theory community has responded with a diverse set of tools. Concrete extensions of the SM, including supersymmetry, extra dimensions, and extended Higgs sectors, are complemented by model-independent frameworks such as effective field theories (EFTs). On the experimental side, the growing volume and complexity of

LHC data have spurred the adoption of advanced statistical techniques and machine learning, including applications that extend well beyond simple classification. In this evolving landscape, channels involving multiple Higgs bosons, exotic resonances, flavour anomalies, and final states with top quarks stand out as especially rich with discovery potential.

This thesis explores several such avenues. It brings together model-specific and model-independent approaches, aiming both to characterise how concrete scenarios of new physics affect collider observables and to build flexible tools that enhance the sensitivity of present and future searches.

The structure is as follows: Chapter 2 provides a brief but comprehensive review of the SM Lagrangian, and its benchmark successes in Higgs and flavour physics. The theory's limitations are also discussed, setting the stage for extensions beyond the Standard Model (BSM). Chapter 3 explores the sensitivity of multi-Higgs production channels to extended scalar sectors. Weak-boson-fusion di-Higgs production is mapped via coupling modifiers across different UV scenarios, while gluon-fusion triple Higgs production is shown to be linked to early universe phenomenology, particularly with the electroweak phase transition. In Chapter 4, the Type-II Seesaw Mechanism is revisited as a motivated explanation for neutrino masses. Collider signatures of the scalar triplet are contrasted with bounds from charged lepton flavour violation. Gauge-invariant dimension-six deformations are shown to open up viable electroweak-scale parameter space, placing the model within HL-LHC reach. Chapter 5 investigates the role of momentum-dependent widths of unstable particles in precision lineshape measurements. A gauge-consistent treatment shows that the top invariant-mass lineshape can be sensitive to new physics effects affecting the momentum-dependent widths and propagators. The resulting constraints on new physics are competitive with global fits and are projected to improve significantly at future muon colliders. Chapter 6 introduces machine learning into the mix. A graph neural network classifier is trained to isolate the four-top final state in same-sign dilepton and trilepton channels. This approach offers improved sensitivity to both contact operators and resonant extensions compared to traditional cut-based analyses. Finally, Chapter 7 gathers the main insights, summarises the tools and strategies developed throughout the thesis, and outlines possible directions for future work.

Chapter 2.

Theoretical Foundations for Standard Model and Beyond

"We have this incredible model that explains so much of physics... and yet we know it's not the whole story."

— David Gross, Nobel Lecture 2004

The Standard Model (SM) of particle physics is widely regarded as one of the crowning achievements of modern science. It summarises the present understanding of the fundamental constituents of matter and the interactions that bind them: electromagnetic, weak and strong, while excluding gravity. Formulated as a renormalisable quantum field theory invariant under the gauge group

$$\mathcal{G}_{\mathrm{SM}} = SU(3)_C \times SU(2)_L \times U(1)_Y, \tag{2.1}$$

the SM embeds quantum chromodynamics (QCD) [12–14] and the Glashow–Weinberg–Salam electroweak theory [15–17] into a single coherent framework that has been scrutinised with remarkable precision at energy scales ranging from a few GeV to multiple TeV.

At its core, the SM rests on several deep theoretical principles: local gauge invariance [18]; the chiral nature of weak interactions; spontaneous symmetry breaking via the Higgs mechanism [19–21]; and the consistency conditions imposed by renormalisability [22], anomaly cancellation [23] and unitarity [24]. This structure enables highly accurate predictions for both collider and low-energy observables, many of which

have been confirmed to per-mille accuracy by data from LEP, the Tevatron and the LHC [25].

Despite its empirical success, the SM is manifestly incomplete. Among the open puzzles are the radiative instability of the Higgs mass (the hierarchy problem [26, 27]), the origin of non-zero neutrino masses and mixings [28, 29], the absence of a viable dark-matter candidate [30], and the strong-CP problem [31]. Moreover, the SM offers no explanation for the observed baryon asymmetry [32] of the Universe and does not incorporate gravity at the quantum level. These shortcomings point compellingly towards physics beyond the Standard Model (BSM) at higher scales.

The goal of this chapter is twofold. First, it provides a detailed and mathematically rigorous account of the SM as a gauge theory of elementary particles.* Topics covered include the gauge-symmetry structure, field content, Lagrangian formulation, spontaneous symmetry breaking, the Higgs mechanism and renormalisability. Second, the chapter identifies and motivates the theoretical tensions and empirical gaps that necessitate BSM frameworks, discussing them both from the standpoint of internal consistency and in the light of experimental evidence.

The presentation is deliberately theoretical and formal; phenomenological or experimental aspects are mentioned only where they illuminate or constrain the theory. The discussion laid out here underpins the analyses of BSM physics developed in the remainder of this thesis.

2.1. The Standard Model of Particle Physics

2.1.1. Local Gauge Invariance and Abelian Gauge Theories

At the heart of quantum field theory lies the principle that physical laws should respect *locality*, meaning that interactions occur at definite points in spacetime and propagate through local, causal processes. The principle of *local* (or gauge) invariance [36] that generalises global symmetries (transformations that are uniform across spacetime) to transformations whose parameters vary from point to point, underpins the full structure of the SM. Requiring invariance under such local transformations compels the

*For pedagogical introductions that have inspired this chapter, see, e.g., Refs. [33–35].

introduction of *gauge fields*, which mediate interactions and transform to compensate for the spacetime dependence of the symmetry parameters [18].

Consider a complex scalar field $\phi(x)$ transforming under a global $U(1)$ symmetry,

$$\phi(x) \longrightarrow \phi'(x) = e^{i\alpha}\,\phi(x), \qquad \alpha \in \mathbb{R}. \tag{2.2}$$

The free scalar Lagrangian

$$\mathcal{L}_{\text{free}} = \partial_\mu \phi^* \,\partial^\mu \phi - m^2 \phi^* \phi, \tag{2.3}$$

is invariant under this global transformation. However, promoting the phase to a *local* spacetime-dependent function $\alpha(x)$,

$$\phi(x) \longrightarrow \phi'(x) = e^{i\alpha(x)}\phi(x), \tag{2.4}$$

spoils the invariance because the derivative doesn't transform appropriately

$$\partial_\mu \phi(x) \longrightarrow \partial_\mu \phi'(x) = e^{i\alpha(x)}\left[\partial_\mu \phi(x) + i(\partial_\mu \alpha)\phi(x)\right]. \tag{2.5}$$

To restore invariance one introduces a vector field $A_\mu(x)$ and defines the *covariant derivative*

$$D_\mu = \partial_\mu - i\,e\,A_\mu(x), \tag{2.6}$$

with transformation laws

$$\phi(x) \longrightarrow e^{i\alpha(x)}\phi(x), \tag{2.7}$$

$$A_\mu(x) \longrightarrow A'_\mu(x) = A_\mu(x) - \frac{1}{e}\,\partial_\mu \alpha(x), \tag{2.8}$$

so that $D_\mu \phi$ transforms like ϕ itself:

$$D_\mu \phi(x) \longrightarrow e^{i\alpha(x)} D_\mu \phi(x). \tag{2.9}$$

The kinetic term $|D_\mu \phi|^2$ is therefore gauge-invariant. Gauge fields acquire their dynamics via the (Abelian) field-strength tensor

$$F_{\mu\nu} = -\frac{i}{e}[D_\mu, D_\nu] = \partial_\mu A_\nu - \partial_\nu A_\mu, \tag{2.10}$$

whose square yields the gauge-invariant kinetic term

$$\mathcal{L} = -\frac{1}{4} F_{\mu\nu} F^{\mu\nu}. \tag{2.11}$$

This construction generalises to non-Abelian groups such as $SU(N)$ where gauge fields are matrix-valued and $F_{\mu\nu}$ acquires commutator terms. The Abelian $U(1)$ case provides the cleanest arena in which to see the gauge principle at work. This motivates a brief review of quantum electrodynamics.

Quantum Electrodynamics

Quantum electrodynamics (QED) is the relativistic quantum field theory of electrons, positrons, and photons. QED is realised as a $U(1)$ gauge theory with the gauge field A_μ representing the photon. The fermionic matter content is described by the Dirac field ψ having an electric charge $-e$. Its Lagrangian reads

$$\mathcal{L}_{\text{QED}} = \bar{\psi} \left(i\gamma^\mu D_\mu - m \right) \psi - \frac{1}{4} F_{\mu\nu} F^{\mu\nu}, \tag{2.12}$$

where γ^μ are the Dirac gamma matrices satisfying the Clifford algebra $\{\gamma^\mu, \gamma^\nu\} = 2g^{\mu\nu}$, and the Dirac adjoint $\bar{\psi} = \psi^\dagger \gamma^0$. The covariant derivative is described as $D_\mu = \partial_\mu + i\, e\, A_\mu$ and $F_{\mu\nu}$ retains the Abelian form above. The interaction term $\bar{\psi}\gamma^\mu A_\mu \psi$ from the covariant derivative follows directly from gauge invariance.

In gauge theories, different field configurations related by a gauge transformation describe the same physical situation, meaning the mathematical description has more variables than physical degrees of freedom. Because gauge symmetry embodies a redundancy of description, one must impose a gauge-fixing condition before quantisation. A common choice is the Lorentz gauge

$$\partial^\mu A_\mu = 0, \tag{2.13}$$

which can be implemented in the path-integral formalism via the Faddeev–Popov procedure [37], introducing a determinant factor ensuring that each physical configuration is counted exactly once [38, 39]. However, the Faddeev–Popov determinant is field-independent and reduces to an overall constant in the path integral. It can therefore be omitted without affecting the dynamics.

Perturbative QED is renormalisable, enabling a systematic loop expansion in the fine-structure constant $\alpha = e^2/(4\pi) \simeq 1/137$, as measured at low energies. Higher-order corrections account for such precision observables as the Lamb shift [40] and the electron's anomalous magnetic moment, for which theory and experiment now agree to better than one part in 10^{10} [41]. The theory also provides quantitatively accurate descriptions of processes like Compton scattering and e^+e^- annihilation, making QED the benchmark against which other quantum field theories are tested.

2.1.2. Non-Abelian Gauge Theories: Yang–Mills

A Yang–Mills theory is a non-Abelian generalisation of the gauge principle described in the previous section for the Abelian $U(1)$, formulated for a compact Lie group $\mathcal{G}$ [18], associated with a Lie algebra whose generators T^a obey the commutation relations

$$[T^a, T^b] = i\, f^{abc}\, T^c, \tag{2.14}$$

where f^{abc} is the structure constant of the gauge group satisfying the Jacobi identity,

$$f^{abe} f^{cde} + f^{bce} f^{ade} + f^{cae} f^{bde} = 0, \tag{2.15}$$

which ensures the consistency of the Lie algebra and the closure of the gauge symmetry under commutation. These relations encode the non-commutative structure of the gauge symmetry and are responsible for the gauge self-interactions. Consider generic matter fields $\phi(x)$ transforming in a representation R of $\mathcal{G}$, which transform as

$$\phi(x) \;\longrightarrow\; U_R(x)\,\phi(x), \qquad U_R(x) = \exp\left(i\,\alpha^a(x)\,T_R^a\right) \in R[\mathcal{G}], \tag{2.16}$$

where T_R^a are the generators of the Lie algebra in the representation R. One restores covariance by introducing the matrix-valued gauge connection

$$\mathbf{A}_\mu(x) = A_\mu^a(x)\,T_R^a \quad \text{with} \quad D_\mu = \partial_\mu - i\,g\,\mathbf{A}_\mu(x). \tag{2.17}$$

Under a local transformation $U_R(x)$, the gauge field transforms as

$$\mathbf{A}_\mu \;\longrightarrow\; U_R\,\mathbf{A}_\mu\,U_R^\dagger - \frac{i}{g}\,(\partial_\mu U_R)\,U_R^\dagger, \tag{2.18}$$

so that $D_\mu \phi \mapsto U_R\, D_\mu \phi$, and the matter kinetic term remains gauge-invariant. The curvature (field-strength) tensor generalises that of QED,

$$\mathbf{F}_{\mu\nu} = \frac{i}{g}[D_\mu, D_\nu] = \partial_\mu \mathbf{A}_\nu - \partial_\nu \mathbf{A}_\mu + i\, g[\mathbf{A}_\mu, \mathbf{A}_\nu] = F^a_{\mu\nu} T^a_R, \tag{2.19}$$

with components

$$F^a_{\mu\nu} = \partial_\mu A^a_\nu - \partial_\nu A^a_\mu + g\, f^{abc} A^b_\mu A^c_\nu. \tag{2.20}$$

The Yang-Mills gauge sector is described by

$$\mathcal{L}^{\text{YM}}_{\text{gauge}} = -\frac{1}{4}\, F^a_{\mu\nu} F^{\mu\nu a}, \tag{2.21}$$

whose commutator term generates three- and four-boson self-interactions. Matter fields, e.g., dirac fermions ψ can then couple to the gauge fields, in representation R as,

$$\mathcal{L}_{\text{fermion}} = \bar{\psi}\big(i\gamma^\mu D_\mu - m\big)\psi, \quad \text{with} \quad D_\mu = \partial_\mu - i\, g\, A^a_\mu T^a_R. \tag{2.22}$$

Quantisation of non-Abelian gauge theories necessitates gauge fixing, and in the path-integral formalism, the Faddeev–Popov procedure [37] introduces ghost fields to preserve unitarity and renormalisability. Gauge-boson self-interactions render the one-loop β-function negative in certain cases, depending on the gauge group and the number of light fermion species. This leads to *asymptotic freedom* [42, 43] in theories like $SU(3)_C$ with sufficiently few fermion flavours. In the infrared, the gauge coupling grows, and the theory is believed to exhibit *confinement*, particularly in pure Yang–Mills theories, where only gauge-invariant states appear in the physical spectrum. While perturbative renormalisability ensures consistency at high energies, non-perturbative features [44] such as confinement and mass gaps remain central to ongoing research.

With the formal machinery in place, one can now specialise to the two Yang-Mills sectors of the Standard Model: quantum chromodynamics, based on $SU(3)_C$, and the electroweak $SU(2)_L \times U(1)_Y$ gauge symmetry, the latter broken via the Higgs mechanism.

2.1.3. The Standard Model as a Non-Abelian Gauge Theory

The SM is a gauge theory built on the group $\mathcal{G}_{\text{SM}} = SU(3)_C \times SU(2)_L \times U(1)_Y$, describing the strong, weak, and electromagnetic interactions in a unified framework. Each factor in this product corresponds to a local symmetry with its own set of gauge fields and associated coupling constant. The non-Abelian nature of $SU(3)_C$ and $SU(2)_L$ gives rise to self-interactions among the corresponding gauge bosons, while the Abelian $U(1)_Y$ does not involve such terms.

The $SU(3)_C$ sector corresponds to quantum chromodynamics (QCD), the theory of strong interactions. It is mediated by eight gluon fields G_μ^A, associated with the generators T^A in the adjoint representation of the colour gauge group. The field strength tensor takes the form

$$G_{\mu\nu}^A = \partial_\mu G_\nu^A - \partial_\nu G_\mu^A + g_s f^{ABC} G_\mu^B G_\nu^C, \tag{2.23}$$

where $A = 1, \ldots, 8$ is the $SU(3)_C$ adjoint index, g_s is the strong coupling constant and f^{ABC} are the structure constants of $SU(3)$. The presence of the last term, quadratic in the gauge fields, leads to gluon self-interactions.

The electroweak sector is described by an $SU(2)_L \times U(1)_Y$ gauge theory, with gauge fields W_μ^a and B_μ, respectively. The $SU(2)_L$ field strength tensor is similarly given by

$$W_{\mu\nu}^a = \partial_\mu W_\nu^a - \partial_\nu W_\mu^a + g\epsilon^{abc} W_\mu^b W_\nu^c, \tag{2.24}$$

where $a = 1, 2, 3$ is the $SU(2)_L$ adjoint index, g is the $SU(2)_L$ coupling constant and ϵ^{abc} are the structure constants of $SU(2)$. The $U(1)_Y$ field strength is simply

$$B_{\mu\nu} = \partial_\mu B_\nu - \partial_\nu B_\mu, \tag{2.25}$$

as expected for an Abelian gauge field, with the gauge coupling given by g'. The gauge sector of the SM Lagrangian consists of the kinetic terms for these gauge fields:

$$\mathcal{L}_{\text{gauge}} = -\frac{1}{4} G_{\mu\nu}^A G^{\mu\nu A} - \frac{1}{4} W_{\mu\nu}^a W^{\mu\nu a} - \frac{1}{4} B_{\mu\nu} B^{\mu\nu}. \tag{2.26}$$

At this stage, all gauge fields are massless, and their interactions are entirely determined by the gauge symmetry and the structure of the field strength tensors.

Field	Spinor content	$(SU(3)_C, SU(2)_L, U(1)_Y)$
Q_L	$\begin{pmatrix} u_L \\ d_L \end{pmatrix}$	$(\mathbf{3}, \mathbf{2}, \frac{1}{6})$
u_R	u_R	$(\mathbf{3}, \mathbf{1}, \frac{2}{3})$
d_R	d_R	$(\mathbf{3}, \mathbf{1}, -\frac{1}{3})$
L_L	$\begin{pmatrix} \nu_L \\ e_L \end{pmatrix}$	$(\mathbf{1}, \mathbf{2}, -\frac{1}{2})$
e_R	e_R	$(\mathbf{1}, \mathbf{1}, -1)$

Table 2.1.: Fermionic field content of one SM generation and their corresponding gauge charges under the SM gauge group [49, 50].

Fermionic matter fields in the SM are organised into three generations, each consisting of identical gauge representations but differing in mass and flavour quantum numbers. The theory is chiral: the fermions' left- and right-handed components transform differently under $SU(2)_L$. Left-handed fields appear in weak isospin doublets, while right-handed fields are singlets. Quarks carry colour charge and thus transform as triplets under $SU(3)_C$, while leptons are colour singlets. The gauge quantum numbers of the fermionic fields in a single generation are summarised in Table 2.1. As one can notice, right-handed neutrinos are absent from the minimal SM; many well-motivated extensions introduce a gauge-singlet field $\nu_R \sim (\mathbf{1}, \mathbf{1}, 0)$, which permits Dirac masses and, through the Type-I Seesaw, naturally small Majorana masses [45–48].

The interactions between fermions and gauge fields are introduced via the covariant derivative [35],

$$D_\mu = \partial_\mu - ig_s G_\mu^A T^A - igW_\mu^a T^a - ig' B_\mu Y. \tag{2.27}$$

Here, capital indices $A = 1, \ldots, 8$ label the eight gluon fields associated with the generators T^A of $SU(3)_C$, while lowercase indices $a = 1, 2, 3$ label the weak gauge bosons W_μ^a and the generators $T^a = \tau^a/2$ of $SU(2)_L$ (here τ^a represent the 2×2 Pauli matrices). The Abelian gauge field B_μ has an associated hypercharge Y. The covariant derivative acts appropriately depending on the gauge representations of each field. The fermionic kinetic terms are then given by

$$\mathcal{L}_{\text{fermion}} = \sum_\psi \bar{\psi} i\gamma^\mu D_\mu \psi, \tag{2.28}$$

where the sum runs over all fermionic matter fields. This form ensures gauge invariance and leads to the characteristic interaction vertices of the SM.

It is important to note that, at this stage, no explicit mass terms for either the gauge bosons or fermions appear in the Lagrangian. This omission is a direct consequence of the requirement of gauge invariance. For instance, a mass term for a gauge boson of the form

$$\mathcal{L}_{\text{gauge}}^{\text{mass}} = \frac{1}{2} m^2 A_\mu A^\mu \tag{2.29}$$

is not invariant under the non-Abelian transformations for $SU(2)_L$ and $SU(3)_C$ gauge fields. As a result, such terms are forbidden in a gauge-invariant theory. Similarly, fermion mass terms of the form

$$\mathcal{L}_{\text{fermion}}^{\text{mass}} = -m_f \bar{\psi}\psi = -m_f(\bar{\psi}_L \psi_R + \bar{\psi}_R \psi_L), \tag{2.30}$$

explicitly couple left- and right-handed components of the fermion field. In the SM, however, ψ_L and ψ_R transform differently under $SU(2)_L \times U(1)_Y$: the left-handed fermions are placed in weak doublets, while the right-handed components are singlets. Consequently, the Dirac mass term is not invariant under the gauge group $\mathcal{G}_{\text{SM}}$ and cannot be included at this stage.

The generation of masses for both fermions and gauge bosons, while preserving gauge invariance, is achieved dynamically through spontaneous symmetry breaking. The formalism and implications of this will be addressed now.

Electroweak Symmetry Breaking

The principle of Electroweak Symmetry Breaking (EWSB) is built on the general concept of spontaneous symmetry breaking (SSB). SSB refers to the phenomenon where the ground state (vacuum) of a quantum field theory does not share the full symmetry of its Lagrangian. In systems with global symmetries, this leads to the appearance of massless scalar particles known as Goldstone bosons [51, 52]. For local (gauge) symmetries, however, the associated Goldstone bosons are absorbed by gauge fields, endowing them with mass. This is the basic principle of the famous *Higgs mechanism* [19–21].

To illustrate the idea of SSB, consider a real scalar field ϕ with a Lagrangian

$$\mathcal{L} = \frac{1}{2}(\partial_\mu \phi)(\partial^\mu \phi) - V(\phi), \quad \text{where} \quad V(\phi) = \frac{\mu^2}{2}\phi^2 + \frac{\lambda}{4}\phi^4. \tag{2.31}$$

For $\mu^2 < 0$, the potential develops minima at $\langle\phi\rangle = \pm v = \pm\sqrt{-\mu^2/\lambda}$, spontaneously breaking the $\mathbb{Z}_2$ symmetry $\phi \to -\phi$.

A more physically relevant example to this end is a complex scalar field Φ with a global $U(1)$ symmetry:

$$\mathcal{L} = (\partial_\mu \Phi)^*(\partial^\mu \Phi) - \mu^2|\Phi|^2 - \lambda|\Phi|^4. \tag{2.32}$$

When $\mu^2 < 0$, the vacuum takes the form $\langle\Phi\rangle = \frac{v}{\sqrt{2}}e^{i\theta}$, breaking the $U(1)$ symmetry spontaneously and yielding a massless Goldstone boson.

If instead the $U(1)$ is gauged, the scalar couples to a gauge field via the covariant derivative $D_\mu = \partial_\mu - ieA_\mu$, and the Lagrangian becomes:

$$\mathcal{L} = -\frac{1}{4}F_{\mu\nu}F^{\mu\nu} + |D_\mu \Phi|^2 - V(\Phi). \tag{2.33}$$

After spontaneous symmetry breaking and working in the unitary gauge, the Goldstone boson disappears from the spectrum, and the gauge field acquires a mass:

$$m_A = ev. \tag{2.34}$$

This is the essence of the Higgs mechanism, which provides a realisation of EWSB in the SM. In the SM, the electroweak gauge group $SU(2)_L \times U(1)_Y$ is spontaneously broken down to $U(1)_{\text{em}}$ when a complex scalar Higgs $SU(2)_L$ doublet Φ [53] given by

$$\Phi = \begin{pmatrix} \phi^+ \\ \phi^0 \end{pmatrix} : \left(\mathbf{1}, \mathbf{2}, \frac{1}{2}\right), \tag{2.35}$$

acquires a vacuum expectation value (vev) v. Φ is defined by the Lagrangian,

$$\mathcal{L}_{\text{Higgs}} = (D_\mu \Phi)^\dagger (D^\mu \Phi) - V(\Phi), \tag{2.36}$$

with the most general renormalisable potential, given by

$$V(\Phi) = -\mu^2 \Phi^\dagger \Phi + \lambda (\Phi^\dagger \Phi)^2, \tag{2.37}$$

with $\lambda > 0$ so that the potential is not unbounded from below, and $\mu^2 > 0$, so that the quadratic term in the potential is negative, rendering the symmetric point $\langle \Phi \rangle = 0$ unstable; the field then rolls to a non-zero minimum, triggering SSB. The vacuum configuration minimising this potential satisfies

$$\left. \frac{\partial V}{\partial \Phi} \right|_{\Phi = \langle \Phi \rangle} = 0, \qquad \text{with } \langle \Phi^\dagger \Phi \rangle = \frac{\mu^2}{2\lambda}. \tag{2.38}$$

The vacuum preserves electromagnetic $U(1)_{\text{em}}$ but breaks the weak symmetry:

$$\langle \Phi \rangle = \frac{1}{\sqrt{2}} \begin{pmatrix} 0 \\ v \end{pmatrix}, \quad v = \sqrt{\frac{\mu^2}{\lambda}} \approx 246\,\text{GeV}. \tag{2.39}$$

Here, v is the Higgs vev [54]. To study fluctuations around this vacuum, the Higgs doublet is expanded in terms of the physical degrees of freedom:

$$\Phi(x) = \begin{pmatrix} G^+ \\ \frac{v + h(x) + iG^0}{\sqrt{2}} \end{pmatrix}. \tag{2.40}$$

Φ contains four real scalar fields ($h(x)$, and the Goldstones G^0, $G^\pm$), but after electroweak symmetry breaking, all the Goldstones are "eaten" to become the longitudinal components of the $W^\pm$ and Z bosons. The remaining scalar degree of freedom $h(x)$ corresponds to the physical Higgs excitation as a perturbation around the vacuum. The parameterisation in Eq. (2.40) explicitly separates the constant vev v from the dynamical fluctuation $h(x)$. The couplings of the physical Higgs field to gauge bosons and fermions arise directly from this expansion.

With the covariant derivative for the Higgs doublet given by

$$D_\mu \Phi = \left(\partial_\mu - \frac{ig}{2} \tau^a W_\mu^a - \frac{ig'}{2} B_\mu \right) \Phi, \tag{2.41}$$

the mass terms for the gauge bosons can be generated by looking at the kinetic term for the Higgs field expanded around its vev (in the unitary gauge where the Goldstones

decouple, i.e., $G^{0,\pm} = 0$),

$$\begin{aligned}\mathcal{L}^{\Phi}_{\text{kin}} &= (D_\mu \Phi)^\dagger (D^\mu \Phi) \\ &\supset \frac{1}{2}(\partial_\mu h)(\partial^\mu h) + \frac{1}{8}(v+h)^2 \left[g^2 (W^1_\mu)^2 + g^2 (W^2_\mu)^2 + (g W^3_\mu - g' B_\mu)^2 \right].\end{aligned} \tag{2.42}$$

To diagonalise the mass matrix, the physical fields can be defined as

$$W^\pm_\mu = \frac{1}{\sqrt{2}}(W^1_\mu \mp i W^2_\mu), \tag{2.43}$$

$$\begin{pmatrix} Z_\mu \\ A_\mu \end{pmatrix} = \begin{pmatrix} \cos\theta_W & -\sin\theta_W \\ \sin\theta_W & \cos\theta_W \end{pmatrix} \begin{pmatrix} W^3_\mu \\ B_\mu \end{pmatrix}, \tag{2.44}$$

where the Weinberg angle θ_W is defined via the gauge couplings:

$$\tan\theta_W = \frac{g'}{g}, \qquad \sin\theta_W = \frac{g'}{\sqrt{g^2 + g'^2}}, \qquad \cos\theta_W = \frac{g}{\sqrt{g^2 + g'^2}}. \tag{2.45}$$

Inserting these into Eq. (2.42) gives:

$$\mathcal{L}^{\text{gauge}}_{\text{mass}} = \frac{1}{4} g^2 v^2 W^+_\mu W^{-\,\mu} + \frac{1}{8} v^2 (g^2 + g'^2) Z_\mu Z^\mu. \tag{2.46}$$

No mass term arises for A_μ, consistent with the photon being massless. The gluons remain massless as well, since they only couple to fields carrying non-trivial colour charges. Thus, the physical gauge boson masses are:

$$M_W = \frac{1}{2} g v, \qquad M_Z = \frac{1}{2}\sqrt{g^2 + g'^2}\, v. \tag{2.47}$$

This implies the well-known tree-level relation:

$$\frac{M_W}{M_Z} = \cos\theta_W. \tag{2.48}$$

This relation is a consequence of an approximate global *custodial isospin symmetry* [55], arising in the SM Higgs sector in the limit where the hypercharge gauge coupling g' vanishes. In this limit, the scalar potential exhibits an enhanced global $SU(2)_L \times SU(2)_R$ symmetry, spontaneously broken to the diagonal subgroup $SU(2)_V$, known as custodial $SU(2)$, which protects the so-called ρ parameter (defined as $\rho \equiv M_W^2 / M_Z^2 \cos^2\theta_W$) from large radiative corrections.

In this basis, the conserved electric charge operator takes its familiar form

$$Q = T_3 + \frac{Y}{2}, \tag{2.49}$$

the Gell-Mann–Nishijima [49,50] relation that links the weak isospin T_3 and hypercharge Y to the observed charge assignments of all SM particles. The scalar potential can also be expanded around the vev (Eq. (2.40)),

$$V(h) \supset -\frac{\mu^2}{2}(v+h)^2 + \frac{\lambda}{4}(v+h)^4, \tag{2.50}$$

which can be expanded as

$$V(h) \supset \frac{1}{2}(2\lambda v^2)h^2 + \lambda v h^3 + \frac{\lambda}{4}h^4. \tag{2.51}$$

The quadratic term gives the physical Higgs mass,

$$m_h^2 = 2\lambda v^2, \tag{2.52}$$

while the cubic and quartic terms correspond to self-interactions. The physical bosonic spectrum contains massive $W^\pm$, Z bosons, a massless photon and a massless gluon, along with the physical Higgs boson.

Yukawa Sector and Fermion Masses The spontaneous breaking of electroweak symmetry enables fermion mass generation through Yukawa interactions. The most general renormalisable Yukawa Lagrangian for SM fields is:

$$\mathcal{L}_{\text{Yukawa}} = -y_u^{ij}\bar{Q}_{L_i}\tilde{\Phi}u_{R_j} - y_d^{ij}\bar{Q}_{L_i}\Phi d_{R_j} - y_e^{ij}\bar{L}_{L_i}\Phi e_{R_j} + \text{h.c.}, \tag{2.53}$$

with Q_L, L_L, u_R, d_R, e_R being the fermionic fields described previously, $i,j = 1,2,3$ representing generation indices, $y_{u,d,e}^{ij}$ are complex Yukawa matrices in flavour space, and $\tilde{\Phi} = i\tau^2\Phi^*$. After EWSB, expanding Φ around its vev v (Eq. (2.40)) in the unitary gauge, the fermions acquire mass:

$$m_f^{ij} = \frac{y_f^{ij}v}{\sqrt{2}}, \quad f = u,d,e. \tag{2.54}$$

These mass matrices are, in general, non-diagonal and are subsequently diagonalised to obtain the physical mass eigenstates. The Yukawa matrices, which are free parameters in the SM, reproduce the observed charged-fermion mass spectrum and quark mixing encoded in the Cabibbo-Kobayashi-Maskawa (CKM) matrix [56, 57]. The physical spectrum contains six quarks (up, down, charm, strange, top, bottom) and three charged leptons (electron, muon, tau), as well as their antiparticles. The (anti)neutrinos remain massless in the minimal model due to the absence of right-handed neutrinos, at odds with neutrino-oscillation data predicting non-zero masses. Despite this shortcoming, the Higgs mechanism's elegant generation of gauge-boson and charged-fermion masses stands as one of the SM's major successes.

Putting pieces of the jigsaw described in the section together, the following compact expression encapsulates the full dynamics of the SM in a unified framework:

$$\mathcal{L}_{\text{SM}} = \mathcal{L}_{\text{gauge}} + \mathcal{L}_{\text{fermion}} + \mathcal{L}_{\text{Higgs}} + \mathcal{L}_{\text{Yukawa}}. \tag{2.55}$$

Quantisation

To extract physical observables from the Standard Model, one must quantise the classical Lagrangian. The path-integral formalism [58] is a manifestly Lorentz-covariant approach and is especially convenient for gauge theories like the SM.

To start off, the generating functional for Green's functions is

$$Z[J] \;=\; \int \mathcal{D}\phi \, \exp\Big\{ iS_{\text{SM}}[\phi] + i \int d^4x \, J(x)\, \phi(x) \Big\}, \tag{2.56}$$

where ϕ collects all dynamical fields and J is an auxiliary source. The action $S_{\text{SM}}[\phi]$ contains the full classical SM Lagrangian presented before. The generating functional $Z[J]$ encodes all time-ordered Green functions; functional differentiation with respect to J yields n-point correlation functions.

The procedure is implemented by inserting a representation of unity,

$$1 \;=\; \int \mathcal{D}\alpha^a \; \delta\Big(G^a[A^\alpha]\Big) \; \det\left(\frac{\delta G^a[A^\alpha]}{\delta \alpha^b} \right), \tag{2.57}$$

where $A_\mu^{a\alpha}$ denotes the gauge-transformed field, and $G^a[A] = 0$ is the gauge-fixing condition. The Jacobian of this change of variables yields the Faddeev–Popov determi-

nant. Insertion of this identity into the path integral restricts the functional measure to a single representative per gauge orbit,

$$Z = \int \mathcal{D}A^a_\mu \; \delta\Big(G^a[A]\Big) \; \det\left(\frac{\delta G^a[A^\alpha]}{\delta \alpha^b}\right) \; e^{iS[A]}. \tag{2.58}$$

The delta-functional form is not suitable for perturbative computations, and therefore, a Gaussian representation is adopted,

$$\delta\big(G^a[A]\big) \;\longrightarrow\; \exp\left(-\tfrac{i}{2\xi}\int d^4x\,[G^a(x)]^2\right), \tag{2.59}$$

introducing the familiar covariant gauge-fixing Lagrangian,

$$\mathcal{L}_{\rm GF} = -\frac{1}{2\xi}\big(\partial^\mu A_\mu\big)^2, \tag{2.60}$$

for an Abelian field, and

$$\mathcal{L}_{\rm GF} = -\frac{1}{2\xi}\big(\partial^\mu A^a_\mu\big)^2, \tag{2.61}$$

for a non-Abelian multiplet A^a_μ, with a common parameter ξ chosen for simplicity. In spontaneously broken gauge theories such as the electroweak SM, the gauge-fixing functions are generalised to include scalar fields in order to eliminate gauge–Goldstone mixing. For instance, the Z-boson gauge-fixing function reads

$$G[Z] = \partial_\mu Z^\mu + \xi_Z M_Z G^0, \tag{2.62}$$

where denotes the neutral Goldstone boson. Analogous functions are introduced for the charged gauge bosons, ensuring that the propagator matrix is diagonalised in the gauge–Goldstone sector.

Gauge fixing introduces the Faddeev–Popov determinant, which is expressed as a path integral over auxiliary anticommuting fields. Using the identity

$$\det\left(\frac{\delta G^a[A^\alpha]}{\delta\alpha^b}\right) = \int \mathcal{D}\bar{c}\,\mathcal{D}c \;\exp\left(i\int d^4x\;\bar{c}^a(x)\,\frac{\delta G^a[A^\alpha(x)]}{\delta\alpha^b(y)}\,c^b(y)\right), \tag{2.63}$$

the determinant is exponentiated with Grassmann-valued scalars c^a, $\bar{c}^a$, which are the Faddeev–Popov ghost fields. For the covariant gauge choice $G^a[A] = \partial^\mu A^a_\mu$, one

obtains explicitly

$$\frac{\delta G^a[A^\alpha]}{\delta \alpha^b} = -\partial^\mu D_\mu^{ab}[A], \tag{2.64}$$

where D_μ^{ab} is the gauge-covariant derivative in the adjoint representation. The ghost Lagrangian in unbroken Yang–Mills theories is therefore

$$\mathcal{L}_{\text{ghost}} = \bar{c}^a \left(-\partial^\mu D_\mu^{ab}\right) c^b. \tag{2.65}$$

After electroweak symmetry breaking, the gauge-fixing condition $G^a[A, \phi]$ depends on scalar fields, and the ghost sector acquires mass terms as well as interactions with the Goldstone and Higgs fields. Ghosts are Lorentz scalars but obey Fermi–Dirac statistics, and they contribute only through loop diagrams.

The gauge-fixed action $S_{\text{SM}} + \int d^4x \left(\mathcal{L}_{\text{GF}} + \mathcal{L}_{\text{ghost}}\right)$ is invariant under a global fermionic transformation called the *Becchi–Rouet–Stora–Tyutin (BRST) symmetry* [59,60]. BRST invariance ensures unitarity and makes physical observables independent of the gauge parameter. At the quantum level, it yields the *Slavnov–Taylor identities*, the non-Abelian extension of Ward identities, which constrain Green functions and play a central role in renormalisation theory [61,62].

The effective Lagrangian employed in perturbation theory is therefore

$$\mathcal{L}_{\text{SM}}^{\text{eff.}} = \mathcal{L}_{\text{gauge}} + \mathcal{L}_{\text{fermion}} + \mathcal{L}_{\text{Higgs}} + \mathcal{L}_{\text{Yukawa}} + \mathcal{L}_{\text{GF}} + \mathcal{L}_{\text{ghost}}. \tag{2.66}$$

The quadratic part defines the free propagators. For example, in the R_ξ gauge, a massive gauge boson has the following propagator,

$$D_{\mu\nu}(k) = \frac{-i}{k^2 - M^2}\left[g_{\mu\nu} - \frac{k_\mu k_\nu}{k^2}\right] - \frac{i\,\xi\,k_\mu k_\nu}{(k^2 - \xi M^2)\,k^2}, \tag{2.67}$$

which reduces to the familiar Feynman-'t Hooft form when $\xi = 1$. Connected Green functions follow from

$$W[J] \;=\; -i\,\ln Z[J], \tag{2.68}$$

and the one-particle-irreducible (1PI) generating functional is obtained via the Legendre transform [63]

$$\Gamma[\phi] \;=\; W[J] \;-\; \int d^4x\, J(x)\,\phi(x), \qquad \phi(x) = \frac{\delta W[J]}{\delta J(x)}, \tag{2.69}$$

where $\phi(x)$ corresponds to the vacuum expectation value of the field in the presence of the source J. The functional $\Gamma[\phi]$ plays the role of the effective action; its stationary points yield the quantum-corrected equations of motion, and its vertices correspond to 1PI amplitudes. Expanding the path integral in powers of the couplings yields the perturbative series that underpins all practical SM calculations. The diagrammatic Feynman rules for these perturbative expansions are systematically derived from the interaction terms in the Lagrangian via Wick contractions in the interaction picture. In modern computations, tools such as `FeynRules` [64] automate this derivation by taking a user-defined Lagrangian as input and generating the corresponding Feynman rules in a format compatible with event generators and symbolic calculators. The same formal machinery is also employed in the various effective field theory extensions of the SM.

Renormalisation

At the tree level, particularly in the unitary gauge, the parameters in the Lagrangian appear to have direct physical meaning. Mass terms, for instance, correspond straightforwardly to the physical masses of particles. However, when quantum corrections are included via loop diagrams, this simple interpretation no longer holds. Loop integrals typically introduce divergences, and as a result, the bare parameters in the Lagrangian become ill-defined without further modification.

To address this, the theory is first *regularised* to make divergent expressions well-defined. One such regularisation method is dimensional regularisation [65], where the number of spacetime dimensions is taken as $d = 4 - 2\epsilon$, and divergences manifest as poles in $1/\epsilon$. A simple example is a one-loop self-energy diagram, which can be schematically written as:

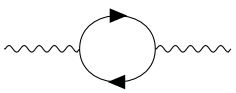

$$= \mu^{2\epsilon} \int \frac{d^d k}{(2\pi)^d} \frac{\mathrm{Tr}[\gamma^\mu (\not{k} + m)\gamma^\nu (\not{k} - \not{p} + m)]}{(k^2 - m^2)[(k-p)^2 - m^2]}, \tag{2.70}$$

where μ is the arbitrary renormalisation scale introduced so that the loop integral has the correct mass dimension in d dimensions, and $\not{p} = \gamma^{\alpha} p_{\alpha}$. This integral diverges for $d \geq 4$, for large loop momentum k and requires renormalisation.

After regularisation, the next step is *renormalisation*, where the bare parameters are redefined in terms of finite, physical (renormalised) quantities. Consider a generic coupling g and a field ϕ. In $d = 4 - 2\epsilon$ dimensions, the bare coupling must carry mass dimension, so the renormalisation scale μ ensures that the renormalised coupling remains dimensionless. The bare quantities g_0 and ϕ_0 are then related to their renormalised counterparts g_R and ϕ_R via:

$$g_0 = \mu^{2\epsilon} Z_g(\mu)\, g_R = \mu^{2\epsilon} \left(1 + \delta Z_g(\mu)\right) g_R, \tag{2.71}$$

$$\phi_0 = Z_\phi^{1/2}(\mu)\, \phi_R = \left(1 + \frac{1}{2}\delta Z_\phi(\mu)\right) \phi_R, \tag{2.72}$$

where Z_g, Z_ϕ are the renormalisation constants, δZ_g, δZ_ϕ are called *counterterms*, and μ is the renormalisation scale introduced in dimensional regularisation to preserve the correct dimensions. The original Lagrangian expressed in terms of bare quantities can then be rewritten as:

$$\mathcal{L}(g_0, \phi_0) = \mathcal{L}(g_R, \phi_R) + \mathcal{L}_{\text{ct}}(g_R, \phi_R, \delta Z_g, \delta Z_\phi), \tag{2.73}$$

where $\mathcal{L}_{\text{ct}}$ contains the counterterms. These counterterms generate Feynman rules that cancel the divergences arising from loop diagrams.

In dimensional regularisation, divergences typically show up as:

$$\Delta = \frac{1}{\epsilon} + \log(4\pi) - \gamma_E + \mathcal{O}(\epsilon), \tag{2.74}$$

where γ_E is the Euler–Mascheroni constant. Subtraction schemes differ in how they handle this divergence:

- The on-shell scheme imposes renormalisation conditions such that the propagators have poles at physical masses and residues equal to i.
- The Minimal Subtraction (MS) scheme removes only the $1/\epsilon$ pole.
- The Modified Minimal Subtraction ($\overline{\text{MS}}$) scheme removes the entire Δ term [66].

A theory is *renormalisable* if all ultraviolet divergences can be absorbed into a finite number of parameters and field redefinitions. The SM satisfies this criterion. In such cases, a finite set of experimental measurements is sufficient to determine the theory's free parameters and make finite predictions.

The power-counting technique [67] allows one to determine whether a theory is renormalisable by evaluating the *superficial degree of divergence* D of a Feynman diagram. For a diagram with E_f external fermion lines, E_ϕ scalar lines, E_V vector lines, and vertex couplings with mass-dimension $[g_v]$, the degree of divergence is:

$$D = 4 - \frac{3}{2}E_f - E_\phi - E_V - \sum_v [g_v]. \tag{2.75}$$

If any $[g_v] < 0$, then D can become arbitrarily large with increasing loop order, and an infinite number of divergent diagrams may appear. Such theories are termed *non-renormalisable*. A well-known example is the four-fermion interaction in Fermi's theory,

$$\mathcal{L}_{\text{Fermi}} = -\frac{G_F}{\sqrt{2}}(\bar{\psi}\gamma^\mu\psi)(\bar{\psi}\gamma_\mu\psi), \tag{2.76}$$

where G_F represents the Fermi constant, which is a coupling with mass-dimension of $[G_F] = -2$. These theories formally require an infinite number of counterterms but can still yield valid predictions when interpreted as effective field theories, valid below a certain energy scale.

2.1.4. The facets and the successes of the SM

With the formal machinery now in place, one can and should now ask how the SM stands up to real measurements. Three lines of evidence will guide the discussion. First come the precision tests and predictive power, where an abundance of accurately measured observables lets us chase down loop effects and box in possible new physics. Next is Higgs physics: the 2012 discovery of the scalar resonance that rounds out the particle roster, and whose properties give us a direct view of electroweak symmetry breaking. Finally, flavour physics, where the subtle pattern of quark and lepton mixing still supplies some of the tightest constraints on physics beyond the SM.

Though they may seem like separate chapters, these themes weave together: gauge symmetry sets the stage for precision tests, the Higgs completes the story of symmetry

breaking, and flavour exposes the model's internal scaffolding, thus showing both the coherence of the theory and the variety of ways in which it is put to the test. At the same time, certain theoretical constraints, most notably the requirement of perturbative unitarity in high-energy scattering, lead to the necessity of including key elements such as the Higgs boson and indicate the energy scales at which new physics would be required for the SM to remain consistent. A closer examination of perturbative unitarity now follows, as its constraints anticipate several of the structural features that are built into the SM.

Perturbative Unitarity in the SM

Perturbative unitarity [24, 68, 69] provides a key consistency requirement in quantum field theory. It restricts the energy dependence of scattering amplitudes and often indicates the scale at which new physics must emerge. The condition follows from the unitarity of the S-matrix, which relates the initial and final states in a scattering process:

$$S^\dagger S = \mathbb{1}. \tag{2.77}$$

Writing $S = \mathbb{1} + iT$ leads to the identity

$$-i(T - T^\dagger) = T^\dagger T. \tag{2.78}$$

Taking the forward matrix element between asymptotic states $|i\rangle$ gives the optical theorem [70]:

$$\mathrm{Im}\,\mathcal{M}_{ii} = \frac{1}{2}\sum_X \int d\mathrm{LIPS}\,(2\pi)^4\delta^4(p_i - p_X)\,|\mathcal{M}_{i\to X}|^2, \tag{2.79}$$

where $\mathcal{M}_{i\to X}$ is the amplitude for scattering into any allowed intermediate state X, and dLIPS denotes the Lorentz-invariant phase space.

For $2 \to 2$ scattering in the centre-of-mass frame, the amplitude may be expanded in partial waves labelled by total angular momentum J:

$$\mathcal{M}(s,\theta) = 16\pi \sum_{J=0}^{\infty} (2J+1)\, a_J(s)\, P_J(\cos\theta), \tag{2.80}$$

with $a_J(s)$ the partial wave amplitudes and P_J the Legendre polynomials. The inverse relation is

$$a_J(s) = \frac{1}{32\pi} \int_{-1}^{1} d\cos\theta \, P_J(\cos\theta) \, \mathcal{M}(s,\theta). \tag{2.81}$$

Unitarity then requires that, for elastic scattering,

$$\mathrm{Im}(a_J) \geq |a_J|^2. \tag{2.82}$$

This confines a_J to lie within the Argand circle of radius $1/2$ centred at $(0, 1/2)$ in the complex plane. In particular, the real part must satisfy the model-independent bound

$$|\mathrm{Re}(a_J)| \leq \frac{1}{2}. \tag{2.83}$$

For processes involving spin, the more general Jacob–Wick formalism [68] extends the partial wave expansion to helicity amplitudes, by projecting onto states of definite angular momentum and helicities λ_i. The amplitude can then be written as

$$\mathcal{M}_{\lambda_3\lambda_4;\lambda_1\lambda_2}(s,\theta,\phi) = 8\pi \sum_J (2J+1) \, d^J_{\lambda,\lambda'}(\theta) \, e^{i(\lambda-\lambda')\phi} \, T^J_{\lambda_3\lambda_4;\lambda_1\lambda_2}(s), \tag{2.84}$$

where $\lambda = \lambda_1 - \lambda_2$, $\lambda' = \lambda_3 - \lambda_4$, and the $d^J_{\lambda,\lambda'}(\theta)$ are Wigner d-matrices. The quantities T^J are the partial wave helicity amplitudes. Unitarity then implies

$$\mathrm{Im}\, T^J = T^{J\dagger} T^J, \tag{2.85}$$

and for elastic scattering simplifies to

$$|\mathrm{Re}\, T^J_{\lambda_3\lambda_4;\lambda_1\lambda_2}| \leq \frac{1}{2}. \tag{2.86}$$

This allows unitarity constraints to be applied channel by channel, while keeping track of spin and angular momentum.

A classic example is provided by Fermi's four-fermion theory of weak interactions:

$$\mathcal{L}_{\mathrm{Fermi}} = -\frac{G_F}{\sqrt{2}} (\bar{\psi}\gamma^\mu\psi)(\bar{\psi}\gamma_\mu\psi), \tag{2.87}$$

with G_F the Fermi constant. This yields amplitudes that grow with centre-of-mass energy as $\mathcal{M} \sim G_F s$, violating the unitarity bound for $\sqrt{s} \gtrsim 300$ GeV. This signals the breakdown of the effective theory and the need for a UV completion. The discovery of the W boson provided exactly that, restoring unitarity through propagator suppression at high energies.

One of the most striking cases involves the scattering of longitudinally polarised vector bosons. The longitudinal polarisation vectors scale as $\epsilon_L^\mu \sim p^\mu / M$ at high energies, so the amplitude increases with energy. In the process $W_L^+ W_L^- \to W_L^+ W_L^-$, the amplitude receives contributions from gauge interactions, Goldstone boson exchange, and Higgs exchange. If the Higgs contribution is omitted, the amplitude grows as $\mathcal{M} \sim E^2/v^2$, eventually exceeding the unitarity limit. This can be made precise by computing the $J = 0$ partial wave:

$$a_0 = \frac{1}{32\pi} \int_{-1}^{1} d\cos\theta \, \mathcal{M}(s, \theta). \tag{2.88}$$

For longitudinal W^+W^- scattering at high energy, the leading term behaves as

$$a_0 \sim \frac{s}{16\pi v^2}. \tag{2.89}$$

Requiring $|\mathrm{Re}(a_0)| \leq 1/2$ leads to the constraint

$$\sqrt{s} \lesssim 1.2 \text{ TeV}. \tag{2.90}$$

This is the essence of the Lee–Quigg–Thacker bound [71], which showed that new physics must appear below the TeV scale to preserve unitarity in electroweak vector boson scattering. The discovery of a 125 GeV scalar confirmed that the Standard Model Higgs is sufficient to cancel the leading energy growth and maintain consistency.

Perturbative unitarity, therefore, plays a dual role: it serves as a theoretical check on self-consistency and offers practical guidance on the energy range over which a theory can be trusted. When amplitudes exceed the unitarity bound, new particles must be introduced or a strongly coupled regime must be entered. In either case, unitarity constraints act as signposts toward ultraviolet completions.

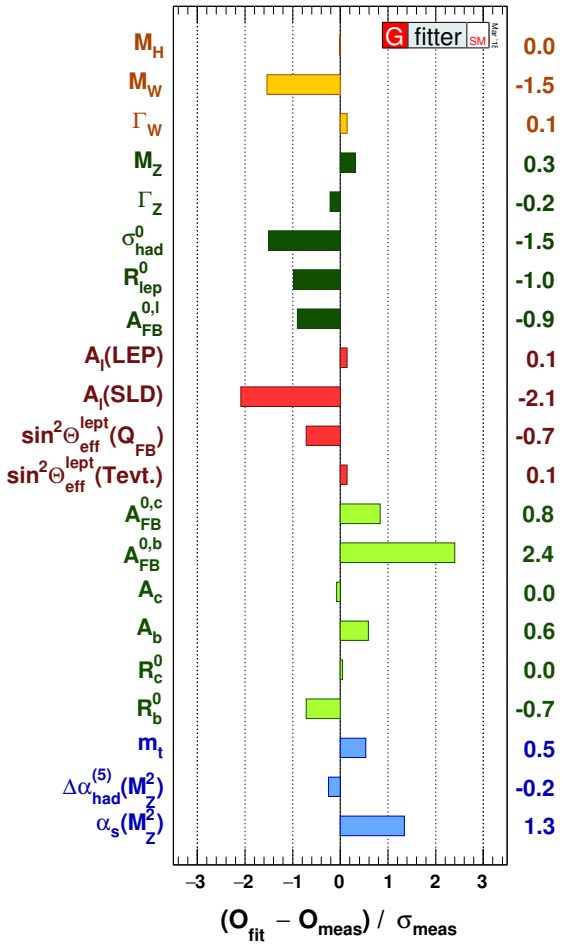

Figure 2.1.: One-dimensional pull plot for every electroweak-precision observable (or SM input) $\mathcal{O}_i$, showing the difference between its direct measurement and the value inferred from the global fit. [72]

The Predictive Power and Precision Tests of the Standard Model

The SM's enduring success rests as much on its predictive power as on its descriptive breadth. Once the gauge group and particle content are fixed, local gauge invariance dictates the form of kinetic and interaction terms and determines the couplings between matter and gauge fields through the covariant derivative. As a result, all interaction vertices involving gauge bosons and fermions are fixed by symmetry principles, leaving only a relatively small set of free parameters: three gauge couplings, six quark masses, three charged-lepton masses, the Higgs mass and vev, and four CKM parameters (discussed later in this section).

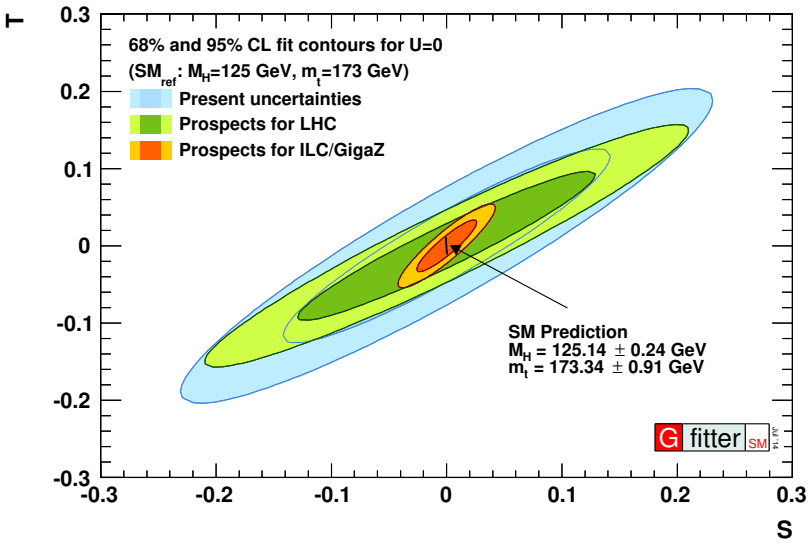

Figure 2.2.: Best fit to the Peskin-Takeuchi S and T parameters at the LHC and its prospect at a benchmark future collider by the GFITTER collaboration [72].

Because of this economy of input, many observables are over-constrained. Electroweak quantities, for example, can be expressed in terms of the precisely measured inputs like G_F, M_W and M_Z, enabling robust predictions. Notably, the masses of the top quark and the Higgs boson were estimated indirectly well before their discovery. At the tree level, one finds the familiar relation

$$\sin^2\theta_W \;=\; 1 - \frac{M_W^2}{M_Z^2}, \tag{2.91}$$

which is modified by loop corrections. A convenient diagnostic for these radiative effects is the ρ-parameter discussed previously, which equals unity at tree level due to custodial $SU(2)$ symmetry. Any deviation parameterised as $\Delta\rho \equiv \rho - 1$, signals loop effects or new sources of custodial breaking. For example, in the SM, the leading one-loop contribution arises from the top-bottom mass splitting, and for $m_b \ll m_t$,

$$\Delta\rho \;=\; \frac{3\,G_F\,m_t^2}{8\sqrt{2}\,\pi^2}, \tag{2.92}$$

which once provided a sensitive indirect probe of the top-quark mass [73].

Such relations form the backbone of global electroweak fits, which synthesise results from many observables across a range of energy scales. The one-dimensional pull plot shown in Fig. 2.1 illustrates the internal consistency of the SM: each point compares a

direct measurement to its value inferred from the global fit. Particularly valuable are the measurements from LEP and SLC, which determine the Z boson's total and partial widths, forward-backward and left-right asymmetries, the effective weak mixing angle $\sin^2\theta_{\text{eff}}$, and the W mass to unprecedented precision. Additional constraints come from low-energy observables such as atomic parity violation, Møller scattering, and neutrino–nucleon scattering. Among these, the extraction of the number of light neutrino species from the invisible Z width stands out as a textbook success of the model [74].

Beyond the level of individual observables, global fits like those from the GFITTER collaboration [72] test the SM at the quantum level. These analyses not only verified the internal consistency of the theory but also anticipated the values of m_t and m_h within narrow windows before the LHC era. The same framework is used to constrain new physics indirectly by incorporating its virtual effects. Oblique corrections, defined as new physics contributions to the vacuum polarisation (self-energy) diagrams of electroweak gauge bosons, are encapsulated by the Peskin–Takeuchi parameters S, T, and U [75]. These parameters provide a compact and model-independent way to characterise the impact of heavy new states on precision observables, assuming that new physics primarily affects gauge boson propagators rather than their vertices or box diagrams. The T parameter is sensitive to custodial symmetry breaking, while S can be shifted by the presence of additional chiral fermions or extended gauge sectors. The current and projected fits to these parameters are illustrated in Fig. 2.2, which also highlights the significant improvements anticipated from future colliders.

There are several ongoing efforts to sharpen electroweak tests, particularly improving the precision of Z-pole observables. While the original LEP and SLC programs already achieved unprecedented accuracy in many such measurements, a new generation of e^+e^- colliders operating at $\sqrt{s} = M_Z$ could reduce experimental uncertainties by one or two orders of magnitude [76–78]. This level of precision would enable exceptional sensitivity to loop-level effects and subtle deviations from SM predictions. Such improvements can reveal new physics through shifts in electroweak input schemes and the global fit landscape, while also enhancing the discriminating power of precision observables [79].

Additional theoretical constraints stem from the requirement of anomaly cancellation, which is non-trivially satisfied by the chiral structure and charge assignments of one SM fermion generation [23]. At much higher energies, the approximate conver-

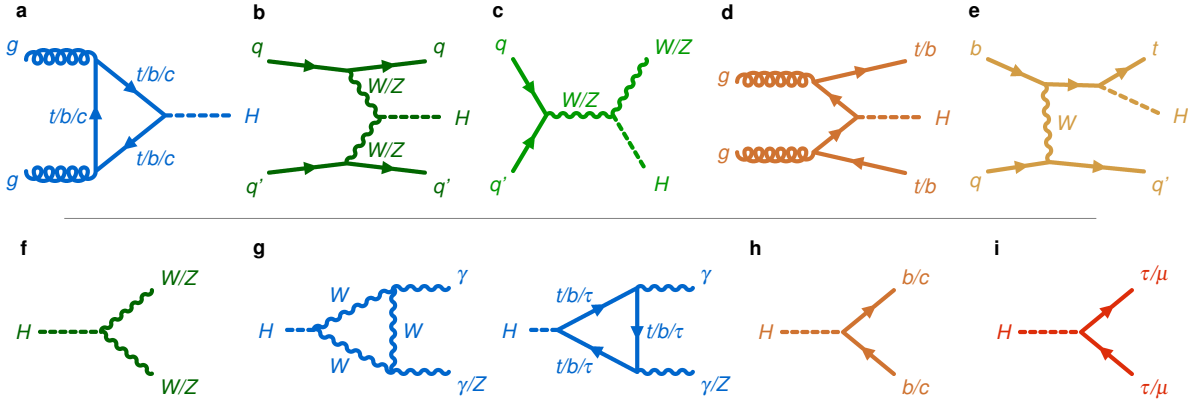

Figure 2.3.: Feynman topologies representing the various dominant production and decay modes of the Higgs boson [81].

gence of the three gauge couplings [80] suggests the intriguing possibility of grand unification, providing another layer of theoretical coherence.

The SM's gauge symmetry, renormalisability, and minimal field content, therefore, give rise to a remarkably predictive theory. Precision tests rooted in these foundations continue to serve as some of the most powerful indirect probes of new physics, placing stringent constraints on a wide range of possible extensions to the SM.

Higgs Physics

The discovery of the Higgs boson at the LHC in 2012 [10, 11] marked a milestone in particle physics, finally completing the SM particle roster, by confirming the Higgs mechanism and an explanation of particle masses. Beyond its role in the theoretical consistency of the SM, the Higgs boson is a unique scalar particle whose couplings and quantum numbers are subject to stringent experimental scrutiny. The various production and decay topologies relevant to these tests are shown in Fig. 2.3.

At hadron colliders such as the LHC, the Higgs boson is predominantly produced via gluon fusion ($gg \to h$, ggF), mediated primarily by a top-quark loop, accounting for 85% of total production at $\sqrt{s} = 13$ TeV. Other important production mechanisms include weak/vector boson fusion (WBF/VBF), associated production with a vector boson ($q\bar{q}' \to Vh$, with $V = W^{\pm}, Z$), and associated production with top quarks ($t\bar{t}h$, th). Each production mode provides sensitivity to different aspects of Higgs couplings

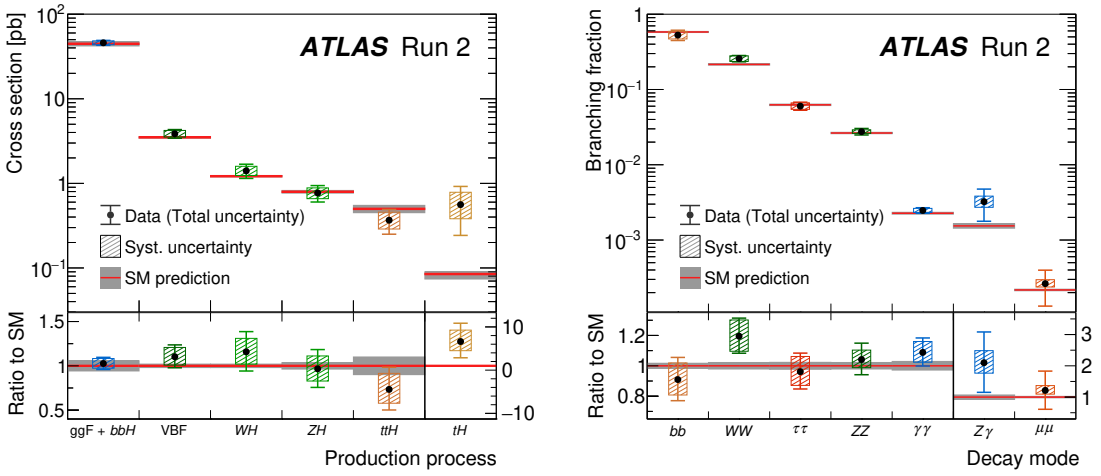

(a) (b)

Figure 2.4.: Measured and SM expectations for **(a)** Higgs-boson production cross-sections for fixed SM-like branching ratios, and **(b)** Higgs branching fractions for the dominant decay channels for fixed SM-like production cross-sections. In both cases, the panels underneath display the ratio of the measurement to the SM prediction. Vertical bars denote the $\pm 1\sigma$ uncertainties [82].

and offers complementary experimental coverage, as illustrated by the cross-section measurements in Fig. 2.4(a).

The decay channels of the SM Higgs boson with $m_h \simeq 125\,\text{GeV}$ reflect its couplings to mass and loop-induced processes. The dominant mode is $h \to b\bar{b}$, followed by decays to $\tau^+\tau^-$ and to massive vector bosons through off-shell transitions, $h \to WW^*$ and ZZ^*. Loop-induced decays such as $h \to \gamma\gamma$, $Z\gamma$ and gg also occur, with $h \to \gamma\gamma$ being especially important because of its clean experimental signature, playing a crucial role in the discovery of the Higgs. The total decay width is extremely narrow, $\Gamma_h^{\text{SM}} \approx 4\,\text{MeV}$ [81], and cannot be measured directly, necessitating indirect methods (see the branching-ratio comparison in Fig. 2.4(b)).

Spin and parity analyses have confirmed that the observed resonance is a spin-0, CP-even scalar, which is in agreement with SM expectations. This identification relies on angular correlations in decays such as $h \to ZZ^* \to 4\ell$, which robustly exclude alternative spin hypotheses with high confidence [83].

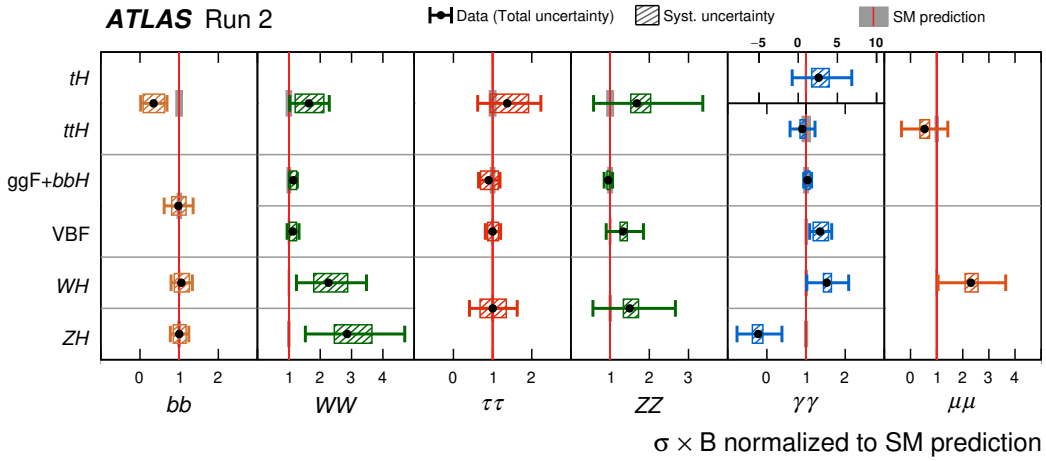

Figure 2.5.: Signal-strength ratios shown for a range of Higgs-boson production and decay channel combinations. Horizontal bars indicate the $\pm 1\sigma$ experimental uncertainties, and the narrow grey bands mark the SM theory errors [82].

Measurements of Higgs signal strengths (μ_h) in various production and decay channels are parametrised as

$$\mu_h = \frac{\sigma(pp \to h) \cdot \mathrm{BR}(h \to X)}{\sigma^{\mathrm{SM}} \cdot \mathrm{BR}^{\mathrm{SM}}}, \tag{2.93}$$

and currently show good agreement with SM predictions, as summarised in Fig. 2.5. These measurements place important constraints on possible deviations from SM couplings, which could arise in scenarios with extended Higgs sectors or from higher-dimensional operators in an effective field-theory framework. A distinctive prediction of the Higgs mechanism is the presence of self-interactions in the scalar potential:

$$\mathcal{L} \supset -\lambda v h^3 - \frac{\lambda}{4} h^4, \quad \text{with} \quad \lambda = \frac{m_h^2}{2v^2}. \tag{2.94}$$

At zero temperature, the cubic term fixes the trilinear coupling, $g_{hhh} = 3m_h^2/v$, while the quartic term yields the quartic coupling $g_{hhhh} = 3m_h^2/v^2$. The former can be accessed through di-Higgs production ($pp \to hh$), already a major target for the HL-LHC, whereas the latter can reveal itself in the much rarer triple Higgs process ($pp \to hhh$) [84] and therefore calls for the higher energies and luminosities envisioned at future facilities.

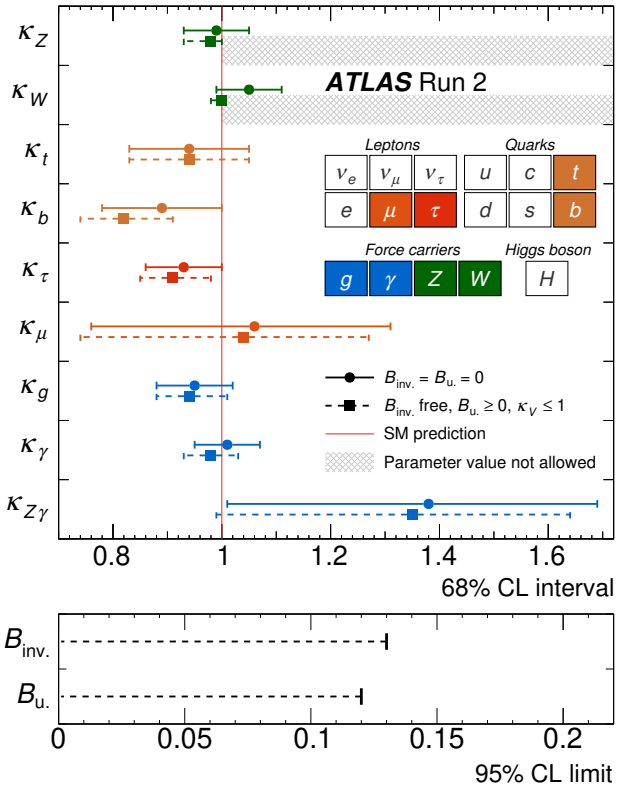

Figure 2.6.: Best-fit Higgs coupling modifiers in the κ-framework, for each particle species, including the effective κ_γ, $\kappa_{Z\gamma}$ and κ_g vertices. Horizontal bars give the 68% confidence intervals. Solid circles show the fit obtained when no invisible ($B_{\text{inv.}}$) or undetected ($B_{\text{u.}}$) decays are allowed; this fit agrees with the SM at the 61% p-value level. Dashed squares correspond to a fit in which $B_{\text{inv.}}$ and $B_{\text{u.}}$ may contribute to the total width, subject to $\kappa_V \leq 1$ and $B_{\text{u.}} \geq 0$. The lower strip presents the 95% CL upper limits on $B_{\text{inv.}}$ and $B_{\text{u.}}$ [82].

Both self-couplings are more than just bookkeeping parameters: they shape the Higgs potential at finite temperature and, in turn, the nature of the electroweak phase transitions (EWPT). Any departure of g_{hhh} or g_{hhhh} from their SM values could modify the electroweak vacuum structure, hence the strength of EWPTs, opening the door to electroweak baryogenesis and leaving imprints in precision electroweak observables. Higgs self-interaction measurements thus link collider physics to the early Universe, making them a uniquely powerful probe of BSM physics.

The κ-Framework A widely used and model-independent approach to parameterising potential deviations from SM Higgs predictions is the so-called κ-framework [85],

where the Higgs couplings to SM particles are rescaled by dimensionless factors κ_i,

$$\kappa_i = \frac{g_i}{g_i^{\mathrm{SM}}}, \tag{2.95}$$

such that $\kappa_i = 1$ corresponds to the SM expectation and any deviations can serve as signposts of new physics. For example, the relevant fermion and gauge interaction terms (in the broken phase) are modified as

$$\mathcal{L} \supset \kappa_f \frac{m_f}{v} h \bar{f} f + \kappa_V \frac{2M_V^2}{v} h V_\mu V^\mu + \ldots, \tag{2.96}$$

with κ_f and κ_V rescaling the Higgs couplings to fermions and vector bosons, respectively. Loop-induced processes such as $h \to \gamma\gamma$ and $h \to gg$ are similarly parametrised by effective couplings κ_γ and κ_g, which can capture contributions from new particles running in the loops.

The global fit to these coupling modifiers is illustrated in Fig. 2.6 [82]. Such fits provide a systematic way to constrain deviations from SM couplings without assuming a specific UV completion. Although the framework neglects possible energy-dependent shape effects, it remains a robust benchmark for testing the SM Higgs paradigm and for bounding new-physics scenarios that might alter the observed pattern of Higgs interactions.

As of today, Higgs physics remains a central focus of the LHC programme and of future collider proposals. While current measurements are broadly consistent with SM expectations, a full characterisation of the Higgs sector will be essential for either revealing or further constraining new physics.

Flavour Physics

Flavour physics studies transitions between the three generations of quarks and leptons. In the quark sector, such transitions arise because the weak–interaction eigenstates are not aligned with the mass eigenstates that diagonalise the Yukawa matrices. The resulting charged-current interactions are governed by the unitary CKM matrix V_{CKM} [56, 57]:

$$\mathcal{L}_W \;=\; -\frac{g}{\sqrt{2}}\, \bar{u}_L^i\, \gamma^\mu\, V_{\mathrm{CKM}}^{ij}\, d_L^j\, W_\mu^+ + \mathrm{h.c.}, \tag{2.97}$$

where $i, j = 1, 2, 3$ label the generations. Unitarity forces V_{CKM} to contain just three mixing angles and one irreducible CP-violating phase. Its hierarchical pattern implies a strong suppression of flavour change between distant generations.

In the Wolfenstein parameterisation [86], the CKM matrix takes the approximate form:

$$V_{\text{CKM}} \approx \begin{pmatrix} 1 - \frac{\lambda^2}{2} & \lambda & A\lambda^3(\rho - i\eta) \\ -\lambda & 1 - \frac{\lambda^2}{2} & A\lambda^2 \\ A\lambda^3(1 - \rho - i\eta) & -A\lambda^2 & 1 \end{pmatrix} + \mathcal{O}(\lambda^4), \tag{2.98}$$

with $\lambda \simeq 0.226$ the sine of the Cabibbo angle and (A, ρ, η) encoding the remaining mixing strength and CP phase. Phenomenology often employs the resummed parameters $(\bar{\rho}, \bar{\eta})$, which absorb higher-order unitarity corrections.

Flavour observables provide some of the most stringent tests of the SM and of potential new physics. Neutral-meson mixing in the K^0, B_d^0 and B_s^0 systems; rare loop-induced decays such as $b \to s\gamma$ and $B_s \to \mu^+\mu^-$ [87]; and both direct and indirect CP violation have been measured with increasing accuracy. Direct CP violation refers to asymmetries in decay amplitudes themselves, while indirect CP violation arises from interference between mixing and decay in neutral meson systems. Because these processes occur at one-loop or higher order, they are sensitive to heavy virtual particles and, therefore, probe energy scales well beyond the direct reach of current colliders.

A crucial test of the SM flavour sector is the global consistency of all such measurements with the unitarity of the CKM matrix. This is typically visualised in terms of the so-called unitarity triangle, derived from the condition

$$V_{ud}V_{ub}^* + V_{cd}V_{cb}^* + V_{td}V_{tb}^* = 0, \tag{2.99}$$

which describes a triangle in the complex plane. Its apex, $(\bar{\rho}, \bar{\eta})$, and its internal angles are accessible through a wide variety of tree-level and loop-level measurements. Global fits by the CKMFITTER [89] and UTFIT [90] collaborations show that all constraints converge on a common point (Fig. 2.7), providing a striking confirmation of the SM picture of quark mixing and CP violation.

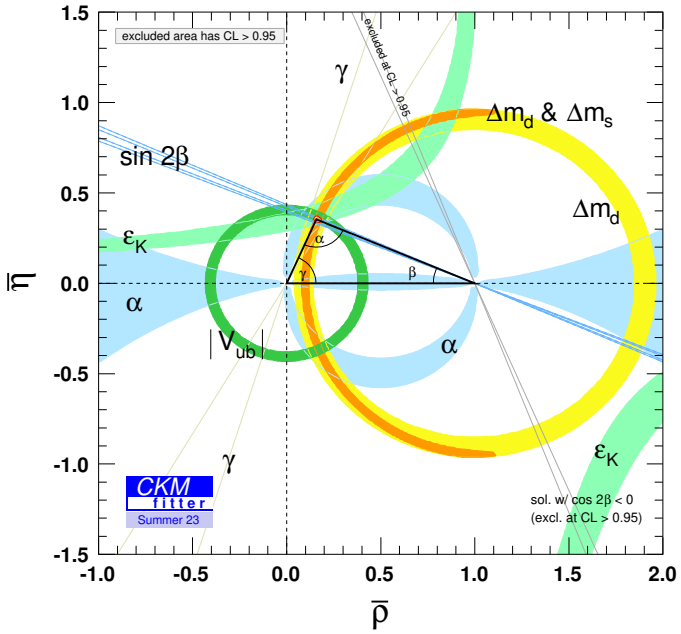

Figure 2.7.: Global fit constraints in the $(\bar{\rho},\bar{\eta})$ plane. The red hashed region of the global combination corresponds to 68% CL [88].

2.2. Physics beyond the Standard Model

2.2.1. Why physics beyond the SM?

While the SM has been extraordinarily successful in describing the fundamental particles and their interactions, it is widely understood to be incomplete. Both experimental evidence and theoretical considerations point towards the existence of BSM. In this section, the principal motivations for BSM physics are outlined, combining both conceptual arguments and quantitative indications of the SM's limitations.

The Hierarchy Problem

A longstanding theoretical concern within the SM is the so-called hierarchy problem [26, 27], which questions the stability of the Higgs mass under quantum radiative corrections. In a hard cutoff regularisation scheme, the one-loop correction to the

Higgs mass squared due to a generic fermion loop takes the form

$$\delta m_h^2 \propto -\frac{|y_f|^2}{8\pi^2}\Lambda^2 + \cdots , \tag{2.100}$$

where y_f is the relevant Yukawa coupling and Λ denotes the ultraviolet cutoff. Bosonic contributions have a similar structure:

$$\delta m_h^2 \propto \frac{g^2}{16\pi^2}\Lambda^2 + \cdots . \tag{2.101}$$

These quadratic divergences indicate that unless Λ is near the electroweak scale, an enormous amount of fine-tuning is required to keep the physical Higgs mass at its observed value of around 125 GeV. For example, with Λ approaching the Planck scale (10^{19} GeV), the tuning is of the order of

$$\frac{m_h^2}{\Lambda^2} \sim \left(\frac{125\ \text{GeV}}{10^{19}\ \text{GeV}}\right)^2 \sim 10^{-34}. \tag{2.102}$$

While such quadratic sensitivity is not manifest in dimensional regularisation [91], where only logarithmic divergences appear, the physical concern remains once the SM is embedded into a more complete theory. Heavy states with masses $M \gg v$ generically induce finite threshold corrections of order $\Delta m_h^2 \sim M^2$, driving the Higgs mass towards the highest scale present in the spectrum. Within the renormalisable SM taken in isolation this does not pose a problem, but in the presence of heavier degrees of freedom it requires an unnatural fine-tuning between bare and radiative contributions. This tension motivates mechanisms to protect m_h from large corrections. Supersymmetry achieves this by pairing each fermionic degree of freedom with a bosonic partner whose loop contribution cancels the quadratic term [92], while Composite-Higgs and extra-dimensional models replace the elementary scalar by a bound state or a pseudo-Goldstone boson, softening the sensitivity to Λ.

Dark matter and Dark Energy

Roughly 27% of the Universe's energy density is composed of dark matter, yet the SM supplies no suitable particle candidate. Evidence is many-fold: the flat rotation curves of spiral galaxies [93], gravitational-lens mass reconstructions such as the Bullet Cluster [94], and the anisotropy spectrum of the cosmic microwave background

(CMB) measured most recently by PLANCK [30] all require a cold, non-baryonic matter component.

A minimal and widely studied possibility is a weakly interacting massive particle (WIMP) [95]. In the early Universe, a stable species χ would have remained in thermal equilibrium until its annihilation rate fell below the Hubble expansion rate, leaving a relic abundance

$$\Omega_\chi h^2 \simeq \frac{0.1\ \text{pb}}{\langle \sigma v \rangle}, \tag{2.103}$$

where $\langle \sigma v \rangle$ is the thermally averaged annihilation cross-section. Matching the observed value $\Omega_{\text{DM}} h^2 \simeq 0.12$ requires $\langle \sigma v \rangle \sim 1$ pb, corresponding to an interaction strength and mass at the electroweak scale, a coincidence often dubbed the "WIMP miracle". Because no SM particle possesses the requisite stability, mass and couplings, dark-matter phenomenology strongly motivates BSM physics. Proposed solutions range from supersymmetric neutralinos [96, 97] and extra-dimensional Kaluza–Klein modes [98, 99] to axions [31, 100, 101] and feebly interacting massive particles [102], each with distinct signatures for direct, indirect and collider searches [103–105].

An even larger component $\sim$68% is dark energy, inferred from the accelerating expansion of the Universe [106, 107]. While consistent with a cosmological constant, its small but non-zero value remains unexplained by the SM and represents a major theoretical puzzle.

Neutrino Masses

A further, unequivocal signal of physics beyond the SM is provided by neutrino oscillations [28, 29], firmly establishing that at least two neutrino species carry non-zero mass. The minimal SM, which contains no right-handed neutrinos, forbids such masses; the theory must, therefore, be extended. In a model-independent language, the leading modification to the SM Lagrangian is the dimension-five Weinberg operator [46]

$$\mathcal{L}_5 = \frac{c_{ij}}{\Lambda} \left(\overline{L}^c_{L_i} \tilde{\Phi} \right) \left(\tilde{\Phi}^\dagger L_{L_j} \right) + \text{h.c.}, \tag{2.104}$$

where L_L are the lepton doublets, i, j represent lepton flavour indices, $\tilde{\Phi} = i\tau^2 \Phi^*$, c_{ij} are dimensionless coefficients and Λ denotes the scale of new physics that has been

integrated out. After EWSB, the operator generates Majorana masses

$$(m_\nu)_{ij} = \frac{c_{ij}\, v^2}{\Lambda}, \tag{2.105}$$

with $v = 246\,\text{GeV}$ the Higgs vev. Taking $m_\nu \sim 0.1$ eV and $c_{ij} \sim 1$ points to $\Lambda \sim 10^{14}$ GeV, far above the electroweak scale and well beyond the Standard Model's reach. Concrete ultraviolet completions of the Weinberg operator–the Type-I, -II or -III Seesaw Mechanisms, radiative models, extra dimensions, realise the operator in different ways; the Type-II Seesaw Mechanism will be discussed in detail in Chapter 4.

Baryon asymmetry of the Universe

Observations of primordial light-element abundances and the CMB constrain the baryon-to-photon ratio to be

$$\eta_B = \frac{n_B - n_{\bar{B}}}{n_\gamma} \simeq 6 \times 10^{-10}, \tag{2.106}$$

where $n_{B,\bar{B},\gamma}$ represent the number of baryons, anti-baryons, and photons respectively, illustrating a small but well-established excess of matter over antimatter [30]. Sakharov showed that any dynamical explanation of this asymmetry must satisfy three conditions: baryon-number violation, C and CP violation, and a departure from thermal equilibrium [32].

Within the SM, the first two ingredients are present but quantitatively insufficient. Non-perturbative electroweak processes (sphalerons) violate baryon and lepton number at high temperature [108], and the CKM phase provides CP violation, but the latter is far too small to account for the observed η_B [109]. Moreover, lattice simulations indicate that the electroweak phase transition is a smooth crossover for a 125 GeV Higgs boson, rather than the strong first-order transition required for electroweak baryogenesis [110, 111].

The baryon asymmetry therefore points to new physics capable of introducing additional sources of CP violation and strengthening the electroweak transition, for instance through extended Higgs sectors. Chapter 3 will revisit this question in the context of triple-Higgs production in two Higgs doublet extensions, whose sensitivity to the thermal potential makes them promising probes of electroweak baryogenesis.

The Flavour Puzzle

The SM reproduces most known flavour observables with remarkable precision, barring a few persistent tensions and anomalies [54]. It, however, offers no explanation for the pattern of fermion masses and mixings that underlie those successes. The Yukawa sector contains three *a priori* arbitrary complex 3×3 matrices $y_{u,d,e}$. After electroweak symmetry breaking, their eigenvalues generate fermion masses that span six orders of magnitude, from $y_e \simeq 10^{-6}$ to $y_t \simeq 1$, with no organising principle apparent.

In the quark sector, the misalignment of y_u and y_d produces the unitary CKM matrix, whose near-diagonality reflects the smallness of quark flavour mixing. Flavour-changing neutral currents are further suppressed by the Glashow–Iliopoulos–Maiani (GIM) mechanism [112], and the single CP-violating phase in V_{CKM} is far too small to account for the baryon asymmetry of the universe. By contrast, neutrino oscillations reveal large mixing angles in the lepton sector, encoded in the PMNS matrix, deepening the mystery of why the two sectors differ so dramatically.

Why do three generations exist? What dynamical principle selects the extreme hierarchies $m_u : m_c : m_t \sim 10^{-5} : 10^{-2} : 1$ and simultaneously allows order-one lepton mixing? These questions define the *flavour puzzle*. Popular ideas invoke horizontal (family) symmetries, or Froggatt–Nielsen mechanisms [113], some others appeal to extra dimensions or partial compositeness. Yet the very success of the CKM fit and the strong experimental bounds on flavour-changing processes mean that any new physics at the TeV scale must possess a highly non-generic flavour structure, a tension often called the *new-physics flavour problem*. Frameworks such as minimal flavour violation (MFV) [114] attempt to reconcile TeV-scale dynamics with the observed suppression of flavour change, but a compelling, UV-complete solution is still lacking. Resolving the flavour puzzle, therefore, remains a central goal of BSM physics.

The Strong *CP* problem

The QCD Lagrangian allows for a CP–violating term of the form

$$\mathcal{L}_\theta = \theta \, \frac{g_s^2}{32\pi^2} \, G^a_{\mu\nu} \, \tilde{G}^{\mu\nu a}, \tag{2.107}$$

where $\tilde{G}^{\mu\nu a} = \frac{1}{2}\epsilon^{\mu\nu\rho\sigma} G^a_{\rho\sigma}$ is the dual field-strength tensor. This term violates CP and is expected to contribute to a permanent electric dipole moment (EDM) for the neutron

through non-perturbative QCD effects. However, the current experimental bound, $|d_n| < 1.0 \times 10^{-26}\, e\,\mathrm{cm}$ [115], implies an extraordinarily small value $|\theta| \lesssim 10^{-10}$, which is difficult to explain naturally. This fine-tuning is known as the *strong CP problem*. A compelling solution is the Peccei–Quinn mechanism [31], which promotes θ to a dynamical field. The resulting pseudo-Goldstone boson, the axion [116, 117], dynamically relaxes the effective θ to zero and, at the same time, offers a viable dark matter candidate.

Gravity and gauge-coupling unification

Gravity is absent from the SM, and its gauge couplings (g_i) fail to meet at a single scale under renormalisation-group (RG) running. The evolution is given in terms of the coefficients b_i appearing in the one-loop β-function,

$$\frac{dg_i}{d\ln\mu} = \frac{b_i}{16\pi^2}\, g_i^3, \tag{2.108}$$

so the three couplings draw near but do not coincide. In the Minimal Supersymmetric Standard Model for example, the couplings unify at $M_{\mathrm{GUT}} \simeq 2 \times 10^{16}\,\mathrm{GeV}$ [80]. The SM's lack of exact unification, therefore, hints at additional particle content or symmetry, possibly a grand-unified gauge group that emerges above the TeV scale.

These issues, ranging from fine-tuning to unexplained observations, point strongly towards the necessity of new physics. In the next section, some of the theoretical frameworks that aim to address these problems and extend the understanding beyond the Standard Model are highlighted.

2.2.2. Approaches to Beyond Standard Model physics

The need for BSM physics has been motivated by numerous theoretical puzzles and experimental anomalies, as discussed in the preceding section. A complete resolution of these issues ultimately requires a consistent UV description that extends the SM at high energies; some of the later chapters will examine explicit examples of such UV completions. Until the underlying dynamics are revealed, however, one can adopt effective strategies that are broadly applicable.

When the scale of new physics Λ lies well above the electroweak scale, the heavy degrees of freedom can be integrated out, and their low-energy effects systematically captured by an effective field theory (EFT). A particularly well-studied instance is the Standard Model Effective Field Theory (SMEFT) [118], which assumes a linear realisation of electroweak symmetry breaking. The SMEFT Lagrangian expands the SM by an infinite tower of higher-dimensional (here dimension refers to the canonical mass dimension) operators that respect the SM gauge symmetry:

$$\mathcal{L}_{\text{SMEFT}} = \mathcal{L}_{\text{SM}} + \sum_{d>4} \sum_{i} \frac{C_i^{(d)}}{\Lambda^{d-4}} \mathcal{O}_i^{(d)}, \tag{2.109}$$

where the single operator at dimension five is the Weinberg term that has already been discussed, generating Majorana neutrino masses. At dimension six, there are 59 independent baryon- and lepton-number-conserving operators (in the Warsaw basis [119]), which dominate current phenomenology. The expansion in SMEFT is organised both in terms of the operator dimension and powers of E/Λ, where E is the relevant energy scale of the process under consideration. Higher-dimension terms, such as those at $d = 8$, can be included as required by the precision of data. The SMEFT framework accommodates both *top-down* and *bottom-up* approaches. In a top-down setting, a given UV model is matched onto SMEFT at the high scale $\mu \simeq \Lambda$ by integrating out the heavy fields, leading to specific predictions for the Wilson coefficients $C_i^{(d)}$ [120–123]. These coefficients evolve down to the electroweak scale via renormalisation group equations, known to one loop for dimension-six operators [124–127]. Bottom-up analyses, on the other hand, start from experimental data, constraining the $C_i^{(d)}$ from global fits [128], and potentially identifying patterns that can be traced back to plausible UV completions. SMEFT thereby offers a unifying language in which a diverse range of measurements, spanning Higgs and electroweak precision observables, flavour constraints, and high-energy collider tails, can be consistently interpreted.

Nonetheless, SMEFT relies on the assumption that the Higgs is part of an $SU(2)_L$ doublet and that new physics is weakly coupled and decouples cleanly. In scenarios where this is not the case, such as in composite Higgs models, strongly interacting sectors, or when the scale separation is modest, electroweak symmetry may be non-linearly realised [129–132]. The Higgs Effective Field Theory (HEFT) [133, 134] framework provides a more general formalism for such cases. It decouples the Higgs field from the Goldstone modes associated with electroweak symmetry breaking, and

its Lagrangian takes the form (in the bosonic sector, for example)

$$\mathcal{L}_{\text{HEFT}} = \frac{v^2}{4}\,\mathcal{F}\Big(\tfrac{h}{v}\Big)\,\text{Tr}\big[D_\mu U^\dagger D^\mu U\big] + \frac{1}{2}(\partial_\mu h)^2 - V(h) + \sum_k a_k(h/v)\,\mathcal{O}_k, \tag{2.110}$$

where $U = \exp\big(i\tau^a\pi^a/v\big) \in SU(2)$ contains the longitudinal Goldstone modes associated with the spontaneous breaking of the global $SU(2)_L \times SU(2)_R \to SU(2)_V$ symmetry. The functions $\mathcal{F}$ and a_k encode arbitrary analytic polynomial dependence on the Higgs field h. The higher-order operators include terms and custodial-symmetry-violating structures demonstrating the theory's flexibility in capturing non-decoupling and strongly coupled phenomena. HEFT smoothly reduces to SMEFT in the limit where the Higgs-dependent functions match those arising from a linear doublet representation, e.g. $\mathcal{F}(h/v) \to (1 + h/v)^2$, but remains valid in regimes where SMEFT fails to converge, such as in the presence of strong dynamics or light composite resonances. It is, therefore, a more general EFT compatible with the SM symmetry structure, ensuring no relevant effects are omitted due to restrictive assumptions on the Higgs sector.

Complementing the EFT approach, recent years have witnessed a growing role for machine learning (ML) techniques in particle physics [135][†]. ML has proven useful in a wide range of tasks: from real-time event selection and tracking to fast detector simulation, jet substructure, and anomaly detection. Of particular relevance to the present thesis are *graph neural networks* (GNNs), which naturally accommodate the complex relational structure of LHC final states. In these applications, each event is represented as a graph, with reconstructed particles or jets forming the nodes, and kinematic or spatial correlations encoded in the edges. GNNs learn event-level features through iterative message passing, uncovering subtle correlations that are difficult to access with traditional methods. Chapter 6 will employ a GNN in a supervised setting, sharpening signal discrimination in rare final states such as four-top production, and enabling efficient exploration of the parameter spaces. Together with the EFT tools discussed above, such ML methods offer a powerful complement, enhancing the ability to interpret current collider data and uncover signs of new physics that might otherwise go unnoticed.

[†]See [136] for a living review of ML applications in particle physics

2.3. Summary

This chapter surveyed the theoretical framework and empirical successes of the SM. The gauge structure, the Higgs mechanism and the consequent generation of gauge-boson and fermion masses were reviewed before turning to observables that test these ingredients with high precision: electroweak measurements, Higgs production and decay rates at the LHC, and a broad set of flavour processes governed by the CKM matrix. All of these taken together confirm the SM to be of impressive accuracy, yet leave only a modest set of free parameters.

The second part of the chapter highlighted where the SM falls short. The hierarchy problem threatens the stability of the Higgs mass; astrophysical and cosmological observations demand a non-baryonic dark-matter component; neutrino oscillations require new sources of lepton mass; and the baryon asymmetry of the Universe calls for additional CP violation and out-of-equilibrium dynamics. In addition, the flavour puzzle, the strong-CP problem, and the absence of gauge-coupling unification or a quantum description of gravity all point to physics beyond the SM.

To bridge present experiments and unknown UV dynamics, a few novel approaches to corner BSM physics have been introduced. The groundwork laid here prepares the discussion in the following chapters, where concrete UV completions are examined, along with their collider signatures and low-energy constraints, including a detailed exploration of modern theoretical techniques that can guide the search for physics beyond the Standard Model.

Chapter 3.

The BSM potential of Multi-Higgs Processes

"The more Higgses, the more chaos—and the more answers."
— ***Inspired*** *by* The Three Body Problem

The discovery of the Higgs boson has ushered in a new era of precision studies, with a central goal of scrutinising the structure of the scalar sector and testing the mechanism of electroweak symmetry breaking. While current measurements remain broadly consistent with SM expectations, they still allow for sizeable deviations, particularly in Higgs couplings and interactions, offering a valuable window into possible new physics.

As the LHC progresses towards its high-luminosity upgrade, rare processes such as double and triple Higgs production will become increasingly accessible. These multi-Higgs final states are particularly sensitive to modifications of the Higgs potential and its interactions, and hence offer a unique probe of extended scalar sectors. Although a subdominant process, weak boson fusion (WBF) production of Higgs pairs is particularly important, as it allows for the disentanglement of modifications in the trilinear Higgs self-coupling and the quartic couplings between Higgs and vector bosons from single Higgs couplings, which can be conveniently parameterised in terms of the effective scaling parameters κ_λ, κ_V, and κ_{2V} in the κ-framework. Mapping out the viable parameter space in this framework and identifying the classes of models that can saturate the allowed regions provides a model-independent bridge between LHC measurements and BSM physics.

In addition, triple Higgs production, though extremely rare in the SM, can receive significant enhancements in theories with extended scalar sectors such as the Two Higgs Doublet Model (2HDM). In these scenarios, new resonant contributions can drastically modify the production rates, particularly in gluon-initiated channels, offering complementary sensitivity to both Higgs self-couplings and the underlying scalar dynamics.

This chapter is organised as follows: Sec. 3.1 presents the constraints on the Higgs self- and gauge-boson couplings in the κ-framework from WBF Higgs pair production. The corresponding BSM scenarios capable of populating the allowed parameter space are discussed in Sec. 3.2. In Sec. 3.3, the prospects for observing triple Higgs production via gluon-gluon fusion in 2HDM extensions are examined in detail. Finally, a summary and concluding remarks are provided in Sec. 3.4.

3.1. Scalar couplings in WBF Higgs pair production

The κ-framework [85], as discussed in Chapter 2, is a widely used tool in the context of Higgs physics, as it provides an intuitive approach for capturing deviations in Higgs couplings. Even though it is not gauge-invariant and becomes theoretically inconsistent beyond leading order, the κ framework remains useful in specific experimental contexts, such as WBF di-Higgs production, where recent results [137] constrain key parameters like the Higgs self-coupling κ_λ and the quartic gauge-Higgs interaction κ_{2V}. The scalar couplings relevant for WBF Higgs pair production, κ_V, κ_{2V}, and κ_λ, are defined by the tree-level Gauge-Higgs interaction Lagrangian as shown (assuming tree-level custodial symmetry, *i.e.*, $\kappa_W = \kappa_Z = \kappa_V$ and $\kappa_{2W} = \kappa_{2Z} = \kappa_{2V}$)

$$\mathcal{L} = \frac{1}{2}(\partial h)^2 + M_W^2 \left(W_\mu^+ W^{-\mu} + \frac{1}{2c_W^2} Z_\mu Z^\mu \right) \left[1 + \kappa_V \frac{2h}{v} + \kappa_{2V} \frac{h^2}{v^2} \right] - \kappa_\lambda \frac{m_h^2}{2v} h^3 \,, \quad (3.1)$$

where the Higgs vev $v = 246$ GeV and $c_W = \cos\theta_W$ is the cosine of the Weinberg angle. Theoretically, the trilinear Higgs coupling modifier κ_λ can be embedded consistently within the dimension-6 effective field theory (EFT) expansion [119], and several studies have explored its effects at loop level [138–141]. In contrast, $\kappa_{2V} \neq 1$ violates gauge invariance and challenges renormalisability [142]. Yet, this coupling is highly relevant in probing BSM scenarios like Higgs compositeness [143, 144], where deviations scale with the parameter ξ as $\kappa_V = \sqrt{1-\xi}$ and $\kappa_{2V} = 1 - 2\xi$. Alternative models like

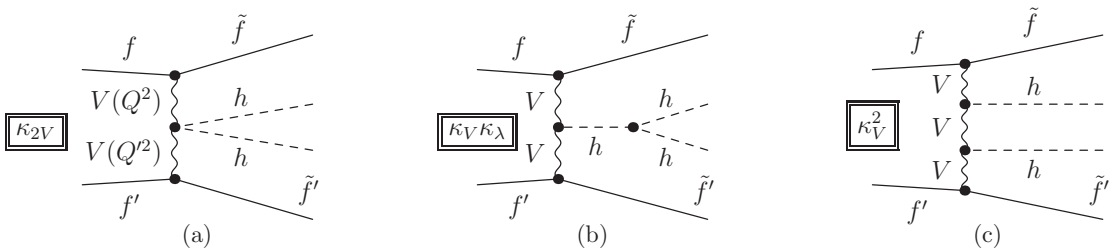

Figure 3.1.: Representative Feynman diagram topologies contributing to κ_{2V} sensitivity via weak boson fusion.

scalar singlet mixing predict $\kappa_V = \cos\alpha$, $\kappa_{2V} = \cos^2\alpha$, where α is the scalar mixing angle. These parameterisations map out different regions of the κ parameter space. In addition, the weaker constraints on κ_{2V} imply that it can therefore act as a powerful discriminator between qualitatively different BSM dynamics.

The WBF Higgs production process probes the incoming weak bosons at space-like momenta in the diagrams of Fig. 3.1. However, the analysis of $Wh \to Wh$ scattering for physical momenta (the crossed process that enters WBF subdiagrams of Fig. 3.1) provides insight into gauge-symmetry cancellations that carry over into qualitative phenomenological outcomes via the effective W approximation [145, 146]. In the high energy limit $\sqrt{s} \gg m_h + M_W$, the polarised amplitudes scale as*

$$\frac{M_W^2}{s}\mathcal{A}(W_L h \to W_L h) \sim \frac{M_W}{\sqrt{s}}\mathcal{A}(W_T h \to W_L h) \sim \kappa_{2V} - \kappa_V^2 \,. \tag{3.2}$$

This shows that to maintain unitarity at high energies, one can expect a significant destructive interference in the SM (as well as for direct Higgs mixing). The scaling with energy in the WBF process is pdf-suppressed for massless partons (including in the effective W approximation); however, large enough deviations from the SM correlation manifest themselves as an enhanced cross-section so that limits can be set. Note that κ_λ does not enter the Wh amplitude with energy enhancement, and its constraints are therefore set by *a priori* perturbativity limits (see [149–151] for more model-specific considerations).

*This result is obtained with `FeynArts` [147], `FormCalc` [148], and `LoopTools` [148]. Phase-space and polynomial suppression of the valence quark parton distribution functions significantly modify these naive expectations.

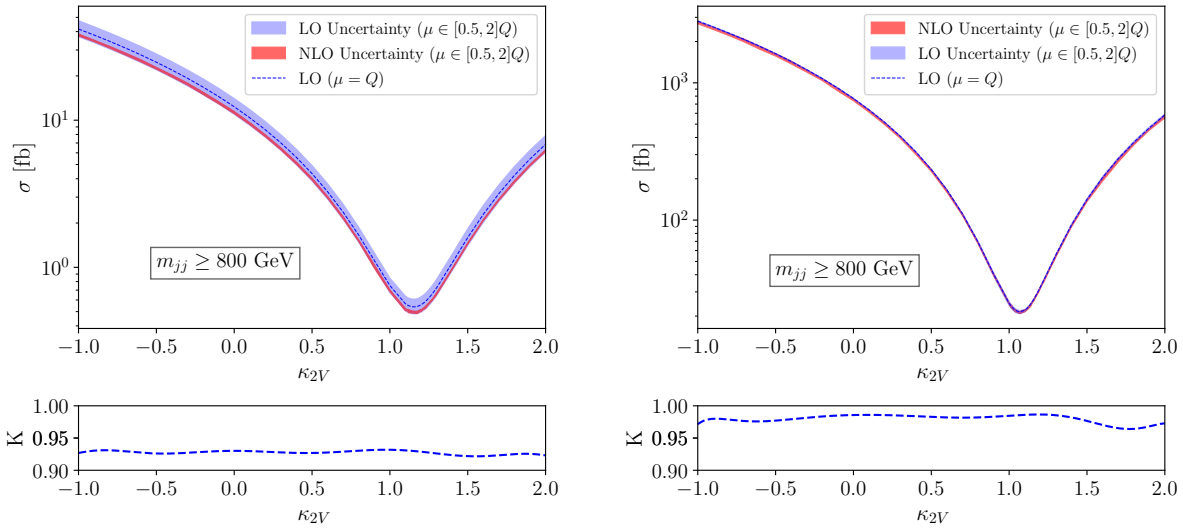

Figure 3.2.: Next-to-leading order QCD corrections to WBF $pp \to hhjj$ production in the large invariant tagging jet mass region $m_{jj} \geq 800$ GeV at the LHC (a) and FCC-hh (b) as a function of κ_{2V} for all other parameters chosen to be SM-like.

3.1.1. Hadron collider constraints on κ_V and κ_{2V}

WBF $pp \to hhjj$ production follows hjj production from the point of view of QCD, with the search region that is selected by the LHC experiments exploiting the usual WBF paradigm [152–155]. Similar to the findings in single-Higgs and double-Higgs production via WBF [156, 157], the QCD corrections can be formidably captured through an adapted choice of the renormalisation and factorisation scales, due to the 'double-Deep Inelastic Scattering' structure of the process. The κ_{2V} measurement region selected by the LHC experiments then becomes extraordinarily stable. The $pp \to hhjj$ WBF cross-section component at NLO QCD in comparison to the LO estimate is illustrated in Fig. 3.2, employing the central scale choice $\mu = Q$ (*cf.* Fig. 3.1) for the signal region characterised by an invariant jet mass of $m_{jj} \geq 800$ GeV.[†] This extends to the FCC-hh at a significantly increased cross-section, Fig. 3.2. The cross-section is well-approximated by the LO $\mu = Q$ choice, and the NLO corrections are modest $\sim 5\%$ at the LHC, decreasing in relevance at the FCC-hh, running at 100 TeV [162]. The key limitation of setting constraints on κ_{2V} is then statistics and background systematics.

[†]This is obtained through a modification of the publicly available `Vbfnlo` Monte Carlo program [155, 158, 159]. Modifications have been cross-checked against `Madgraph5_aMC@NLO` [160]. See also [161] for studies of rescalings of the Higgs self-coupling.

The ATLAS Collaboration has previously published search results for non-resonant $hh \to b\bar{b}b\bar{b}$ production using 27 fb^{-1} of early Run 2 data [163], as well as a dedicated search for VBF hh production in 126 fb^{-1} of data collected between 2016 and 2018 [164]. The latest analysis [137] builds on these earlier results by incorporating the 2016-2018 data for both production channels and taking advantage of improvements in jet reconstruction and b-tagging techniques. Notably, the analysis employs an entirely data-driven technique for background estimation, utilising an artificial neural network to perform kinematic reweighting of data to model the background in the region of interest, and it currently restricts κ_{2V} to

$$\kappa_{2V} \in [-0.0, 2.1]\ ([-0.1, 2.1]),\ \text{observed (expected) 95\% CL.} \tag{3.3}$$

The CMS Collaboration has also published results of a search for non-resonant $hh \to b\bar{b}b\bar{b}$ with its full Run 2 dataset [165], which restricts the allowed interval for κ_λ to $[-2.3, 9.4]$ $([-5.0, 12.0])$, at 95% confidence level (CL). Furthermore, a more recent CMS publication [166] that exploits topologies arising from highly energetic Higgs boson decays into $b\bar{b}$, restricts the allowed interval for κ_{2V} to

$$\kappa_{2V} \in [0.62, 1.41]\ ([0.66, 1.37]),\ \text{at observed (expected) 95\% CL.} \tag{3.4}$$

ATLAS and CMS have conducted investigations into non-resonant hh in the $b\bar{b}\tau^+\tau^-$ [167–171] and $b\bar{b}\gamma\gamma$ [171–173] decay channels as well. Considering the final state topologies for the highest di-Higgs branching ratios, *i.e.*,

$$pp \to hhjj \to b\bar{b}b\bar{b}jj, \tag{3.5a}$$

and,

$$pp \to hhjj \to b\bar{b}\tau^+\tau^-jj, \tag{3.5b}$$

Events are generated for each process scanning over the space of κ_V and κ_{2V}, keeping $\kappa_\lambda = 1$ fixed, utilising a χ^2 fit to obtain the limits on the corresponding coupling modifiers.

Event generation and fiducial selection

Events are generated on `Madgraph5_aMC@NLO` [160] at LO at $\sqrt{s} = 13$ TeV, with stringent cuts at the generator level on the WBF jet pair's invariant mass ($m_{jj} > 800$ GeV). Additionally, the pseudorapidity of the b-jets is set to be $|\eta_b| < 2.5$ to ensure that the b-jets produced from the Higgs pair are centrally located. The `Madgraph5_aMC@NLO` [160] source code is modified to include the κ modifiers for event generation. The events are subsequently showered with `Pythia8.3` [174], utilising `MadAnalysis` [175] interfacing `FastJet` [176, 177] to reconstruct the final states with a 70% b-tagging efficiency.

Forward-jets are required to satisfy $p_T^j > 30$ GeV and $2.5 < |\eta_j| < 4.5$, while the central-jets are required to have $p_T^j > 40$ GeV and $|\eta_j| < 2.5$. To select events in the $hh \to b\bar{b}b\bar{b}$ channel, firstly, the jet pair with the highest invariant mass are identified as the WBF-jets, imposing the forward-jet criteria. The WBF-jets are required to have a pseudorapidity separation cut of $|\eta_{jj}| > 3$ and an invariant mass cut of $m_{jj} > 1$ TeV. At least 4 central-jets are required in the final state, all of which must be b-tagged. To isolate the WBF region, the transverse component of the momentum vector sum of the two WBF jets and the four jets forming the Higgs boson candidates is required to be less than 65 GeV. The Higgs pair is constructed from the 4 b-jets with a minimum invariant mass requirement on the Higgs pair invariant mass of $M_{hh} > 400$ GeV.

For the $hh \to b\bar{b}\tau^+\tau^-$ channel, the WBF-jets are chosen applying the same cuts as previously. However, only two centrally located b-tagged jets are required in this case. The τ-leptons can decay either hadronically or leptonically, with the latter being selected using the criteria outlined in the latest ATLAS analysis [167], with a minimum p_T of 15 GeV and limited to $|\eta_l| < 2.47$. The light jets arising from the hadronic decay of the τ-leptons are selected with a minimum p_T of 10 GeV and $|\eta_j| < 2.5$. Additionally, the leptonic decay of the τ's results in missing energy. The di-Higgs invariant mass is then reconstructed using the two b-jets and the τ-decay products, with a minimum invariant mass requirement of $M_{hh} > 400$ GeV.

Sensitivity and projections

The current and the projected collider sensitivities of κ_V and κ_{2V} are obtained from the distribution of the reconstructed kinematic observable M_{hh}. The χ^2 statistic for this

analysis is computed as

$$\chi^2(\kappa_V, \kappa_{2V}) = (b^i_{\text{BSM}}(\kappa_V, \kappa_{2V}) - b^i_{\text{SM}}) V^{-1}_{ij} (b^j_{\text{BSM}}(\kappa_V, \kappa_{2V}) - b^j_{\text{SM}}), \tag{3.6a}$$

where $b^i_{\text{BSM}}(\kappa_V, \kappa_{2V})$ represents the combined number of events in the ith bin of M_{hh} from both decay channels, considering their respective cross-sections and acceptances, at a given luminosity for a particular value of κ_V and κ_{2V}, and b^i_{SM} corresponds to the expected number of events solely from the SM for $\kappa_V = 1$ and $\kappa_{2V} = 1$. The covariance matrix V_{ij} is the sum-in-quadrature of two terms: 1) the statistical uncertainties computed from the root of bin entries, *i.e.*, the Poisson uncertainty associated with each bin, b^i_{SM}, and 2) fully correlated relative fractional uncertainties ($\varepsilon_{\text{rel.}}$), *i.e.*,

$$V_{ij} = b^i_{\text{SM}} \delta_{ij} + \varepsilon^2_{\text{rel.}} b^i_{\text{SM}} b^j_{\text{SM}} \,. \tag{3.6b}$$

To fix $\varepsilon_{\text{rel.}}$, κ_V is set to unity, the 95% CL limit of $\kappa_{2V} \in [0.2, 2.0]$ at 126 fb^{-1} at the LHC, comparable to the limits set by ATLAS [137] and CMS [166] is reproduced scanning over κ_{2V}.

Once the methodology is validated through a comparison of the obtained κ_{2V} constraints with the predictions of ATLAS (Eq. (3.3)) and CMS (Eq. (3.4)), the 95% CL constraints are obtained scanning over the entire parameter space of κ_V and κ_{2V}. The results are presented on the left hand side Fig. 3.3, where the 95% confidence bands are shown for the LHC with an integrated luminosity of 126 fb^{-1}, the constraints for the High-Luminosity (HL-LHC) frontier with an integrated luminosity of 3 ab^{-1}, as well as the projected constraints for the Future Circular Collider (FCC-hh) with $\sqrt{s} = 100$ TeV and an integrated luminosity of 30 ab^{-1}, assuming the same $\varepsilon_{\text{rel.}}$ as for the LHC case. It should be added that using the χ^2 calibrated to [137, 166] is a conservative extrapolation for the FCC-hh. A limiting factor in this environment is the reduction of QCD multi-jet contributions, as central jet vetoes are not available to suppress these efficiently. This can lead to a considerable variation of the expected sensitivity [178–180], in particular when considering the rejection of the irreducible gluon fusion component.

3.1.2. Lepton collider constraints on κ_V and κ_{2V}

The potential of di-Higgs processes has garnered significant attention at future lepton colliders because of their exceptional sensitivity range, mainly attributed to a sig-

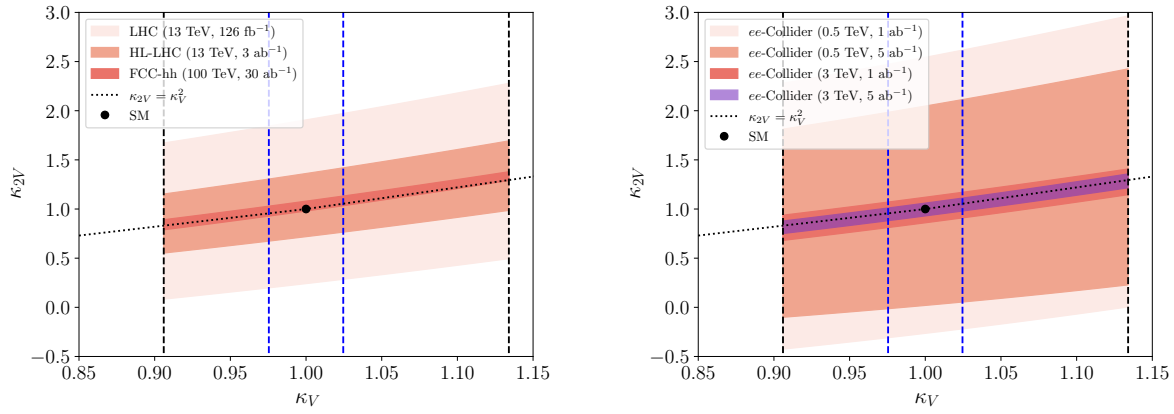

(a) (b)

Figure 3.3.: Current and projected constraints on κ_V and κ_{2V} for various colliders. The current LHC and projected HL-LHC limits on κ_V, represented by the black and blue dashed lines respectively, have been set using Higgs data from ATLAS [82].

nificantly lower background interference compared to hadron colliders. The works of [181–184] (see also Refs. [185, 186]) have been instrumental in investigating the di-Higgs sector and obtaining exclusion limits on κ_λ and κ_V. Building on this success, the scope of this exploration can be extended to obtain limits on κ_V and κ_{2V} for e^+e^--colliders, adopting a methodology similar to that presented in Sec. 3.1.1. In this scenario, the di-Higgs decay into four b-quarks is very attractive since the background is orders of magnitude smaller, making it the primary focus of this analysis. The process to be looked at is, therefore,

$$e^+e^- \to hhe^+e^-/\nu_e\bar{\nu}_e \to b\bar{b}b\bar{b}e^+e^-/\nu_e\bar{\nu}_e. \tag{3.7}$$

The dominant contributions to the production cross-section come from the WBF process and Higgs-strahlung. Events are generated on `Madgraph5_aMC@NLO` [160] for two benchmark collider beam energies of 0.5 TeV and 3 TeV. The WBF signal region is selected following analysis in [181]. A strict missing energy cut greater than 30 GeV imposed, requiring four centrally located b-tagged jets with $p_T > 20\,\text{GeV}$ and $|\eta| < 2.5$. In order to reconstruct the Higgses individually from the b's, the four b-jets, b_i are labelled in a way that minimises the quantity $(m_{12}/\text{GeV} - 125)^2 + (m_{34}/\text{GeV} - 125)^2$, where m_{ij} represents the invariant mass formed by jets b_i and b_j. b_1, b_2 result from one of the Higgs decay, and b_3, b_4 are the decay products of the other. The corresponding jets are then used to reconstruct the two Higgs bosons within the on-shell window (90 GeV, 130 GeV).

With the selected signal events, a χ^2 as described in Sec. 3.1.1 is constructed, again, scanning over κ_V and κ_{2V}. The constraints for both the benchmark points are presented on the right-hand side of Fig. 3.3, at integrated luminosities of $\mathcal{L} = 1$ ab^{-1} and 5 ab^{-1}. The analysis reproduces the CLIC projection [187],

$$\kappa_{2V} \in [0.97, 1.05], \text{ expected 95\% CL., 3 TeV, 5 ab}^{-1}. \tag{3.8}$$

However, the potential to exploit beam polarisations in [187] (which is out of scope for the comparison here) indicates that the obtained sensitivity estimates are conservative.

In the previous sections, the κ_V single Higgs constraints are treated independently from the $\kappa_{2V}, \kappa_\lambda$ constraints for presentation purposes (in the discussion below, these limits correspond to qualitatively different phenomenological parameters). Of course, the individual rectangular regions indicated in Fig. 3.3 are simultaneously constrained by these (correlated) data sets. To gauge how the rectangular regions map onto the elliptical constraints in a combination of this information for the most sensitive environments, a combination of single Higgs and WBF hh production is illustrated in Fig. 3.4. This demonstrates that in the very sensitive future collider environments that enable tight constraints on κ_{2V}, this parameter will remain less constrained compared to κ_V.

An additional promising avenue for probing κ_V and κ_{2V} at lepton colliders lies in high-energy muon colliders [188], which offer an exceptional environment for precision Higgs measurements. Thanks to their clean experimental conditions and high centre-of-mass energies potentially reaching 10 TeV, muon colliders can enhance sensitivity to WBF processes, thereby accessing the same di-Higgs production channels as in e^+e^- colliders but at substantially higher rates. The significantly boosted final states at these energies also improve the resolution in reconstructing Higgs bosons from b-jets, allowing for more robust discrimination of new physics effects in the gauge-Higgs sector. Although a detailed simulation is beyond the scope of this chapter, the combination of large cross-sections, suppressed backgrounds, and precise tracking capabilities could render muon colliders competitive or even superior in constraining κ_{2V}, particularly when beam-induced background mitigation strategies are effectively implemented.

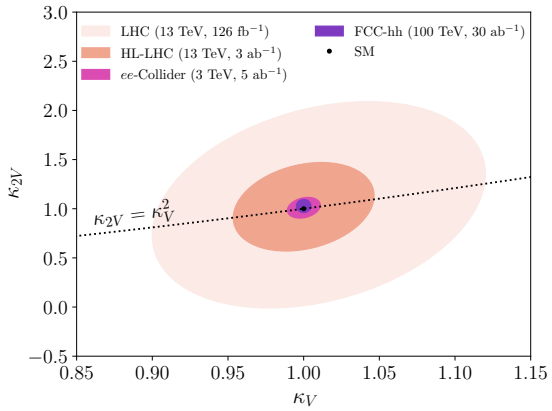

Figure 3.4.: The 95% CL constraints on κ_V and κ_{2V} parameter space resulting from the combination of WBF di-Higgs and single Higgs production for various collider options. Single Higgs constraints for future colliders are taken from the κ_W bounds in [189].

Remarks on κ_λ

WBF processes at hadron colliders play a less relevant role in constraining Higgs self-interactions, predominantly the trilinear Higgs coupling, as Higgs pair production from gluon fusion $gg \to hh$ is more abundant. Representative extrapolations to the HL-LHC phase [190] indicate that this coupling could be constrained at 50% around its SM expectation. The environment of an FCC-*hh* at 100 TeV will increase the sensitivity to 3-5% [191].

Higgs self-coupling measurements at lepton colliders are dominated by Z-boson associated Higgs pair production for low centre-of-mass energies and WBF at large energies, *e.g.*, at CLIC. The latter, maximising the WBF potential, has a projected sensitivity of about $\kappa_\lambda = 1^{+0.25}_{-0.15}$ with some level of degeneracy between κ_λ and κ_{2V} [187]. As for hadron colliders, the constraint on κ_{2V} is stronger compared to κ_λ, which highlights the need for constraining κ_λ at hadron colliders such as the LHC. The sensitivity at CLIC compares to an estimated ILC sensitivity (in the 250 GeV+500 GeV combined phase) of $\kappa_\lambda = 1 \pm 0.25$ [192].

The WBF channel in particular is primarily sensitive to κ_V, κ_{2V} due to Eq. (3.2). κ_λ however is relevant in comparison to κ_{2V}, κ_V and therefore requires a discussion in Sec. 3.2. κ_λ is known to be relatively efficiently constrainable in gluon fusion Higgs pair production through sensitivity in the threshold region, whose inclusive cross-section [193, 194] is an order of magnitude larger than WBF. κ_λ can therefore be

understood as a potential additional constraint when considering κ_{2V} measurements as performed by the experiments.

3.2. κ_V, κ_{2V} and κ_λ in BSM models

This section shifts the focus to BSM models that populate the space of κ_V, κ_{2V}, and κ_λ, paying particular attention to those that predict order-of-magnitude larger deviations in either κ_{2V} or κ_λ relative to κ_V; in such cases future measurements of either κ_{2V} or κ_λ are likely to provide significant discriminating power. As discussed recently in [195], a large deviation in κ_{2V} relative to κ_V will require non-decoupling TeV-scale new physics.

3.2.1. Extended scalar sectors at tree level

Consider a generic extended scalar sector built out of a set M of electroweak multiplets Φ_A. Let Φ_A have an SU(2) irreducible representation (irrep) of dimension d_A, and a hypercharge Y_A, with the renormalisable lagrangian

$$\mathcal{L} = \sum_{A\in M} |D\Phi_A|^2 - V(\Phi)\,. \tag{3.9}$$

The charged current part of the covariant derivative is defined to be

$$D_\mu \Phi_A = \left(\partial_\mu - \frac{1}{\sqrt{2}} i g_W (W_\mu^+ T_A^+ + W_\mu^- T_A^-) - \dots\right) \Phi_A\,, \tag{3.10}$$

where the components of the generators in the SU(2) irrep of dimension d_A are given by

$$[T_A^\pm]_{\alpha\beta} = \begin{cases} \sqrt{\left(\frac{d_A+1}{2}\right)(\alpha+\beta-1) - \alpha\beta} & \text{if } \alpha \pm 1 = \beta \\ 0 & \text{otherwise} \end{cases}, \tag{3.11}$$

with the SU(2) indices α, β running between 1 (labelling the component with maximum third component of isospin, T^3) and d_A (labelling the component with minimum T^3).

The $\left[\left(\frac{d_A+1}{2}\right)+Y_A\right]$-th component is electrically neutral, and after electroweak symmetry breaking can be decomposed into vevs, v_R and v_I, and vev-free fields h_R and h_I

$$[\Phi_A]_{\left(\frac{d_A+1}{2}\right)+Y_A} = \frac{1}{\sqrt{2}}(v_R + h_R) + \frac{i}{\sqrt{2}}(v_I + h_I)\,. \tag{3.12}$$

These are separated into real (R) and imaginary (I) parts. The imaginary components are absent from real irreps, as well as, without loss of generality, from one complex irrep due to the freedom of gauging it away. Assuming the scalar sector contains a hypercharge-$\frac{1}{2}$ doublet, its imaginary component is gauged away.

Substituting Eqs. (3.10) and (3.12) into Eq. (3.9), in the broken phase, the charged current interactions of the neutral Higgses are governed by

$$\mathcal{L} = \sum_i \frac{1}{2}(\partial h_i)^2 - V(v,h) + \frac{1}{4}g^2 W^+W^- \left[C_{ij}v_iv_j + 2C_{ij}v_ih_j + C_{ij}h_ih_j\right] + \dots\,, \tag{3.13}$$

where i, j index the neutral Higgses, and repeated indices are summed over, and the matrix C is diagonal with entries

$$C_{ij} = \delta_{ij}\left(\frac{1}{2}(d_A^2 - 1) - 2Y_A^2\right)\,. \tag{3.14}$$

d_A, Y_A are the dimension and hypercharge of the multiplet from which the ith component came: real and imaginary components of the same multiplet have the same entry. C_{ij} is normalised to be the identity matrix in an n-Higgs doublet model.

The 125 GeV Higgs, h, is defined as a unit direction in the space of neutral Higgs components:

$$h_i = h\,\hat{n}_i\,,\ \text{where}\ \hat{n}_i\hat{n}_i = 1\,. \tag{3.15}$$

The above relation is substituted into Eq. (3.13) and compared with Eq. (3.1). Identifying the total vev as

$$v \equiv \left(C_{ij}v_iv_j\right)^{\frac{1}{2}} = 246\,\text{GeV}\,, \tag{3.16}$$

the coupling modifiers (κs) can be written as

$$\kappa_V = \frac{C_{ij} v_i \hat{n}_j}{\left(C_{ij} v_i v_j\right)^{\frac{1}{2}}}, \qquad \kappa_{2V} = C_{ij} \hat{n}_i \hat{n}_j \,. \tag{3.17}$$

Note that it is assumed that the electroweak multiplets form complete custodial irreps, so that $\kappa_V = \kappa_W = \kappa_Z$ and $\kappa_{2V} = \kappa_{2W} = \kappa_{2Z}$.

κ_V and κ_{2V} are therefore correlated in particular extended scalar sectors, *i.e.* for particular C_{ij}, and can now be computed at tree level in specific extended scalar sectors, using the master formulae Eqs. (3.14) and (3.17).

Higgs + scalar $SU(2)$ singlet In unitary gauge, there is one neutral component of the Higgs doublet and one from the singlet, with the C matrix

$$C_{ij} = \begin{pmatrix} 1 & 0 \\ 0 & 0 \end{pmatrix} . \tag{3.18}$$

Writing $v_i = (v_1, v_2)^T$ and $\hat{n}_i = (\cos\alpha, \sin\alpha)^T$, it is straightforward to obtain

$$\kappa_V = \cos\alpha \,, \tag{3.19}$$

$$\kappa_{2V} = \cos^2\alpha \,, \tag{3.20}$$

with α being the scalar mixing angle, as expected.

2 Higgs Doublet Models In unitary gauge, there are two scalar neutral components, which both generically contain vevs and mix with each other, and a pseudoscalar neutral component which, when custodial symmetry is imposed, obtains no vev and does not mix with the other neutral components [196]. The C matrix is the identity matrix,

$$C_{ij} = \begin{pmatrix} 1 & 0 & 0 \\ 0 & 1 & 0 \\ 0 & 0 & 1 \end{pmatrix} . \tag{3.21}$$

Writing

$$\hat{n}_i = (\sin\alpha, \cos\alpha, 0)^T \tag{3.22}$$
$$v_i = v\,(\cos\beta, \sin\beta, 0)^T \tag{3.23}$$

where the third entry is associated with the pseudoscalar component, one can obtain

$$\kappa_V = \sin(\alpha - \beta)\,, \tag{3.24}$$
$$\kappa_{2V} = 1\,. \tag{3.25}$$

Triplet extensions Looking at the Georgi-Machacek model [197], ordering the neutral components respectively as that of the Higgs doublet, the two components of the complex $Y = 1$ triplet and the one component of the real $Y = 0$ triplet, the C matrix is

$$C_{ij} = \begin{pmatrix} 1 & 0 & 0 & 0 \\ 0 & 2 & 0 & 0 \\ 0 & 0 & 2 & 0 \\ 0 & 0 & 0 & 4 \end{pmatrix} \tag{3.26}$$

Custodial symmetry implies that $v_2 = v_3 = v_4$ among the triplet components, and also that the mass matrix is invariant under permutations among the 2, 3 and 4 indices, meaning $n_2 = n_3 = n_4$ in the light Higgs eigenvector. Thus,

$$\hat{n}_i = \left(\cos\alpha, \frac{1}{\sqrt{3}}\sin\alpha, \frac{1}{\sqrt{3}}\sin\alpha, \frac{1}{\sqrt{3}}\sin\alpha\right)^T \tag{3.27}$$
$$v_i = v\left(\cos\beta, \frac{1}{2\sqrt{2}}\sin\beta, \frac{1}{2\sqrt{2}}\sin\beta, \frac{1}{2\sqrt{2}}\sin\beta\right)^T \tag{3.28}$$

which implies that

$$\kappa_V = \cos\beta\cos\alpha + 2\sqrt{\frac{2}{3}}\sin\beta\sin\alpha\,, \tag{3.29}$$
$$\kappa_{2V} = \cos^2\alpha + \frac{8}{3}\sin^2\alpha\,. \tag{3.30}$$

This result is reproduced using the mass matrices of [197], see also [195].

In Fig. 3.7, the lines and regions that the models discussed above can populate in the κ_V-κ_{2V} plane are shown. Notably, for *any* tree-level model

$$v^2\left(\kappa_{2V}-\kappa_V^2\right) = C_{ij}\hat{n}_i\hat{n}_j\,C_{kl}v_kv_l - \left(C_{ij}v_i\hat{n}_j\right)^2 \geq 0\,, \tag{3.31}$$

which follows from the Cauchy-Schwarz inequality when C is a positive definite matrix. It is only zero in the alignment limit, when $\hat{n}_i \propto v_i$, or in the case of mixing with singlets, when C is only positive semidefinite.

Thus, one requires electroweak triplets or higher representations to obtain a large deviation in κ_{2V} but not κ_V in an extended scalar sector, as well as a departure from the alignment limit (*i.e.*, a departure from the parabola $\kappa_{2V} = \kappa_V^2$), see also [196]. This, in turn, implies significant mixing of components of the Higgs doublet with other states that cannot be made arbitrarily heavy. This is likely to cause some tension with direct searches. For instance, a significant triplet component to electroweak symmetry breaking introduces resonant tell-tale same-sign WW WBF production [198] which drives constraints on the triplet nature of the observed Higgs boson [199] (see also [200]). In the decoupling limit, both κ_V and κ_{2V} approach 1, and in principle do so from different directions in the κ_V-κ_{2V} plane, depending on the model — compare, for instance, the singlet and 2HDM trajectories in Fig. 3.7. However, in the decoupling limit, the deviations from the Standard Model in $WW \to hh$ due to κ_V, κ_{2V} are comparable to the short-distance contributions from heavy Higgs exchange. These latter exchange contributions are calculated for the singlet and 2HDM model in [201], where this effect is discussed in detail. The effect of both κ_{2V} and the short distance heavy Higgs exchange can be combined into a κ_{2V}^{eff}, which satisfies

$$1-\kappa_V^2 = \kappa_V^2 - \kappa_{2V}^{\text{eff}}\,, \tag{3.32}$$

in the decoupling limit. This corresponds to the pattern predicted by the SMEFT at dimension 6 (see, for example, [195]).

Turning now to κ_λ, this is generally a free parameter for renormalisable potentials $V(\Phi)$ containing cubic interactions among the electroweak irreps. However, if the cubic interactions are absent (as often happens accidentally due to the charges of the multiplets, or is imposed by certain $\mathbb{Z}_2$ symmetries), the range of κ_λ can be understood close to the alignment limit. The potential among the neutral components before

electroweak symmetry breaking will have the generic form

$$V = \frac{1}{2}\mu_{ij}^2 r_i r_j + \frac{1}{4}\lambda_{ijkl} r_i r_j r_k r_l \,, \tag{3.33}$$

where the tensors μ^2 and λ are necessarily symmetric in their indices, and $r_i = 0$ corresponds to the electroweak symmetry preserving vacuum. After electroweak symmetry breaking, substituting $r_i = v_i + h_i$ leads to

$$V = \text{const.} + \frac{1}{2}\mu_{ij}^2 h_i h_j + \frac{3}{2}\lambda_{ijkl} h_i h_j v_k v_l + \lambda_{ijkl} h_i h_j h_k v_l + \mathrm{O}(h^4) \tag{3.34}$$

using the vev condition

$$\mu_{ij}^2 v_j + \lambda_{ijkl} v_j v_k v_l = 0 \,. \tag{3.35}$$

From comparison with Eq. (3.1), κ_λ takes the form

$$\kappa_\lambda = \left(C_{ij} v_i v_j\right)^{\frac{1}{2}} \frac{2\lambda_{ijkl}\hat{n}_i \hat{n}_j \hat{n}_k v_l}{m_h^2} \tag{3.36}$$

Close to the alignment limit, Eq. (3.36) can be expressed in terms of mass parameters and the degree of alignment. Without loss of generality, in the mass basis where the mass matrix of Eq. (3.34) satisfies

$$\begin{aligned} \mu_{11}^2 + 3\lambda_{11kl} v_k v_l &= m_h^2 \\ \mu_{1a}^2 + 3\lambda_{1akl} v_k v_l &= 0 \\ \mu_{ab}^2 + 3\lambda_{abkl} v_k v_l &= m_a^2 \delta_{ab} \end{aligned} \tag{3.37}$$

can be used, where $a, b = 2, 3, \ldots$ label heavy Higgs directions, each with mass m_a^2. In this basis, v_i satisfies

$$v_i = v\left(1 - \frac{1}{2}\epsilon_a \epsilon_a,\, \epsilon_2,\, \epsilon_3, \ldots\right)^T + \mathrm{O}(\epsilon^3) \,, \tag{3.38}$$

for some small parameters ϵ_a describing the amount of the vev in the heavy Higgs directions when close to the alignment limit. The summation over repeated a indices is implied.

Expanding μ_{11}^2, μ_{1a}^2, μ_{ab}^2 and $\lambda_{111l}v_l$, $\lambda_{11al}v_l$, $\lambda_{1abl}v_l$ order-by-order in ϵ_a, Eqs. (3.35) and (3.37) can be expanded to solve for

$$\kappa_\lambda = \frac{2v\lambda_{111l}v_l}{m_h^2} = 1 + \frac{1}{2}\epsilon_a\epsilon_a - 2\epsilon_a\epsilon_b\frac{\left(\lim_{\epsilon_a\to 0}\mu_{ab}^2\right)}{m_h^2} + \mathrm{O}(\epsilon^3)\,. \tag{3.39}$$

In the decoupling limit, where m_a^2 are large, the model is necessarily aligned and $\epsilon_a \sim \mathrm{O}\left(\frac{1}{m_a^2}\right)$ are correspondingly small. The quartic couplings of the model are limited in size by perturbative unitarity, and so from Eq. (3.37) μ_{ab}^2 approaches $m_a^2\delta_{ab}$. In this case

$$\kappa_\lambda \approx 1 - 2\sum_a \epsilon_a^2\left(\frac{m_a^2}{m_h^2} - \frac{1}{4}\right)\,, \tag{3.40}$$

and the deviation in κ_λ enjoys a parametric enhancement of $\frac{m_a^2}{m_h^2}$ relative to the deviations in κ_V^2 and κ_{2V} which are both $\mathrm{O}(C\times\epsilon_a^2)$. This enhancement does not necessarily happen in the case of *alignment without decoupling*.

3.2.2. Extended scalar sectors at loop level

Turning to the case of an arbitrary electroweak scalar multiplet, Φ_A, with a $\mathbb{Z}_2$ symmetry that prevents it from acquiring a vev, and a cross-quartic interaction λ with the SM Higgs doublet Φ:

$$\mathcal{L} = |D\Phi_A|^2 - m_\varphi^2|\Phi_A|^2 - 2\lambda|\Phi_A|^2\left(\Phi^\dagger\Phi - \frac{v^2}{2}\right)\,. \tag{3.41}$$

If the scalar is sufficiently heavy, $2m_\varphi > m_h$, its leading order effects are at one-loop level. When augmented with a small amount of $\mathbb{Z}_2$ splitting to allow charged particles to decay, Eq. (3.41) presents a minimal class of models that includes multiple viable candidates for BSM particles of mass $m_\varphi^2 \lesssim 1$ TeV [131]. If the cross-quartic is large, such that $m_\varphi^2 \sim \lambda v^2$, there can be sizeable effects in the electroweak phase transitions [202].

In the simplest case of a $\mathbb{Z}_2$ symmetric singlet, $\sqrt{2}\Phi_A \sim \sqrt{2}\Phi_A^\dagger \sim S$ and Eq. (3.41) reads

$$\mathcal{L} = \mathcal{L}_{\text{SM}} + \frac{1}{2}(\partial_\mu S)^2 - \frac{m_S^2}{2}S^2 - \lambda S^2\left(\Phi^\dagger\Phi - \frac{v^2}{2}\right). \tag{3.42}$$

In this scenario, the $WW \to hh$ subamplitudes (as any amplitude) can be renormalised, in the on-shell scheme as described in Ref. [203], which is the common scheme used for electroweak corrections (treating tadpoles as parameters as in Ref. [204]).[‡] The effects of the singlet, to order $\mathrm{O}(\lambda^3)$, can be accounted for by substituting the following finite expressions into Fig. 3.1

$$\begin{aligned}
\kappa_{2V} - 1 = & -\frac{\lambda^2 v^2}{8\pi^2}\text{Re}\left[B_0'(m_h^2, m_S^2, m_S^2)\right] \simeq \kappa_V^2 - 1\,, \\
\kappa_\lambda - 1 = & -\frac{\lambda^3 v^4}{6\pi^2 m_h^2}C_0(M_{hh}^2, m_h^2, m_S^2) \\
& -\frac{\lambda^2 v^2}{8\pi^2}\frac{1}{M_{hh}^2 - m_h^2}\left(B_0(M_{hh}^2, m_S^2, m_S^2) - \text{Re}[B_0(m_h^2, m_S^2, m_S^2)]\right) \\
& -\frac{\lambda^2 v^2}{48\pi^2 m_h^2}\left(4B_0(m_h^2, m_S^2, m_S^2) + 2B_0(M_{hh}^2, m_S^2, m_S^2)\right. \\
& \qquad \left. - \text{Re}[6B_0(m_h^2, m_S^2, m_S^2) - 3m_h^2 B_0'(m_h^2, m_S^2, m_S^2)]\right).
\end{aligned} \tag{3.43}$$

Here B_0, B_0' are the Passarino–Veltman [206] two-point function and its derivative, respectively, C_0 is the 3-point function (see App. A for explicit definitions), and M_{hh} is the di-Higgs invariant mass. κ_λ becomes a M_{hh}^2-dependent form factor; this momentum dependence is particularly useful for light scalar masses m_S which do not admit a reliable EFT description and can modify the phenomenology at threshold.

Note that, for the loop-level singlet, the correction to κ_V and κ_{2V} is purely through the wavefunction renormalisation of the Higgs, and therefore follows a characteristic $\kappa_V^2 \simeq \kappa_{2V}$ pattern, the corrections to both scaling as λ^2. κ_λ, on the other hand, receives a λ^3 contribution from a 1PI singlet loop. When λ is large, this generically means the κ_λ sensitivity to this model at HL-LHC is greater than that of κ_V, κ_{2V}, as illustrated in Fig. 3.5.

[‡]Specifically choosing $\{M_W, M_Z, \alpha\}$ as input parameters for the electroweak sector. The Weinberg angle is then a derived quantity [205].

In principle, a Φ_A with non-trivial electroweak charges can contribute 1PI corrections to hWW and $hhWW$ vertices; in practice, however, these states' corrections to the κ parameters are parametrically similar to the singlet case. To see this, take Φ_A to be a second (inert) Higgs doublet as a representative example, and work to order $\mathrm{O}(m_\varphi^{-2})$, assuming the extra states are sufficiently heavy for their effects in $WW \to hh$ to be well approximated by constant κs. Performing the same calculations as before in the on-shell scheme for the off-shell SM-like 1PI vertex functions Γ,

$$
\begin{aligned}
\left.\frac{\Gamma^{WWh}}{\Gamma^{WWh}_{\mathrm{LO}}}\right|_{\mathrm{SM}} &= \bar{\kappa}_W = 1 - \frac{g_W^2}{1920\pi^2 m_\varphi^2}\left(2M_W^2 + M_Z^2\right) - \frac{\lambda^2 v^2}{24\pi^2 m_\varphi^2}\,, \\
\left.\frac{\Gamma^{WWh}}{\Gamma^{WWh}_{\mathrm{LO}}}\right|_{\mathrm{SM}} &= \bar{\kappa}_Z = \bar{\kappa}_W + \frac{g_Y^2}{960\pi^2 m_\varphi^2}(M_W^2 - M_Z^2)\,, \\
\left.\frac{\Gamma^{WWhh}}{\Gamma^{WWhh}_{\mathrm{LO}}}\right|_{\mathrm{SM}} &= \bar{\kappa}_{2W} = 1 - \frac{g_W^2}{480\pi^2 m_\varphi^2}\frac{c_W^2}{s_W^2}\left(M_W^2 + M_Z^2\right) - \frac{\lambda^2 v^2}{12\pi^2 m_\varphi^2}\,, \\
\left.\frac{\Gamma^{ZZhh}}{\Gamma^{ZZhh}_{\mathrm{LO}}}\right|_{\mathrm{SM}} &= \bar{\kappa}_{2Z} = \bar{\kappa}_{2W} + \frac{e^4 v^2}{1920\pi^2 m_\varphi^2}\frac{g_Y^2}{g_W^2}\,, \\
\left.\frac{\Gamma^{hhh}}{\Gamma^{hhh}_{\mathrm{LO}}}\right|_{\mathrm{SM}} &= \bar{\kappa}_\lambda = 1 - \frac{g_W^2 M_Z^2}{1920\pi^2 m_\varphi^2} - \frac{\lambda^2 v^2}{72\pi^2 m_\varphi^2}\left(7 + 2\frac{M_{hh}^2}{m_h^2}\right) + \frac{\lambda^3 v^2}{3\pi^2 m_\varphi^2}\frac{v^2}{m_h^2}\,.
\end{aligned}
\tag{3.44}
$$

These are now no longer related to physical quantities by introducing the bar. The physical couplings in the amplitudes are the product of both these corrections to the κs, and the corrections to the electroweak couplings due to the non-trivial gauge quantum numbers of the new fields. In particular, for non-vanishing hypercharge, the new states are additional sources of custodial isospin violation as directly visible above. The gaugeless part of the corrections mirrors those of the singlet Eq. (3.43). In particular, the $\mathrm{O}(\lambda^2)$ corrections to κ_V and κ_{2V} come exclusively from wavefunction normalisation of the Higgs boson.[§]

The results above clearly show that additional gauge interactions can sculpt the κ_V, κ_{2V} parameter regions, however, in a phenomenologically highly suppressed way compared to new additional inter-scalar interactions. Focussing on the gauge-independent part in practical $\kappa_{2V}, \kappa_V, \kappa_\lambda$ analyses, the λ contributions all scale with the number of real degrees of freedom, D. This gives approximate values for an arbitrary

[§]Parametrically comparable 1PI contributions to hWW and $hhWW$ arise from dimension-six operators $\sim |\Phi|^2 V_\mu V^\mu$. In cases where couplings are forbidden by gauge-invariance, the dimension-6 contributions are conventionally included to the κ definition as is the case for $\kappa_\gamma, \kappa_g, \kappa_{Z\gamma}$, see *e.g.* [207, 208].

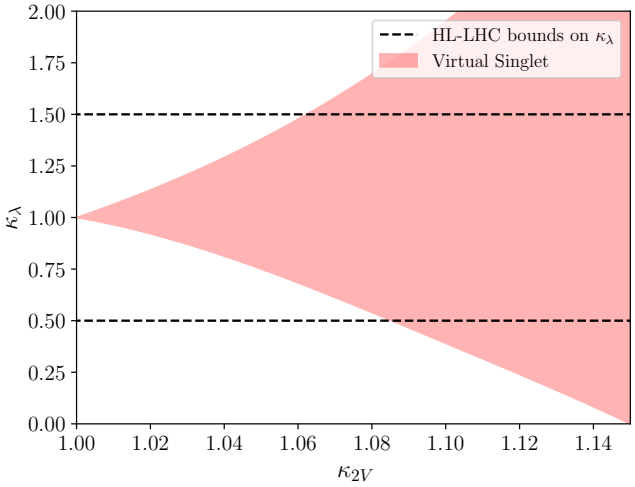

Figure 3.5.: κ_λ-κ_{2V} plot for the aforementioned singlet mixing scenario for a representative value of $M_{hh} = 300$ GeV $\gtrsim 2m_h$ which provides the region sensitive to κ_λ investigations in Higgs pair production from gluon fusion. The HL-LHC projected sensitivity bound on κ_λ is represented by the dashed black lines [190]. The range on the κ_{2V} axis comes from HL-LHC bounds on κ_V, assuming $\kappa_{2V} = \kappa_V^2$ as in this singlet model. $m_S \in [90, 400]$ GeV and $\lambda \in [-2, 2]$ are varied to obtain the contour.

irrep of

$$\begin{aligned} \kappa_V &\simeq \bar{\kappa}_V \approx 1 - D\,\frac{\lambda^2 v^2}{96\pi^2 m_\varphi^2}\,, \\ \kappa_{2V} &\simeq \bar{\kappa}_{2V} \approx 1 - D\,\frac{\lambda^2 v^2}{48\pi^2 m_\varphi^2}\,, \\ \kappa_\lambda &\simeq \bar{\kappa}_\lambda \approx 1 + D\,\frac{\lambda^3 v^2}{12\pi^2 m_\varphi^2}\,\frac{v^2}{m_h^2}\,. \end{aligned} \tag{3.45}$$

assuming $\lambda v^2 \gg m_h^2$ to drop the λ^2 piece in κ_λ, and focussing on the HL-LHC measurement region $M_{hh} \gtrsim 2m_h$. The full momentum dependence for any such irrep can be restored from Eq. (3.43) by multiplying by the dimension D.

3.2.3. Compositeness and dilaton mixing

The κ values of a composite Higgs model depend on the details of the symmetry breaking. In the minimal composite Higgs model (MCHM), the components of the Higgs doublet chart the coset SO(5)/SO(4) [143, 144, 209], whose relevant dynamics

are readily constructed through the linear sigma model, see [210]. The five components $\phi^1, \ldots, \phi^5$ have kinetic terms

$$\mathcal{L} = \frac{1}{2}\sum_{M=1}^{4}\left((D\phi)^M\right)^2 + \frac{1}{2}(\partial\phi^5)^2\,, \tag{3.46}$$

where the first four components have SM-like gauge couplings to the W and Z. The components are restricted to the surface

$$\sum_{M=1}^{4}(\phi^M)^2 + (\phi^5)^2 = f^2 \tag{3.47}$$

which, in unitary gauge, can be parameterised by

$$\left(\phi^1, \phi^2, \phi^3, \phi^4, \phi^5\right) = \left(0, 0, 0, f\sin\frac{\mathfrak{h}}{f}, f\cos\frac{\mathfrak{h}}{f}\right) \tag{3.48}$$

where $\mathfrak{h}$ is understood to be the Higgs coordinate shifted such that $\mathfrak{h} = 0$ in the absence of electroweak symmetry breaking. Substitution of Eq. (3.48) into Eq. (3.46) yields the unitary gauge Lagrangian

$$\mathcal{L} = \frac{1}{2}(\partial\mathfrak{h})^2 + \frac{g^2 f^2}{4}\sin^2\left(\frac{\mathfrak{h}}{f}\right)\left[W^+W^- + \frac{1}{2c_W^2}Z^2\right]\,, \tag{3.49}$$

and expanding about the vacuum $\mathfrak{h} = \langle\mathfrak{h}\rangle + h$ then gives

$$\begin{aligned}\kappa_V &= \sqrt{1-\xi}\,,\\ \kappa_{2V} &= 1 - 2\xi\,,\end{aligned} \tag{3.50}$$

in terms of $\xi = \frac{v^2}{f^2}$. While this pattern will change for different cosets, it was shown in [211] that for all custodial-symmetry-preserving cosets arising from the breaking of a compact group, it is guaranteed that

$$\begin{aligned}1 - \kappa_V^2 &\geq 0\,,\\ \kappa_V^2 - \kappa_{2V} &\geq 0\,.\end{aligned} \tag{3.51}$$

By contrast, this can be violated for non-compact groups. A non-compact coset $SO(4,1)/SO(4)$ can be constructed via the linear sigma model Lagrangian [210]

$$\mathcal{L} = \frac{1}{2}\sum_{M=1}^{4}\left((D\phi)^M\right)^2 - \frac{1}{2}(\partial\phi^5)^2\,, \tag{3.52}$$

restricted to the surface

$$\sum_{M=1}^{4}(\phi^M)^2 - (\phi^5)^2 = -f^2 \tag{3.53}$$

which is then parameterised in unitary gauge by

$$\left(\phi^1,\phi^2,\phi^3,\phi^4,\phi^5\right) = \left(0,0,0,f\sinh\frac{\mathfrak{h}}{f},f\cosh\frac{\mathfrak{h}}{f}\right)\,. \tag{3.54}$$

(Note that trigonometric functions in Eq. (3.48) become hyperbolic ones in Eq. (3.54), similar in spirit to the compactification of the Lorentz group.) This yields

$$\begin{aligned}\kappa_V &= \sqrt{1+\xi}\,,\\ \kappa_{2V} &= 1+2\xi\,,\end{aligned} \tag{3.55}$$

for the hyperbolic composite Higgs model.

In composite Higgs theories, the Higgs potential can be written schematically in MCHM5 (and MCHM5-like theories such as Ref. [212], where the 5 refers to the spurionic irrep of the top quark) as

$$f^{-4}V_{\rm CH}\left(\frac{\mathfrak{h}}{f}\right) = \alpha\cos\left(\frac{2\mathfrak{h}}{f}\right) - \beta\sin^2\left(\frac{2\mathfrak{h}}{f}\right) = \frac{m_h^2}{8v^2(1-\xi)}\left[\sin^2\left(\frac{\mathfrak{h}}{f}\right) - \xi\right]^2 + V_0\,, \tag{3.56}$$

where V_0 is a constant, see also [213]. The coefficients α,β are related to two and four-point functions of the underlying strongly interacting theory [214, 215] responsible for partial compositeness, and they can be replaced as a function of ξ and the Higgs mass. These coefficients can, in principle, be inferred from lattice computations (for recent progress see [216, 217]) to uncover realistic UV completions. The Higgs trilinear

coupling modifier is then given by

$$\kappa_\lambda = \frac{1-2\xi}{\sqrt{1-\xi}} \tag{3.57}$$

The expression for the hyperbolic composite Higgs model is again obtained from the replacement $\xi \to -\xi$ [210].

The above expressions satisfy

$$\kappa_V \kappa_\lambda = \kappa_{2V} \,. \tag{3.58}$$

Therefore, Fig. 3.1(a) reproduces the behaviour of Fig. 3.1(b) at leading order in the MCHM5 scenario. This is due to the symmetry breaking potential being of the same functional form as the interaction of the Goldstone bosons.[¶]

Ultimately, the value of κ_λ depends on the (spurionic) representations of the explicit $SO(4)$ symmetry breaking in the model. Larger representations, leading to higher order Gegenbauer polynomials of $\sin\left(\frac{h}{f}\right)$ in the potential, can break the above correlation between κ_λ and κ_V, κ_{2V}, and generally lead to a parametric enhancement in the deviations of κ_λ from the SM [219].

Deforming the MCHM with a dilaton

The MCHM, together with its hyperbolic counterpart, define a line in the κ_V-κ_{2V} plane (shown in green and blue in Fig. 3.6) corresponding to the maximally symmetric coset spaces of constant positive or negative curvature [220]. Ref. [195] considered deformations away from this line that can arise from deformations of the coset space. A viable model for these deformations comes from the mixing of the composite Higgs with a TeV-scale dilaton.

Practically, the coset space can be deformed by replacing the constant radius f in Eqs. (3.47) and (3.53) with a mildly ϕ^5 dependent function

$$f^2 \to f^2(\phi^5) \approx f_0^2 + f_0^2 \frac{(\phi^5)^2}{f_t^2} \,, \tag{3.59}$$

[¶]In MCHM4 the potential reads $f^{-4} V_{\rm CH}\left(\frac{h}{f}\right) = \alpha \cos\left(\frac{h}{f}\right) - \beta \sin^2\left(\frac{h}{f}\right)$ leading to $\kappa_\lambda = \sqrt{1-\xi}$, see also [218]. In this scenario, which suffers from tension with electroweak precision constraints, one also has $\kappa_V \kappa_\lambda \neq \kappa_{2V}$.

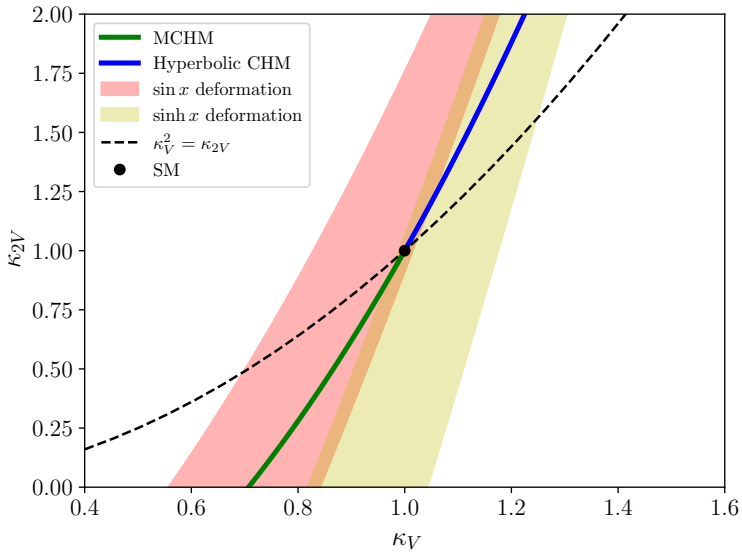

Figure 3.6.: κ_V-κ_{2V} predictions for the composite Higgs models and their deformation through Eq. (3.59) as described in the text, for $\kappa_V \in [0.5, 1.5]$, $\xi = v^2/f^2 \in [0, 1]$, and f_t as a consistent solution of the W mass given κ_V, ξ. This leaves κ_{2V} determined as a function of these parameters.

for some $f_t^2 > f_0^2$. This promotes ϕ^5 to a modulus that is common in higher-dimensional theories of electroweak symmetry breaking.[‖] The function is expanded to order $(\phi^5)^2$, assuming the linear term is forbidden by symmetry, so a linear deformation doesn't alter the findings qualitatively. The modifications κ_V, κ_{2V} are calculated to linear order in f_0^2/f_t^2, after performing a field redefinition to canonically normalise the kinetic terms (This field redefinition necessarily introduces momentum-dependent self-interactions of the would-be Higgs boson, which is discussed below.). Scanning over f_0^2/f_t^2, as illustrated in Fig. 3.6, it can be seen that such manifolds deviate from the line of uniform curvature in the κ_V-κ_{2V} plane.

The effective ϕ^5 dependence of f can be brought about through mixing with a dilaton direction, χ, which can be analysed using the approach of [222]. χ measures the departure from conformal symmetry through its vacuum expectation value $\langle\chi\rangle$ [223]. In a UV completion where the composite Higgs components are mesonic states arising from a confining gauge group $SU(N_c)$, $\langle\chi\rangle \sim f$ if the dilaton is another mesonic state, $\langle\chi\rangle \sim f\sqrt{N_c}$ if the dilaton is a glueball like state [222]. Here $\langle\chi\rangle$ is a free parameter,

[‖]The motivation of the scalar metric from which this theory derives also follows the discussion presented in [221].

required to be O(TeV) in order to get sizeable mixing effects with the composite Higgs states.

Interaction terms with the composite Higgs can be constructed by multiplying operators by $(\chi/\langle\chi\rangle)^n$, where n is the canonical mass dimension of the operator, in order to restore conformal symmetry. Thus

$$\mathcal{L} \supset \frac{g_W^2 f^2}{4}\left(\frac{\chi}{\langle\chi\rangle}\right)^2 \sin^2\left(\frac{\mathfrak{h}}{f}\right)\left[W^+W^- + \frac{1}{2c_W^2}Z^2\right] - \left(\frac{\chi}{\langle\chi\rangle}\right)^4 V_{\rm CH}\left(\frac{\mathfrak{h}}{f}\right). \tag{3.60}$$

in terms of the composite Higgs model operators Eqs. (3.49) and (3.56). Expanding this Lagrangian around the minimum $\langle\mathfrak{h}\rangle, \langle\chi\rangle$ and including effects of Higgs-dilaton mixing through the usual isometry

$$\begin{pmatrix} h \\ \chi - \langle\chi\rangle \end{pmatrix} = \begin{pmatrix} c_\phi & s_\phi \\ -s_\phi & c_\phi \end{pmatrix}\begin{pmatrix} h' \\ \chi' \end{pmatrix}, \tag{3.61}$$

from the couplings of the mass eigenstate h', one can obtain

$$\begin{aligned} \kappa_V &= c_\phi\sqrt{1-\xi} - s_\phi\sqrt{\zeta}\,, \\ \kappa_{2V} &= (1-2\xi)c_\phi^2 + \zeta s_\phi^2 - 2\sqrt{\zeta(1-\xi)}s_{2\phi}\,, \\ \kappa_\lambda &= c_\phi^3\frac{1-2\xi}{\sqrt{1-\xi}} - 4c_\phi^2 s_\phi\sqrt{\zeta} - 8\frac{V_0}{m_h^2 v^2}s_\phi^3\zeta^{\frac{3}{2}}\,, \end{aligned} \tag{3.62}$$

where $\zeta = v^2/\langle\chi\rangle^2$, with the MCHM5 potential for $V_{\rm CH}$ taken from Eq. (3.56).

These couplings indeed cover, *a priori*, a wide area in the κ_V-κ_{2V} plane. In particular, the area $\kappa_{2V} < 1 < \kappa_V$, which was not populated by the models considered in previous sections, can be reached if the Higgs is considered mostly as a pseudo-dilaton. This area partially overlaps with the geometric deformations shown in Fig. 3.6 (Eq. (3.59) can be thought of as approximating the leading order effects of dilaton mixing).

κ_λ can also accommodate large deviations from 1 in the case of significant Higgs-dilaton mixing. In addition, the dilaton χ has additional χ^3 terms from explicit sources of conformal symmetry violation as described in [223, 226]. This means that trilinear interactions will receive momentum-dependent interactions as a consequence of the

Model	κ_V	κ_{2V}	cref.
Singlet	$\cos\alpha$	$\cos^2\alpha$	§Sec. 3.2.1
2HDM	$\sin(\alpha-\beta)$	1	§Sec. 3.2.1
Georgi-Machacek	$\cos\alpha\cos\beta + \sqrt{\frac{8}{3}}\sin\alpha\sin\beta$	$\cos^2\alpha + \frac{8}{3}\sin^2\alpha$	§Sec. 3.2.1
Tree-level scalar	$\frac{C_{ij}v_i\hat{n}_j}{\left(C_{ij}v_iv_j\right)^{\frac{1}{2}}}$	$C_{ij}\hat{n}_i\hat{n}_j$	§Sec. 3.2.1
Loop-level scalar (large λ)	$1 - D\frac{\lambda^2v^2}{96\pi^2m_\varphi^2}$	$1 - D\frac{\lambda^2v^2}{48\pi^2m_\varphi^2}$	§Sec. 3.2.2
SMEFT	free	$\simeq 2\kappa_V^2 - 1$	*e.g.* [119, 224]
MCHM	$\sqrt{1-\xi}$	$1-2\xi$	§Sec. 3.2.3
MCHM + Dilaton	$c_\phi\sqrt{1-\xi} - s_\phi\sqrt{\zeta}$	$(1-2\xi)c_\phi^2 + \zeta s_\phi^2 - 2\sqrt{\zeta(1-\xi)}s_{2\phi}$	§Sec. 3.2.3
HEFT	free	free	*e.g.* [225]

Table 3.1.: A collection of κ_V, κ_{2V} values of the simplified models described in Sec. 3.2.

a-theorem [227], leading to

$$\mathcal{L} \supset \frac{4\,\Delta a}{\langle\chi\rangle^3}(\partial\chi)^2\Box\chi + \dots \tag{3.63}$$

where the ellipses denote higher order terms in the dilaton and $\Delta a = \mathrm{O}(\%)$ (see [227, 228]). This leads to an additional momentum-dependent modification of κ_λ of

$$\Delta\kappa_\lambda = s_\phi^3\frac{4\,\Delta a}{3}\,\zeta\left[\frac{M_{hh}}{\langle\chi\rangle}\right]^2\left[\frac{M_{hh}}{m_h}\right]^2\left(1-\frac{4m_h^2}{M_{hh}^2}\right), \tag{3.64}$$

with M_{hh} denoting the invariant di-Higgs mass. Modifications vanish close to the threshold, but can lead to a large modification of the invariant di-Higgs mass spectrum for considerable mixing.

The examples discussed so far exhaust the phenomenological possibilities in the κ_V-κ_{2V} plane, and therefore provide a theoretical avenue to interpret the results of associated analyses. Of course, κ_V constraints are also informed by single Higgs measurements, and therefore, there are significant constraints on these scenarios from a range of experimental findings. Similarly, both momentum-dependent and momentum-independent modifications to κ_λ are best constrained in measurements of gluon fusion Higgs pair production, given the larger rate and the generic sensitivity

of WBF to (multi-) gauge boson interactions. Table 3.1 presents a collection of κ_V, κ_{2V} values of the simplified models described in Sec. 3.2.

3.2.4. Running of coupling modifiers

Going beyond tree level, the correlations of κ_V, κ_{2V}, and κ_λ become scale and scheme dependent. In the HEFT framework, the leading-order operators that modify κ_V, κ_{2V}, and κ_λ (free, uncorrelated parameters in HEFT) not only run into each other, but also into higher derivative, next-to-leading-order operators (in a chiral dimension power-counting scheme) that modify the measured κs, as shown in Table 3.2. To encapsulate these effects, an effective κ_V can be defined from the coefficient of $g^{\mu\nu}$ in the effective vertex for hWW (as defined in [134, 142])

$$Z_h^{\frac{1}{2}} \hat{\Gamma}^{\mu\nu}_{hW^-W^+}\,, \tag{3.65}$$

with all legs on-shell. The wavefunction normalisation of the Higgs is

$$Z_h^{-1} = 1 + 4\frac{m_h^2}{v^2} a_{\Box\Box} \tag{3.66}$$

in terms of the operator coefficient $a_{\Box\Box}$ defined in Table 3.2 [134]. One can then obtain

$$\kappa_V^{\text{eff}} = \kappa_V + \frac{m_h^2}{v^2}\left(2a_{hWW} + a_{d2} + 2a_{\Box\mathcal{V}\mathcal{V}} - a_{h\mathcal{V}\mathcal{V}} - 2\kappa_V a_{\Box\Box}\right) - \frac{M_W^2}{v^2} 4a_{hWW} \tag{3.67}$$

Similarly, from the value of

$$Z_h^{\frac{3}{2}} \hat{\Gamma}_{hhh} \tag{3.68}$$

with all legs on-shell, an effective coupling can be defined as

$$\kappa_\lambda^{\text{eff}} = \kappa_\lambda + \frac{m_h^2}{v^2}\left(-2a_{h\Box\Box} + a_{dd\Box} - a_{hdd} - 6\kappa_\lambda a_{\Box\Box}\right)\,. \tag{3.69}$$

These effective couplings serve the purpose of effectively field-redefining the redundant higher derivative operators generated by the running back into κ_V and κ_λ, respectively. An analogous on-shell κ_{2V}^{eff} would be a complicated function of components of the $hhWW$ effective vertex and components of diagrams containing, *e.g.*, hWW and

$\mathcal{O}_{hWW}$	$-2a_{hWW}\, g_W^2 \frac{h}{v}\mathrm{Tr}\left[W_{\mu\nu}W^{\mu\nu}\right]$	$\mathcal{O}_{h\mathcal{V}\mathcal{V}}$	$-a_{h\mathcal{V}\mathcal{V}}\frac{m_h^2}{2}\frac{h}{v}\mathrm{Tr}\left[\mathcal{V}_\mu\mathcal{V}^\mu\right]$
$\mathcal{O}_{\Box\mathcal{V}\mathcal{V}}$	$a_{\Box\mathcal{V}\mathcal{V}}\frac{\Box h}{v}\mathrm{Tr}\left[\mathcal{V}_\mu\mathcal{V}^\mu\right]$	$\mathcal{O}_{h\Box\Box}$	$a_{h\Box\Box}\frac{h}{v}\frac{\Box h\Box h}{v^2}$
$\mathcal{O}_{d2}$	$ia_{d2}\, g\frac{\partial^\nu h}{v}\mathrm{Tr}\left[W_{\mu\nu}\mathcal{V}^\mu\right]$	$\mathcal{O}_{dd\Box}$	$a_{dd\Box}\frac{\partial^\mu h\partial_\mu h}{v^3}$
$\mathcal{O}_{\Box\Box}$	$a_{\Box\Box}\frac{\Box h\Box h}{v^2}$	$\mathcal{O}_{hdd}$	$a_{hdd}\frac{m_h^2}{v^2}\frac{h}{v}\partial^\mu h\partial_\mu h$

Table 3.2.: HEFT operators $\mathcal{O}_i$ relevant for the RGE analysis, a_i are the corresponding HEFT coefficients. $\mathcal{V}_\mu = (D_\mu U)U^\dagger$ and $D_\mu\mathcal{V}^\mu = \partial_\mu\mathcal{V}^\mu + i[gW_\mu, \mathcal{V}^\mu]$. W, B are the standard gauge field and field strengths. The non-linear sigma model parametrising the Goldstone fields is $U(\pi^a) = \exp\left(i\pi^a\tau^a/v\right)$.

hhh vertices. Using the results of [134, 225] (see also [142, 229–233]), the couplings run according to

$$
\begin{aligned}
16\pi^2\frac{\mathrm{d}}{\mathrm{d}\log\mu^2}\kappa_V^{\mathrm{eff}} &= \frac{m_h^2}{v^2}\left(\frac{3}{2}(\kappa_{2V}-\kappa_V^2)(\kappa_\lambda-\kappa_V) - \kappa_V(1-\kappa_V^2)\right)\\
&\quad + \frac{M_W^2}{2v^2}\left(3\kappa_V(1-\kappa_V^2) + \frac{20}{3}\kappa_V(\kappa_{2V}-\kappa_V^2)\right)\\
&\quad + \frac{M_Z^2}{2v^2}3\kappa_V(1-\kappa_V^2)\,,\\
16\pi^2\frac{\mathrm{d}}{\mathrm{d}\log\mu^2}\left[\kappa_{2V}-(\kappa_V^{\mathrm{eff}})^2\right] &= \frac{m_h^2}{2v^2}\Big(2(\kappa_{2V}-\kappa_V^2)^2 + 4\kappa_V^2(1-\kappa_V^2)\\
&\qquad - (\kappa_{2V}-\kappa_V^2)(4\kappa_{2V} - 16\kappa_V^2 + 18\kappa_\lambda\kappa_V - 3\kappa_4)\Big)\\
&\quad + \frac{M_W^2}{v^2}\left(3(\kappa_{2V}-\kappa_V^2)^2 + (3-\frac{20}{3}\kappa_V^2)(\kappa_{2V}-\kappa_V^2)\right)\\
&\quad + \frac{M_Z^2}{2v^2}3(\kappa_{2V}-\kappa_V^2)(1-\kappa_V^2)\,,\\
16\pi^2\frac{\mathrm{d}}{\mathrm{d}\log\mu^2}\kappa_\lambda^{\mathrm{eff}} &= \frac{m_h^2}{2v^2}\Big(9(\kappa_\lambda-\kappa_V)\kappa_\lambda^2 + (\kappa_\lambda+3\kappa_V)(\kappa_{2V}-\kappa_V^2)\\
&\quad + 6\kappa_\lambda\kappa_4 - 6\kappa_V^3\Big) + \frac{3(M_W^2+M_Z^2)}{2v^2}3\kappa_\lambda(1-\kappa_V^2)\,.
\end{aligned}
\tag{3.70}
$$

κ_4 is the multiplicative modifier of the h^4 vertex, and is set to 1 in the following. The running of κ_{2V} is presented in terms of that of the combination $\kappa_{2V} - (\kappa_V^{\mathrm{eff}})^2$, which controls the energy growth of the $WW \to hh$ process.

The SM is a fixed point of the running, as the RHSs of Eq. (3.71) vanish when $\kappa_V = \kappa_{2V} = \kappa_\lambda = 1$.[**] Linearising the RGEs about this point by defining

$$\begin{aligned} \delta\kappa_V &= \kappa_V^{\text{eff}} - 1\,, \\ \delta K_{2V} &= \kappa_{2V} - (\kappa_V^{\text{eff}})^2\,, \\ \delta\kappa_\lambda &= \kappa_\lambda^{\text{eff}} - 1\,, \end{aligned} \tag{3.71}$$

one can find

$$\begin{aligned} 16\pi^2 \frac{\mathrm{d}}{\mathrm{d}\log\mu^2}\delta\kappa_V &= \delta\kappa_V\left(2\frac{m_h^2}{v^2} - \frac{3(M_W^2+M_Z^2)}{2v^2}\right) + \delta K_{2V}\left(\frac{3M_W^2}{v^2}\right) \\ 16\pi^2 \frac{\mathrm{d}}{\mathrm{d}\log\mu^2}\delta K_{2V} &= \delta\kappa_V\left(-4\frac{m_h^2}{v^2}\right) + \delta K_{2V}\left(-\frac{3m_h^2}{2v^2} - \frac{40M_W^2}{3v^2}\right) \\ 16\pi^2 \frac{\mathrm{d}}{\mathrm{d}\log\mu^2}\delta\kappa_\lambda &= \delta\kappa_V\left(-\frac{27m_h^2}{2v^2} - \frac{9(M_W^2+M_Z^2)}{2v^2}\right) + \delta K_{2V}\left(\frac{2m_h^2}{v^2}\right) + \delta\kappa_\lambda\left(\frac{15m_h^2}{2v^2}\right) \end{aligned} \tag{3.72}$$

up to $\mathrm{O}((\delta\kappa)^2)$ corrections. Note that, to expand the RHS of Eq. (3.71), it is assumed that the couplings are running from a point where all higher order a coefficients are zero.

From Eq. (3.72) it can be noted that $\delta\kappa_\lambda$, which is experimentally the least constrained of the three parameters, self-renormalises significantly stronger than the other two. Also, the negative coefficient for the self-renormalisation of δK_{2V} means that a positive δK_{2V}, as is the case for all renormalisable models, grows in the IR, away from the $\delta K_{2V} = 0$ alignment limit.

3.3. Triple-Higgs at Hadron Colliders

Di-Higgs production via gluon fusion or WBF has already been explored [137,170], and there is growing interest in triple Higgs production as a deeper probe of the structure of the Higgs potential and the nature of electroweak symmetry breaking. Unlike single or double Higgs processes, which have already been observed or constrained with increasing precision, the production of three Higgs bosons remains largely uncharted

[**] Without defining $\kappa_\lambda^{\text{eff}}$ to take account of the effect of the higher derivative operators, κ_λ would appear to run even at the Standard Model point.

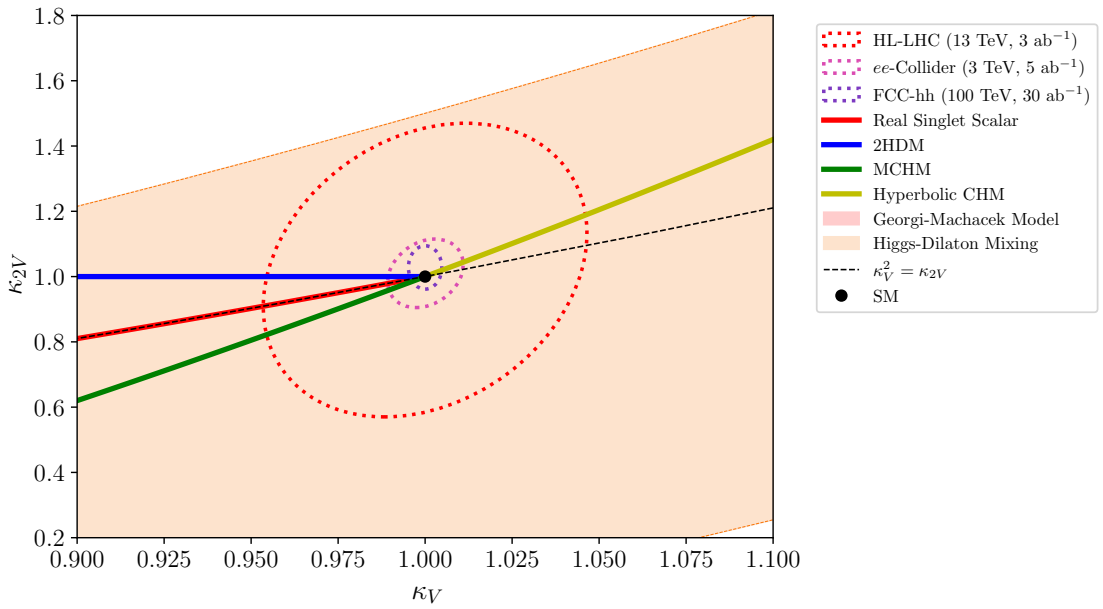

Figure 3.7.: κ_V-κ_{2V} correlation for different 95% CL collider sensitivity extrapolations, assuming $\kappa_\lambda = 1$. The BSM model discussion of Sec. 3.2 is overlaid to highlight regions for which κ_{2V} can provide information beyond κ_V. In particular, the fourth quadrant (where $\kappa_{2V} < 1 < \kappa_V$) is populated by scenarios of large dilaton-Higgs mixing (we scan $-1 \leq \kappa_{2V} \leq 2, |s_\theta| \leq 1$ with a physical solution of $\zeta > 0$; again assuming $M_{hh} = 300$ GeV as before). Note that the dilaton includes effects beyond the deformation truncated in Eq. (3.59). Hence, the covered area is comparatively larger. The black dashed line represents $\kappa_V^2 = \kappa_{2V}$ and all BSM renormalisable models lie in the region above this line, *i.e.*, $\kappa_V^2 \leq \kappa_{2V}$.

territory at current collider energies. As such, it provides a unique window into potential new dynamics in the scalar sector.

In the SMEFT framework, gauge invariance enforces tight correlations between single, double, and triple Higgs couplings [119], limiting the extent to which one can independently modify the hhh interaction. In contrast, HEFT allows for more freedom [134, 225, 234], enabling significant deviations in triple Higgs couplings without necessarily affecting h or hh rates. This opens the door to scenarios where the hhh production rate could be enhanced by an order of magnitude or more [234, 235], making it a promising avenue for uncovering signs of physics beyond the Standard Model (BSM).

Beyond EFT considerations, many UV extensions of the Higgs sector, such as models with additional scalar fields or extended gauge symmetries, predict resonant enhancements in multi-Higgs final states [236, 237]. These enhancements often

emerge in connection with mechanisms that address fundamental shortcomings of the Standard Model. One compelling example is the generation of the observed baryon asymmetry of the Universe via a strong first-order electroweak phase transition (SFOEWPT) [32, 238], which necessitates alterations to the Higgs potential. Such modifications generically affect the shape of the potential in a way that leaves characteristic imprints on the rates of di-Higgs and, more prominently, triple Higgs production.

Given these motivations, triple Higgs production stands out as a powerful probe of the scalar sector self-interactions, with sensitivity to both low-energy effective couplings and high-scale resonant phenomena. This section explores its implications for BSM physics, with particular emphasis on SFOEWPT scenarios and prospects for future collider experiments.

3.3.1. Models, Scans and Cross-Sections

Resonant extensions of the SM have the potential to enhance cross-sections through new on-shell contributions that are not present in the continuum production expected in the SM. Such modifications of scalar couplings are ubiquitous in Higgs sector extensions, with related interference effects between different new physics and modified SM contributions can lead to an intricate interplay of different phase space regions. Together, these can lead to either a net enhancement or a reduction of the cross-sections of $hh(h)$ production. Whilst some differential information might be obtainable for the hh final states at the HL-LHC, this is less likely for hhh production. However, experimental proof-of-principle investigations have yet to be made available. It is therefore imperative to focus on the integrated cross-sections as relevant physical observables, including the interplay of different phase space regions that highlight resonance and interference contributions in relation to the SM.

Along these lines, a particularly motivated class of models is the extension of the SM by an additional doublet, as in 2HDMs and the latter's complex and singlet-extended variation. These models introduce all aforementioned phenomenological modifications in clear relation to existing Higgs measurements and exotics searches; they further enable a direct correlation of multi-Higgs rates with an SFOEWPT (see in particular [239]). This is most transparently expressed through the so-called "real" 2HDM (R2HDM), where all the 2HDM parameters are assumed to be real variables,

thus making clear distinctions between CP-even and -odd exotic Higgs bosons. The R2HDM is generalised by admitting complex phases (giving rise to the “complex" 2HDM, C2HDM), which provides a natural interface to incorporate CP-violation as an avenue to satisfy Sakharov’s criteria further. Extensions of the R2HDM by an additional real singlet field (the Next-to-Minimal 2HDM, N2HDM) generalise the typical correlations of the R2HDM through additional contributions to the potential and a richer mixing structure [240] of states with given CP quantum numbers. The following analysis considers these three scenarios to discuss correlations and their modifications when requiring a sufficient SFOEWPT.

The 2HDM Extensions

The potential for the 2HDM is given by

$$V_{\text{2HDM}} = m_{11}^2 \Phi_1^\dagger \Phi_1 + m_{22}^2 \Phi_2^\dagger \Phi_2 - \left(m_{12}^2 \Phi_1^\dagger \Phi_2 + \text{h.c.} \right) + \frac{\lambda_1}{2} \left(\Phi_1^\dagger \Phi_1 \right)^2 + \frac{\lambda_2}{2} \left(\Phi_2^\dagger \Phi_2 \right)^2 + \lambda_3 \left(\Phi_1^\dagger \Phi_1 \right) \left(\Phi_2^\dagger \Phi_2 \right) + \lambda_4 \left(\Phi_1^\dagger \Phi_2 \right) \left(\Phi_2^\dagger \Phi_1 \right) + \left[\frac{\lambda_5}{2} \left(\Phi_1^\dagger \Phi_2 \right)^2 + \text{h.c.} \right], \tag{3.73}$$

with

$$\Phi_i = \frac{1}{\sqrt{2}} \begin{pmatrix} \phi_i^+ \\ \varphi_i + i a_i \end{pmatrix}, \; i = 1, 2, \tag{3.74}$$

transforming as $(\mathbf{1}, \mathbf{2}, 1/2)$ under the SM gauge group. The potential obeys the usual $\mathbb{Z}_2$ symmetry assignments to remove flavour-changing interactions [241], which is softly broken by the m_{12}^2 term in V_{2HDM}. In the case of the R2HDM, all parameters in this potential are taken to be real

$$m_{11}^2, m_{22}^2, m_{12}^2, \lambda_{1,\ldots,5} \in \mathbb{R} \qquad \text{(R2DHM)}, \tag{3.75}$$

whereas in the CP-violating version

$$m_{11}^2, m_{22}^2, \lambda_{1,\ldots,4} \in \mathbb{R}, \; m_{12}^2, \lambda_5 \in \mathbb{C} \quad \text{(C2DHM)} \tag{3.76}$$

(with independent phases for m_{12}^2 and λ_5 so that they cannot be absorbed by field redefinitions).

The usual equations to obtain the minimum for this potential alongside the physical masses and mixing angles hold, e.g., for the R2HDM, the physical neutral Higgs masses are related to the Lagrangian eigenstates via

$$\begin{pmatrix} H \\ h \end{pmatrix} = R_2(\alpha) \begin{pmatrix} \varphi_1 \\ \varphi_2 \end{pmatrix}, \tag{3.77}$$

where $R_2(\alpha)$ is the standard 2-dimensional orthogonal rotation matrix. Furthermore,

$$\tan\beta = \frac{\langle \Phi_2 \rangle}{\langle \Phi_1 \rangle} = \frac{v_2}{v_1} \tag{3.78}$$

denotes the diagonalisation angle of $R_2(\beta)$ for the CP-odd and charged fields (including the massless Goldstone mode). The brackets around the fields denote their respective vacuum expectation values (vevs), with the total vev, $\sqrt{v_1^2 + v_2^2} \equiv v \approx 246.22$ GeV.

In the C2HDM, due to explicit CP violation, one can still define massless Goldstone modes through $R_2(\beta)$ (i.e. the vacuum expectation values $\langle \Phi_{1,2} \rangle$ can be aligned), but the neutral electromagnetic fields no longer have defined CP quantum numbers and are now diagonalised by a 3-dimensional orthogonal rotation matrix $R_3(\alpha_1, \alpha_2, \alpha_3)$.

Extending the 2HDM with an additional real singlet under the SM gauge group $\Phi_S \sim (\mathbf{1}, \mathbf{1})_0$ leads to the N2HDM with the potential,

$$V_{\text{N2HDM}} = V_{\text{R2HDM}} + \frac{1}{2} m_S^2 \Phi_S^2 + \frac{\lambda_6}{8} \Phi_S^4 + \frac{\lambda_7}{2} \left(\Phi_1^\dagger \Phi_1 \right) \Phi_S^2 + \frac{\lambda_8}{2} \left(\Phi_2^\dagger \Phi_2 \right) \Phi_S^2, \tag{3.79}$$

which generalises the mixing in the CP-even sector compared to the R2HDM to a 3-dimensional orthogonal rotation after expanding Φ_S around a non-vanishing VEV $\langle \Phi_S \rangle$, $\Phi_S = \langle \Phi_S \rangle + \varphi_3$. The potential is invariant under the usual (softly broken) $\mathbb{Z}_2$ symmetry and an additional $\mathbb{Z}_2'$ symmetry, under which $\Phi_{1,2} \to \Phi_{1,2}$ and $\Phi_S \to -\Phi_S$.

In all these scenarios, the interactions of the Higgs boson(s) with known matter are changed as a consequence of the $\mathbb{Z}_2$ assignments giving rise to the usual classification of 2HDM models (see Ref. [242] for a review) as well as mixing. The focus of this analysis is on the type-I scenario in the following, as this provides a wider range of acceptably strong phase transitions [243–245]. The couplings of the extended Higgs

spectrum to the SM quarks in the R2HDM are then given by

$$\begin{aligned} \xi_h^{u,d} &= \frac{\cos\alpha}{\sin\beta}\,, \\ \xi_H^{u,d} &= \frac{\sin\alpha}{\sin\beta}\,, \\ \xi_A^{u,d} &= \cot\beta\,, \end{aligned} \tag{3.80}$$

relative to the SM Higgs couplings. In the extended 2HDM, these couplings are then further modified by the aforementioned rotations in the C2HDM and N2HDM, respectively.

The inter-Higgs interactions obtained from expanding the potential in the mass basis further impact the multi-Higgs production through modified trilinear and quartic Higgs boson interactions. Depending on the realisations considered, these can be very different, ranging from relatively rigid correlations in the 2HDM to relaxing them in the N2HDM and the C2HDM along the lines of singlet admixture and explicit CP violation, respectively. This enables comments on the impact of these various phenomenological variations on the expected $hh(h)$ production rates in light of the strength of the electroweak phase transition. A notable exception to the phenomenology discussed is provided by the 2HDM with additional symmetry protection that achieves alignment through an enhanced custodial symmetry [246–248].

Scanning for SFOEWPTs and multi-Higgs cross-sections

Fixing the Higgs mass at $m_h = 125.09$ GeV, viable parameter points are generated on `ScannerS` [249, 250], where all other input parameters (such as the masses of the heavier exotics and mixing angles) are varied randomly in wide ranges to cover the parameter space allowed by the relevant theoretical constraints and by the experimental constraints given by the Higgs measurements (as checked via an interface to `HiggsTools` [251–253]), flavour constraints ($\mathcal{R}_b$ [254, 255] and $B \to X_s\gamma$ [255–260]), and electroweak precision data (by demanding the S, T, and U parameters [75] to be within 2σ of the SM fit [72]).

The finite temperature phenomenology of the scalar extensions is explored using `BSMPTv3` [261–263]. The strength of the phase transition is assessed during the

percolation stage, and a phase transition is deemed to be of first order and strong when

$$\xi_p = \frac{v_p(T_p)}{T_p} > 1\,, \tag{3.81}$$

i.e. when the vev at the percolation temperature T_p is larger than unity in units of T_p. This is a conventional measure to safeguard against sphaleron washout effects when considering electroweak baryogenesis (see also [264,265] for further discussions). For a given parameter choice that is consistent with the theoretical constraints and the current experimental outcome as verified by `ScannerS`, the thermal history of the corresponding model is tried using `BSMPT`, which achieves this by including the following finite-temperature potential up to one-loop order

$$V_{\text{eff}}(T) = V_0(T=0) + V_{\text{CW}}(T=0) + V_{\text{CT}}(T=0) + V_{\text{T}}(T) + V_{\text{daisy}}(T) \tag{3.82}$$

including thermal corrections (see e.g. [266–268] for excellent reviews of the subject) as well as Daisy-resummation (concretely considering these in the Arnold-Espinosa approach [269]). As in Refs. [243,270,271], the finite counterterm contributions are included to identify the minima of the potential, the Higgs masses and mixing angles at tree level (V_0) and at one loop ($V_0 + V_{\text{CW}} + V_{\text{CT}}$) at $T = 0$, to facilitate tests for the compatibility with experimental constraints. Here V_{CW} and V_{CT} denote the one-loop Coleman-Weinberg and the counterterm potential, respectively. With `BSMPT`, the trilinear and quartic Higgs self-couplings are computed from the third and fourth derivatives of the potential, respectively, whose tree-level values are used as input to the $hh(h)$ cross-sections.

To compare the results of the EWPT with the expected LHC phenomenology, the various (extended) 2HDMs are implemented using `FeynRules` [64] and `NLOCT` [272], which is interfaced via a `Ufo` [273] model with `Madgraph5_aMC@NLO` [160]. Cross-sections are generated for $hh(h)$ production through gluon fusion, $pp \to hh(h)$, at leading, i.e. one-loop order, including top and bottom quark contributions (derived from Eq. (3.80) directly or as part of the parameter scan). Points from the `ScannerS` + `HiggsTools` + `BSMPT` scan are interfaced with this toolchain for centre-of-mass energies $\sqrt{s} = 13, 100$ TeV to compare ξ_p and cross-section modifications of multi-Higgs modes at the LHC and a future FCC-hh. It is known that the dominant QCD corrections that largely increase the parton-level leading order cross-section generalise qualitatively to BSM resonance structures, see e.g. [274].

3.3.2. Results and Discussion

Turning to the results, all scenarios considered are defined by fixed charge assignments under the electroweak group, leading to an expected tight correlation between hh and hhh phenomenology. In such cases, one would anticipate that deviations from the Standard Model should appear first in the more abundant hh final states. However, the presence of new resonant structures can make a significant difference, particularly given that the continuum Standard Model expectation for

$$\sigma(pp \to hhh) \simeq 50 \text{ ab} \tag{3.83}$$

at the LHC [235] is deceptively small. For comparison, the gluon fusion Higgs pair production cross-section at next-to-leading order in QCD is approximately [276–279]

$$\sigma(pp \to hh) \simeq 27 \text{ fb} \tag{3.84}$$

for 13 TeV collisions in the Standard Model. In scenarios with new resonances, the hhh cross-section could be enhanced to a level where it becomes experimentally relevant at the HL-LHC and serves as a meaningful cross-check of potential discoveries in

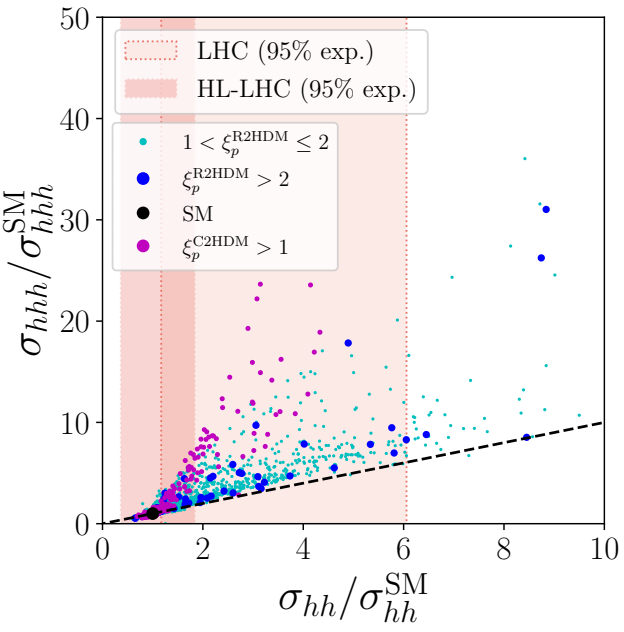

Figure 3.8.: 2HDM scan results for gluon fusion $hh(h)$ production relative to the non-resonant SM expectation for $\xi_p > 1$ at the LHC and 13 TeV collisions. The colours denote the various phase transition strengths in the R2HDM and the C2HDM. The red shaded region shows the current and HL-LHC hh sensitivity [275].

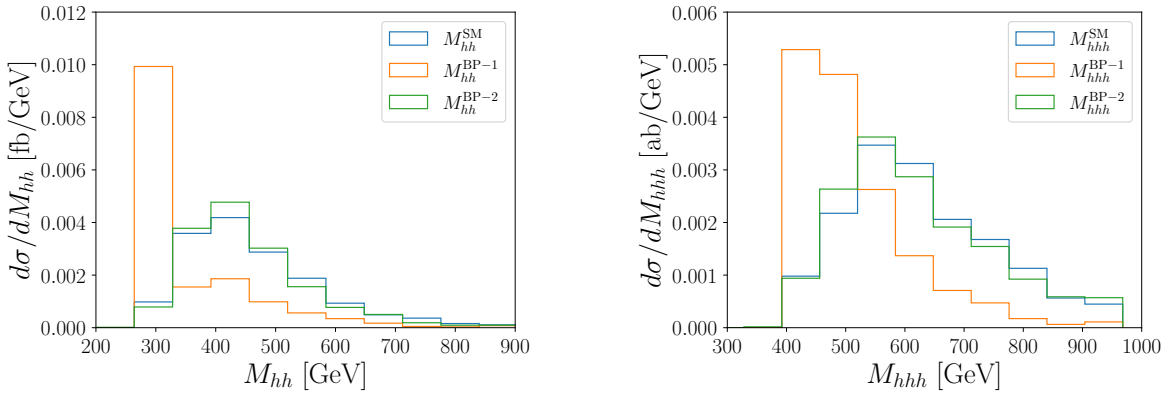

Figure 3.9.: Invariant di- and triple-Higgs mass distributions for the SM as well as for benchmark points with a large (BP-1) and representatively small (BP-2) enhancement for the *hhh*-production cross-sections. The respective cross-sections and parameter choices for the points are shown in Table 3.3.

Benchmark Points	$\sigma_{hh}/\sigma_{hh}^{\mathrm{SM}}$	$\sigma_{hhh}/\sigma_{hhh}^{\mathrm{SM}}$	m_h [GeV]	Γ_H [GeV]	C_{ffh}	C_{ffH}
largely enhanced	3.24	15.26	274.29	0.20	1.027	-0.124
SM-like	1.02	1.02	469.30	2.49	0.997	-0.484

Benchmark Points	g_{hhh} [GeV]	g_{hhH} [GeV]	g_{hhhh}	g_{hhhH}
largely enhanced	167.26	75.28	0.661	0.203
SM-like	190.54	-7.11	0.774	-0.011

Table 3.3.: Cross-sections and parameter choices for chosen benchmark points with large (BP-1) and representatively small (BP-2) enhancements in *hhh*-production cross-sections.

hh production. That said, depending on the parameter space, deviations could also arise primarily in the *hhh* channel, with little to no visible effect in *hh*. Either outcome would motivate a follow-up analysis at a future hadron collider such as the FCC-hh. The obtained cross-sections for di- and triple-Higgs production, normalised to the respective SM expectation, are illustrated in Fig. 3.8 for the R2HDM and the C2HDM scans for phase transition strengths $\xi_p > 1$. Underproduction relative to the SM is possible, but phenomenologically is largely uninteresting; however, new resonant contributions can greatly enhance the $hh(h)$ rates. As expected, there is a clear correlation between *hh* and *hhh* cross-sections, yet the relative enhancement tends to be greater for *hhh* production. A fully differential analysis of triple Higgs final states will always be a serious experimental challenge, yet the

$$M_{hhh}^2 = (p_{h_1} + p_{h_2} + p_{h_3})^2 \tag{3.85}$$

distribution is a particularly telling observable to quantitatively understand the observed cross-section modifications as illustrated in Fig. 3.9.

In case the heavy state is close to the $m_h \simeq 2m_h$ threshold, $pp \to hh$ receives a large enhancement in the resonance region which in turn is accompanied by underproduction for $M_{hh}^2 = (p_{h_1} + p_{h_2})^2 \gtrsim m_h^2$ compared to the SM expectation as these contributions effectively enhance the destructive interference between the involved triangle and box topologies [151, 194, 280]. This situation is mirrored in $pp \to hhh$ where the threshold region $M_{hhh} \simeq 3m_h$ probes a wider range of $M_{h_i h_j} \simeq 2m_h$, $i, j = 1, 2, 3$, $j > i$ enhancement (effectively isolating $pp \to Hh, H \to hh$). This can lead to a comparably larger enhancement of hhh production compared to hh. One can find such maximum enhancements up to factors of ~ 4 of hhh over hh production (relative to their respective SM values) for the R2HDM in the performed scan.

For parameter choices that lead to heavier spectra, enhancements can again arise from $H \to hh$ resonance structures. These are, however, small when compared to enhancements arising from three-body decays $H \to hhh$. While the latter correspond to small branching ratios of the typically top-philic states, the excess over the relatively small SM expectation can be considerable.

These observations can be used to correlate to the strength of the first-order phase transition; given a thermodynamic process, the EWPT is driven by the physics of the light degrees of freedom. For the concrete example of the R2HDM with relatively rigid coupling constraints of the Higgs bosons to other matter (in particular when considering the Higgs signal strength constraints inferred from LHC measurements), this is achieved by making the non-SM degrees of freedom more accessible via lighter spectra. This is visible from Fig. 3.10, which distils the results of a scan of the strength of the phase transition ξ_p at the percolation stage as a function of the mass of the neutral CP-even heavy Higgs boson H.

A priori, this is good news for multi-Higgs final states and their observation at the LHC. Triple Higgs production can receive new contributions from nested Hh production, but, more importantly, new resonant $H \to hhh$ decays. Cross-section enhancements for moderately strong transitions[††] $\xi_p \gtrsim 1$, are $\sigma_{hhh}/\sigma_{hhh}^{\text{SM}} \simeq 40$ and $\sigma_{hh}/\sigma_{hh}^{\text{SM}} \simeq 20$ (the relation with an SFOEWPT is discussed below as these numbers

[††] In fact, there are percent-level differences between the nucleation and percolation temperatures. For the models discussed, the distinction between these temperatures is somewhat irrelevant; however, they have very different meanings for the phenomenology of the early Universe, see [281, 282].

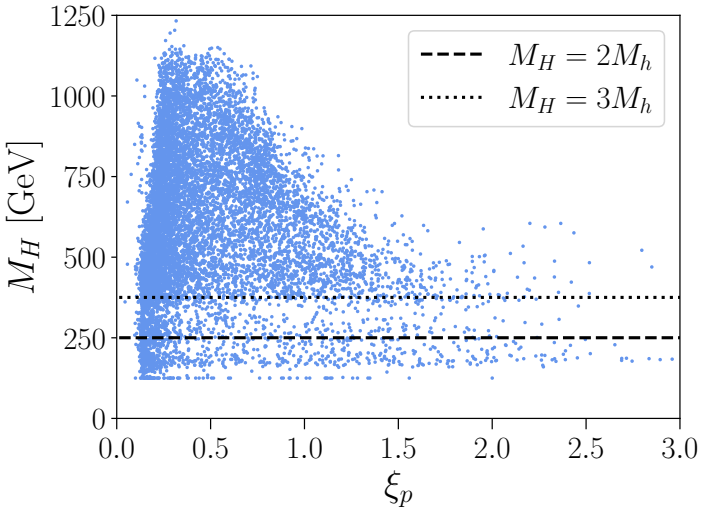

Figure 3.10.: Mass spectra, here specifically for the resonance H, explored in the scan.

can also be found for $\xi_p < 1$.). Enhancements of this size in the triple Higgs rate of Eq. (3.83) amount to around 140 events in the 6 b final state after applying a 70% b-tagging efficiency at the HL-LHC phase (13 TeV, 3 ab^{-1}). Whilst this is undeniably challenging, the appearance of additional resonance structures in the b jet distribution can be exploited to combat backgrounds. Cross-relating such an enhancement with hh and exotics measurements will enable the phenomenological dissection of the TeV scale's relation with electroweak baryogenesis: To guide the eye in identifying which enhancements can be relevant from hh limits, the red bands in Fig. 3.8 highlight estimates of current and HL-LHC hh sensitivity [275].

Moving to stronger phase transitions, the three-Higgs threshold $H \to hhh$ becomes decreasingly relevant, and most observations are from correlated resonant $H \to hh$ and $Hh \to hhh$ contributions. There is a wider phase space available for $Hh \to hhh$ compared to $H \to hh$, which leads to a comparably larger enhancement in hhh production, however, compared to a small baseline rate expected in the SM. As the hh rate starts from a much larger expectation compared to hhh production, it is clear that the former will statistically dominate the multi-Higgs phenomenology at the HL-LHC if agreement with the SM prevails. Should a discovery be made, factors of ten enhancements in the triple Higgs rate might provide further motivation to target hhh production at the HL-LHC. The multi-resonant structures described above will then also contribute to further control backgrounds compared to non-resonant considerations, which are harder to isolate from continuum backgrounds. Overall, the strength of the phase transition is predominantly driven by the mass scale of the non-SM states. These will

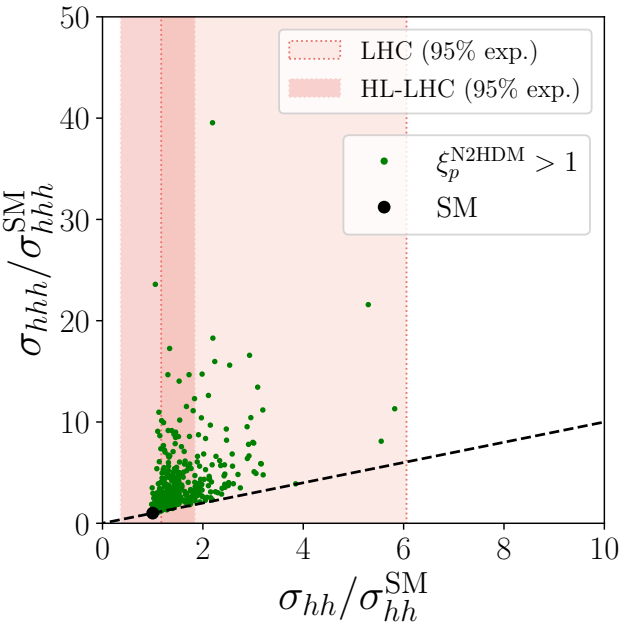

Figure 3.11.: Double and triple Higgs production cross-sections relative to the SM expectation for a scan over the N2HDM for $\xi_p > 1$ at the LHC (for a centre-of-mass energy of 13 TeV).

leave correlated effects in the rates, but the neutral Higgs rates alone are not indicative of the strength of the phase transition in the R2HDM.

Introducing additional resonances into the spectrum opens up significant regions of parameter space for non-standard phenomenology. This is evident in the cross-sections obtained in the complex extension of the R2HDM, namely the C2HDM, particularly along the hhh direction compared to hh, as shown in Fig. 3.8. The cross-section enhancements discussed earlier such as those from $H \to hh$ and $H \to hhh$, can occur simultaneously when both of the new scalar degrees of freedom in the C2HDM are kinematically accessible in two- and three-body decays. As a result, the phenomenology of the $hh(h)$ final states becomes considerably richer.

Nevertheless, tight constraints from electric dipole moment measurements [283] (see also the discussion on the C2HDM in [284, 285]) imply that the complex phases associated with the top- and bottom-Higgs interactions remain small. The Higgs mixings absent in the R2HDM are also suppressed, so the departure from the R2HDM framework is modest. This is also reflected in the size of the CP admixture, which quantifies the scalar-pseudoscalar mixing in the SM-like Higgs. For the Type-I C2HDM,

following Refs. [284, 286], the pseudoscalar admixture is defined as

$$\Psi_i^{\text{C2HDM}} = (R_{i3})^2, \tag{3.86}$$

where R is the orthogonal matrix that diagonalises the neutral scalar mass matrix. In this setup, the maximum CP admixture observed for the SM-like Higgs reaches about 9.5% for $\xi_p > 1$, and around 10% for $\xi_p < 1$.

As in the C2HDM, the presence of additional resonances in the N2HDM leads to distinct features in the M_{hh} and M_{hhh} invariant mass distributions. These features can enhance triple Higgs production by factors of around 20 compared to di-Higgs production, as shown in Fig. 3.11. Interestingly, some of the benchmark points do not exhibit particularly unusual behaviour in the hh final state. This is likely due to the limited number of scan points where the heavier exotic scalars lie close to the $2m_h$ threshold, where double Higgs production is most enhanced. While enhancements of up to a factor of 10 in triple Higgs production would remain extremely difficult to observe at the HL-LHC, they represent a promising target for future colliders such as the FCC-hh. In this context, it is worth noting that all the results discussed so far can be directly extrapolated to the FCC-hh, with reference cross-sections of $\sigma_{hh}^{\text{SM}} \approx 800$ fb [287] and $\sigma_{hhh}^{\text{SM}} \approx 2.9$ fb [288].

The results presented here are based on a leading-order study of the electroweak sector. While QCD corrections are generally insensitive to the new mass scales involved in multi-Higgs production, an assumption commonly used in higher-precision calculations, weak radiative corrections may still impact the results quantitatively. For discussions of their effect on the Higgs self-coupling at 125 GeV, see [280, 289–291]. These corrections form only part of the full resonant amplitude and deserve more detailed investigation. Even so, the key observations related to the mass spectrum of the new degrees of freedom should remain qualitatively robust under higher-order effects.

3.4. Conclusions

This chapter details a comprehensive study of multi-Higgs production channels at hadron colliders, combining phenomenological projections with theoretical analyses of representative BSM scenarios, with a particular emphasis on WBF Higgs pair

production and triple Higgs production via gluon-gluon fusion, motivated by their distinct sensitivity to modifications of the Higgs sector.

In WBF di-Higgs production, κ_{2V} is subject to considerably weaker experimental constraints than κ_V. This relative looseness makes WBF di-Higgs production an ideal channel for probing deviations in κ_{2V} that remain hidden in single-Higgs processes. In the context of SMEFT, where a decoupling structure is assumed, κ_{2V} and κ_V are expected to exhibit a tight correlation. In contrast, more general HEFT frameworks allow these parameters to vary independently, enabling larger and structurally different deviations.

Significant departures of κ_{2V} from its SM value require the presence of extended scalar sectors featuring tree-level mixing with electroweak multiplets of dimension greater than one, such as triplets or quadruplets. In these scenarios, large positive shifts in κ_{2V} arise naturally, with loop-induced effects typically aligned with the SMEFT expectation $\kappa_{2V} = \kappa_V^2$, up to small corrections. All renormalisable extensions to the SM satisfy the inequality $\kappa_{2V} - \kappa_V^2 \geq 0$, and this quantity increases under renormalisation group running. However, non-renormalisable completions, including composite Higgs models with dilaton admixtures or strongly coupled conformal sectors, can generate negative values of $\kappa_{2V} - \kappa_V^2$. This distinctive behaviour offers an experimentally testable signature of non-decoupling UV dynamics.

While κ_λ has only a mild effect on WBF di-Higgs production, substantial deviations can be identified in a wide range of BSM theories, including models with strong scalar quartic couplings, softly broken symmetries, or extended scalar sectors. Since κ_λ is most directly constrained via ggF-induced di-Higgs production, correlations with WBF observables can significantly strengthen overall exclusion or discovery potential.

The latter part of the chapter focuses on triple Higgs production via gluon-gluon fusion in 2HDM extensions and its singlet-augmented variant. Parameter scans targeting regions of the model parameter space compatible with a strong first-order electroweak phase transition show that triple Higgs cross-sections are largely enhanced over the SM expectations compared to the corresponding di-Higgs values. Enhancements by up to a factor of 40 over the SM prediction for $pp \to hhh$ can be observed, primarily due to resonant production mechanisms such as $pp \to H \to hhh$ and cascade decays of heavy scalars into multiple Higgs bosons. These enhancements broaden the kinematic reach of triple-Higgs searches and offer a unique probe of otherwise elusive exotic scalar states. Therefore, despite the inherent challenges posed by the small SM rate for

triple-Higgs production, the signal has been shown to become relevant at the HL-LHC for the realistic BSM scenarios under consideration. These results provide strong motivation for the continued development of experimental strategies targeting this channel, especially in light of its direct sensitivity to scalar dynamics associated with the electroweak phase transition and the early thermal history of the Universe.

Multi-Higgs production channels thus offer a powerful and complementary window into Higgs sector extensions. The distinct sensitivities of the myriad processes to different scalar couplings and model structures underscore their relevance in a future precision Higgs program, both at the HL-LHC and at potential future colliders.

Chapter 4.

Phenomenology of a (deformed-) Type-II Seesaw Mechanism

"Neutrino masses are perhaps the most compelling evidence for physics beyond the Standard Model."

— Every BSM collider physicist talking about neutrinos.

The quest to dynamically explain the smallness of neutrino masses [292–295] has been both extensive and long-standing. Unlike charged leptons, neutrinos admit a broad range of model-building possibilities for generating their mass terms. Continuing the discussion on neutrino mass generation from Chapter 2, a key theoretical insight in this quest is provided by the unique canonical mass dimension-5 Weinberg operator,

$$\mathcal{O}_5 = (\overline{L}_L^c \tilde{\Phi})(\tilde{\Phi}^\dagger L_L), \tag{4.1}$$

and its hermitian-conjugate, where L_L represents the left-handed lepton doublet, the superscript c represents charge-conjugation, and $\tilde{\Phi} = i\tau^2\Phi^*$, where Φ is the SM Higgs doublet. This operator offers a powerful bottom-up clue for understanding how neutrino masses can arise once the Higgs field acquires a vacuum expectation value (vev). Despite being non-renormalisable, the Weinberg operator can be UV-completed at tree level in precisely three ways, corresponding to the well-known Seesaw Mechanisms. These include the introduction of right-handed neutrino SM singlets (Type-I) [45, 48], extensions of the scalar sector (Type-II) [296–301], and the inclusion of fermionic triplets (Type-III). Loop-level completions, such as those in the Zee and Babu models [302, 303], also offer viable alternatives.

Gauge invariance connects neutrinos to the charged lepton sector in the SM, making precision measurements in the latter highly relevant for probing neutrino mass generation. Among the Seesaw Mechanisms, the Type-II Seesaw, characterised by the inclusion of a complex scalar triplet, has particularly rich phenomenological implications. It offers distinctive collider signatures, notably via Drell-Yan-like production processes [304, 305], and is actively being explored at the LHC [306–309]. In addition, the presence of charged scalar states enables complementary probes via low-energy meson decays and off-shell processes [310, 311].

Nevertheless, it remains plausible that the mass scale of the new degrees of freedom responsible for neutrino mass generation lies beyond the direct reach of the LHC. This expectation is particularly true in the minimal Type-II scenario, where the scalar triplet mass is often constrained to be very large by experimental bounds. However, deviations from the minimal assumptions, such as through the inclusion of higher-dimensional operators, can lead to modified phenomenological outcomes. Moreover, stringent constraints from rare decay processes such as $\mu \to 3e$ and $\mu \to e\gamma$ frequently push the mass scale of new states beyond LHC sensitivity, further motivating the study of non-minimal extensions.

This chapter investigates a modified version of the Type-II Seesaw Mechanism, incorporating higher-dimensional effective operators. A specific set of couplings is identified, under which compatibility with electroweak precision observables and low-energy muon decays can be maintained, while allowing for new resonant signatures at collider-accessible energy scales. Such a scenario demands a departure from the standard Type-II framework at the TeV scale, leading to novel and testable implications. The vanilla Type-II Seesaw model is introduced in Sec. 4.1, followed by a detailed analysis of the parameter constraints in Sec. 4.1.1. The non-minimal, TeV-scale modifications are presented in Sec. 4.2, where it is shown that the relevant mass scales can be lowered to within reach of current and future collider experiments. Finally, the connection between low-energy precision observables, particularly from muon physics and their TeV-scale implications via renormalisation group evolution is explored in Sec. 4.2.

4.1. The Type-II Seesaw Mechanism

The Type-II Seesaw Mechanism offers a natural and minimal framework to account for the smallness of observed neutrino masses, which comes about by extending the

SM scalar sector minimally by a $\mathrm{SU}(2)_L$ triplet scalar Δ, with a hypercharge $Y_\Delta = 1$, thus transforming as $(\mathbf{1},\mathbf{3},1)$ under the SM gauge group $SU(3)_C \times SU(2)_L \times U(1)_Y$. The inclusion of Δ leads to new terms in the scalar potential $V(\Phi,\Delta)$,

$$\begin{aligned} V(\Phi,\Delta) = -m_H^2\,(\Phi^\dagger\Phi) + \lambda_H(\Phi^\dagger\Phi)^2 + m_\Delta^2 \mathrm{Tr}[\Delta^\dagger\Delta] + \lambda_{\Delta_1}(\mathrm{Tr}[\Delta^\dagger\Delta])^2 + \lambda_{\Delta_2}\mathrm{Tr}[(\Delta^\dagger\Delta)^2] \\ + \lambda_{\Delta_3}(\Phi^\dagger\Phi)\mathrm{Tr}[\Delta^\dagger\Delta] + \lambda_{\Delta_4}\Phi^\dagger\Delta\Delta^\dagger\Phi + \left[\mu_\Delta \Phi^\dagger i\sigma^2\Delta^\dagger\Phi + \mathrm{h.c.}\right] , \end{aligned} \tag{4.2}$$

with Φ denoting the SM $\mathrm{SU}(2)_L$ Higgs doublet. In addition to the neutral components, Δ also comprises singly-charged and doubly-charged scalars, holding significant phenomenological implications as direct probes of the Type-II Seesaw Mechanism and its characteristics in various collider experiments [307, 312–319]. Δ can be explicitly expanded around its vacuum expectation value v_Δ,

$$\Delta = \frac{1}{\sqrt{2}} \begin{pmatrix} \delta^+ & \sqrt{2}\Delta^{++} \\ (\delta^0 + v_\Delta + i\chi) & -\delta^+ \end{pmatrix} . \tag{4.3}$$

The addition of the complex triplet results in novel Yukawa interactions between Δ and the left-handed lepton doublet (L_L),

$$\mathcal{L}^{\mathrm{BSM}}_{\mathrm{Yukawa}} = -Y_\Delta\, \overline{L}_L^c \Delta L_L + \mathrm{h.c.}\,. \tag{4.4}$$

Here, Y_Δ is the BSM Yukawa coupling matrix, and the c superscript represents charge-conjugation. These are quintessential for generating non-zero neutrino masses through the non-zero vev of the complex triplet Δ after electroweak symmetry breaking (EWSB). The Lagrangian for the Type-II Seesaw Mechanism is therefore given by,

$$\mathcal{L}_{\text{Type-II}} = \mathcal{L}_{\mathrm{SM}} + \mathrm{Tr}[D_\mu\Delta^\dagger D^\mu\Delta] - V(\Phi,\Delta) + \mathcal{L}^{\mathrm{BSM}}_{\mathrm{Yukawa}} , \tag{4.5}$$

where $\mathcal{L}_{\mathrm{SM}}$ represents the full SM Lagrangian excluding the scalar potential. After EWSB, the two vevs v_Φ and v_Δ contribute to the masses of the gauge bosons, with,

$$M_{W^\pm}^2 = \frac{g^2}{4}(v_\Phi^2 + 2v_\Delta^2), \quad M_Z^2 = \frac{g^2+g'^2}{4}(v_\Phi^2 + 4v_\Delta^2)\,, \tag{4.6}$$

where g and g' are the gauge couplings corresponding to the $SU(2)_L$ and $U(1)_Y$ gauge groups, respectively. The masses of the scalars become,

$$M^2_{\text{neutral, CP-even}} = \begin{pmatrix} 2\lambda_H v_\Phi^2 & -\sqrt{2}\mu_\Delta v_\Phi + v_\Delta v_\Phi(\lambda_{\Delta_3}+\lambda_{\Delta_4}) \\ -\sqrt{2}\mu_\Delta v_\Phi + v_\Delta v_\Phi(\lambda_{\Delta_3}+\lambda_{\Delta_4}) & \dfrac{\mu_\Delta v_\Phi^2}{\sqrt{2}v_\Delta} + 2v_\Delta^2(\lambda_{\Delta_1}+\lambda_{\Delta_2}) \end{pmatrix}, \tag{4.7}$$

$$M^2_{\text{neutral, CP-odd}} = \begin{pmatrix} 2\sqrt{2}\mu_\Delta v_\Delta & -\sqrt{2}\mu_\Delta v_\Phi \\ -\sqrt{2}\mu_\Delta v_\Phi & \dfrac{\mu_\Delta v_\Phi^2}{\sqrt{2}v_\Delta} \end{pmatrix}, \tag{4.8}$$

$$M^2_{\text{charged}} = \begin{pmatrix} \dfrac{\mu_\Delta v_\Phi^2}{\sqrt{2}v_\Delta} - \dfrac{1}{4}v_\Phi^2\lambda_{\Delta_4} & -\mu_\Delta v_\Phi + \dfrac{v_\Phi v_\Delta \lambda_{\Delta_4}}{2\sqrt{2}} \\ -\mu_\Delta v_\Phi + \dfrac{v_\Phi v_\Delta \lambda_{\Delta_4}}{2\sqrt{2}} & \sqrt{2}\mu_\Delta v_\Delta - \dfrac{1}{2}v_\Delta^2\lambda_{\Delta_4} \end{pmatrix}, \tag{4.9}$$

$$M^2_{\Delta^{\pm\pm}} = \frac{\mu_\Delta v_\Phi^2}{\sqrt{2}\,v_\Delta} - v_\Delta^2\lambda_{\Delta_2} - \frac{1}{2}v_\Phi^2\lambda_{\Delta_4}\,. \tag{4.10}$$

Since Δ acquires a non-zero vev, the scalar sector, apart from the doubly charged scalar ($\Delta^{\pm\pm}$), involves non-trivial mixing, as can be seen in Eqs. (4.7) to (4.9). The physical states can be recovered in the following manner,

$$\begin{pmatrix} h \\ \Delta^0 \end{pmatrix} = \begin{pmatrix} \cos\alpha & \sin\alpha \\ -\sin\alpha & \cos\alpha \end{pmatrix}\begin{pmatrix} \phi \\ \delta^0 \end{pmatrix}, \quad \begin{pmatrix} G^0 \\ A \end{pmatrix} = \begin{pmatrix} \cos\beta_0 & \sin\beta_0 \\ -\sin\beta_0 & \cos\beta_0 \end{pmatrix}\begin{pmatrix} \eta \\ \chi \end{pmatrix},$$
$$\begin{pmatrix} G^\pm \\ \Delta^\pm \end{pmatrix} = \begin{pmatrix} \cos\beta_\pm & \sin\beta_\pm \\ -\sin\beta_\pm & \cos\beta_\pm \end{pmatrix}\begin{pmatrix} \phi^\pm \\ \delta^\pm \end{pmatrix}, \tag{4.11}$$

with

$$\tan 2\alpha = \frac{v_\Phi\left[\sqrt{2}\mu_\Delta - v_\Delta(\lambda_{\Delta_3}+\lambda_{\Delta_4})\right]}{\left[v_\Phi^2\left(\dfrac{1}{2\sqrt{2}}\dfrac{\mu_\Delta}{v_\Delta} - \lambda_H\right) + v_\Delta^2(\lambda_{\Delta_1}+\lambda_{\Delta_2})\right]}, \tag{4.12}$$

$$\tan\beta_0 = 2v_\Delta/v_\Phi\,, \qquad \tan\beta_\pm = \sqrt{2}v_\Delta/v_\Phi\,. \tag{4.13}$$

In addition to the three Goldstone bosons (G^0 and $G^\pm$), this gives rise to additional singly-charged scalars $\Delta^\pm$, one CP-odd scalar A, and CP-even scalars Δ^0 and h. The lighter CP-even neutral scalar (h) is identified with the observed 125 GeV Higgs boson. Diagonalising $M^2_{\text{neutral,CP-even}}$, $M^2_{\text{neutral,CP-odd}}$ and M^2_{charged} determines the masses of the CP-even neutral scalars, CP-odd scalars and charged scalars respectively, while the masses of the Goldstone bosons are identically zero. The electroweak vev is defined as $v^2 \equiv v_\Phi^2 + 2v_\Delta^2 \approx (246\,\text{GeV})^2$, signalising a violation of custodial isospin: the ratio of the gauge boson masses is parameterised by the ρ-parameter, given by $\rho = M_W^2/(M_Z^2\cos^2\theta_W)$, and the current electroweak precision constraints on ρ, sets an upper limit on the triplet vev $v_\Delta < 4.8$ GeV [313,316] at 95% CL. Upon EWSB, the new physics contributions to the Yukawa interactions in the neutrino sector are given by,

$$\mathcal{L}^{\text{BSM}}_{\text{Yukawa}} \supset \frac{v_\Delta}{\sqrt{2}}\left[(Y_\Delta + Y_\Delta^T)_{ij}\,\bar{\nu}_i^c \nu_j\right] , \tag{4.14}$$

where i, and j are flavour indices. The neutrino mass-mixing matrix (M_ν) originating from the Lagrangian is diagonalised by the unitary Pontecorvo–Maki–Nakagawa–Sakata (PMNS) matrix [320,321],

$$M_\nu = U^*_{\text{PMNS}}\, M_\nu^{\text{diag}}\, U^\dagger_{\text{PMNS}} , \tag{4.15}$$

where $M_\nu^{\text{diag}} = \text{diag}(m_{\nu_1}, m_{\nu_2}, m_{\nu_3})$. The different m_{ν_i} represent the three physical neutrino masses. The PMNS matrix (U_{PMNS}) is given in terms of the neutrino oscillation parameters,

$$U_{\text{PMNS}} = \begin{pmatrix} c_{12}c_{13} & s_{12}c_{13} & s_{13}e^{-i\delta} \\ -s_{12}c_{23} - c_{12}s_{23}s_{13}e^{i\delta} & c_{12}c_{23} - s_{12}s_{23}s_{13}e^{i\delta} & s_{23}c_{13} \\ s_{12}s_{23} - c_{12}c_{23}s_{13}e^{i\delta} & -c_{12}s_{23} - s_{12}c_{23}s_{13}e^{i\delta} & c_{23}c_{13} \end{pmatrix} , \tag{4.16}$$

where $c_{ij} = \cos\theta_{ij}$ and $s_{ij} = \sin\theta_{ij}$, θ_{ij} representing the mixing angles between the neutrino flavours, and δ being the CP-phase. The two additional Majorana phases in U_{PMNS} are set to zero for simplicity since no experimental bounds are available. The Yukawa matrix, therefore, is given by

$$Y_\Delta = \frac{M_\nu}{\sqrt{2}v_\Delta} . \tag{4.17}$$

The nature of the Yukawa matrix is thus determined by neutrino oscillation parameters

Parameter	Best-fit
Δm^2_{21} $[10^{-5}$ eV$^2]$	$7.55^{+0.20}_{-0.16}$
Δm^2_{31} $[10^{-3}$ eV$^2]$	2.50 ± 0.03
$\sin\theta_{12}/0.1$	$3.20^{+0.20}_{-0.16}$
$\theta_{12}/^\circ$	$34.5^{+1.2}_{-1.0}$
$\sin\theta_{23}/0.1$	$5.47^{+0.20}_{-0.30}$
$\theta_{23}/^\circ$	$47.7^{+1.2}_{-1.7}$
$\sin\theta_{13}/0.1$	$2.160^{+0.083}_{-0.069}$
$\theta_{13}/^\circ$	$8.45^{+0.16}_{-0.14}$
δ/π	$1.21^{+0.21}_{-0.15}$
$\delta/^\circ$	218^{+38}_{-27}

Table 4.1.: Best-fit constraints from the global-fit of neutrino oscillation data by the NuFit collaboration [322] for normal ordering in neutrino masses, i.e., $m_{\nu_1} < m_{\nu_2} < m_{\nu_3}$.

(see Table 4.1 for the best-fit constraints for a normal ordering in neutrino masses), v_Δ and m_{ν_1}. Non-zero neutrino mass-splittings allow for non-zero flavour off-diagonal couplings, which can lead to interesting lepton flavour violating signatures [323–325].

4.1.1. Constraints

The addition of a complex $SU(2)_L$ triplet leads to a wide range of theoretical and phenomenological implications. The rich scalar spectra introduce distinctive collider signatures, precision constraints, and novel low-energy interactions and decay modes. These features offer multiple ways to probe and constrain the viable parameter space. Existing studies, such as Ref. [313], have analysed combined theoretical bounds from vacuum stability, perturbative unitarity, electroweak precision data, and Higgs observables and signal strengths, particularly in terms of the triplet mass splitting ($\Delta M = M_{\Delta^\pm} - M_{\Delta^{\pm\pm}}$) and the mass $M_{\Delta^{\pm\pm}}$. With the LHC Run-3 underway, its high-luminosity upgrade on the horizon, and future colliders under consideration [76, 77, 162, 326], this analysis revisits collider bounds using recent ATLAS and CMS results [306–309] as benchmarks, exploring the potential of improved electroweak precision tests and constraints from lepton flavour-violating processes.

Direct Collider Constraints

The parameter space of the Type-II Seesaw model can be constrained significantly using the wealth of collider analyses. The production of $\Delta^{\pm\pm}$ is the primary LHC

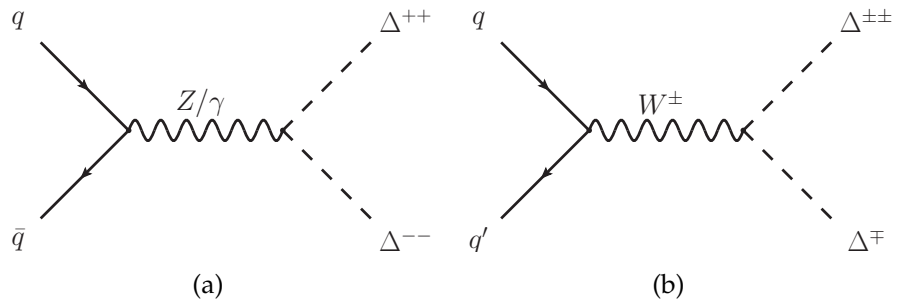

Figure 4.1.: Representative Feynman diagrams for the production of doubly charged scalars through (a) pair production via neutral-current DY and (b) associated production via charged-current DY processes.

search channel and the smoking gun signal for the model. The main production process is the pair production of doubly charged scalars through the neutral-current Drell-Yan (DY)-like process mediated by virtual Z/γ contribution. Another relevant mode of production is via the charged-current interactions mediated by W bosons (see Fig. 4.1). The primary decay channels for $\Delta^{\pm\pm}$ for these searches are mainly the decays into same-sign lepton pairs ($\Delta^{\pm\pm} \to l_\alpha^\pm l_\beta^\pm$ with $l = e, \mu$), and the decays into gauge bosons ($\Delta^{\pm\pm} \to W^\pm W^\pm$). In the limit of $v_\Delta \ll 0.1$ MeV$(\ll v)$, the dilepton channel dominates, and therefore, the four-lepton channel ($\Delta^{++}\Delta^{--} \to l^+l^+l^-l^-$) arising from the neutral-current DY process, will provide a clear BSM signature. This can be utilised to dramatically suppress expected backgrounds in the SM through sideband analyses of the same-sign mass spectra, which are experimentally under very good control (see [309, 327–330]). The branching ratios related to the exclusive final states of the $\Delta^{\pm\pm}$ decay depend on the neutrino mass-mixing matrix and thus serve as a probe of its structure.

The ATLAS and CMS collaborations have been able to exclude masses of $M_{\Delta^{\pm\pm}} <$ 850 GeV in their analyses, assuming a 100% decay into a light-lepton pair (ee, $\mu\mu$, or $e\mu$) [306, 307]. Model-specific constraints can be obtained by direct rescaling of the corresponding branching ratios (including tau contributions). For larger v_Δ, the triplet Yukawa couplings become small, and the diboson decay channel dominates (at the price of rising tension with the ρ parameter). The current upper limit set by ATLAS on $M_{\Delta^{\pm\pm}}$ is 220 GeV for $v_\Delta = 0.1$ GeV [308], which corresponds to a smaller collider sensitive region compared to the dilepton search channels. The collider analyses carried out by ATLAS and CMS, however, are not representative of the full parameter space of the model. They probe specific regions of the triplet vev (in particular, to the very low and very high values of v_Δ for the two decay channels), whilst assuming

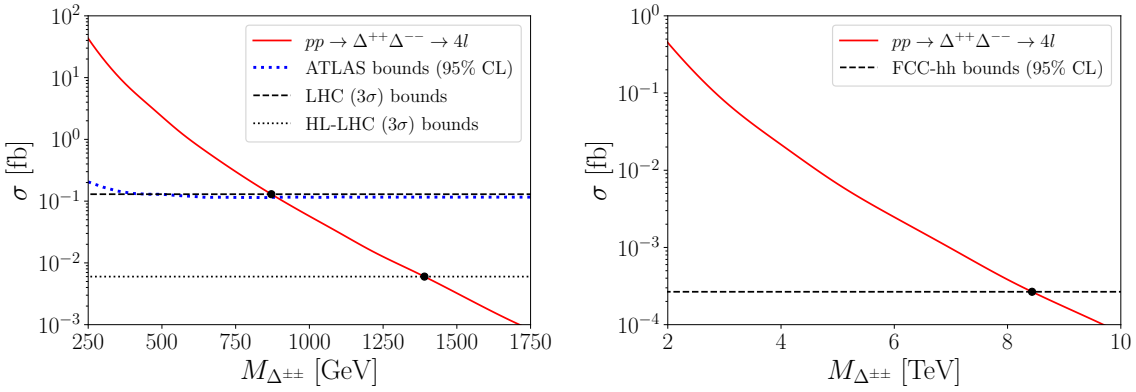

(a) (b)

Figure 4.2.: Cross-section for pair production of the doubly-charged scalars through neutral DY currents for (a) $\sqrt{s} = 14$ TeV and (b) $\sqrt{s} = 100$ TeV in the four-lepton final state (assuming a 100% branching ratio as Ref. [307,314]). The 3σ LHC (139 fb^{-1}) and HL-LHC (3 ab^{-1}) exclusion bounds are shown by the black dashed and dotted lines, respectively, on subfigure (a). The 95% CL on the search for $\Delta^{\pm\pm}$ with a 100% branching ratio into light leptons, cf. Ref. [307] is represented by the blue dotted line, showing a good agreement. The 95% confidence bound for FCC-*hh* (30 ab^{-1}) is shown by the black dashed line on subfigure (b). These plots show that the LHC is sensitive to doubly charged scalars up to masses $\sim$870 GeV currently, and up to masses $\sim$1390 GeV in its high-luminosity phase. The FCC-*hh* will be sensitive to similar final states up to a mass scale of $\sim$8.5 TeV.

mass degeneracy of the scalar triplet masses. These assumptions render the decays of $\Delta^{\pm\pm}$ into same-sign leptons and dibosons phenomenologically dominant. The analyses conducted by the LHC experiments can be extended to obtain the expected direct future bounds from the HL-LHC phase, as well as a future hadron-hadron machine.

To this end, the model is implemented on `FeynRules` [64] with normal ordering in the neutrino mass hierarchy (i.e., $m_{\nu_1} < m_{\nu_2} < m_{\nu_3}$), which is then interfaced with `Madgraph5_aMC@NLO` [160] as a `Ufo` [273] model. Events are generated at centre-of-mass energies of $\sqrt{s} = 14,\ 100$ TeV for the neutral current Drell-Yan-like pair production process: $pp \to \Delta^{++}\Delta^{--} \to l^+l^+l^-l^-$ (see Fig. 4.1), assuming a 100% branching ratio. The analysis strategy is centred around the search for doubly charged scalars [305,307] with parton-level cuts to provide qualitative sensitivities at present and future colliders. Specific cuts are imposed, requiring all leptons ($l = e/\mu$) to be within the central part of the detector ($|\eta(l)| < 2.5$) and with a transverse momentum $p_T > 30$ GeV. Only leptons with no jet activity within the cone radius are considered ($\Delta R(j,l) < 0.4$), and

the final states containing exactly one positively-charged and one negatively-charged lepton pair are selected; otherwise, the event is vetoed. An invariant mass cut is always applied for each lepton pair $M_{l^\pm l^\pm} > 200$ GeV.

Given that the same-signed leptons should result from $\Delta^{\pm\pm}$ decays, the consistency of the two masses is checked by calculating,

$$\overline{M} = \frac{M_{l^+l^+} + M_{l^-l^-}}{2}, \tag{4.18}$$

$$\Delta M = |M_{l^+l^+} - M_{l^-l^-}|. \tag{4.19}$$

The two masses are consistent if $\Delta M/\overline{M} < 0.25$, imposing a resonant signal character. Additionally, an event is vetoed if there exists an opposite-signed same-flavour lepton pair with an invariant mass in the range $M_{l^+l^-} \in [81.2, 101.2]$ GeV to suppress background resulting from Z decays.

The total number of signal events is then determined as $N_S = \sigma \times L_{\text{int.}} \times A$, where A represents acceptance. Assuming a good background subtraction which is possible through sideband analyses [309, 327–329, 331], the statistical significance at integrated luminosities $L_{\text{int.}} = 139$ fb^{-1} and 3 ab^{-1} at $\sqrt{s} = 14$ TeV is calculated as $\sqrt{N_S}$, obtaining 3σ mass sensitivities at the LHC and the high-luminosity limit, as depicted in Fig. 4.2(a). The acceptances are calibrated to reproduce the bounds from the ATLAS search for doubly charged scalars reported in [307]. The expected 95% confidence limit (CL) shown by the blue dotted line in Fig. 4.2(a) [307] demonstrates a very good agreement as the reference point for the extrapolation. These mass limits also align with those reported in [307, 319]. The same methodology can be applied to a future hadron collider with $\sqrt{s} = 100$ TeV. The exclusion limit at an integrated luminosity of 30 ab^{-1} shown in Fig. 4.2(b) elucidates the fact that, in searches at low backgrounds, the sensitivity gain when moving to 100 TeV entirely stems from the much larger relevant partonic energy range that can be obtained. The scaling of sensitivities, therefore, directly reflects the available centre-of-mass energy.

Electroweak Precision Constraints

The model parameter space can be constrained indirectly (e.g. at a future lepton machine) from electroweak precision observables, namely the S, T, and U oblique parameters. Following [332], the oblique parameters for the Type-II Seesaw Mechanism

can be written as,

$$S = -\frac{1}{3\pi}\ln\frac{M^2_{\Delta^{\pm\pm}}}{M^2_{\Delta^0}} - \frac{2}{\pi}\left[(1-2s^2_W)^2\xi\left(\frac{M^2_{\Delta^{\pm\pm}}}{M^2_Z},\frac{M^2_{\Delta^{\pm\pm}}}{M^2_Z}\right) + s^4_W\xi\left(\frac{M^2_{\Delta^{\pm}}}{M^2_Z},\frac{M^2_{\Delta^{\pm}}}{M^2_Z}\right) + \xi\left(\frac{M^2_{\Delta^0}}{M^2_Z},\frac{M^2_{\Delta^0}}{M^2_Z}\right)\right], \tag{4.20}$$

$$T = \frac{1}{8\pi c^2_W s^2_W}\left[\eta\left(\frac{M^2_{\Delta^{\pm\pm}}}{M^2_Z},\frac{M^2_{\Delta^{\pm}}}{M^2_Z}\right) + \eta\left(\frac{M^2_{\Delta^{\pm\pm}}}{M^2_Z},\frac{M^2_{\Delta^{\pm}}}{M^2_Z}\right)\right], \tag{4.21}$$

$$U = \frac{1}{6\pi}\ln\frac{M^4_{\Delta^{\pm}}}{M^2_{\Delta^{\pm\pm}}M^2_{\Delta^0}} + \frac{2}{\pi}\left[(1-2s^2_W)^2\xi\left(\frac{M^2_{\Delta^{\pm\pm}}}{M^2_Z},\frac{M^2_{\Delta^{\pm\pm}}}{M^2_Z}\right) + s^4_W\xi\left(\frac{M^2_{\Delta^{\pm}}}{M^2_Z},\frac{M^2_{\Delta^{\pm}}}{M^2_Z}\right) + \xi\left(\frac{M^2_{\Delta^0}}{M^2_Z},\frac{M^2_{\Delta^0}}{M^2_Z}\right)\right] - \frac{2}{\pi}\left[\xi\left(\frac{M^2_{\Delta^{\pm\pm}}}{M^2_W},\frac{M^2_{\Delta^{\pm}}}{M^2_W}\right) + \xi\left(\frac{M^2_{\Delta^{\pm\pm}}}{M^2_W},\frac{M^2_{\Delta^{\pm}}}{M^2_W}\right)\right], \tag{4.22}$$

where the functions ξ and η are defined as,

$$\begin{aligned}
\xi(x,y) &= \frac{4}{9} - \frac{5}{12}(x+y) + \frac{1}{6}(x-y)^2 \\
&\quad + \frac{1}{4}\left[x^2 - y^2 - \frac{1}{3}(x-y)^3 - \frac{x^2+y^2}{x-y}\right]\ln\frac{x}{y} - \frac{1}{12}d(x,y)f(x,y)\,, \\
\eta(x,y) &= x + y - \frac{2xy}{x-y}\ln\frac{x}{y}\,, \\
d(x,y) &= -1 + 2(x+y) - (x-y)^2\,, \\
f(x,y) &= \begin{cases} -2\sqrt{d(x,y)}\left[\arctan\frac{x-y+1}{\sqrt{d(x,y)}} - \arctan\frac{x-y-1}{\sqrt{d(x,y)}}\right], & d(x,y) > 0, \\ \sqrt{-d(x,y)}\ln\frac{x+y-1+\sqrt{-d(x,y)}}{x+y-1-\sqrt{-d(x,y)}}, & d(x,y) \leq 0. \end{cases}
\end{aligned} \tag{4.23}$$

Assuming a degeneracy in the physical triplet masses ($M_{\Delta^0} \simeq M_{\Delta^\pm} \simeq M_{\Delta^{\pm\pm}}$), constraints reported by the GFITTER collaboration [333] impose $M_{\Delta^{\pm\pm}} \gtrsim 35$ GeV at 95% CL. The constraints on the said oblique parameters are expected to improve dramatically with the high luminosity Z-pole programs of circular lepton colliders like the FCC-*ee* and CEPC. To get an estimate on the constraints in future from electroweak precision observables [334,335], motivated from TLEP [336] and GigaZ [337], the uncertainties in S, T and U obtained from GFITTER are reduced by an order of magnitude, and the limit relaxes to $M_{\Delta^{\pm\pm}} \gtrsim 105$ GeV at 95% CL. This implies that even dramati-

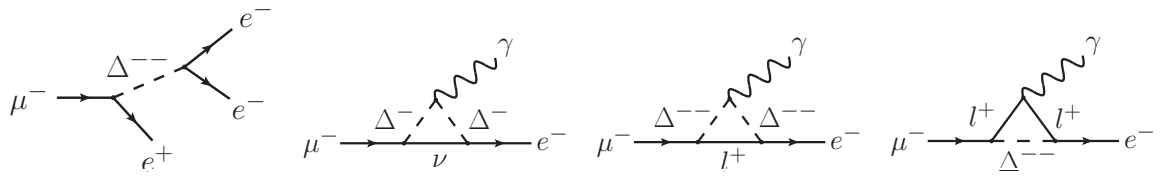

Figure 4.3.: Representative Feynman diagrams for the lepton flavour violating decays $\mu \to 3e$ and $\mu \to e\gamma$.

cally improved electroweak precision measurements of oblique parameters at future lepton colliders will not lead to significant sensitivity enhancements. Non-oblique vertex corrections, on the other hand, might provide a complementary avenue to probe non-trivial flavour structures in case such high precision related to the electroweak input parameter set of the SM is achieved.

Constraints from Lepton Flavour Violating Decays

The Yukawa interactions presented in Eq. (4.4), naturally lead to flavour-changing lepton decays such as $l_i^- \to l_j^+ l_k^- l_l^+$ and $l_i^- \to l_j^- \gamma$ [323, 338–340]. Two such lepton flavour-violating (LFV) decays that have been widely explored for the Type-II Seesaw Mechanism are highlighted in this section, $\mu \to 3e$ and $\mu \to e\gamma$* (see Fig. 4.3). The former arises at tree-level, mediated by the doubly charged scalar ($\Delta^{\pm\pm}$), and its branching ratio is given by,

$$\mathrm{BR}(\mu \to 3e) = \frac{|(Y_\Delta)_{ee}(Y_\Delta)^*_{\mu e}|^2}{4G_F^2 M^4_{\Delta^{\pm\pm}}}, \tag{4.24}$$

where $G_F \simeq 1.166 \times 10^{-5}$ GeV^{-2} is the Fermi constant. Setting $v_\Delta = 1$ eV, and $m_{\nu_1} = 0.05$ eV, using the global fit of neutrino oscillations data (Table 4.1), the latest $\mathrm{BR}(\mu \to 3e) < 10^{-12}$ constraint [343] sets a lower limit of $M_{\Delta^{\pm\pm}} \gtrsim 1650$ GeV, which is well beyond the reach of the current LHC sensitivity regime, as obtained in Fig. 4.2. $\mu \to e\gamma$ on the other hand occurs through one-loop diagrams as illustrated in Fig. 4.3, mediated by $\Delta^\pm$ or $\Delta^{\pm\pm}$. In the process mediated by $\Delta^\pm$, the photon is emitted exclusively from the $\Delta^\pm$ boson at one-loop, whereas for the $\Delta^{\pm\pm}$ contribution, the photon can be emitted from either $\Delta^{\pm\pm}$ or the charged fermion propagator in the

*The results in this chapter rely on the earlier measurement of the $\mu \to e\gamma$ branching ratio [341]. A more recent update [342] has lowered the value by roughly a factor of two; this revision, however, does not alter the phenomenological conclusions presented here.

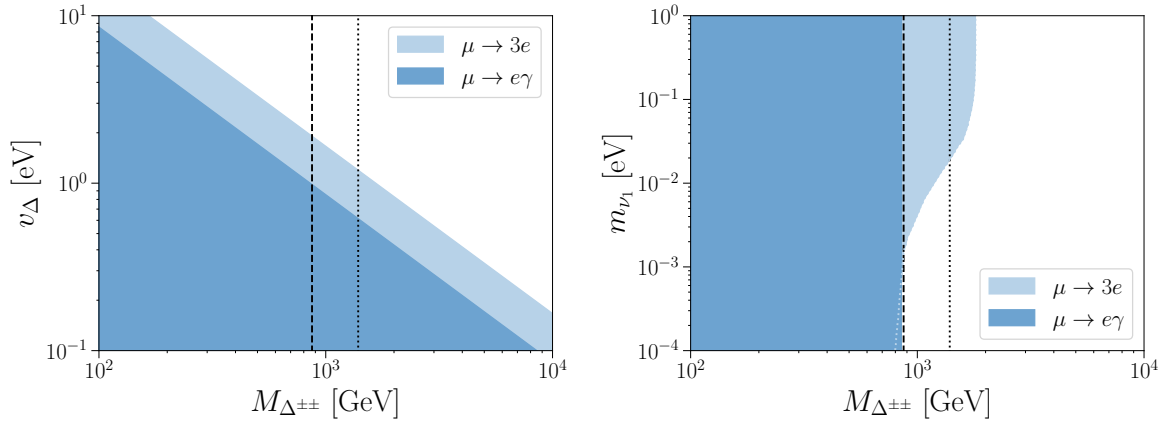

Figure 4.4.: Constraints from $\mu \to 3e$ and $\mu \to e\gamma$ for (a) $m_{\nu_1} = 0.05$ eV, and (b) $v_\Delta = 1$ eV. The black dashed and dotted lines on both plots represent the 3σ LHC and HL-LHC exclusion limits, respectively.

loop. The contributions from both scalars interfere coherently as they couple to leptons with the same chirality, resulting in a branching fraction [313],

$$\mathrm{BR}(\mu \to e\gamma) = \frac{\alpha_{\mathrm{EM}}}{192\pi G_F^2} |Y_\Delta^\dagger Y_\Delta|^2_{\mu e} \left(\frac{1}{M^2_{\Delta^\pm}} + \frac{8}{M^2_{\Delta^{\pm\pm}}} \right)^2 , \tag{4.25}$$

with the electromagnetic fine-structure constant $\alpha_{\mathrm{EM}} \simeq 1/137$.

Setting $v_\Delta = 1$ eV, $M_{\Delta^\pm} \sim M_{\Delta^{\pm\pm}}$, and $m_{\nu_1} = 0.05$ eV the lower bounds on the triplet mass is $M_{\Delta^{\pm\pm}} \gtrsim 850$ GeV from the current $\mathrm{BR}(\mu \to e\gamma) < 3.1 \times 10^{-13}$ constraint [341, 344]. Assuming degeneracy in the masses of the charged triplet scalars, and using the neutrino oscillation data from NuFIT (Table 4.1), both the branching ratios contain three free parameters, v_Δ, m_{ν_1} and $M_{\Delta^{\pm\pm}}$. The current limits on both these branching ratios can be used to obtain constraints on the resulting parameter space as illustrated in Fig. 4.4, where the shaded regions show the parts of the parameter space currently excluded by these constraints. The plots indicate that the regions not already excluded by the lepton flavour violating constraints lie mostly beyond the reach of current LHC sensitivity, as well as the HL-LHC, especially for the $\mu \to 3e$ process. More precise measurements for these decays are going to push the mass limit even further beyond the reach of colliders. Any potential discovery at the LHC that phenomenologically fits the experimentally clean $\Delta^{\pm\pm}$ expectation could therefore

point towards a richer phenomenology of the TeV scale than predicted by the vanilla Type-II Seesaw model.

4.2. Implications of EFT deformations

To analyse the implications of a reduced $\Delta^{\pm\pm}$ mass scale within the LHC's sensitivity reach, the parameter space of the Type-II Seesaw Model is extended by gauge invariant dimension-6 operators that incorporate at least one Δ alongside the usual SMEFT interactions [119], suppressed by a UV cutoff $\Lambda \gg M_\Delta$. This provides a new perspective for accommodating or predicting TeV-scale resonances in the light of highly constraining LFV experiments. This construction, also referred to as a "BSM-EFT" scenario, is justified by the possibility that the lightest non-SM particle might exist not very far from the electroweak scale, making it accessible to upcoming collider experiments, including improved analysis techniques for the HL-LHC phase [345]. The potential discovery of charged scalars in future colliders has been extensively studied in the literature within various BSM models, e.g., complex singlets [346–350], the two-Higgs doublet model (2HDM) [351–355], or complex-triplet extensions [305, 356–359]. This further motivates the idea of extending these scenarios with EFT interactions to obtain a qualitative understanding of energy scales beyond the reach of current colliders. In parallel, these interactions highlight the correlation constraints that are theoretically imposed by the most direct implementation of a certain model [†]. The relevant gauge-invariant operators have been adopted from Refs. [119, 361].

Given that the constraints from $\mu \to 3e$ set the mass scale well beyond the reach of the LHC sensitive regime as discussed in Sec. 4.1.1, it is imperative to focus on the impact of EFT deformations on this particular LFV process. The gauge-invariant dimension-6 operators for the SM extended by a complex triplet scalar, relevant for $\mu \to 3e$ have been tabulated in Table 4.2. Their phenomenological relevance can be traced, again by implementing the additional operators on `FeynRules` [64], and using `FeynArts` [147], and `FormCalc` [148] for the analytical computation of the $\mu \to 3e$ branching ratio including the EFT extensions. The dimension-6 modifications to

[†] For instance, EFT deformations can significantly modify the phase transition history of the early universe physics, thereby accessing parameter regions that are seemingly excluded by LHC measurements of the 2HDM [353] with implications for the LHC exotics program [354]. Similar observations have been made to reconcile the anomalous muon $g-2$ with leading order constraints of Higgs sector extensions [305, 360].

$\mathcal{O}^{(1)}_{L\Phi\Delta,ij}$	$(\overline{L}^c_{L_i}\Delta L_{L_j})(\Phi^\dagger\Phi)$	$\mathcal{O}^{(2)}_{L\Phi\Delta,ij}$	$\overline{L}^c_{L_i,\alpha}\Delta\Phi^\alpha\Phi^\dagger_\beta L^\beta_{L_j}$
$\mathcal{O}^{(1)}_{L\Delta,ij}$	$(\overline{L}^c_{L_i}\Delta L_{L_j})\mathrm{Tr}[(\Delta^\dagger\Delta)]$	$\mathcal{O}^{(2)}_{L\Delta,ij}$	$\overline{L}^c_{L_i}\Delta\Delta^\dagger\Delta L_{L_j}$
$\mathcal{O}^{ijkm}_{ll}$	$(\overline{L}_{L_i}\gamma_\mu L_{L_j})(\overline{L}_{L_k}\gamma^\mu L_{L_m})$	$\mathcal{O}^{ijkm}_{ee}$	$(\bar{e}_{R_i}\gamma_\mu e_{R_j})(\bar{e}_{R_k}\gamma^\mu e_{R_m})$
$\mathcal{O}^{ijkm}_{le}$	$(\overline{L}_{L_i}\gamma_\mu L_{L_j})(\bar{e}_{R_k}\gamma^\mu e_{R_m})$	$\mathcal{O}^{ij}_{e\phi}$	$(\Phi^\dagger\Phi)(\overline{L}_{L_i}e_{R_j}\Phi)$

Table 4.2.: Relevant dimension-6 operators for SM extended by a complex triplet scalar (Δ) [119, 361, 362], contributing to $\mu \to 3e$, where i, j, k, m are flavour indices, and α, β are SU(2) indices. Φ represents the SM Higgs doublet.

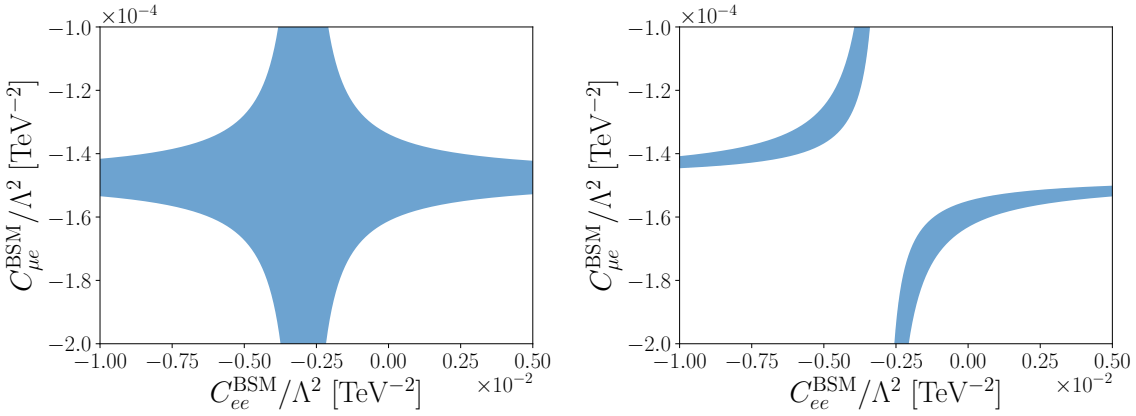

Figure 4.5.: Allowed regions from $\mu \to 3e$ on Wilson coefficients ($C^{\mathrm{BSM}}_{\mu e}$, and C^{BSM}_{ee}) for $M_{\Delta^{\pm\pm}} = 500$ GeV (a) without contributions from the SMEFT 4-lepton operators, and (b) setting $C^{1112}_{ll}/\Lambda^2 = C^{1112}_{le}/\Lambda^2 = C^{1211}_{le}/\Lambda^2 = C^{1112}_{ee}/\Lambda^2 = 2.5 \times 10^{-6}$ TeV^{-2}.

the Yukawa couplings have a significant impact on the mass constraints arising from $\mu \to 3e$. These corrections originate from the effective operators $\mathcal{O}^{(1)}_{L\Phi\Delta,ij}$, $\mathcal{O}^{(2)}_{L\Phi\Delta,ij}$, $\mathcal{O}^{(1)}_{L\Delta,ij}$, and $\mathcal{O}^{(2)}_{L\Delta,ij}$ after EWSB. Among these, the contributions from $\mathcal{O}^{(1)}_{L\Phi\Delta,ij}$ are absorbed into the Yukawa matrix Y_Δ, playing a role in the generation of neutrino masses. The contributions from $\mathcal{O}^{(1)}_{L\Delta,ij}$ and $\mathcal{O}^{(2)}_{L\Delta,ij}$ are suppressed since $v^2_\Delta \ll v^2$. In the parameter space of interest, the dominant corrections to the Yukawas arise from the operator $\mathcal{O}^{(2)}_{L\Phi\Delta,ij}$. The modified Yukawa couplings can be expressed as:

$$Y^{\mathrm{mod.}}_{ij} = (Y_\Delta)_{ij} - \frac{C^{\mathrm{BSM}}_{ij} v^2}{2\Lambda^2}, \tag{4.26}$$

where C_{ij}^{BSM} denotes the Wilson coefficient associated with the effective operator $\mathcal{O}^{(2)}_{L\Phi\Delta,ij}$. Plugging in the modified Yukawa couplings into the BR($\mu \to 3e$) in Eq. (4.24), setting $v_\Delta = 1$ eV, $m_{\nu_1} = 0.05$ eV, and $M_{\Delta^{\pm\pm}} = 500$ GeV such that exotics searches imply a discovery at the LHC, the Wilson coefficients can be constrained to the region depicted in Fig. 4.5(a). Since the diagonal Yukawas are $\sim$2 orders of magnitude larger than their off-diagonal counterparts, Fig. 4.5(a) clearly illustrates that larger cancellations ($\sim$2 orders of magnitude) are required in the ee direction compared to μe. $\mu \to 3e$ also gets direct contributions from SMEFT 4-lepton operators ($\mathcal{O}_{ll}^{ijkm}$, $\mathcal{O}_{ee}^{ijkm}$, and $\mathcal{O}_{le}^{ijkm}$). There can be additional contributions from $\mathcal{O}_{e\phi}^{ij}$, which are, however, suppressed and therefore not included in this analysis. Non-zero Wilson coefficients for the relevant SMEFT operators (in particular $\mathcal{O}_{ll}^{1112}$, $\mathcal{O}_{ee}^{1112}$, $\mathcal{O}_{le}^{1112}$, $\mathcal{O}_{le}^{1211}$) change the allowed parameter space for the Wilson coefficients of $\mathcal{O}^{(2)}_{L\Phi\Delta,ij}$, which can be seen from Fig. 4.5(b).

To check how far the mass scales can be brought down for $v_\Delta = 1$ eV, $m_{\nu_1} = 0.05$ eV, the relevant Wilson Coefficients are set to equal values, i.e., $C_{ee}^{\text{BSM}} = C_{\mu e}^{\text{BSM}}$. This condition was assumed to obtain the tightest constraints on the BSM-EFT Wilson coefficients, assuming them to be of the same order of magnitude. The $\mu \to 3e$ constraints manifest into the plots shown in Fig. 4.6, which illustrate that mass scales well within the region sensitive to the LHC are achievable whilst satisfying constraints from the LFV decay. To present a complete argument on this front, a similar analysis is performed for $\mu \to e\gamma$. The modified Yukawas outlined in Eq. (4.26) directly contribute to the $\mu \to e\gamma$ branching ratio given in Eq. (4.25). Additionally, the SMEFT operators that contribute to $\mu \to e\gamma$ at tree-level [363] are listed in Table 4.3. The results in this front are illustrated on Fig. 4.6, elucidating the fact that mass scales within (HL-)LHC sensitivity can still be probed. As anticipated, cancellations from the SMEFT operators fine-tune and tighten the constraints on the BSM-EFT Wilson coefficients.

The combined exclusion contours from $\mu \to 3e$ on the Wilson coefficients corresponding to the SMEFT 4-lepton operators and the relevant BSM-EFT operators are presented in Fig. 4.7, for three chosen benchmark mass scales, $M_{\Delta^{\pm\pm}} = 870$ GeV

$\mathcal{O}_{eW}$	$(\bar{L}_{L_i}\sigma^{\mu\nu}e_{R_j})\tau^\alpha\Phi W^\alpha_{\mu\nu}$	$\mathcal{O}_{eB}$	$(\bar{L}_{L_i}\sigma^{\mu\nu}e_{R_j})\Phi B_{\mu\nu}$

Table 4.3.: Relevant SMEFT dimension-6 operators [119], contributing to $\mu \to e\gamma$, where i, j are flavour indices, μ, ν are Lorentz indices, and α, β are SU(2) indices. Φ represents the SM Higgs doublet.

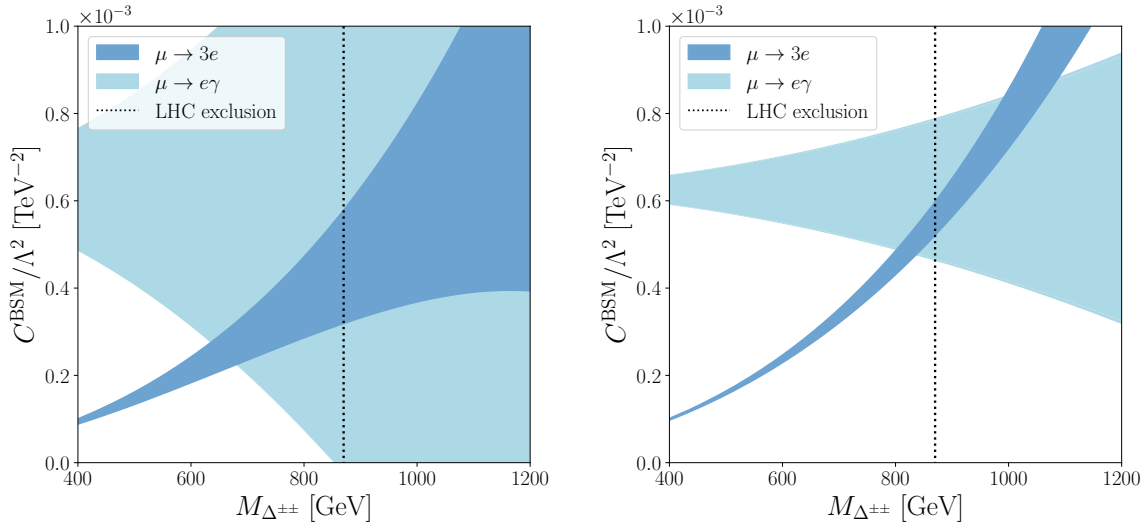

Figure 4.6.: The allowed parameter space of the BSM-EFT Wilson coefficients and $M_{\Delta^{\pm\pm}}$ for (a) $C_{ll}^{1112} = C_{le}^{1112} = C_{le}^{1211} = C_{ee}^{1112} = C_{4f}^{\text{SMEFT}} = 0$, $C_{eB} = C_{eW} = C_{\mu\to e\gamma}^{\text{SMEFT}} = 0$ and (b) $C_{4f}^{\text{SMEFT}}/\Lambda^2 = 2.5\times10^{-6}$ TeV^{-2}, and $C_{\mu\to e\gamma}^{\text{SMEFT}}/\Lambda^2 = 0.5\times10^{-6}$ TeV^{-2}. Here, $C_{ee}^{\text{BSM}} = C_{\mu e}^{\text{BSM}} = C^{\text{BSM}}$. The black dotted lines on both plots represent the LHC exclusion limits.

(representing the current LHC-exclusion limit), 1 TeV and 1.4 TeV (representing the projected HL-LHC exclusion limit). This plot further elucidates the decrease in the allowed parameter space as one tries to bring the mass scale down to the LHC observable region. The constraints on the SMEFT-parameterised Wilson coefficients that improve the tension between the $\Delta^{\pm\pm}$ states and low energy measurements are relatively weak, and further discrimination of the two directions would predominantly be driven by a direct resolution of the cutoff scale, e.g. at a future hadron machine with a higher centre-of-mass energy. It is worth noting that experiments like MUONE [364,365] are unlikely to provide additional constraints as they predominantly fingerprint the low q^2 behaviour of the scattering process, although the experiment should be sensitive to the signature of $\mu e \to ee$.

TeV-modified Seesaw at Colliders

The SMEFT four-lepton operators relevant to $\mu \to 3e$ can be probed directly at electron-positron machines through the process $e^+e^- \to e^\pm\mu^\pm$. To check the constraints at

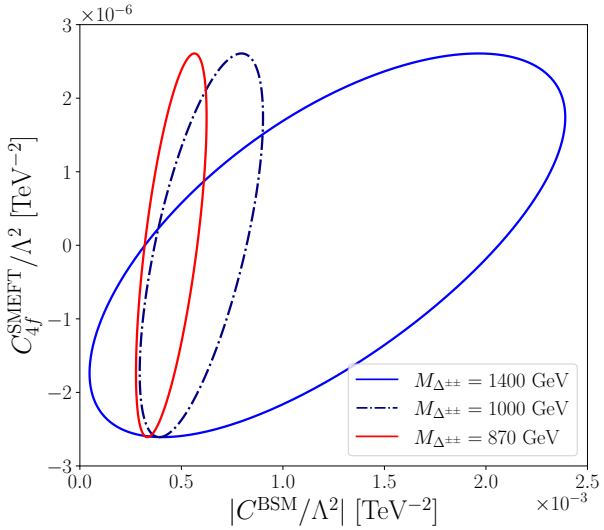

Figure 4.7.: Exclusion contours on SMEFT and BSM-EFT Wilson coefficients for $M_{\Delta^{\pm\pm}} = 870,\ 1000,\ 1400$ GeV from BR($\mu \to 3e$) limits, where $C_{ee}^{\mathrm{BSM}} = C_{\mu e}^{\mathrm{BSM}} = C^{\mathrm{BSM}}$, and $C_{ll}^{1112} = C_{le}^{1112} = C_{le}^{1211} = C_{ee}^{1112} = C_{4f}^{\mathrm{SMEFT}}$.

future colliders, events are generated for this process on `Madgraph5_aMC@NLO` [160] with the `Ufo` [273] model updated with the relevant dimension-6 operators, for the FCC-*ee* running at the Z boson pole at 192 ab^{-1}, callibrating the acceptances to reproduce the bounds on 4-lepton operators presented in Refs. [128, 366]. The 2σ-bounds on these operators is $|C_{4f}^{\mathrm{SMEFT}}| \lesssim 10^{-4}$ TeV^{-2}. At a future high centre-of-mass energy e^+e^--collider with $\sqrt{s} = 3$ TeV, with an integrated luminosity of 5 ab^{-1} this improves to $|C_{4f}^{\mathrm{SMEFT}}| \lesssim 10^{-5}$ TeV^{-2} [366], therefore implying that $\mu \to 3e$ will set more stringent bounds on these Wilson coefficients than future *ee*-Colliders.

In the context of hadron colliders, these effective operators do not play a role in the production processes of triplet scalars. The dimension-6 BSM-EFT operators that modify the Yukawa couplings do influence the branching ratios; however, given that dominant branching ratios have been considered for the doubly charged scalar decaying into leptons, this does not imply a sensitivity enhancement compared to the

$\mathcal{O}_{\Phi\Delta D}^{(1)}$	$\left[\Phi^\dagger (D_\mu \Delta)\right]\left[(D^\mu \Delta)^\dagger \Phi\right]$	$\mathcal{O}_{\Phi\Delta D}^{(2)}$	$\left[\Delta^\dagger (D_\mu \Phi)\right]\left[(D^\mu \Phi)^\dagger \Delta\right]$
$\mathcal{O}_{\Phi\Delta D}^{(3)}$	$\mathrm{Tr}\left[(\Delta^\dagger \Delta)\right]\left[(D_\mu \Phi)^\dagger (D^\mu \Phi)\right]$	$\mathcal{O}_{\Phi\Delta D}^{(4)}$	$(\Phi^\dagger \Phi)\ \mathrm{Tr}\left[(D_\mu \Delta)^\dagger (D^\mu \Delta)\right]$

Table 4.4.: Dimension-6 operators for SM extended by a complex triplet scalar (Δ) [119,361,362], relevant for Drell-Yan production of $\Delta^{\pm\pm}$.

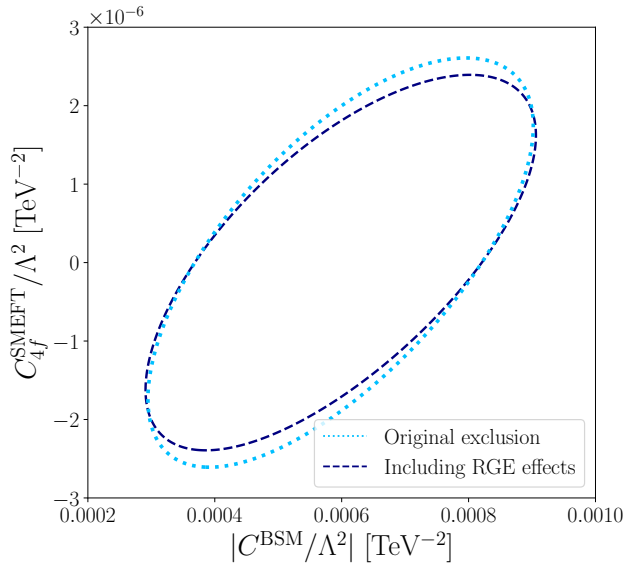

Figure 4.8.: Effect of RGE running on the allowed parameter space of SMEFT and BSM-EFT Wilson coefficients, corresponding to $\mu \to 3e$ constraints, for $M_{\Delta^{\pm\pm}} = 1000$ GeV. Here $C_{ee}^{\mathrm{BSM}} = C_{\mu e}^{\mathrm{BSM}} = C^{\mathrm{BSM}}$, and $C_{ll}^{1112} = C_{le}^{1112} = C_{le}^{1211} = C_{ee}^{1112} = C_{4f}^{\mathrm{SMEFT}}$.

prior analysis. What is more relevant for the production of the doubly-charged scalars is the relevance of the potential EFT deformations to the $Z/\gamma\ \Delta^{++}\Delta^{--}$ vertex. These deformations would induce modifications of the pair production cross-sections.

Table 4.4 tabulates the operators leading to modifications of the $(Z/\gamma)\ \Delta^{++}\Delta^{--}$ interactions. It is worth noting that the contributions from these operators would lead to an enhanced (when including squared dimension-6 contributions) cross-section for the DY production of $\Delta^{\pm\pm}$, which in principle should provide updated and improved limits on $M_{\Delta^{\pm\pm}}$ from collider analyses as functions of these Wilson coefficients. The analyses performed in the context of the renormalisable Type-II scenario therefore provide conservative estimates of the sensitivity reach, predominantly making the mass scales of the Type-II exotic states accessible to collider experiments. More precise measurements of the neutrino oscillation parameters from various experiments, along with updated measurements of the ρ-parameter providing a more accurate estimate of v_Δ, which essentially constrains the Yukawa matrix, would lead to a more precise determination of the hadron-collider sensitive region for the model. Similarly, analyses of the $\Delta^{\pm}$ states can add additional sensitivity, however, with reduced experimental sensitivity due to a significant amount of missing energy and a smaller electroweak coupling.

Impact of RGE running

As the μ experiments probe very different energy scales of the theory compared to the collider searches, RGE effects can *a priori* be important. Below the mass scales of the Higgs sector exotics (which are assumed to be degenerate), the running of the SM couplings is unchanged. To estimate the relevance of these effects, e.g., at the scale of resonance ($M_\Delta \gg m_\mu$) the modified Δ-contributions can be mapped on the SMEFT four-fermion interaction that accurately describes $\mu \to 3e$ at the scale of the muon $m_\mu \ll M_\Delta$. The Wilson coefficients are then parameterised by,

$$C^{1112}_{ll,\,\text{BSM}}(M^2_{\Delta^{\pm\pm}}) = C^{1112}_{ll}(M^2_{\Delta^{\pm\pm}}) - Y^{\text{mod.}}_{ee}(Y^{\text{mod.}}_{\mu e})^*\,, \tag{4.27}$$

where $Y^{\text{mod.}}_{ij}$ is written in terms of BSM Yukawa couplings $(Y_\Delta)_{ij}$ and the BSM-EFT Wilson coefficients as shown in Eq. (4.26). The RGE flow of the SMEFT Wilson coefficients including the BSM effects is computed using `DSixTools` [367, 368] and `wilson` [369], between $\Lambda_\mu = m_\mu = 105$ MeV and the scale of the resonance $\Lambda_{\text{UV}} = M_\Delta$ to obtain a qualitative estimate of the impact of the renormalisation group flow.

The RG evolution of the Wilson coefficients of the four-fermion operators from Λ_μ up to the scale of resonance $\Lambda_{\text{UV}} = 1$ TeV is given by

$$C^{1112}_{ll}(\Lambda_{\text{UV}}) = 1.121 \times C^{1112}_{ll}(\Lambda_\mu) + 0.003 \times C^{1211}_{le}(\Lambda_\mu)\,, \tag{4.28}$$
$$C^{1112}_{ee}(\Lambda_{\text{UV}}) = 1.113 \times C^{1112}_{ee}(\Lambda_\mu) + 0.005 \times C^{1112}_{le}(\Lambda_\mu)\,, \tag{4.29}$$
$$C^{1112}_{le}(\Lambda_{\text{UV}}) = 0.963 \times C^{1112}_{le}(\Lambda_\mu) + 0.021 \times C^{1112}_{ee}(\Lambda_\mu)\,, \tag{4.30}$$
$$C^{1211}_{le}(\Lambda_{\text{UV}}) = 0.968 \times C^{1211}_{le}(\Lambda_\mu) + 0.003 \times C^{1112}_{ll}(\Lambda_\mu)\,. \tag{4.31}$$

For this specific resonance scale ($M_\Delta = 1$ TeV), with $v_\Delta = 1$ eV and $m_{\nu_1} = 0.05$ eV, the expressions in Eqs. (4.28) and (4.31) for the SMEFT Wilson coefficients are plugged into the $\mu \to 3e$ branching ratio. The resulting exclusions on the parameter space of the Wilson coefficients of the relevant SMEFT and BSM-EFT operators are depicted in Fig. 4.8. Thus, RGE flow does not qualitatively change any findings.

4.3. Conclusions

Neutrino masses and oscillations provide direct evidence of physics beyond the SM, with potential implications for TeV-scale phenomena currently under investigation

at the LHC. Simultaneously, precise measurements of lepton observables impose stringent constraints on the parameter space of relevant models at low energies. The precision of these measurements can suggest that new physics resides at energy scales beyond the reach of the LHC or even future colliders. Under what circumstances can colliders and potential discoveries at such facilities continue to play a pivotal role in identifying the underlying dynamics?

The Type-II Seesaw Mechanism and its effective field theory generalisation have been examined in this chapter, with particular emphasis on the complementarity of low-energy coupling measurements and TeV-scale exotic states. Non-minimal extensions of this scenario can be systematically described using effective field theory techniques. The rare decay processes, when attributed to the exchange of the extended scalar sector of the Type-II scenario, can push the particle spectrum to mass scales where experimental sensitivity is challenging. However, it has been demonstrated that TeV-scale modifications of the vanilla Type-II scenario can lower these mass scales to collider-accessible ranges, allowing future discoveries to be contextualised within low-energy neutrino phenomenology. These effects are correlated with a richer spectrum of interactions above the dynamical degrees of freedom of the Type-II framework, which can be further investigated and constrained at the LHC and forthcoming experimental facilities.

As blind directions in the effective field theory-extended parameter space are exploited, it must be acknowledged that the phenomenology discussed in this chapter is associated with fine-tuning, which has not been dynamically addressed through explicit ultraviolet completions. A potential approach to resolving this issue could involve extending “custodial symmetry" to multiple Higgs triplets, akin to the ideas presented in, e.g., [248]. This would correlate coupling modifications with the mass eigenstates of the extended scalar spectrum, similar to how the hierarchy of charged and neutral current interaction strengths is correlated with the gauge boson masses. Although a dynamical realisation of this scenario has not been pursued, it is emphasised that the continued search for lepton-flavour-relevant new states at the LHC remains a well-motivated endeavour, even in light of high-precision low-energy measurements that might suggest otherwise.

Chapter 5.

New physics effects in momentum-dependent widths and propagators

"What would be the use of such extreme refinement in the science of measurement? Very briefly and in general terms, the answer would be that in this direction the greater part of all future discovery must lie. The more important fundamental laws and facts of physical science have all been discovered, and these are so firmly established that the possibility of their ever being supplanted in consequence of new discoveries is exceedingly remote. Nevertheless, it has been found that there are apparent exceptions to most of these laws, and this is particularly true when the observations are pushed to a limit, i.e., whenever the circumstances of experiment are such that extreme cases can be examined."

— A. Michelson, 1903

Collider observables are determined by production cross-sections and decay rates, both of which depend on particle masses, widths, and propagators. A precise treatment of finite particle lifetimes is therefore essential for the accurate interpretation of high-energy physics data. At leading order, implementing particle widths requires care to preserve gauge invariance; the commonly used Breit-Wigner prescription can violate this at tree level [370, 371]. The optical theorem relates the imaginary part of a particle's self-energy to its total decay width [70, 372], but complications arise

when dealing with unstable particles [373]. Their propagators exhibit poles on the second Riemann sheet of the S-matrix [374], complicating the direct application of the LSZ reduction formula. Various approaches have been developed to address this, including resummation schemes and field-theoretic formalisms [375]. Gauge-invariant treatments of unstable particle widths can be constructed using Nielsen identities [376–378], while the complex mass scheme provides a self-consistent and widely adopted framework for loop-level computations [379, 380].

The narrow-width approximation assumes a constant width and is widely used in phenomenology, but it may neglect important momentum-dependent effects, especially in new physics or higher-order contexts. Dyson resummation accounts for this by introducing a running width from the one-loop self-energy function $\Sigma(q^2)$, $\Gamma(q^2) = \mathrm{Im}[\Sigma(q^2)]/m$, modifying both masses and cross-sections:

$$iG(q^2) = \frac{i}{q^2 - m^2 + im\Gamma(q^2)} \,. \tag{5.1}$$

These effects can be significant in precision analyses [381], where mass determinations, especially for the W and Z bosons, can exhibit scheme-dependent shifts larger than experimental uncertainties [382–384].

This chapter examines whether neglecting momentum-dependence in widths introduces phenomenological discrepancies. The validity of the fixed-width approach and potential deviations relevant for precision measurements is explored for SM particles in Sec. 5.1. The sensitivity to new physics effects parameterised by SMEFT-induced deviations is explored in various collider environments, including hadron and lepton colliders in Sec. 5.2.

5.1. Widths of SM particles

Widths naturally enter the propagators of unstable particles through higher-order effects, giving rise to poles in the second Riemann sheet of the S-matrix. This discussion introduces concepts and enables identifying SM particles that are particularly susceptible to lineshape modifications from new physics. These modifications can then result in potential experimental consequences, particularly at the high-precision frontier of future colliders.

5.1.1. The Higgs boson

Due to its scalar nature, the concepts become particularly transparent in the case of the Higgs boson. The renormalised Higgs one-particle irreducible (1PI) two-point function is given by

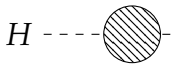

$$= \hat{\Gamma}^H(q^2) = -i(q^2 - m_h^2) - i\Sigma^h(q^2), \tag{5.2}$$

where Σ^h denotes the self-energy of the Higgs boson considered at the one-loop level in the following. The on-shell renormalisation conditions for the Higgs two-point function $\hat{\Gamma}^h(q^2)$ are (see e.g. [385])

$$\begin{aligned} \operatorname{Re} \hat{\Gamma}^h(q^2)\Big|_{q^2=m_h^2} &= 0, \\ \lim_{q^2 \to m_h^2} \frac{1}{q^2 - m_h^2} \operatorname{Re} \hat{\Gamma}^h(q^2)\Big|_{q^2=m_h^2} &= i. \end{aligned} \tag{5.3}$$

The equations shown above result in the following on-shell renormalisation conditions for the Higgs self-energy function $\Sigma^h(q^2)$

$$\operatorname{Re} \Sigma^h(q^2)\Big|_{q^2=m_h^2} = \operatorname{Re} \frac{\partial \Sigma^h(q^2)}{\partial q^2}\Big|_{q^2=m_h^2} = 0. \tag{5.4}$$

The Dyson-resummed Higgs propagator is then given in terms of the renormalised self-energy

$$iG_h(q^2) = \frac{i}{q^2 - m_h^2 + \Sigma^h(q^2)}. \tag{5.5a}$$

By construction, this propagator exhibits unity pole residue when approaching the *real* on-shell Higgs mass value, leaving an imaginary component that can be identified as a running width in comparison with Eq. (5.1):

$$\Gamma_h(q^2) = \frac{\operatorname{Im} \Sigma^h(q^2)}{m_h} \quad \text{with} \quad \Gamma_h(q^2 = m_h^2) \approx 5.5\,\text{MeV}, \tag{5.5b}$$

(for $m_h = 125$ GeV at leading order) which is related to the tree-level computation of $h \to \{\text{SM fields}\}$ via the optical theorem. This value also agrees with current experimental bounds, e.g. as listed by the PDG [54]. Eq. (5.5) implies that, near the on-shell

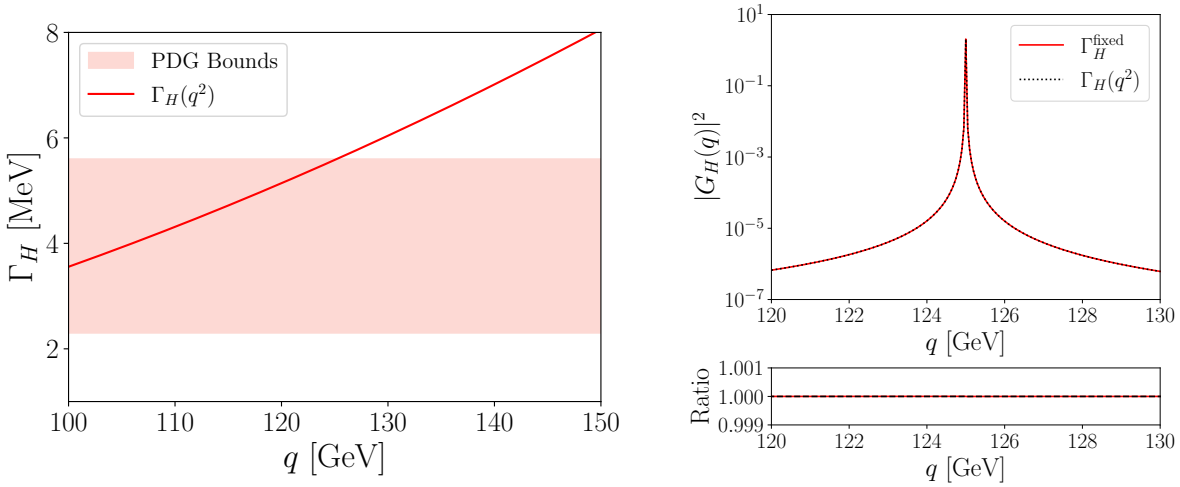

(a) Higgs width.

(b) Higgs propagator.

Figure 5.1.: Plots showing (a) the momentum-dependent Higgs width, and (b) the corresponding invariant masses of the Higgs using the propagators constructed with a fixed and a running width. The lower panel on the right shows the ratios between the two propagators.

Higgs mass, the loop-corrected propagator approximates the Breit-Wigner form. This leads to the familiar exponential decay of the intermediate Higgs state derived from the squared matrix element. Representative plots illustrating the q^2 dependence of Γ_h and the resulting Higgs propagator are shown in Fig. 5.1 for the SM. Given that the Higgs width is much smaller than its mass, the ratio of the two propagators shows minimal deviation from unity, as seen in the lower panel of Fig. 5.1(b). This demonstrates that the ratio Γ/m is a meaningful figure of merit for evaluating the validity of treating unstable particles like the Higgs as asymptotic states in S-matrix analyses, even though the true nature of the resonance is more subtle and scheme-dependent. The same reasoning applies to BSM scenarios [386, 387]. For heavier SM Higgs bosons (as considered pre-discovery [388]), the width grows significantly, affecting the convergence of the electroweak perturbative expansion, and thus highlighting the importance of scheme choice. In the SM, supported by current observations, $\Gamma^h/m_h \sim 10^{-5}$, implying that momentum-related modifications near the on-shell region are difficult to resolve with current or expected experimental resolution [189, 389]. Consequently, scheme dependencies are numerically small [390, 391]. Nonetheless, BSM effects can still alter these observables more significantly through direct modifications of pseudo-observables rather than through distortions of the resonance profile itself [392, 393], making the Higgs less suited for studying finite-width effects in isolation.

5.1.2. The W boson

The W boson can be used as a proxy for the massive gauge bosons; the treatment of the $Z\gamma$ mixing is detailed elsewhere in the literature, e.g. [385], yet the previous discussion of the Higgs boson generalises to all massive gauge bosons in broad terms. The renormalised two-point vertex function for the W field can be written (considering the Feynman-'t Hooft gauge) as

W_μ 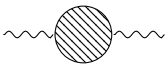 W_ν

$$\begin{aligned} &= \hat{\Gamma}^W_{\mu\nu}(q) \\ &= -ig_{\mu\nu}(q^2 - m_W^2) - i\left(g_{\mu\nu} - \frac{q_\mu q_\nu}{q^2}\right)\Sigma_T^W(q^2) - i\frac{q_\mu q_\nu}{q^2}\Sigma_L^W(q^2), \end{aligned} \tag{5.6}$$

where Σ_T^W and Σ_L^W denote the transverse and longitudinal parts of the W-boson self-energy, respectively. The renormalisation conditions for the W two-point function for on-shell external physical fields are given by

$$\begin{aligned} \text{Re}\,\hat{\Gamma}^W_{\mu\nu}(q)\varepsilon^\nu(q)\Big|_{q^2=m_W^2} &= 0, \\ \lim_{q^2\to m_W^2}\frac{1}{q^2 - m_W^2}\text{Re}\,\hat{\Gamma}^W_{\mu\nu}(q)\varepsilon^\nu(q)\Big|_{q^2=m_W^2} &= -i\varepsilon_\mu(q), \end{aligned} \tag{5.7}$$

where $\varepsilon^\nu(q)$ is the polarisation vector of the external W fields. Gauge-invariance and its manifestation in the gauge-fixed effective theory in terms of Slavnov-Taylor identities [61, 62] ensure that the longitudinal part of the propagator does not affect physical observables through the quartet mechanism [394]. Therefore, only the imaginary part of Σ_W^T contributes directly to the decay width pseudo-observable. From the equations shown above, the following on-shell renormalisation conditions for the transverse part of the self-energy function can be obtained as

$$\text{Re}\,\Sigma_T^W(q^2)\Big|_{q^2=m_W^2} = \text{Re}\,\frac{\partial\Sigma_T^W(q^2)}{\partial q^2}\Big|_{q^2=m_W^2} = 0. \tag{5.8}$$

The Dyson-resummed W-propagator, involving only the renormalised transverse part Σ_T^W, is then given by

$$iG_W^{\mu\nu}(q^2) = \frac{-i}{q^2 - m_W^2 + \Sigma_T^W(q^2)}\left(g^{\mu\nu} - \frac{q^\mu q^\nu}{q^2}\right). \tag{5.9}$$

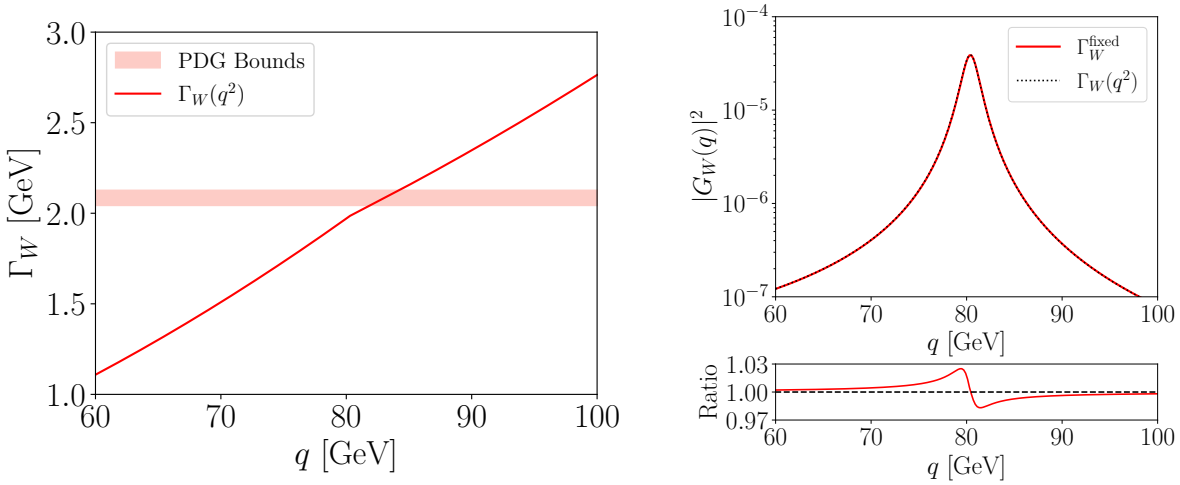

(a) W boson width. (b) W propagator.

Figure 5.2.: Plots showing (a) the momentum-dependent W-width, and (b) the corresponding invariant masses of the W computed using the propagators constructed with a fixed and a running width. The lower panel shows the ratio between the respective propagators.

From the propagator shown in Eq. (5.9), the q^2-dependent running width of the W boson can be identified as

$$\Gamma_W(q^2) = \frac{\text{Im}\,\Sigma_T^W(q^2)}{m_W} \quad \text{with} \quad \Gamma_W(q^2 = m_W^2) \approx 1.99\ \text{GeV}, \tag{5.10}$$

similar to the Higgs boson. The dependence of Γ_W on q^2 and the corresponding W propagator are shown in Fig. 5.2. The variations are at the percent level in the W boson invariant mass lineshape as illustrated in Fig. 5.2(b). It is of interest, however, to explore whether the running width has implications for the precise W-mass measurements reported by CDF [395], ATLAS [396], and very recently CMS [397], where each analysis measured the reconstructed transverse mass of the W (m_W^T). The differential m_W^T distribution for both fixed and running Γ_W is shown in Fig. 5.3. As expected, the percent level differences in the W-propagator do not offer significant deviations in the transverse mass differential distribution. Of course, this momentum-dependence should be viewed against the complete set of electroweak corrections, which are scheme and process-dependent. The conclusion at this point is that the W propagator does not provide significant *a priori* potential to constrain the momentum-dependencies away from the peak observables, resulting in a subleading effect for phenomenological analyses [398].

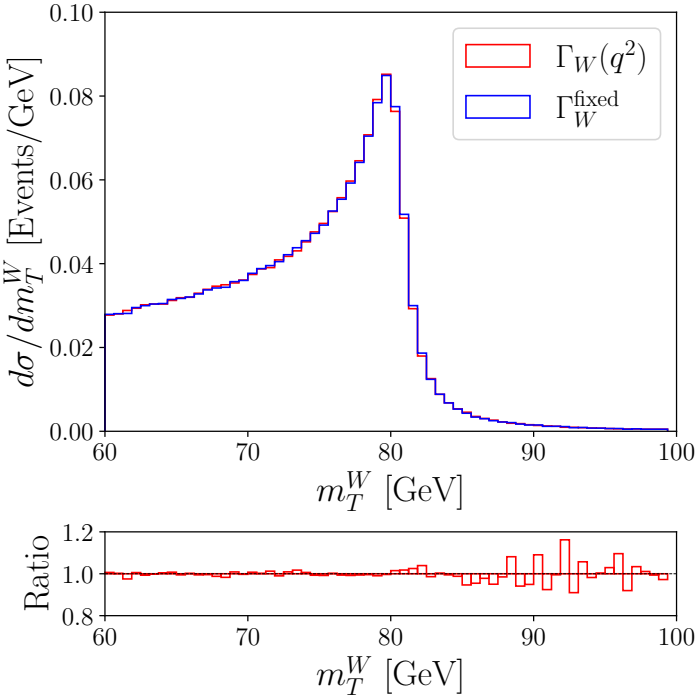

Figure 5.3.: Differential distribution of the reconstructed transverse mass of the W boson in 13 TeV pp collisions comparing results for fixed and running widths. The lower panel shows the ratio of the two distributions.

The momentum-dependent width of the Z boson exhibits a behaviour similar to that of the W boson, with quantitatively distinct contributions from fermion loops. Despite these differences, the variations in the momentum-dependent width of the Z boson are even smaller than those observed for the W boson. Consequently, any potential impacts on the invariant mass or transverse mass distributions of the Z boson are negligible, offering even reduced potential compared to the discussion of the W boson.

5.1.3. The Top Quark

The analysis of calculating the momentum-dependent width can finally be extended to the top quark. The study of the top resonance characteristics provides valuable insights into possible BSM effects. Most analyses so far have relied on peak pseudo-observables (e.g. ATLAS analyses like [399] used in the EFT analyses like [400–406]). Recently, there has been a resurgence in the literature on hypothetical bound states of top and antitop quarks, *toponium* [407–409] triggered by anomalies of LHC data. While

toponium itself remains a short-lived entity due to the rapid decay of the top quark (*before* the bound state is formed), it can alter distributions at threshold production in, e.g., top pair production. Therefore, this currently evolving situation can be considered an additional source of uncertainty for the topics discussed in this section.

The framework established in the previous sections for the W boson and the Higgs can be utilised to delve into the unique features of the top quark width and the corresponding propagator, whose calculations are comparatively more involved than the previous cases. The renormalised 1PI two-point function for the top quark is given by,

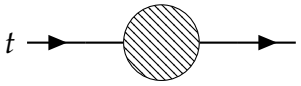

$$\begin{aligned} &= \hat{\Gamma}^t_{ij}(q) \\ &= i(\not{q} - m_t) + i\left[\not{q}\omega_- \Sigma^t_L(q^2) + \not{q}\omega_+ \Sigma^t_R(q^2) + m_t \Sigma^t_S(q^2)\right], \end{aligned} \tag{5.11}$$

where $\omega_\pm = (1 \pm \gamma^5)/2$ are the chiral projectors, Σ^t_L and Σ^t_R correspond to the left- and right-handed wave-function corrections, and Σ^t_S denotes the scalar part of the top-quark self-energy. The renormalisation conditions for on-shell external fields are given by

$$\begin{aligned} &\text{Re}\, \bar{u}_i(q')\hat{\Gamma}^t_{ij}(q')\Big|_{q'^2=m_t^2} = 0, \\ &\lim_{q^2 \to m_t^2} \frac{\not{q} + m_t}{q^2 - m_t^2} \text{Re}\, \hat{\Gamma}^t_{ii}(q) u_i(q) = i u_i(q), \\ &\lim_{q'^2 \to m_t^2} \bar{u}_i(q') \text{Re}\, \hat{\Gamma}^t_{ii}(q') \frac{\not{q}' + m_t}{q'^2 - m_t^2} = i\bar{u}_i(q') \end{aligned} \tag{5.12}$$

where $u(q)$ and $\bar{u}(q')$ are the spinors of the external top quark fields. The renormalisation conditions can then be obtained on the top quark two-point functions

$$\begin{aligned} &\text{Re}\, \Sigma^t_L(q^2)\Big|_{q^2=m_t^2} + \text{Re}\, \Sigma^t_S(q^2)\Big|_{q^2=m_t^2} = 0, \\ &\text{Re}\, \Sigma^t_R(q^2)\Big|_{q^2=m_t^2} + \text{Re}\, \Sigma^t_S(q^2)\Big|_{q^2=m_t^2} = 0, \\ &\text{Re}\, \Sigma^t_L(q^2)\Big|_{q^2=m_t^2} + \text{Re}\, \Sigma^t_R(q^2)\Big|_{q^2=m_t^2} \\ &\qquad + 2m_t^2 \frac{\partial}{\partial q^2}\left[\text{Re}\, \Sigma^t_L(q^2) + \text{Re}\, \Sigma^t_R(q^2) + 2\text{Re}\, \Sigma^t_S(q^2)\right]\Big|_{q^2=m_t^2} = 0. \end{aligned} \tag{5.13}$$

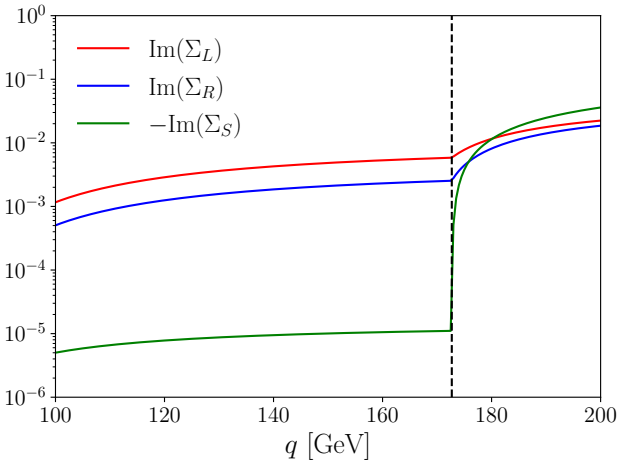

Figure 5.4.: The imaginary parts of the different two-point amplitudes associated with the top quark self-energy.

The plot of the imaginary parts of Σ_L, Σ_R, and Σ_S that are relevant for the top width calculations in the SM are depicted in Figure 5.4. Defining

$$i\Sigma_2^t(q) = i\left[\not{q}\omega_-\Sigma_L^t(q^2) + \not{q}\omega_+\Sigma_R^t(q^2) + m_t\Sigma_S^t(q^2)\right],$$

the full top propagator, including the sum of all 1PI insertions, can be obtained as the sum of an infinite geometric series.

$iG(q) =$ 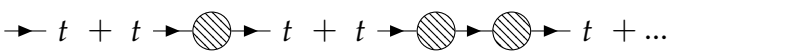

$$= \frac{i}{\not{q} - m_t} + \left[\frac{i}{\not{q} - m_t} i\Sigma_2^t(q) \frac{i}{\not{q} - m_t}\right] + \left[\frac{i}{\not{q} - m_t} i\Sigma_2^t(q) \frac{i}{\not{q} - m_t} i\Sigma_2^t(q) \frac{i}{\not{q} - m_t}\right] + \ldots$$

$$= \frac{i}{\not{q} - m_t + \Sigma_2^t(q)}.$$

The full expression for the top quark propagator is

$$iG(q) = \frac{i}{\not{q}[1 + \omega_-\Sigma_L^t(q^2) + \omega_+\Sigma_R^t(q^2)] - m_t[1 - \Sigma_S^t(q^2)]}. \tag{5.14}$$

The Breit-Wigner form then follows from Eq. (5.14) as

$$iG(q) = i\frac{\not{q}[1 + \omega_-\Sigma_L^t(q^2) + \omega_+\Sigma_R^t(q^2)] + m_t[1 - \Sigma_S^t(q^2)]}{q^2[1 + \Sigma_L^t(q^2)][1 + \Sigma_R^t(q^2)] - m_t^2[1 - \Sigma_S^t(q^2)]^2}. \tag{5.15}$$

Starting from Eq. (5.15), isolating the q^2 term in the denominator, the propagator takes the form,

$$iG(q) = i\frac{\not{q}[1+\omega_-\Sigma_L^t(q^2)+\omega_+\Sigma_R^t(q^2)]+m_t[1-\Sigma_S^t(q^2)]}{(1+\Sigma_L^t(q^2))(1+\Sigma_R^t(q^2))\left(q^2-\frac{m_t^2[1-\Sigma_S^t(q^2)]^2}{[1+\Sigma_L^t(q^2)][1+\Sigma_R^t(q^2)]}\right)}, \tag{5.16}$$

which can then be expressed as (see e.g. [410]),

$$M_{t,\text{pole}}^2 - iM_{t,\text{pole}}\Gamma_t = \left.\frac{m_t^2(1-\Sigma_S)^2}{(1+\Sigma_L)(1+\Sigma_R)}\right|_{q^2=m_t^2}. \tag{5.17}$$

To one-loop order, Eq. (5.17) can be expanded perturbatively

$$M_{t,\text{pole}}^2 - iM_{t,\text{pole}}\Gamma_t = m_t^2\,(1-\Sigma_L-\Sigma_R-2\Sigma_S)\Big|_{q^2=m_t^2}.$$

From this the pole-mass and the width can then be derived [410] (for $m_t = 172.7\,\text{GeV}$ [54])

$$\begin{aligned} M_{t,\text{pole}} &= m_t\left(1-\frac{1}{2}\Sigma_L-\frac{1}{2}\Sigma_R-\Sigma_S\right)\Big|_{q^2=m_t^2} \approx 172.7\,\text{GeV}, \\ \Gamma_t(q^2) &= m_t\,\text{Im}\,(\Sigma_L+\Sigma_R+2\Sigma_S)\,, \quad \Gamma_t(q^2=m_t^2)\approx 1.44\,\text{GeV}. \end{aligned} \tag{5.18}$$

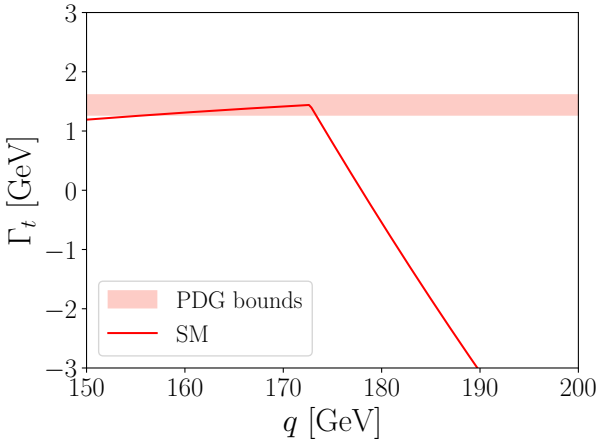

(a) Top width as detailed in the text.

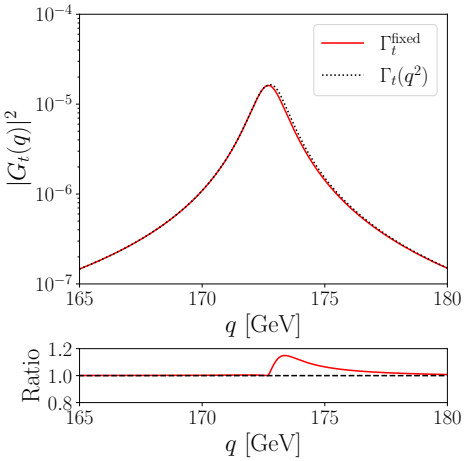

(b) Top propagator for different approximations.

Figure 5.5.: Plots showing (a) the momentum-dependent top width and (b) the corresponding invariant masses of the top using the propagators constructed with a fixed and a running width (right). The lower panel on the right represents the ratio of the two plotted propagators.

This result is consistent with the current PDG value for Γ_t [54]. In the narrow-width approximation, where $\Gamma_t \ll m_t$, the top quark propagator can be written up to one-loop order as

$$iG^t(q) = i\frac{\not{q} + m_t}{q^2 - m_t^2 + im_t^2 \mathrm{Im}\left(\Sigma_L + \Sigma_R + 2\Sigma_S\right)}. \tag{5.19}$$

The q^2-dependent running width described by Eq. (5.18) and the corresponding propagators constructed from the fixed and the running top width have been plotted in Fig. 5.5. A pronounced change in the running width after $q^2 = m_t^2$ is observed, discernible from the two-point amplitudes characterised by Σ_L, Σ_R and notably Σ_S as shown in Fig. 5.4. The marked increase in the imaginary parts of these amplitudes at $q^2 = m_t^2$ arises due to the top quark self-energy contributions, specifically from the gluonic diagrams turning on at $q^2 = m_t^2$ due to the optical theorem. This behaviour is further reflected in the top propagator as depicted in Fig. 5.5, where a significant deviation is observed in the running width from the propagator constructed with the fixed width, as illustrated in the lower panel on the right. Thus, any new physics scenarios that modify the top quark two-point functions may leave a substantial imprint on the running width and, consequently, on the invariant mass, which may be detectable by the extensive array of current and future colliders. It should again be noted that these effects will be part of a larger set of electroweak corrections. Especially when dealing with the massless fields that shape distributions as detailed above, the matching of infrared singularities becomes relevant, e.g. [411] for a detailed discussion. In this context, however, it is worth stressing that, by construction, EFT deformations do not modify the soft and collinear behaviour of the SM [412]. So, while the presence of virtual massless states requires care from the point of view of the dimension-four interactions, the relation of dimension-six interactions to the SM is not sensitive to such an interplay. However, the emission of hard photons or gluons certainly poses a direct avenue to limit interaction modifications.

5.2. New Physics effects in Running Top Quark Widths and Propagators

The SMEFT framework is an ideal candidate to examine the effects of new physics on the q^2-dependent running width and the resulting propagator of the top quark.

$\mathcal{O}_{tG}$	$(\bar{t}_L \sigma^{\mu\nu} T^A t_R)\tilde{\Phi} G^A_{\mu\nu}$	$\mathcal{O}_{tW}$	$(\bar{t}_L \sigma^{\mu\nu} t_R)\tau^I \tilde{\Phi} W^I_{\mu\nu}$
$\mathcal{O}_{t\Phi}$	$(\Phi^\dagger \Phi)(\bar{t}_L t_R \Phi)$	$\mathcal{O}_{tB}$	$(\bar{t}_L \sigma^{\mu\nu} t_R)\tilde{\Phi} B_{\mu\nu}$

Table 5.1.: Dimension-six SMEFT operators [119] in the top quark sector that modify the top quark two-point function. $\tilde{\phi}$ is the charge conjugated SM Higgs doublet.

The top quark two-point function can be modified by introducing dimension-six SMEFT operators in the Warsaw basis [119], which alter the top quark vertices that appear in self-energy diagrams. The SMEFT operators considered in the analysis are listed in Table 5.1, all in the top quark sector. The corresponding Wilson coefficients hold significant BSM potential due to the currently relatively loose constraints on them ($\mathcal{O}(0.1-1)$ TeV^{-2} [128, 405]). The SMEFT operator $\mathcal{O}_{tG}$ directly modifies the ttg vertex, and can therefore capture the effects of new physics affecting the gluonic topologies contributing to the top self-energy. This operator does not affect $\Gamma_t(q^2)$ directly, contributing solely to the tails of the top invariant mass lineshape. However, this scenario changes with the inclusion of additional effective operators, specifically $\mathcal{O}_{tW}$, $\mathcal{O}_{tB}$, and $\mathcal{O}_{t\Phi}$. A notable subtlety arises here, as the operator $\mathcal{O}_{tW}$ directly modifies $\Gamma_t(t \to Wb)$; any phenomenologically relevant momentum-dependence could therefore enhance the new physics potential, but is unlikely to drive it.

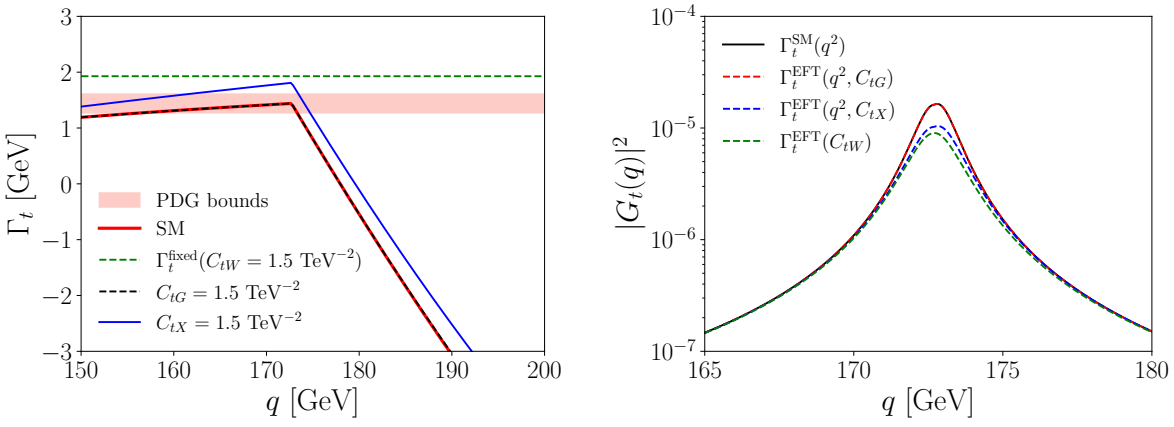

(a) Modified top width.

(b) Modified top propagator.

Figure 5.6.: Plots showing (a) the momentum-dependent top width, and (b) the corresponding invariant masses of the top using the propagators constructed with a running width for different SMEFT insertions, and a fixed width corresponding to a direct modification of $t \to W^+ b$ decay. In both plots, $C_{tW} = C_{tB} = C_{tG} = C_{t\Phi} = C_{tX} = 1.5\ \text{TeV}^{-2}$.

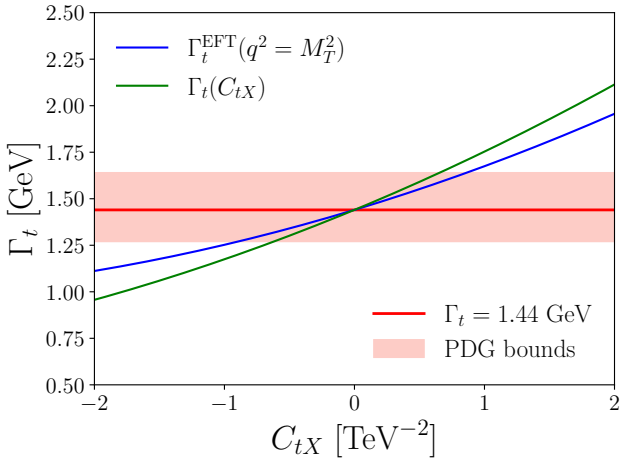

Figure 5.7.: Wilson coefficient dependence of Γ_t computed from (1) running width with SMEFT insertions at $q^2 = m_t^2$, and (2) from $t \to W^+ b$. Here, $C_{tW} = C_{tB} = C_{tG} = C_{t\Phi} = C_{tX}$.

Following the on-shell renormalisation procedure as described in the previous section, the expression for the perturbative width up to one-loop order can be computed as

$$\Gamma_t = \mathrm{Im}\left[m_t(\Sigma_L + \Sigma_R + 2\Sigma_S)\right].$$

The q^2-dependent widths and the corresponding propagators for both scenarios are presented in Fig. 5.6, including the fixed width and the corresponding propagator obtained by examining the direct contribution of $\mathcal{O}_{tW}$ on the $t \to Wb$ decay. As anticipated, the $\mathcal{O}_{tG}$ insertion does not alter the width calculated at $q^2 = m_t^2$. However, by observing the running width at higher q^2, a slight divergence from the SM running width is apparent for the selected values of the associated Wilson coefficient. The running width computed with multiple operator insertions, assuming equal values for the relevant Wilson coefficients, deviates significantly from the SM running width and the modifications induced by the direct alteration of $t \to Wb$. This difference can also be visualised by examining the dependence of the running width on the Wilson coefficients at $q^2 = m_t^2$ and contrasting this with the modification of the fixed decay width, as illustrated in Fig. 5.7. Given that new physics affecting the Wilson coefficients under consideration may lead to observable changes in the running width of the top quark, it is crucial to explore whether observables sensitive to running width effects could provide constraints on these Wilson coefficients comparable to those achieved through global fit methodologies.

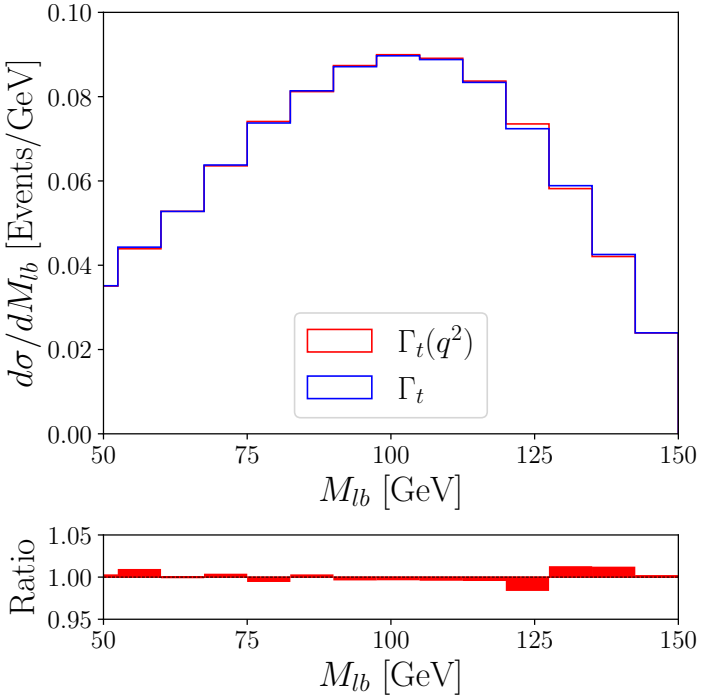

Figure 5.8.: Differential distribution of the reconstructed invariant mass of a lepton and the corresponding b-jet (M_{lb}) in the dileptonic decay of $t\bar{t}$ production in 13 TeV pp-collisions, for fixed and running top widths.

5.2.1. Hadron Colliders

On the hadron collider front, the ATLAS collaboration, for instance, has conducted a direct measurement of the top quark decay width [413] at $\sqrt{s} = 13$ TeV, with an integrated luminosity of $\mathcal{L} = 139$ fb^{-1}. This measurement utilises a profile-likelihood template fit applied to the invariant mass distribution of a charged lepton and its associated b-jet (M_{lb}) in the dileptonic decay channel of $t\bar{t}$ production. Consequently, it is essential to employ their search strategy to assess the impact of running widths on the kinematic properties of the top quark. Following the approach outlined in Ref. [413], the differential distributions for the kinematic observable M_{lb}, comparing the SM fixed and running top quark widths is displayed in Fig. 5.8, indicating that hadron colliders exhibit limited sensitivity (variations only at the percent level) to running width effects of the top quark, feeding into a low BSM potential.

5.2.2. Lepton Colliders

Unlike hadron machines, future lepton colliders offer unique advantages by providing cleaner environments for precision studies due to the absence of hadronic initial states and smaller experimental uncertainties. This structural simplicity is particularly beneficial when analysing processes such as top quark pair production, which yields a cleaner signal in hadronic final states. Lepton colliders are thus well-suited for precise measurements of the top quark mass and electroweak couplings via the s-channel pair production process. Proposed electron-positron machines like FCC-*ee* [76, 77], ILC [414], CEPC [78], and CLIC [415] hold significant potential for probing the top quark invariant mass lineshape should relevant centre-of-mass energies be achieved there, leveraging high luminosity and advanced detector capabilities. While the FCC-*ee* excels near the s-channel $t\bar{t}$ production threshold due to its precise energy calibration, at higher energies, such as CLIC running at $\sqrt{s} = 3$ TeV becomes competitive, with its high luminosity potentially allowing a more detailed exploration of the lineshape over a wide range. However, significant beamstrahlung in CLIC can broaden the energy spectrum and reduce the precision in reconstructing the top invariant mass lineshape [415–417]. Muon colliders [418], on the other hand, offer distinct, exciting advantages over electron-positron colliders, as they can achieve higher centre-of-mass energies without significant synchrotron radiation losses, effectively making them vector boson colliders. This enables muon colliders to probe top quark physics not only through s-channel pair production but also via weak boson fusion (WBF) processes (Fig. 5.9), whose cross-section grows with centre-of-mass energy (see [419–421]). This makes muon colliders ideal for capturing subtle variations in the top invariant mass lineshape influenced by the SMEFT operators discussed previously, hence potentially identifying new physics effects.

Event Simulation Details

The relevant Wilson coefficients are implemented on `FeynRules` [64] using `SmeftFR` [224, 422, 423] and linked to `Madgraph5_aMC@NLO` [160] using a `Ufo` [273] output. Events are generated by combining the processes $\mu^+\mu^- \to t\bar{t}$ and $\mu^+\mu^- \to t\bar{t}\nu_\mu\bar{\nu}_\mu$ to include both s-channel production of $t\bar{t}$ as well as top quark pair production through vector boson collisions. The top quark pairs are subsequently decayed semileptonically into light leptons (e, μ), jets from the resulting W bosons, and b quarks. The effects of a q^2-dependent running top quark width are incorporated by modifying the top

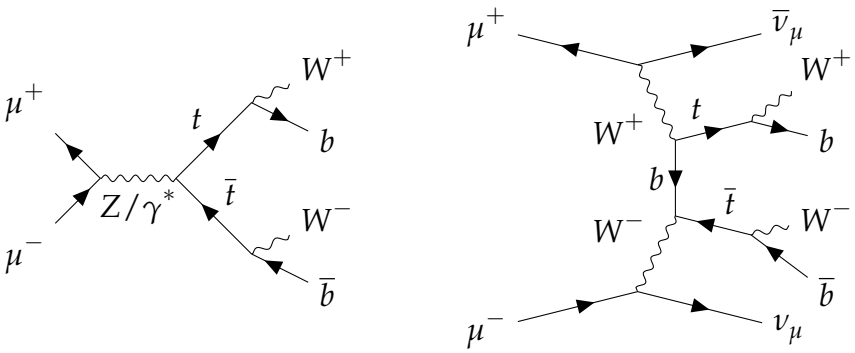

Figure 5.9.: Representative Feynman topologies for s-channel and WBF $t\bar{t}$-production in $\mu^+\mu^-$ colliders.

propagator on the `Helas` [424] routines entering the matrix element calculations for each value of the relevant Wilson coefficients.

Events are simulated for hypothetical future muon colliders with centre-of-mass energies of $\sqrt{s} = 3, 10$ TeV. The top quark candidates are reconstructed closely following the analyses performed in Refs. [425–427] for semileptonically decaying $t\bar{t}$ candidates. The final states are required to have four jets, two of which are b-tagged, and exactly one light lepton with $p_T^l > 10$ GeV. The invariant mass of the two non b-tagged jets and the b-jet that is farther from the lepton is used to reconstruct the lineshape of the top quark candidate.

Bounds from Top Invariant Mass Lineshape

A combined bound on the relevant SMEFT Wilson coefficients can be obtained using the lineshape of the reconstructed top quark invariant mass distribution (M_t). The binned χ^2 statistic for the analysis is constructed as

$$\chi^2(C_{tX}) = (b^i_{\text{SM+EFT}}(C_{tX}) - b^i_{\text{SM}})V^{-1}_{ij}(b^j_{\text{SM+EFT}}(C_{tX}) - b^j_{\text{SM}}). \tag{5.20}$$

where $b^i_{\text{SM+EFT}}(C_{tX})$ denotes the combined number of events in the i^{th} bin of the M_t distribution, incorporating a running top quark width in the SMEFT framework and weighted by the cross-section, for a given value of C_{tX}, and, b^i_{SM} corresponds to the number of events when considering only the SM running width. The covariance matrix V_{ij} is constructed using the statistical Poisson uncertainty associated with each bin b^i_{SM}, along with a fully correlated relative fractional uncertainty (ϵ_r). Thus, the

$\mathcal{L}$	ϵ_r	$\sqrt{s} = 3$ TeV	$\sqrt{s} = 10$ TeV
5 ab^{-1}	25%	$(-0.83, 1.12)$ TeV^{-2}	$(-0.52, 0.48)$ TeV^{-2}
	10%	$(-0.54, 0.60)$ TeV^{-2}	$(-0.23, 0.21)$ TeV^{-2}
10 ab^{-1}	25%	$(-0.72, 0.91)$ TeV^{-2}	$(-0.42, 0.41)$ TeV^{-2}
	10%	$(-0.51, 0.57)$ TeV^{-2}	$(-0.20, 0.18)$ TeV^{-2}

Table 5.2.: 95% CL bounds on the relevant SMEFT Wilson coefficients (C_{tX}) from the top invariant mass lineshape at a future muon collider.

covariance matrix can be expressed as

$$V_{ij} = b^i_{\rm SM}\delta_{ij} + \epsilon_r b^i_{\rm SM} b^j_{\rm SM}. \tag{5.21}$$

The resulting 95% confidence level bounds on $C_{tX} = C_{tW} = C_{tB} = C_{tG} = C_{t\phi}$ for different centre-of-mass energies and integrated luminosities, for $\epsilon_r = 10\%$ and 25% are presented in Table 5.2. How do these bounds compare to global fit analyses? The operators C_{tG}, and $C_{t\Phi}$ are well constrained in hadron collider processes [128]; however, C_{tW} and C_{tB} can be directly probed at lepton colliders near the $t\bar{t}$-production threshold. The methodologies employed in Refs. [428, 429] and TopFitter [400] for e^+e^- colliders (see also [430]), are adapted for muon colliders to assess whether the top invariant mass lineshape can effectively constrain these operators more robustly than the present robust global fit analyses.

Refs. [428, 429] use the sensitivity of both the total cross-section (σ) and the forward-backward asymmetry ($A_{\rm FB}$) to obtain bounds on the effective operators, and consequently, the same analysis methodologies can be adapted for muon collider scenarios. The forward-backward asymmetry is defined as

$$A_{\rm FB} = \frac{\sigma_{\rm FB}}{\sigma}, \tag{5.22}$$

where the forward-backward cross-section $\sigma_{\rm FB}$ is given by

$$\sigma_{\rm FB} = \int_{-1}^{1} d\cos\theta_t \, {\rm sign}(\cos\theta_t) \, \frac{d\sigma}{d\cos\theta_t}, \tag{5.23}$$

with θ_t representing the scattering angle in the centre-of-mass frame. Events are generated in `Madgraph5_aMC@NLO` [160] for various initial beam polarisations of the

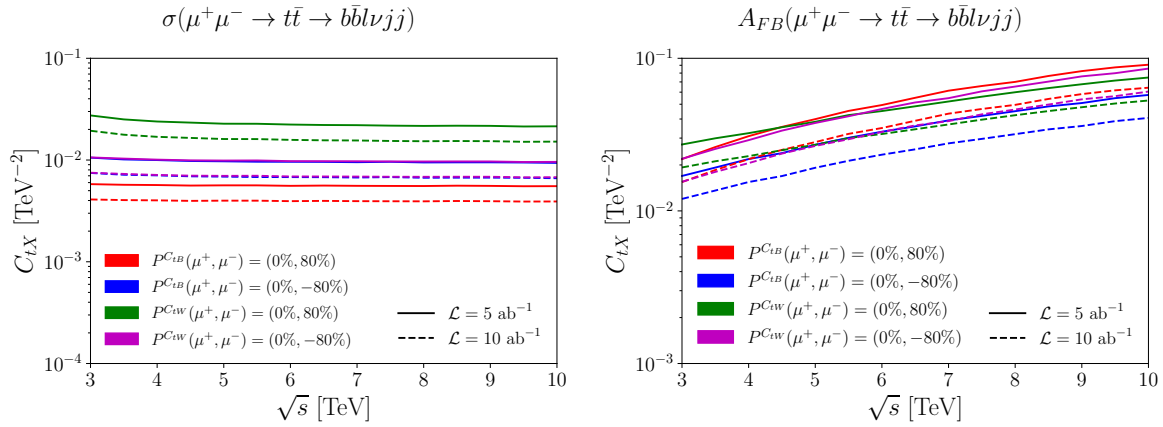

Figure 5.10.: 95% CL upper bounds on C_{tW} and C_{tB} from (left) cross-section and (right) forward-backward asymmetry [428, 429] for different initial beam polarisations.

$\mu^+\mu^-$ states. From the resulting events, the SM, linear, and quadratic dependences of the effective operators on the respective observables can be computed.

The sensitivity of an observable o to a Wilson coefficient C_i (S_i^o) is calculated as per Ref. [428], as its normalised variation around the SM point:

$$S_i^o = \frac{1}{o}\frac{\partial o}{\partial C_i}\bigg|_{C_i=0} = \frac{o_i}{o_{\text{SM}}}, \quad \text{with} \quad o = o_{\text{SM}} + C_i o_i + C_i C_j o_{ij} + \ldots \quad . \tag{5.24}$$

Here, the cutoff scale is conveniently set to $\Lambda = 1$ TeV, which can also be absorbed into the definitions of o_i, o_{ij}, etc. The 95% confidence limit constraints on C_{tB} and C_{tW} from the sensitivities of the cross-section and forward-backward asymmetry as functions of centre-of-mass energy for different initial beam polarisations and integrated luminosities are shown in Fig. 5.10. Fig. 5.10 shows that these constraints offer substantially stronger bounds on the respective effective operators compared to those obtained from the top invariant mass lineshape. The methodology employed by TopFitter [400] can also be used to cross-check the aforementioned bounds. Following Ref. [400], and motivated by the dependence of the total cross-section of the process $\mu^+\mu^- \to t\bar{t}$ on the Wilson coefficients ($\sigma[C_{tX}]$), a polynomial of degree greater than two can be fitted on the total cross-section. Without systematic uncertainties, each observable would ideally follow a second-order polynomial in the coefficients; higher-order terms account for bin uncertainties that introduce deviations from this ideal form. The following χ^2 distribution is constructed to determine the constraints

$\mathcal{L}$	Wilson coefficient	$\sqrt{s} = 3$ TeV	$\sqrt{s} = 10$ TeV
5 ab^{-1}	C_{tB}	$(-0.02, 0.15)$ TeV^{-2}	$(-0.02, 0.04)$ TeV^{-2}
	C_{tW}	$(-0.02, 0.24)$ TeV^{-2}	$(-0.03, 0.05)$ TeV^{-2}
10 ab^{-1}	C_{tB}	$(-0.02, 0.14)$ TeV^{-2}	$(-0.02, 0.03)$ TeV^{-2}
	C_{tW}	$(-0.02, 0.23)$ TeV^{-2}	$(-0.02, 0.05)$ TeV^{-2}

Table 5.3.: 95% CL individual bounds on the relevant SMEFT Wilson coefficients from the TopFitter [400] analysis.

on the Wilson coefficients

$$\chi^2(C_{tX}) = \frac{(\sigma[C_{tX}] - \sigma)^2}{\sigma}, \tag{5.25}$$

where $\sigma = \sigma_{\text{SM}}(1 + \Sigma)$. Here, σ_{SM} represents the SM cross-section for the same process, and Σ represents the combined theoretical and experimental uncertainties associated with the cross-section. Assuming a 10% combined uncertainty in the SM cross-section, the 95% confidence limit constraints for C_{tW} and C_{tB} at various centre-of-mass energies $\sqrt{s}$ and integrated luminosities are presented in Table 5.3. These bounds further demonstrate that direct constraints from global fit analyses are more effective in constraining the relevant Wilson coefficients than those derived from the top invariant mass lineshape.

5.3. Conclusions

Width pseudo-observables have been recognised as essential across past, present, and future collider experiments; however, momentum-dependent widths in the SM have often been overlooked due to their subdominant role given current experimental sensitivity. With increasing discussion on future precision machines, the extent to which these effects become relevant remains uncertain. Additionally, the influence of heavy physics on SM lineshapes under future sensitivity expectations remains poorly understood. This chapter addresses these gaps by parameterising new heavy physics using SMEFT, focusing on electroweak-scale SM particles such as the W boson, the Higgs boson, and the top quark.

For bosonic particles, the running width in the SM introduces minor deviations from the fixed-width approximation, with percent-level effects observed in transverse

mass distributions. These corrections, while subtle, could influence precision W boson mass measurements, as seen in ATLAS and CMS analyses. In contrast, for the Higgs boson, due to its narrow width, momentum dependence has been shown to be negligible. Thus, the W boson appears more sensitive to such effects in future precision measurements. The impact of BSM physics on the momentum-dependence of these widths remains uncertain but may become relevant as precision improves.

For the top quark, significantly larger effects have been observed due their impact in the self-energy contributions. Pronounced deviations between fixed-width and running-width propagators emerge above the mass threshold, attributed to the energy-dependent imaginary parts of self-energy components. With SMEFT operators, these effects are further amplified, modifying the top quark's invariant mass lineshape and reinforcing its role as a promising probe for new physics. At hadron colliders, such as the LHC, reconstructed top quark invariant mass distributions exhibit only percent-level deviations, constrained by detector effects. However, future lepton colliders, such as proposed muon colliders at 3 and 10 TeV, offer a cleaner environment. Simulations indicate that improved constraints on SMEFT-induced deviations in the top propagator and running width can be achieved. These constraints complement global fit analyses, reinforcing the capability of collider experiments to detect subtle BSM effects.

This chapter underscores the relevance of momentum-dependent widths in theoretical predictions, particularly as precision in measurements and calculations advances. While certain effects remain below current experimental sensitivity, next-generation lepton colliders are expected to probe these phenomena with unprecedented accuracy, refining SM particle properties and enhancing discovery potential for new physics.

Chapter 6.

Cornering new physics in four top quark production in the LHC

"These are not incremental improvements... These are very, very, very big improvements people are making by adopting really advanced techniques. It's going to be quite transformative for our field."

— Prof. Mark Thomson on the impact of ML/AI.

The absence of evidence for BSM physics at the array of colliders at disposal remains puzzling. The optimistic expectations of the pre-LHC BSM benchmarking programme have not been realised, necessitating a shift in focus towards less abundant collider processes that may serve as probes for new interactions. Model-independent and theoretically motivated techniques have been increasingly employed, alongside the exploitation of model-(un)specific correlations. Machine learning techniques have seen a resurgence in LHC analyses to capture these correlations, especially to tackle the dearth of sensitivity in rare collider processes. Four top quark final states, for which the ATLAS and CMS collaborations have recently reported evidence of SM-like production [431–436], pose an interesting avenue in this regard. These final states are relevant for EFT deformations of expected SM correlations [437–439], contributing significantly to large-scale EFT fits while also providing insights into electroweak Higgs properties [440]. The large kinematic information available in these final states enhances sensitivity when machine learning techniques (see also [441]) are used to distinguish signals from SM backgrounds [442].

Four top final states are often considered less motivated due to the large production cross-section of $t\bar{t}$ resonances via gluon fusion and the relative experimental ease of top pair resonance searches. However, interference effects with QCD backgrounds [443, 444] can significantly suppress BSM signals in dominant production and decay channels, leaving processes with lower cross-sections as viable discovery modes. Four top final states could offer a more robust alternative in such scenarios.

This chapter aims to clarify these aspects by building on sensitivity enhancements in distinguishing SM four top production and quantitatively assessing the potential for BSM discovery, particularly emphasising the role of interference effects in four top final states. The structure of this chapter is as follows: the details of event simulation and inclusive fiducial selection for the studied lepton-dominated partonic collider processes are presented in Sec. 6.1. The results are outlined in Sec. 6.2, presenting an evaluation of the sensitivity to SM four top production (Sec. 6.2.1), followed by the prospects of BSM sensitivity in Secs. 6.2.2 and 6.2.3. The role of GNN techniques in distinguishing resonant and non-resonant BSM extensions is highlighted, alongside signal-background interference effects. The significance of interference, which is substantial in di-top final states [445–451], is found to be negligible in the dominant four top production modes for resonant BSM extensions.

6.1. Analysis Framework

To assess the reach of four top production both within and beyond the Standard Model, a detailed collider-level study is performed. This section outlines the simulation setup, event selection criteria, and analysis methodology used to probe the relevant final states. The four top final states in consideration include same-sign dilepton production in association with b quarks and light jets,

$$pp \to t\bar{t}t\bar{t} \to \ell^{\pm}\ell^{\pm} + \text{jets} + b \text{ quarks}, \quad \text{(2SSDL)}, \tag{6.1a}$$

and three-lepton production in association with b and light flavour jets,

$$pp \to t\bar{t}t\bar{t} \to \ell^{\pm}\ell^{\pm}\ell^{\mp} + \text{jets} + b \text{ quarks}, \quad \text{(3L)}. \tag{6.1b}$$

where $\ell = e, \mu$, including leptonic decays of τ leptons (see [431, 433] for recent explorations by the ATLAS and CMS experiments).

6.1.1. Event simulation and fiducial selection

Datasets for the selected final state topologies are prepared preselecting the events generated from simulating pp collisions at $\sqrt{s} = 13$ TeV using `Madgraph5_aMC@NLO` [160] at leading order precision. These events are subsequently showered and hadronised using `Pythia8.3` [174]. The final states are reconstructed using `MadAnalysis` [175] that interfaces `FastJet` [176, 177].

Light leptons (e, μ) are defined from a threshold of $p_T > 10$ GeV within the detector coverage of the electromagnetic calorimeter $|\eta| < 2.5$, where p_T and η denote the transverse momentum and pseudorapidity, respectively. Selected b-tagged jets are identified from a threshold $p_T > 20$ GeV within the tracker $|\eta| < 2.5$. Light flavour jets that fall into the hadronic calorimeter coverage, $|\eta| < 4.5$, are required to have $p_T > 20$ GeV. Additionally, a significant amount of missing transverse energy of at least 20 GeV is required, considering the leptonic decays of the W bosons. To isolate the mismeasurement of missing transverse energy ($\vec{\not{E}}_T$) from jets, only the events with azimuthal angle difference $|\phi(j) - \phi(\vec{\not{E}}_T)| > 0.2$ are selected. The analysis for the two signal topologies 2SSDL and 3L closely follows ATLAS and CMS studies [431–436] (see also [452–454] for precision SM analyses informing experimental studies). The 2SSDL final state requires at least 2 leptons, at least two b jets and at least one additional jet selected according to the criteria outlined previously. The 3L topology requires at least three leptons, and at least two b jets, without any restriction on the light flavour jets. A pessimistic 70% flat b-tagging efficiency is employed throughout [455, 456]. This removes large contributions from misidentified b jets [456] for the considered p_T range of b jets; therefore, effects from misidentified b jets can be neglected.

Processes	cross-section (fb)
$pp \to t_{\ell^+}\bar{t}_h W^+_{\ell^+} + t_h\bar{t}_{l^-} W^-_{\ell^-}$	57.67 ± 0.06
$pp \to t_{\ell^+}\bar{t}_h Z_{\ell^+\ell^-} + t_h\bar{t}_{\ell^-} Z_{\ell^+\ell^-} + t_{\ell^+}\bar{t}_{\ell^-} Z_{\ell^+\ell^-}$	10.65 ± 0.01
$pp \to (W^+_{\ell^+} W^-_h W^+_{\ell^+} + W^+_h W^-_{\ell^-} W^-_{\ell^-}) b\bar{b}$	43.29 ± 0.05
$pp \to (W^+_{\ell^+} W^-_h Z_{\ell^+\ell^-} + W^+_h W^-_{\ell^-} Z_{\ell^+\ell^-} + W^+_{\ell^+} W^-_{\ell^-} Z_{\ell^+\ell^-}) b\bar{b}$	12.65 ± 0.02

Table 6.1.: Cross-sections (including the uncertainties) for the different SM processes having the most significant contributions to the 2SSDL background, in accordance with the baseline cuts. The subscript on each particle describes the particle's decay channel ($\ell^\pm$ describes leptonic decay and h refers to a hadronic decay channel).

Processes	cross-section (fb)
$pp \to t_{\ell^+}\bar{t}_{\ell^-}W^{\pm}_{\ell^\pm}$	3.421 ± 0.004
$pp \to t_{\ell^+}\bar{t}_h Z_{\ell^+\ell^-} + t_h\bar{t}_{\ell^-}Z_{\ell^+\ell^-} + t_{\ell^+}\bar{t}_{\ell^-}Z_{\ell^+\ell^-}$	10.65 ± 0.01
$pp \to Z_{\ell^+\ell^-}W^{\pm}_{\ell^\pm}b\bar{b}$	3.296 ± 0.003
$pp \to W^+_{\ell^+}W^-_{\ell^-}W^{\pm}_{\ell^\pm}b\bar{b}$	3.614 ± 0.004
$pp \to (W^+_{\ell^+}W^-_h Z_{\ell^+\ell^-} + W^+_h W^-_{\ell^-}Z_{\ell^+\ell^-} + W^+_{\ell^+}W^-_{\ell^-}Z_{\ell^+\ell^-})b\bar{b}$	12.65 ± 0.02

Table 6.2.: Summary of background cross-sections and Monte-Carlo uncertainties for the different SM processes contributing to the 3L selection, given the baseline cuts. The subscript on each particle denotes the decay channel as in Tab. 6.1.

With the defined fiducial regions, the dominant SM backgrounds contributing to these final states are:

1. The $t\bar{t}W^{\pm}$ channel with leptonic decays of the tops and W is the most dominant background for the 2SSDL case; however, its contributions are subdominant for the 3L channel.

2. Conversely, background contributions from $t\bar{t}Z$ are significant for the 3L case, while contamination of the 2SSDL signal region from this channel is reduced (yet substantial) compared to others.

3. $W^+W^-W^{\pm} + 2b$ -tagged jets, with subsequent decays $W \to \ell\nu_\ell$, is the second largest background for 2SSDL and remains a considerable background for the 3L selection.

4. $W^+W^-Z + 2b$ jets with leptonic decays of vector bosons contributes as a background for both channels, and yields the largest contamination in the 3L case.

5. $ZW^{\pm} + 2b$ jets is a subdominant background to both channels when both Z and W bosons decay leptonically. However, its contribution to 2SSDL is negligible and therefore dropped from Table 6.1.

The cross-sections after decay following the baseline selection criteria are shown in Tables 6.1 and 6.2 contributing to 2SSDL and 3L channels, respectively.

The dataset for the background class of the neural network setup is a combination of the individual background samples, weighed by their cross-sections, to obtain a realistic composition expected at a fixed luminosity. The representative kinematic distributions at the hadron level of the signal and the background classes are shown

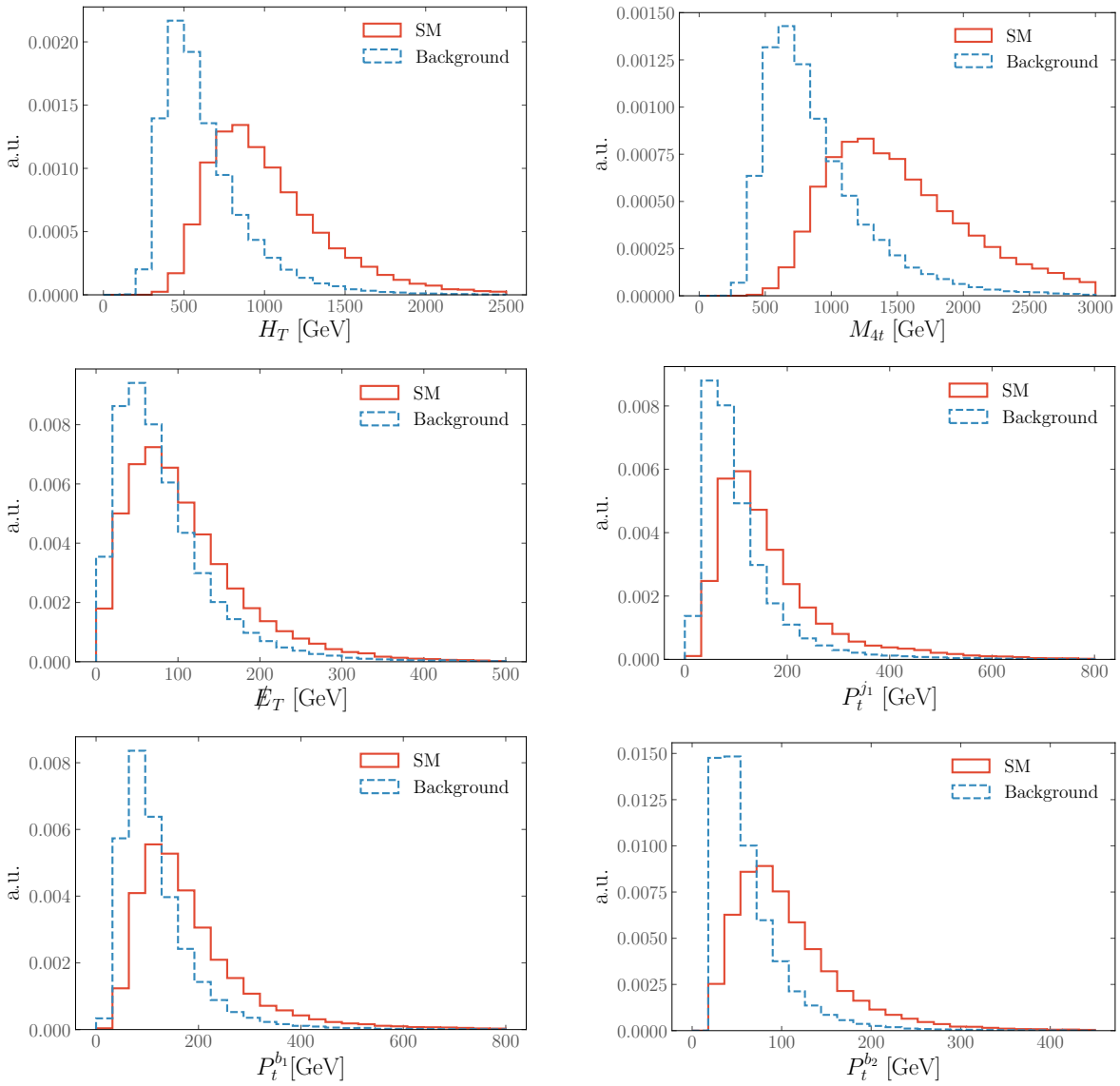

Figure 6.1.: Normalised distributions of the kinematic variables related to 2SSDL channel for SM four top signal and SM backgrounds contributing to the process at the LHC running at 13 TeV.

in Fig. 6.1. It is evident that H_T and M_{4t}* are the most discriminating observables, hardness-related observables can be expected to be the dominant drivers of signal vs. background discrimination. The variables H_T and M_{4t} are significantly correlated since both use energy-momentum information of the process, as shown in Fig. 6.2. The neural network can exploit such correlations (also extending to other observables, see Fig. 6.3) in a non-rectangular and optimised way, thus enabling efficient signal-

*M_{4t} is the total invariant mass of the visible final states, and H_T is the scalar p_T sum of all visible final states of the system.

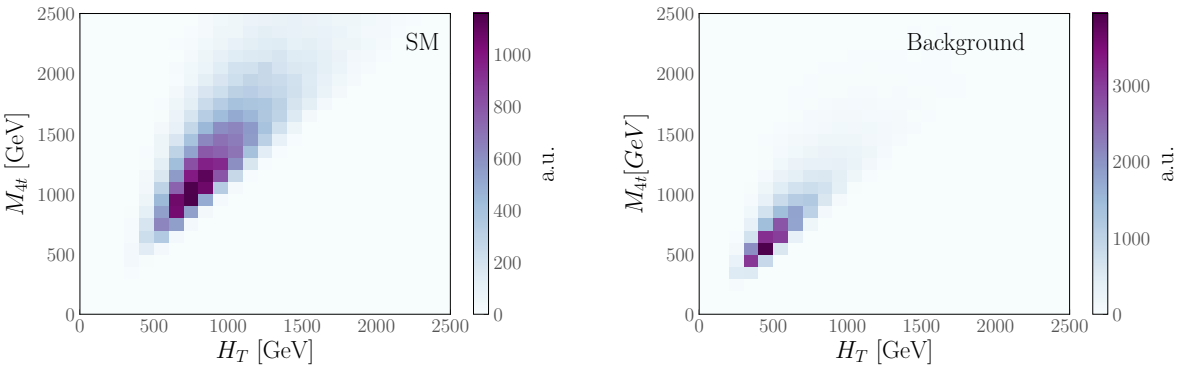

Figure 6.2.: Normalised two-dimensional distributions of the kinematic variables H_T and M_{4t} for 2SSDL channel for SM four tops signal and SM backgrounds contributing to the process at the LHC running at 13 TeV.

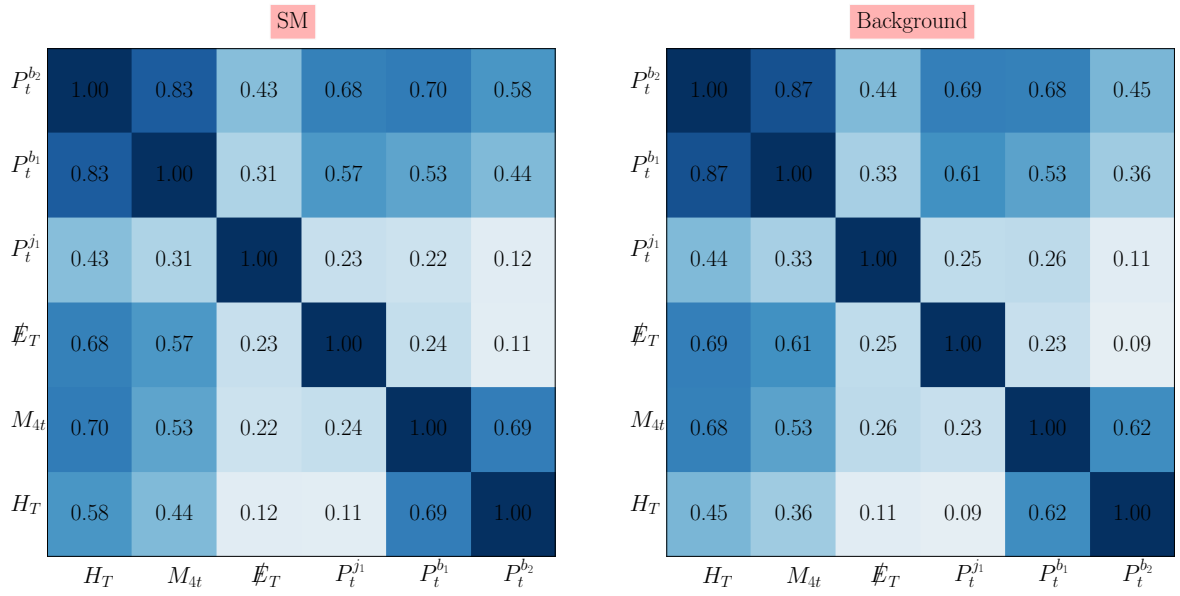

Figure 6.3.: Correlation plots for 2SSDL channel for SM four tops signal and SM backgrounds for different kinematic variables extending Fig. 6.2.

background discrimination. Machine-learned observables can therefore be expected to carry significant discriminating power in isolating (B)SM four top production.

6.1.2. Graph Neural Network Architecture and Data Representation

GNNs are ideal candidate architectures to perform signal-background discrimination tasks, given the complex final states that can be expected from four top topologies, in addition to the process-specific correlations. Applications of GNNs to particle physics

data have a short yet successful history. Their versatility in efficiently discriminating BSM data from the SM expectation beyond traditional observables in a robust way has been highlighted in a series of papers, ranging from designing anomaly detection methods [457–459], over jet tagging [456, 460] to constraining EFT operator deformations in the BSM top-sector fits [461].

Taking inspiration from this evolving success story, the four top signal is discriminated against the relevant SM background using a point-cloud-based GNN. The graph structure is implemented using the `Deep Graph Library` [462] package with the `PyTorch` [463] backend, using an edge-convolution (`EdgeConv`) message-passing network chosen to classify signal and background (with final state particle events interfaced employing `PyLHE` [464]).

The GNN can be divided into (i) message-passing, followed by (ii) node readout. Edge-convolution is known to be particularly suited for extracting internode information (edge) from the given low-level node features (i.e. particle-level properties, see below). The message passing function for the edge convolution is defined as

$$\vec{x}_i^{(l+1)} = \frac{1}{|\mathcal{N}(i)|} \sum_{j \in \mathcal{N}(i)} \texttt{ReLU}\left(\Theta \cdot (\vec{x}_j^{(l)} - \vec{x}_i^{(l)}) + \Phi \cdot (\vec{x}_i^{(l)})\right) . \tag{6.2}$$

Here, $\vec{x}_i^{(l)}$ represents the node features of node i in the l-th message-passing layer, with $l = 0$ denoting the input node features of the graph. The neighbourhood set $\mathcal{N}(i)$ consists of all nodes in the graph connected to node i. The linear layers Θ and Φ take the input vectors $(\vec{x}_j^{(l)} - \vec{x}_i^{(l)})$ and $\vec{x}_i^{(l)}$, respectively, and map them onto alternate dimension spaces where one applies an activation function on their vector sum. The dimensionality of the "hidden" feature space is chosen so that performance is optimised while avoiding overfitting. The GNN uses a fully-connected bidirectional graph as an input for the given signal vs. background discrimination task. Each particle is represented by a node, which is associated with a node feature vector $\vec{x}_i^{(0)} = [p_T, \eta, \phi, E, m, \text{PID}]$ (representing transverse momentum, pseudorapidity, azimuthal angle, energy, mass and particle identification number, respectively). The GNN architecture is inherently permutation-invariant under node reordering, reflecting the physical indistinguishability and lack of canonical ordering among final-state particles. This symmetry is particularly relevant for multi-object final states, where jet or lepton permutations do not carry physical meaning. After a fixed number of message-passing steps Eq. (6.2), a mean graph readout operation is employed on the node features of

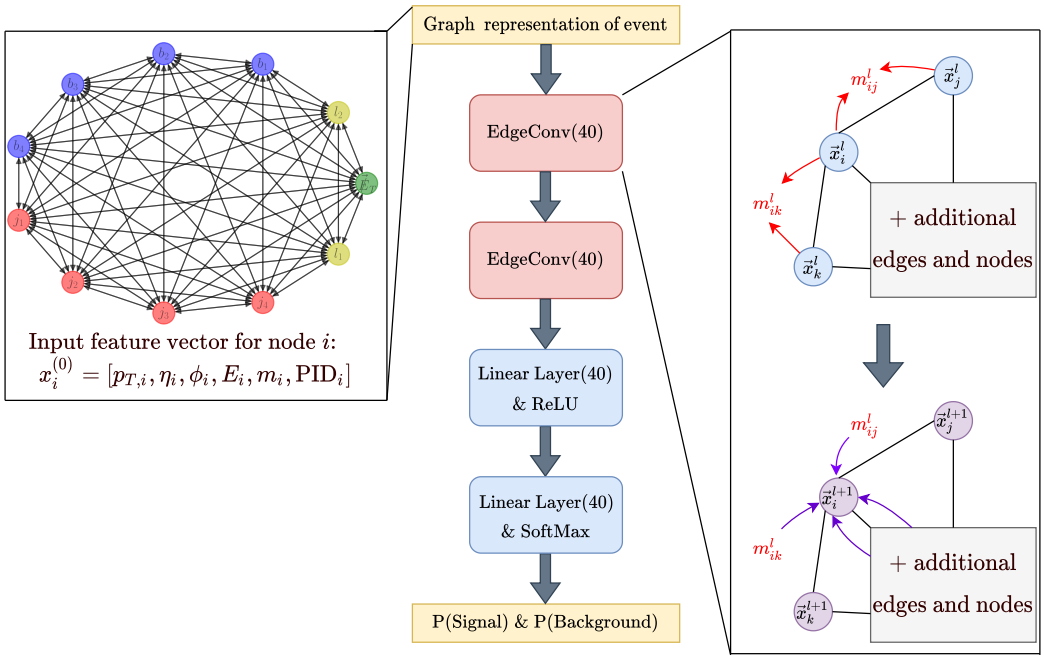

Figure 6.4.: The architecture of the utilised GNN that maps the events embedded into graphs to the probability that they were sourced by signal or background processes. On the left, an example of an input graph with different colours is shown, indicating the different final states that are included in the analysis. On the right the EdgeConv operation is indicated where during the first step (red arrows) the messages $m_{ij}^{(l)} = \mathtt{ReLU}\left(\Theta \cdot (\vec{x}_j^{(l)} - \vec{x}_i^{(l)}) + \Phi \cdot (\vec{x}_i^{(l)})\right)$ are calculated according to Eq. (6.2) and subsequently in the second step they are used to obtain the updated node features by taking the mean (purple arrows).

the final message-passing layer to extract a vector capturing the graph properties of each event. The graph representation obtained this way is then passed into a linear layer with a rectified linear unit ReLU activation function. The final linear layer maps the result to a two-dimensional vector, normalised by the SOFTMAX function, which computes the probability of an event arising from a signal or a background process.

The network is trained to minimise the *binary cross-entropy (BCE)* loss (L_{BCE}), a standard objective for binary classification tasks, defined as

$$L_{\mathrm{BCE}} = -\left[y \log p + (1-y)\log(1-p)\right], \tag{6.3}$$

where $y \in \{0,1\}$ is the true label and p is the predicted probability of the signal class. Optimisation is performed using the ADAM algorithm [465], starting with an initial *learning rate (LR)* of 0.001. The LR determines the step size at each iteration during gradient descent; larger values result in faster but potentially unstable training,

while smaller values ensure stable but slower convergence. The dataset is split into 75% training and 25% testing, with the training set further divided into a 75%-25% training-validation split. The LR is reduced by a factor of 10 if the validation loss does not improve for three consecutive epochs. Training is carried out for up to 100 epochs using mini-batches of 100 graphs, with early stopping triggered if the validation loss stagnates for ten epochs. The architecture consists of two edge-convolution layers followed by two linear layers with 40 hidden units each, as illustrated in Fig. 6.4. Training and validation performance are monitored throughout to avoid overfitting, which is particularly relevant for deeper networks.

A variety of ML algorithms have been explored in Ref. [442] to assess their efficiency for the four top processes, including the graph-based `ParticleNet` [466], also utilising the edge-convolution operation.[†] The authors of Ref. [442] demonstrate that `ParticleNet` does indeed provide superior performance in comparison with the alternative algorithms that are considered there. This analysis finds a qualitatively similar behaviour.

6.2. Results

6.2.1. Cornering the SM four tops at the LHC

The ATLAS and CMS collaborations have considerably explored the SM four top production. ATLAS currently observes four tops with a sensitivity of 1.9σ over the background-only hypothesis with a production cross-section of 26 fb [433]. CMS observes 2.6σ at a cross-section of 12.6 fb [431] in comparison.

The GNN performance for SM four top production is first analysed by exploring the sensitivity estimates given by the backgrounds described in Sec. 6.1. The network is first trained for the 2SSDL samples using the SM four top as the signal class and the corresponding backgrounds (listed in Table 6.1) as the background class, with a similar procedure followed for the 3L final state. The network performance is assessed using the receiver operating characteristic (ROC) curves of the network, which are shown in Fig. 6.5 for the two different final states under consideration. The areas under the

[†] `ParticleNet` uses the k-nearest-neighbours algorithm for the embedding of particles to graphs according to their separation $\Delta R = \sqrt{\Delta\eta^2 + \Delta\phi^2}$, while this analysis focused on fully-connected graphs.

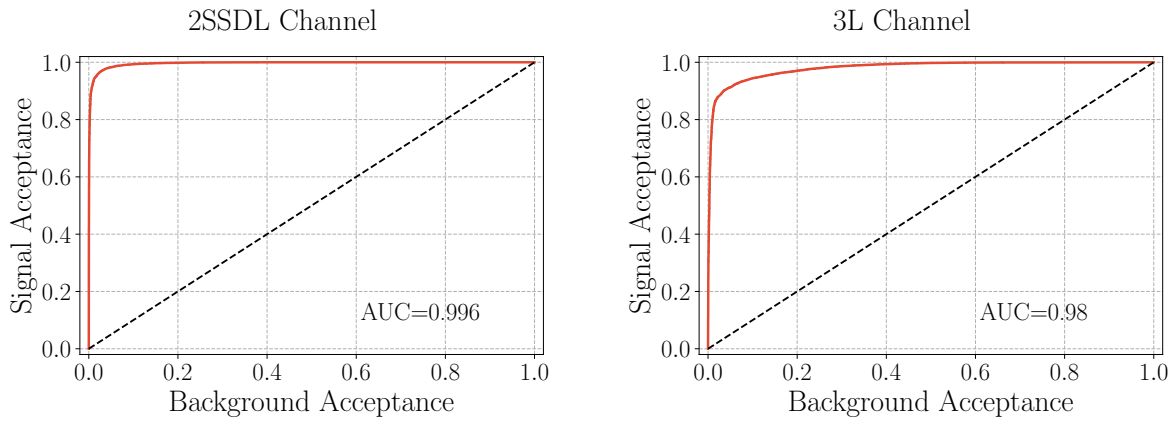

(a) (b)

Figure 6.5.: ROC curves for discriminating the SM four top quark signal in the (a) 2SSDL and (b) 3L final states.

curves (AUCs) of 0.994 for 2SSDL and 0.968 for 3L imply a very high classifier performance, as expected by the correlations of Figs. 6.1 and 6.2 (as well as the findings of Ref. [442]). With the GNN setup optimised, the sensitivity encoded in the ROC curve can be cast into exclusion limits by considering the significance $\sigma = N_s/\sqrt{N_s + N_b}$, where N_s is the number of signal events and N_b is the number of background events at a particular luminosity. The number of signal events N_s is given by $\sigma^s \times \varepsilon_{s(GNN)} \times L_{\text{int.}}$ and number of background events N_B is given by $\sigma^b \times \varepsilon_{b(GNN)} \times L_{\text{int.}}$, where $\sigma^{s/b}$ is the cross-section of signal/background after the baseline cuts, $L_{\text{int.}}$ is the integrated luminosity and $\varepsilon_{s/b(GNN)}$ are the efficiencies obtained at the best working point from the ROC curve such that the sensitivity $\sigma = N_s/\sqrt{N_s + N_b}$ is maximised. The impact of systematic uncertainties is also analysed considering 20% and 50% as benchmarks.

For the 2SSDL final state, the four top production cross-section can be measured at 4.4 fb with a systematic uncertainty of 50%, and 4.1 fb with a systematic uncertainty of 20%, at $L_{\text{int.}} = 139$ fb^{-1} with a significance of 2.7σ over the background-only hypothesis using the GNN. These findings indicate that the GNN selection could indeed provide an avenue to further hone the sensitivity in ATLAS and CMS by integrating these techniques into their analysis flow. For the 3L final state, the four top production cross-section can be measured at 18.6 fb with a systematic uncertainty of 50%, and 17.3 fb with a systematic uncertainty of 20%, at $L_{\text{int.}} = 139$ fb^{-1} with a 2σ significance over the background-only hypothesis using GNN, implying a similar potential improvement. The performance of the GNN in either channel reveals excel-

lent discriminating power for the busy multi-top states at the LHC, with prospects of significantly improving cross-section measurements.

6.2.2. Prospects in modified Higgs boson interactions

New physics modifications to four top final states from non-resonant interactions have been considered in a range of phenomenological studies [438, 439]. The so-called $\hat{H}$ parameter is an EFT-related example motivating a more comprehensive analysis of four top interactions from EFT perspectives [439, 461]; Ref. [440] emphasises the relevance of four top final states for associated searches (bounds have since been provided by CMS [431]).

The $\hat{H}$ parameter is the analogue of the $\hat{W}, \hat{Y}$ operators [467] of the gauge sector and can be understood as an oblique correction taking the form

$$\mathcal{L}_{\hat{H}} = \frac{\hat{H}}{m_h^2} |D_\mu D^\mu \Phi|^2 \,, \tag{6.4}$$

with D_μ being the usual covariant derivative acting on the Higgs doublet Φ.[‡] The presence of this interaction modifies the propagation of the physical Higgs boson (suppressing the Higgs width, since the Higgs boson is probed off-shell in four top production)

$$-i\Delta(p^2, m_h^2) = \frac{1}{p^2 - m_h^2} - \frac{\hat{H}}{m_h^2}, \tag{6.5}$$

with associated coupling modifications of the Higgs boson's couplings to massive vectors $V = W^\pm, Z$ and heavy fermions (here the top quark)

$$\frac{g^{\hat{H}}_{VVh}(p^2)}{g^{\text{SM}}_{VVh}} = 1 - \hat{H}\left(1 - \frac{p^2}{m_h^2}\right) \,, \quad \frac{g^{\hat{H}}_{t\bar{t}h}}{g^{\text{SM}}_{t\bar{t}h}} = 1 - \hat{H} \,, \tag{6.6}$$

[‡]It is worthwhile mentioning that the modification of the propagator probes a genuine direction of Higgs Effective Field Theory (HEFT), that can be radiatively sourced in the κ-framework [85], see e.g. [142, 225]. The associated coupling modifications can then be understood as a probe of the linearity of the Higgs boson's interactions in the SM and its dimension-6 extension [119].

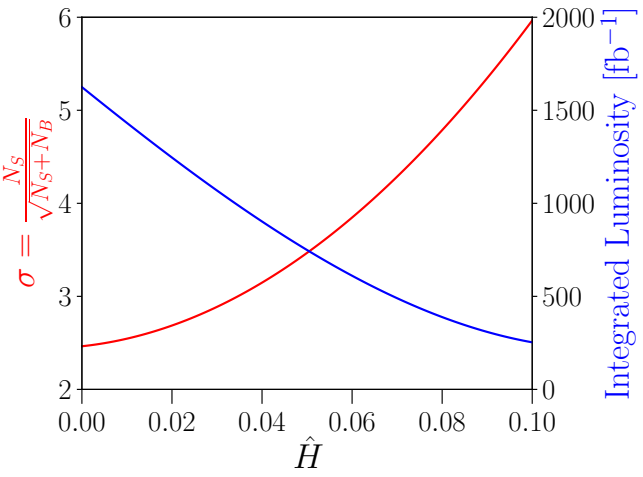

Figure 6.6.: Significance as a function of $\hat{H}$ at 13 TeV LHC with a 1000 fb^{-1} integrated luminosity (red curve). The required luminosity as a 3σ confidence level for different $\hat{H}$ values is also presented (blue curve).

for canonically normalised fields. The correlation of HVV interactions and H propagator resulting in a cancellation is a consequence of gauge symmetry [440]

$$g^{\hat{H}}_{VVh}\,\Delta(p^2, m_h^2) = g^{\text{SM}}_{VVh}\,\Delta^{\text{SM}}_{\hat{H}=0}(p^2, m_h^2) + \mathcal{O}(\hat{H}^2)\,, \tag{6.7}$$

which highlights multi-top final states as particularly suitable process to put constraints on the interaction of Eq. (6.4) beyond Higgs coupling measurements.

The effects of $\hat{H}$ are gauged by modifying the `Helas` [424] routines of the $pp \to t\bar{t}t\bar{t}$ implementation, to reflect the modifications of propagators, vertices and their cancellation to linear order in the amplitude. As a benchmark for non-resonant new interactions, $\hat{H}$ is set to a value of 0.1 as a new physics modification (this value is motivated by the HL-LHC measurement sensitivity provided in Ref. [440]). A SM-rich sample is selected by applying a cut on $H_T > 900$ GeV to enable a coupling measurement that is more geared to SM modifications, see Fig. 6.1. The GNN is then trained to discriminate between SM interaction with $\hat{H} = 0$ from the non-resonant new interaction with $\hat{H} = 0.1$. The kinematical differences are not dramatic (which is highlighted by the $\sim$10% sensitivity in the first place), and therefore further motivate the inclusion of as much correlated information as possible achievable through GNN applications.

An AUC of 60% is testimony to the difficulty of extracting electroweak properties from QCD-busy final states. The observed sensitivity can be used to set limits for

in the parameter range $\hat{H} \in [0.0, 0.10]$ shown in Fig. 6.6. The blue curve shows the luminosity required to obtain the 3σ bound on that particular $\hat{H}$ value, while the red curve shows the significance obtained at a fixed luminosity $L = 1000\ \text{fb}^{-1}$. The GNN analysis again gives rise to an expected sensitivity improvement beyond the estimates of cut-and-count analyses [431, 440]. While the realistic analysis in the LHC environment is likely more limited in sensitivity, the addition of the GNN techniques described above could significantly improve the sensitivity to $\hat{H}$, which also indicates an improved sensitivity to generic EFT deformations.

6.2.3. Interference from resonant interactions and 2HDM reach

Four top final states in the context of resonant extensions of the SM have been studied in a range of analyses [468–476], typically relying on traditional collider observables alongside cut-and-count strategies. Whilst new resonant structures lend themselves to such approaches, a significant sensitivity enhancement can also be expected when turning to ML approaches (see also [477–482]).

A qualitative analysis of the interference effects that are known to be large in direct gluon-fusion production $gg \to t\bar{t}$ of extra scalar resonances [443, 444] is essential before a GNN analysis. Such interference effects can severely limit the sensitivity estimates and are not straightforward to include in ML-based selections due to negative weights. To this end, one can consider a simplified scalar resonance S with Higgs-like couplings to the top quark[§]

$$\mathcal{L}_{\text{simp}} = \frac{1}{2}(\partial S)^2 - \frac{M_S^2}{2}S^2 - \frac{m_t}{v}\left[\xi_S\, \bar{t}_L t_R S + \text{h.c.}\right] , \tag{6.8}$$

keeping the width of S as a free parameter in a scan to qualitatively assess S resonance-distortion (ξ_S plays the role of the Higgs coupling modifier for $S = H$). The resonance structures stemming from the new-physics-only (resonance) interactions are compared to assess the relevant interference effects,

$$\mathrm{d}\sigma^{\text{new}} \sim |\mathcal{M}_{\text{res}}|^2\ \mathrm{dLIPS}, \tag{6.9}$$

[§]The phenomenological Lagrangian is implemented with `FeynRules` [64] and exported into the `Ufo` [273] format. The same toolchain with the addition of `MadSpin` [483, 484] is used.

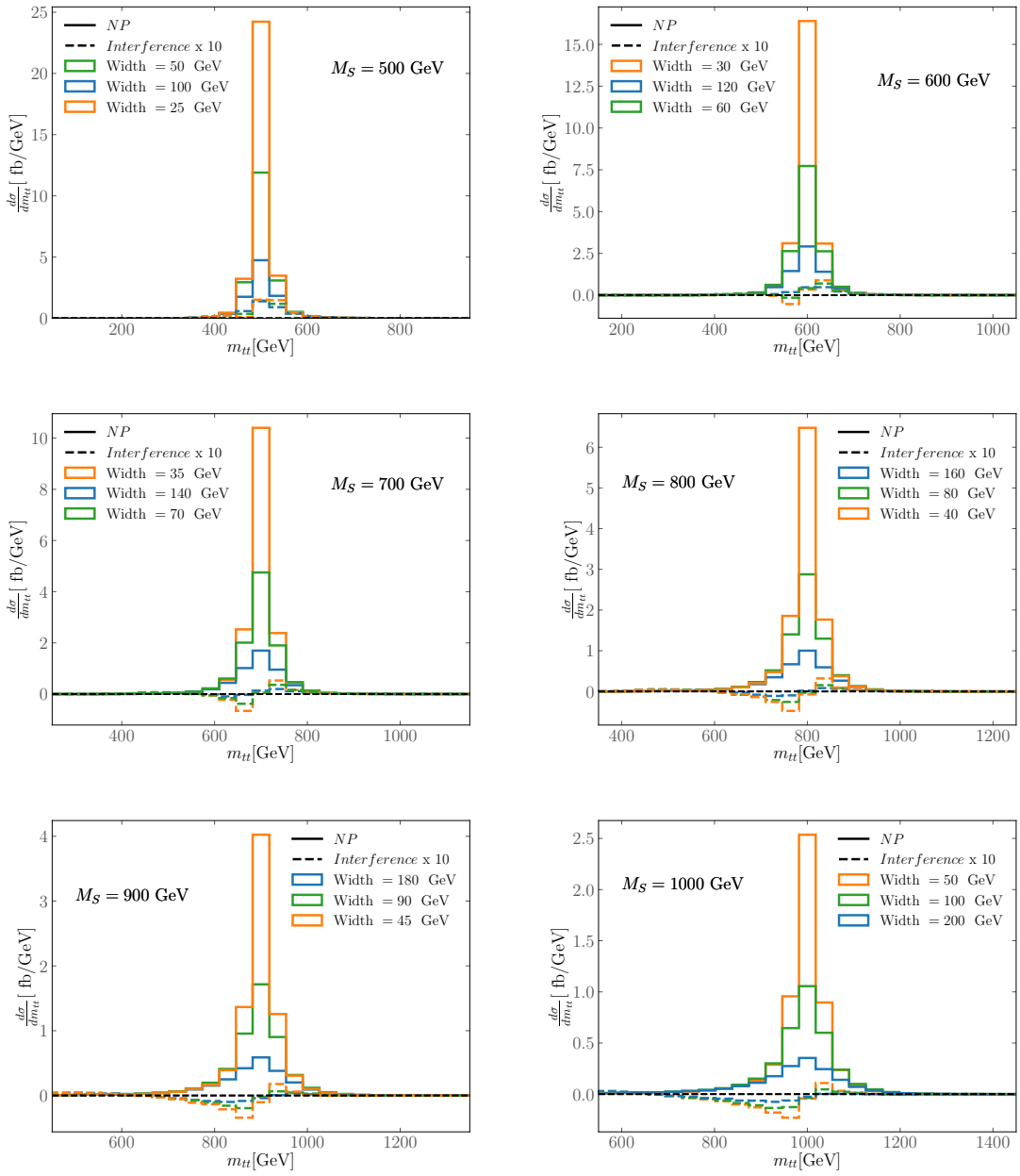

Figure 6.7.: The invariant mass distribution of m_{tt} system closest to the mass of the new scalar S as detailed in the text.

with interference-only contributions

$$d\sigma^{\text{inf}} \sim 2\,\text{Re}\left(\mathcal{M}_{\text{bkg}}\,\mathcal{M}^{*}_{\text{res}}\right) d\text{LIPS}\,, \tag{6.10}$$

where 'bkg' refers to any non-resonant amplitude contribution (e.g. the continuum QCD background). A good qualitative understanding of the signal distribution distor-

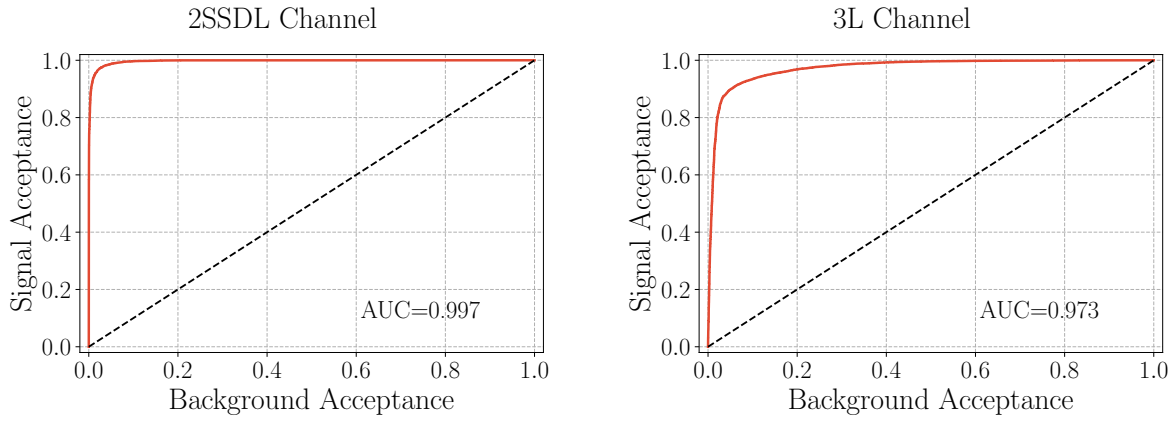

(a) (b)

Figure 6.8.: ROC curves for training a four top quark signal for a BSM CP-even scalar with $M_S = 600$ GeV for (a) 2SSDL and (b) 3L final states.

M_S [GeV]	significance for 2SSDL	significance for 3L
500	10.6σ	1.4σ
600	9.9σ	1.3σ
700	8.4σ	1.1σ
800	6.9σ	0.9σ
900	5.5σ	0.7σ
1000	4.3σ	0.5σ

Table 6.3.: Significances for different masses M_S for a coupling choice $\xi_S = 1$ and $\Gamma_S/M_S = 0.1$, Eq. (6.8). The luminosity is taken to be 3000 fb^{-1} for 13 TeV LHC collisions.

tion can be obtained by isolating the peaked $m_{t\bar{t}}$ distribution: all possible combinations of $m_{t\bar{t}}$ are constructed, and the invariant mass which is closest to the candidate mass M_S is chosen. The resulting distributions are shown in Fig. 6.7 for a range of masses $M_S = [500, 600, 700, 800, 1000]$ GeV and width choices $\Gamma_S/M_S = 5\%, 10\%, 20\%$ for $\xi_S = 1$.

The interference effects that distort the mass peak are comparably small, as illustrated in Fig. 6.7. More sensitivity-limiting distortions can be encountered closer to the decoupling limit $\xi_S \to 0$; however, this will happen at quickly vanishing BSM resonance cross-sections, so that a (ML-assisted) bump-hunt will not provide any sensitivity when considering the backgrounds. In the case of imaginary phases of ξ_S, i.e. CP-odd coupling structures, the interference effects will be qualitatively similar, see [445] (they can also vanish in processes when interference with CP-even back-

grounds removes such effects [479]). Having identified interference effects as largely irrelevant, the network is trained for the same two final states, this time with the added new interactions (i.e., the newly added CP-even scalar with $\xi_S = 1$) for the different benchmark points listed in Table 6.3. The ROC curves for one such benchmark point ($M_S = 600$ GeV) for both the final states and their corresponding AUCs are shown in Fig. 6.8. The corresponding significance for each benchmark point for the different decay channels is also listed in Table 6.3 for $\xi_S = 1$ and $\Gamma_S/M_S = 0.1$. These limits are interpreted as bounds on the coupling modifier ξ_S as shown in Fig. 6.9.

Although the 2SSDL predominantly can constrain $\xi_S < 1$ region, the resulting bounds are relatively weak. For instance, in singlet mixing scenarios, the parameter range that this analysis is sensitive to is already highly constrained from Higgs signal strength measurements. The next logical step is turning to phenomenologically richer scenarios like the 2HDM of type II, which features new neutral CP-odd and CP-even states. In this model, the Higgs sector consists of two distinct complex doublets, both with a non-zero vacuum expectation value (vev). One of these doublets couples to the up-type quarks and the other to down-type quarks and leptons in the type II model, thereby leading to fermion mass terms. After electroweak symmetry breaking, one is left with 5 Higgs bosons; 4 of which are CP even: h, H and $H^{\pm}$, and a CP odd particle, A. The lighter of the two neutral CP even states is identified as the observed Higgs boson. The phenomenology of this model then depends on the masses of the new Higgs bosons, the ratio of the two vevs, defined as $\tan\beta = v_2/v_1$ and $\cos(\beta - \alpha)$,

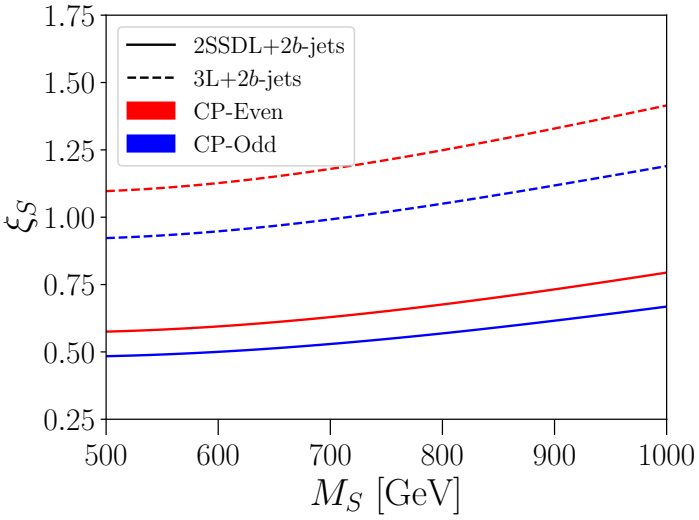

Figure 6.9.: 2σ confidence level limits on scalar mass with respect to CP-even and CP-odd couplings for 3000 fb^{-1} for 13 TeV LHC collisions.

where α is the mixing angle between the two neutral CP even states. The simplified Lagrangian of Eq. (6.8) can be mapped onto the 2HDM type II Yukawa sector

$$\mathcal{L}_{\text{2HDM}} \supset -\frac{m_t}{v}\left(\xi_h\,\bar{t}th + \xi_H\,\bar{t}tH - i\xi_A\,\bar{t}\gamma^5 tA\right)\,, \tag{6.11}$$

where charged Higgs contributions and non-top interactions have been suppressed. For the 2HDM type-II, the coupling modifiers related to the top quark are

$$\xi_h = \sin(\beta-\alpha) + \cos(\beta-\alpha)\cot\beta\,, \tag{6.12a}$$
$$\xi_H = \cos(\beta-\alpha) - \sin(\beta-\alpha)\cot\beta\,, \tag{6.12b}$$
$$\xi_A = \cot\beta\,. \tag{6.12c}$$

As discussed in Chapter 3, the 2HDM is a particularly well-motivated BSM model, as it is, in principle, capable of resolving a number of tensions between current experimental values and SM predictions, as well as opening avenues to satisfy the Sakharov criteria for required baryogenesis [32], therefore well studied in the literature [243–245, 485–490]. This model can therefore explore the validity of the benchmark points examined above. In order to satisfy the theoretical considerations, the masses of the new particles are set to be entirely degenerate. Similarly, to fall in line with the signal strength data of the SM Higgs, $\cos(\beta-\alpha)$ is set to 0; the alignment limit which recovers exactly the SM phenomenology of h.

The `2HDecay` [148, 204, 491–494] and `HiggsBounds` [251, 495–500] packages are used to examine the mass range of the above benchmark points in the face of the collider searches for additional Higgs bosons. Additionally, the LHC search data is extrapolated to 3000 fb^{-1} at 13 TeV. Performing a scan over 20000 random points, the results of this analysis are shown in Fig. 6.10, with points in blue allowed by current and extrapolated data, while orange points are allowed only by the current data. The improvement in sensitivity is led by searches for the decays $H^+ \to t\bar{b}$ and $H^0 \to \tau^+\tau^-$ [501, 502]. This shows that a large swathe of the parameter space taken for benchmark points in the above analysis is possible within the framework of the 2HDM of type II.

Given that four top final states are far less abundant than other processes, they can be expected to exhibit a reduced sensitivity to new states (this is already visible from Fig. 6.9). Nonetheless, repeating the above analysis also including the CP odd state, a complementary sensitivity can be achieved for the 2HDM scenario with the GNN-assisted resonance search detailed above: Overlaying the constraints found from

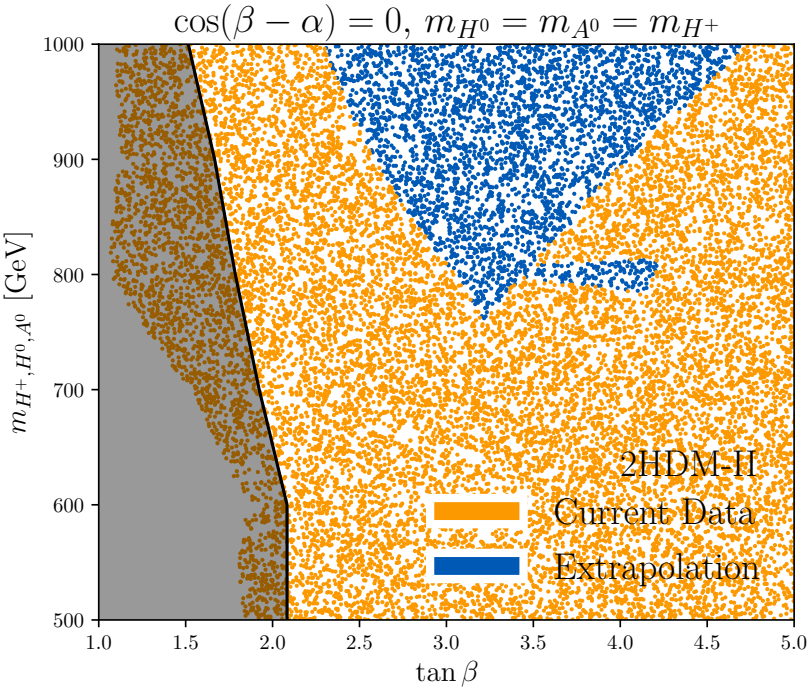

Figure 6.10.: Scan of the parameter space of the type II 2HDM in the face of current collider data, and LHC search data extrapolated to 3000 fb^{-1} at 13 TeV, with a 2σ confidence level exclusion contour from 2SSDL final states. Points in blue are allowed by current and expected future datasets, and orange points are allowed by current data only. The shaded area gives the sensitivity of the 2SSDL resonance search detailed in the text at 3000 fb^{-1}. Interference effects from $gg \to t\bar{t}$ sensitivity estimates are not included.

2SSDL final states (shaded area), there is a non-trivial parameter range of the 2HDM type II's alignment limit that can be accessed four top final states at 2σ confidence and 3000 fb^{-1}. This example contains only the more sensitive channel; additional final states are likely to improve this result further.

6.3. Conclusions

The growing sensitivity to four top final states at the LHC bears great potential for BSM physics. While the complexity of the final states requires a dedicated search strategy compared to lower multiplicity processes, the plethora of kinematic information that can be accessed in these processes to highlight departures from the SM can be formidably exploited by means of adapted search strategies, e.g. building on ML approaches. These not only provide support in establishing sensitivity to SM four

top production as shown in Sec. 6.2.1 (see also [442]), but they become particularly relevant when four top final states will be scrutinised from a BSM perspective in the future. Significant sensitivity to well-motivated representative non-resonant physics can be achieved (Sec. 6.2.2), but also that sensitivity to resonances is gained by turning to GNNs (Sec. 6.2.3). The GNN exploits the hierarchical graph structure of particle physics events that is particularly accentuated when dealing with new resonances. In this case, the four top final states can also fill a potential sensitivity gap in s-channel gluon fusion production of top-philic states $gg \to t\bar{t}$ that results from destructive signal-background interference, distorting or removing the resonance structure. The dominant partonic channels of four top final states show no such behaviour and therefore remain robust processes even when interference removes sensitivity in top pair gluon fusion production. In particular, this can add complementary sensitivity to BSM searches for (but not limited to) two Higgs doublet models, as shown in a representative parameter scan for the 2HDM type II.

Chapter 7.

Summary and Outlook

*"Future colliders are **not** just a wild punt for BSM, the wealth of information they provide about the most fundamental quantum processes we can directly access experimentally make colliders a unique, irreplaceable, and crucial instrument for the job of fundamental physics: **to better understand our universe**. Particle physics must be reframed in same way as astro/cosmo: **about doing good science.**"*

— Dr. Tevong You, WIN 2025.

So, the thesis reaches its end, a stopping point that is also a beginning. The Standard Model remains one of the most elegant and predictive frameworks in science, yet its neatness continues to be haunted by what it leaves out. A decade after the Higgs discovery, the LHC has produced a vast trove of data, much of which stubbornly confirms SM expectations. Still, a handful of anomalies and unexplained features keep the hope alive that something new might be just around the corner. This work has taken a few steps in that direction, combining model-building, precision studies, and machine learning tools to better understand what the SM might be hiding.

The journey began by returning to fundamentals. Chapter 2 laid out the complete SM Lagrangian, not just for completeness but to highlight the theory's internal consistency and its remarkable ability to predict observables in Higgs and flavour physics. At the same time, the chapter made the limitations clear and introduced a set of approaches to extend the SM, from explicit models to effective field theory.

Chapter 3 explored how multi-Higgs production channels provide a sensitive handle on scalar-sector extensions. Using coupling modifiers, patterns in weak-boson-fusion Higgs pair production were traced across renormalisable and composite Higgs scenarios. Gluon-fusion triple-Higgs production was shown to be sensitive to the strength of a first-order electroweak phase transition, offering a collider link to the thermal history of the early Universe.

In Chapter 4, the focus shifted to the Type-II seesaw mechanism as a solution to neutrino mass generation. LHC bounds from multilepton signatures were placed in tension with limits from charged lepton flavour violation. That tension was resolved by embedding the scalar triplet in a dimension-6 effective field theory, enabling viable phenomenology within the sensitivity reach of the HL-LHC.

Chapter 5 examined how finite-width effects, often neglected in collider analyses, can subtly shift the top-quark invariant mass lineshape. A consistent treatment of momentum-dependent widths for the Higgs, W, and top fields was implemented, and new physics deviations for the top quark lineshape were parameterised using SMEFT. The constraints obtained on the parameter space were found to be competitive with current global fits, and projections at future muon colliders indicated that this approach will remain a pseudo, yet powerful methodology in the high-energy regime.

Chapter 6 brought the thesis into the machine-learning domain. A graph neural network classifier was trained to isolate four-top events in same-sign dilepton and trilepton channels. These final states, rich in kinematic complexity, benefited from the ability of GNNs to capture correlations between multiple final-state objects. The trained classifier produced improved sensitivity to both nonresonant and resonant BSM scenarios, underscoring the importance of ML techniques in modern collider analyses.

A common thread runs through these studies: the search for new physics is increasingly guided by precision and complementarity. Whether through probing complex and previously less-accessible final states, targeting heavier exotic resonances, detecting minute deviations in precision observables, or deploying machine-learning techniques to enhance collider sensitivity, each approach seeks to expose subtle departures from SM expectations. The tools developed in this thesis aim not only to sharpen constraints on BSM scenarios, but also to ensure that emerging signals are recognised and not dismissed as background fluctuations or modelling artefacts.

The path ahead is far from straightforward, but it is clearly charted. The HL-LHC will push both detector performance and theoretical predictions to their limits. Future lepton colliders promise pristine conditions for precision studies of the Higgs boson and top quark, while a next-generation hadron collider would extend the kinematic reach dramatically. The methods developed in this thesis are designed to meet the demands of these environments and are adaptable to the evolving experimental landscape.

Ultimately, the Standard Model should be viewed not as a final answer, but as a foundation. As precision continues to tighten the noose around possible deviations, even the smallest anomaly may carry profound implications. Whether the first confirmed sign of new physics appears in a distorted invariant-mass spectrum, a displaced vertex, an unexpected multi-Higgs signature, or an excess of four-top events, the tools and strategies assembled here aim to be ready when that signal finally emerges.

Appendix A.

Passarino–Veltman Functions

In the evaluation of loop amplitudes it is convenient to reduce all tensor integrals to a set of standard scalar integrals, known as the Passarino–Veltman (PV) functions [206]. In dimensional regularisation with $d = 4 - 2\epsilon$, and introducing the renormalisation scale μ, the basic scalar integrals are defined as follows:*

One-point function

$$A_0(m^2) \;=\; \frac{(2\pi\mu)^{4-d}}{i\pi^2} \int d^d k \, \frac{1}{k^2 - m^2 + i0} \,. \tag{A.1}$$

Two-point function

$$B_0(p^2; m_1^2, m_2^2) \;=\; \frac{(2\pi\mu)^{4-d}}{i\pi^2} \int d^d k \, \frac{1}{\left(k^2 - m_1^2 + i0\right)\left((k+p)^2 - m_2^2 + i0\right)} \,. \tag{A.2}$$

Three-point function

$$C_0(p_1^2, p_2^2, (p_1+p_2)^2; m_1^2, m_2^2, m_3^2) \;=\; \frac{(2\pi\mu)^{4-d}}{i\pi^2} \int d^d k \, \frac{1}{D_1 \, D_2 \, D_3} \,, \tag{A.3}$$

*Following the conventions of `LoopTools` [148].

with the denominators D_i defined as,

$$\begin{aligned} D_1 &= k^2 - m_1^2 + i0, \\ D_2 &= (k+p_1)^2 - m_2^2 + i0, \\ D_3 &= (k+p_1+p_2)^2 - m_3^2 + i0. \end{aligned} \tag{A.4}$$

Four-point function

$$D_0(p_1, p_2, p_3; m_1^2, m_2^2, m_3^2, m_4^2) \;=\; \frac{(2\pi\mu)^{4-d}}{i\pi^2} \int d^d k \, \frac{1}{D_1 \, D_2 \, D_3 \, D_4}\,, \tag{A.5}$$

where the denominators D_i are defined as

$$\begin{aligned} D_1 &= k^2 - m_1^2 + i0, \\ D_2 &= (k+p_1)^2 - m_2^2 + i0, \\ D_3 &= (k+p_1+p_2)^2 - m_3^2 + i0, \\ D_4 &= (k+p_1+p_2+p_3)^2 - m_4^2 + i0. \end{aligned} \tag{A.6}$$

Tensor integrals

Tensor integrals with loop momenta in the numerator are reduced to linear combinations of scalar functions with external momenta as coefficients. For example,

$$\int \frac{d^d k}{i\pi^{d/2}} \frac{k^\mu}{D_1 D_2} \;=\; p^\mu \, B_1(p^2; m_1^2, m_2^2), \tag{A.7}$$

$$\int \frac{d^d k}{i\pi^{d/2}} \frac{k^\mu k^\nu}{D_1 D_2} \;=\; g^{\mu\nu} \, B_{00}(p^2; m_1^2, m_2^2) + p^\mu p^\nu \, B_{11}(p^2; m_1^2, m_2^2), \tag{A.8}$$

and analogously for higher-point integrals. The coefficients $B_1, B_{00}, \ldots$ are expressed algebraically in terms of A_0 and B_0.

In practical calculations, these integrals are evaluated numerically using dedicated libraries, but the definitions above fix the conventions and normalisations employed throughout this thesis.

Bibliography

[1] C. Englert, W. Naskar and D. Sutherland, *BSM patterns in scalar-sector coupling modifiers*, *JHEP* **11** (2023) 158 [2307.14809].

[2] L. Biermann, C. Borschensky, C. Englert, M. Mühlleitner and W. Naskar, *Double and triple Higgs boson production to probe the electroweak phase transition*, *Phys. Rev. D* **110** (2024) 095012 [2408.08043].

[3] U. Banerjee, C. Englert and W. Naskar, *Resurrecting the LHC discovery potential in the extended type-II seesaw model*, *Phys. Rev. D* **110** (2024) 055010 [2403.17455].

[4] C. Englert, W. Naskar and M. Spannowsky, *Impact of new physics on momentum-dependent particle widths and propagators*, *Phys. Rev. D* **111** (2025) 055017 [2501.08407].

[5] Anisha, O. Atkinson, A. Bhardwaj, C. Englert, W. Naskar and P. Stylianou, *BSM reach of four-top production at the LHC*, *Phys. Rev. D* **108** (2023) 035001 [2302.08281].

[6] U. Banerjee, J. Chakrabortty, C. Englert, W. Naskar, S.U. Rahaman and M. Spannowsky, *EFT, decoupling, Higgs boson mixing, and higher dimensional operators*, *Phys. Rev. D* **109** (2024) 055035 [2303.05224].

[7] A. Bhardwaj, C. Englert, W. Naskar, V.S. Ngairangbam and M. Spannowsky, *Equivariant, safe and sensitive — graph networks for new physics*, *JHEP* **07** (2024) 245 [2402.12449].

[8] C. Englert, C. Mayer, W. Naskar and S. Renner, *Doubling down on down-type diquarks*, *JHEP* **03** (2025) 011 [2410.00952].

[9] B. Allanach, C. Englert and W. Naskar, *A $B-$anomaly motivated Z' boson at the energy and precision frontiers*, 2503.21319.

[10] ATLAS collaboration, *Observation of a new particle in the search for the Standard*

Model Higgs boson with the ATLAS detector at the LHC, Phys. Lett. B **716** (2012) 1 [1207.7214].

[11] CMS collaboration, *Observation of a New Boson at a Mass of 125 GeV with the CMS Experiment at the LHC*, Phys. Lett. B **716** (2012) 30 [1207.7235].

[12] S. Weinberg, *Nonabelian Gauge Theories of the Strong Interactions*, Phys. Rev. Lett. **31** (1973) 494.

[13] H. Fritzsch, M. Gell-Mann and H. Leutwyler, *Advantages of the Color Octet Gluon Picture*, Phys. Lett. B **47** (1973) 365.

[14] W.A. Bardeen, H. Fritzsch and M. Gell-Mann, *Light cone current algebra, π^0 decay, and e^+e^- annihilation*, in *Topical Meeting on the Outlook for Broken Conformal Symmetry in Elementary Particle Physics*, 7, 1972 [hep-ph/0211388].

[15] S.L. Glashow, *Partial Symmetries of Weak Interactions*, Nucl. Phys. **22** (1961) 579.

[16] S. Weinberg, *A Model of Leptons*, Phys. Rev. Lett. **19** (1967) 1264.

[17] A. Salam, *Weak and Electromagnetic Interactions*, Conf. Proc. C **680519** (1968) 367.

[18] C.-N. Yang and R.L. Mills, *Conservation of Isotopic Spin and Isotopic Gauge Invariance*, Phys. Rev. **96** (1954) 191.

[19] P.W. Higgs, *Broken symmetries, massless particles and gauge fields*, Phys. Lett. **12** (1964) 132.

[20] F. Englert and R. Brout, *Broken Symmetry and the Mass of Gauge Vector Mesons*, Phys. Rev. Lett. **13** (1964) 321.

[21] G.S. Guralnik, C.R. Hagen and T.W.B. Kibble, *Global Conservation Laws and Massless Particles*, Phys. Rev. Lett. **13** (1964) 585.

[22] G. 't Hooft, *Renormalizable Lagrangians for Massive Yang-Mills Fields*, Nucl. Phys. B **35** (1971) 167.

[23] C. Bouchiat, J. Iliopoulos and P. Meyer, *An Anomaly Free Version of Weinberg's Model*, Phys. Lett. B **38** (1972) 519.

[24] H.E. Logan, *Lectures on perturbative unitarity and decoupling in Higgs physics*, 2207.01064.

[25] ALEPH, DELPHI, L3, OPAL, SLD, LEP ELECTROWEAK WORKING GROUP,

SLD ELECTROWEAK GROUP, SLD HEAVY FLAVOUR GROUP collaboration, *Precision electroweak measurements on the Z resonance*, *Phys. Rept.* **427** (2006) 257 [hep-ex/0509008].

[26] L. Susskind, *THE GAUGE HIERARCHY PROBLEM, TECHNICOLOR, SUPERSYMMETRY, AND ALL THAT.*, *Phys. Rept.* **104** (1984) 181.

[27] G. 't Hooft, *Naturalness, chiral symmetry, and spontaneous chiral symmetry breaking*, *NATO Sci. Ser. B* **59** (1980) 135.

[28] SNO collaboration, *Direct evidence for neutrino flavor transformation from neutral-current interactions in SNO*, *AIP Conf. Proc.* **646** (2002) 43.

[29] SUPER-KAMIOKANDE collaboration, *Evidence for oscillation of atmospheric neutrinos*, *Phys. Rev. Lett.* **81** (1998) 1562 [hep-ex/9807003].

[30] PLANCK collaboration, *Planck 2018 results. VI. Cosmological parameters*, *Astron. Astrophys.* **641** (2020) A6 [1807.06209].

[31] R.D. Peccei and H.R. Quinn, *CP Conservation in the Presence of Instantons*, *Phys. Rev. Lett.* **38** (1977) 1440.

[32] A.D. Sakharov, *Violation of CP Invariance, C asymmetry, and baryon asymmetry of the universe*, *Pisma Zh. Eksp. Teor. Fiz.* **5** (1967) 32.

[33] M. Bohm, A. Denner and H. Joos, *Gauge theories of the strong and electroweak interaction* (2001), 10.1007/978-3-322-80160-9.

[34] M.E. Peskin and D.V. Schroeder, *An Introduction to quantum field theory*, Addison-Wesley, Reading, USA (1995), 10.1201/9780429503559.

[35] M.D. Schwartz, *Quantum Field Theory and the Standard Model*, Cambridge University Press (3, 2014).

[36] H. Weyl, *Electron and Gravitation. 1. (In German)*, *Z. Phys.* **56** (1929) 330.

[37] L.D. Faddeev and V.N. Popov, *Feynman Diagrams for the Yang-Mills Field*, *Phys. Lett. B* **25** (1967) 29.

[38] J.C. Ward, *An Identity in Quantum Electrodynamics*, *Phys. Rev.* **78** (1950) 182.

[39] Y. Takahashi, *On the generalized Ward identity*, *Nuovo Cim.* **6** (1957) 371.

[40] H.A. Bethe, *The Electromagnetic shift of energy levels*, *Phys. Rev.* **72** (1947) 339.

[41] D. Hanneke, S. Fogwell and G. Gabrielse, *New Measurement of the Electron Magnetic Moment and the Fine Structure Constant*, *Phys. Rev. Lett.* **100** (2008) 120801 [0801.1134].

[42] D.J. Gross and F. Wilczek, *Ultraviolet Behavior of Nonabelian Gauge Theories*, *Phys. Rev. Lett.* **30** (1973) 1343.

[43] H.D. Politzer, *Reliable Perturbative Results for Strong Interactions?*, *Phys. Rev. Lett.* **30** (1973) 1346.

[44] K.G. Wilson, *Confinement of Quarks*, *Phys. Rev. D* **10** (1974) 2445.

[45] P. Minkowski, $\mu \to e\gamma$ *at a Rate of One Out of* 10^9 *Muon Decays?*, *Phys. Lett. B* **67** (1977) 421.

[46] S. Weinberg, *Baryon and Lepton Nonconserving Processes*, *Phys. Rev. Lett.* **43** (1979) 1566.

[47] T. Yanagida, *Horizontal Symmetry and Masses of Neutrinos*, *Prog. Theor. Phys.* **64** (1980) 1103.

[48] R.N. Mohapatra and G. Senjanovic, *Neutrino Mass and Spontaneous Parity Nonconservation*, *Phys. Rev. Lett.* **44** (1980) 912.

[49] M. Gell-Mann, *The interpretation of the new particles as displaced charge multiplets*, *Nuovo Cim.* **4** (1956) 848.

[50] T. Nakano and K. Nishijima, *Charge Independence for V-particles*, *Prog. Theor. Phys.* **10** (1953) 581.

[51] J. Goldstone, *Field Theories with Superconductor Solutions*, *Nuovo Cim.* **19** (1961) 154.

[52] J. Goldstone, A. Salam and S. Weinberg, *Broken Symmetries*, *Phys. Rev.* **127** (1962) 965.

[53] T.W.B. Kibble, *Symmetry breaking in nonAbelian gauge theories*, *Phys. Rev.* **155** (1967) 1554.

[54] PARTICLE DATA GROUP collaboration, *Review of particle physics*, *Phys. Rev. D* **110** (2024) 030001.

[55] P. Sikivie, L. Susskind, M.B. Voloshin and V.I. Zakharov, *Isospin Breaking in*

Technicolor Models, *Nucl. Phys. B* **173** (1980) 189.

[56] N. Cabibbo, *Unitary Symmetry and Leptonic Decays*, *Phys. Rev. Lett.* **10** (1963) 531.

[57] M. Kobayashi and T. Maskawa, *CP Violation in the Renormalizable Theory of Weak Interaction*, *Prog. Theor. Phys.* **49** (1973) 652.

[58] R.P. Feynman and A.R. Hibbs, *Quantum mechanics and path integrals*, International series in pure and applied physics, McGraw-Hill, New York, NY (1965).

[59] C. Becchi, A. Rouet and R. Stora, *Gauge Field Models*, pp. 242–270, 10, 1975.

[60] I.V. Tyutin, *Gauge Invariance in Field Theory and Statistical Physics in Operator Formalism*, 0812.0580.

[61] A.A. Slavnov, *Ward Identities in Gauge Theories*, *Theor. Math. Phys.* **10** (1972) 99.

[62] J.C. Taylor, *Ward Identities and Charge Renormalization of the Yang-Mills Field*, *Nucl. Phys. B* **33** (1971) 436.

[63] J. Iliopoulos, C. Itzykson and A. Martin, *Functional Methods and Perturbation Theory*, *Rev. Mod. Phys.* **47** (1975) 165.

[64] A. Alloul, N.D. Christensen, C. Degrande, C. Duhr and B. Fuks, *FeynRules 2.0 - A complete toolbox for tree-level phenomenology*, *Comput. Phys. Commun.* **185** (2014) 2250 [1310.1921].

[65] G. 't Hooft, *Dimensional regularization and the renormalization group*, *Nucl. Phys. B* **61** (1973) 455.

[66] W.A. Bardeen, A.J. Buras, D.W. Duke and T. Muta, *Deep Inelastic Scattering Beyond the Leading Order in Asymptotically Free Gauge Theories*, *Phys. Rev. D* **18** (1978) 3998.

[67] S. Weinberg, *Multiparticle sum rules*, *Phys. Rev. D* **5** (1972) 900.

[68] M. Jacob and G.C. Wick, *On the General Theory of Collisions for Particles with Spin*, *Annals Phys.* **7** (1959) 404.

[69] L. Di Luzio, J.F. Kamenik and M. Nardecchia, *Perturbative unitarity bounds on di-boson scalar resonances*, *EPJ Web Conf.* **164** (2017) 07026.

[70] H. Lehmann, K. Symanzik and W. Zimmermann, *On the formulation of quantized*

field theories, *Nuovo Cim.* **1** (1955) 205.

[71] B.W. Lee, C. Quigg and H.B. Thacker, *Weak Interactions at Very High-Energies: The Role of the Higgs Boson Mass*, *Phys. Rev. D* **16** (1977) 1519.

[72] GFITTER GROUP collaboration, *The global electroweak fit at NNLO and prospects for the LHC and ILC*, *Eur. Phys. J. C* **74** (2014) 3046 [1407.3792].

[73] M.J.G. Veltman, *Limit on Mass Differences in the Weinberg Model*, *Nucl. Phys. B* **123** (1977) 89.

[74] S. Mele, *The Measurement of the Number of Light Neutrino Species at LEP*, *Adv. Ser. Direct. High Energy Phys.* **23** (2015) 89.

[75] M.E. Peskin and T. Takeuchi, *Estimation of oblique electroweak corrections*, *Phys. Rev. D* **46** (1992) 381.

[76] FCC collaboration, *FCC Physics Opportunities: Future Circular Collider Conceptual Design Report Volume 1*, *Eur. Phys. J. C* **79** (2019) 474.

[77] FCC collaboration, *FCC-ee: The Lepton Collider: Future Circular Collider Conceptual Design Report Volume 2*, *Eur. Phys. J. ST* **228** (2019) 261.

[78] CEPC STUDY GROUP collaboration, *CEPC Conceptual Design Report: Volume 1 - Accelerator*, 1809.00285.

[79] L. Allwicher, M. McCullough and S. Renner, *New physics at Tera-Z: precision renormalised*, *JHEP* **02** (2025) 164 [2408.03992].

[80] U. Amaldi, W. de Boer and H. Furstenau, *Comparison of grand unified theories with electroweak and strong coupling constants measured at LEP*, *Phys. Lett. B* **260** (1991) 447.

[81] LHC HIGGS CROSS SECTION WORKING GROUP collaboration, *Handbook of LHC Higgs Cross Sections: 3. Higgs Properties*, 1307.1347.

[82] ATLAS collaboration, *A detailed map of Higgs boson interactions by the ATLAS experiment ten years after the discovery*, *Nature* **607** (2022) 52 [2207.00092].

[83] CMS collaboration, *Combined measurements of the Higgs boson's couplings at* $\sqrt{s} = 13$ *TeV*, .

[84] ATLAS collaboration, *HL-LHC prospects for the measurement of triple-Higgs*

production in the 6b final state at the ATLAS experiment, .

[85] LHC HIGGS CROSS SECTION WORKING GROUP collaboration, *Handbook of LHC Higgs Cross Sections: 1. Inclusive Observables*, 1101.0593.

[86] L. Wolfenstein, *Parametrization of the Kobayashi-Maskawa Matrix*, *Phys. Rev. Lett.* **51** (1983) 1945.

[87] CMS collaboration, *Combination of the ATLAS, CMS and LHCb results on the $B^0_{(s)} \to \mu^+\mu^-$ decays*, .

[88] CKMFITTER GROUP collaboration, *CP violation and the CKM matrix: Assessing the impact of the asymmetric B factories*, *Eur. Phys. J. C* **41** (2005) 1 [hep-ph/0406184].

[89] CKMFITTER GROUP collaboration, *Recent CKMfitter updates on global fits of the CKM matrix*, *PoS* **CKM2021** (2023) 074.

[90] M. Bona et al., *Unitarity Triangle global fits beyond the Standard Model: UTfit 2021 NP update*, *PoS* **EPS-HEP2021** (2022) 500.

[91] C. Branchina, V. Branchina, F. Contino and N. Darvishi, *Dimensional regularization, Wilsonian RG, and the naturalness and hierarchy problem*, *Phys. Rev. D* **106** (2022) 065007 [2204.10582].

[92] E. Witten, *Dynamical Breaking of Supersymmetry*, *Nucl. Phys. B* **188** (1981) 513.

[93] V.C. Rubin, N. Thonnard and W.K. Ford, Jr., *Rotational properties of 21 SC galaxies with a large range of luminosities and radii, from NGC 4605 /R = 4kpc/ to UGC 2885 /R = 122 kpc/*, *Astrophys. J.* **238** (1980) 471.

[94] D. Clowe, M. Bradac, A.H. Gonzalez, M. Markevitch, S.W. Randall, C. Jones et al., *A direct empirical proof of the existence of dark matter*, *Astrophys. J. Lett.* **648** (2006) L109 [astro-ph/0608407].

[95] K. Griest and D. Seckel, *Three exceptions in the calculation of relic abundances*, *Phys. Rev. D* **43** (1991) 3191.

[96] G. Jungman, M. Kamionkowski and K. Griest, *Supersymmetric dark matter*, *Phys. Rept.* **267** (1996) 195 [hep-ph/9506380].

[97] J.R. Ellis, J.S. Hagelin, D.V. Nanopoulos, K.A. Olive and M. Srednicki, *Supersymmetric Relics from the Big Bang*, *Nucl. Phys. B* **238** (1984) 453.

[98] G. Servant and T.M.P. Tait, *Is the lightest Kaluza-Klein particle a viable dark matter candidate?*, *Nucl. Phys. B* **650** (2003) 391 [hep-ph/0206071].

[99] H.-C. Cheng, K.T. Matchev and M. Schmaltz, *Radiative corrections to Kaluza-Klein masses*, *Phys. Rev. D* **66** (2002) 036005 [hep-ph/0204342].

[100] J. Preskill, M.B. Wise and F. Wilczek, *Cosmology of the Invisible Axion*, *Phys. Lett. B* **120** (1983) 127.

[101] L.F. Abbott and P. Sikivie, *A Cosmological Bound on the Invisible Axion*, *Phys. Lett. B* **120** (1983) 133.

[102] L.J. Hall, K. Jedamzik, J. March-Russell and S.M. West, *Freeze-In Production of FIMP Dark Matter*, *JHEP* **03** (2010) 080 [0911.1120].

[103] XENON collaboration, *Dark Matter Search Results from a One Ton-Year Exposure of XENON1T*, *Phys. Rev. Lett.* **121** (2018) 111302 [1805.12562].

[104] FERMI-LAT collaboration, *Searching for Dark Matter Annihilation from Milky Way Dwarf Spheroidal Galaxies with Six Years of Fermi Large Area Telescope Data*, *Phys. Rev. Lett.* **115** (2015) 231301 [1503.02641].

[105] J. Abdallah et al., *Simplified Models for Dark Matter Searches at the LHC*, *Phys. Dark Univ.* **9-10** (2015) 8 [1506.03116].

[106] SUPERNOVA SEARCH TEAM collaboration, *Observational evidence from supernovae for an accelerating universe and a cosmological constant*, *Astron. J.* **116** (1998) 1009 [astro-ph/9805201].

[107] SUPERNOVA COSMOLOGY PROJECT collaboration, *Measurements of Ω and Λ from 42 High Redshift Supernovae*, *Astrophys. J.* **517** (1999) 565 [astro-ph/9812133].

[108] V.A. Kuzmin, V.A. Rubakov and M.E. Shaposhnikov, *On the Anomalous Electroweak Baryon Number Nonconservation in the Early Universe*, *Phys. Lett. B* **155** (1985) 36.

[109] M.B. Gavela, P. Hernandez, J. Orloff, O. Pene and C. Quimbay, *Standard model CP violation and baryon asymmetry. Part 2: Finite temperature*, *Nucl. Phys. B* **430** (1994) 382 [hep-ph/9406289].

[110] K. Kajantie, M. Laine, K. Rummukainen and M.E. Shaposhnikov, *A Nonperturbative analysis of the finite T phase transition in SU(2) x U(1) electroweak*

theory, *Nucl. Phys. B* **493** (1997) 413 [hep-lat/9612006].

[111] M. D'Onofrio and K. Rummukainen, *Standard model cross-over on the lattice*, *Phys. Rev. D* **93** (2016) 025003 [1508.07161].

[112] S.L. Glashow, J. Iliopoulos and L. Maiani, *Weak Interactions with Lepton-Hadron Symmetry*, *Phys. Rev. D* **2** (1970) 1285.

[113] C.D. Froggatt and H.B. Nielsen, *Hierarchy of Quark Masses, Cabibbo Angles and CP Violation*, *Nucl. Phys. B* **147** (1979) 277.

[114] G. D'Ambrosio, G.F. Giudice, G. Isidori and A. Strumia, *Minimal flavor violation: An Effective field theory approach*, *Nucl. Phys. B* **645** (2002) 155 [hep-ph/0207036].

[115] C. Abel et al., *Measurement of the Permanent Electric Dipole Moment of the Neutron*, *Phys. Rev. Lett.* **124** (2020) 081803 [2001.11966].

[116] S. Weinberg, *A New Light Boson?*, *Phys. Rev. Lett.* **40** (1978) 223.

[117] F. Wilczek, *Problem of Strong P and T Invariance in the Presence of Instantons*, *Phys. Rev. Lett.* **40** (1978) 279.

[118] I. Brivio and M. Trott, *The Standard Model as an Effective Field Theory*, *Phys. Rept.* **793** (2019) 1 [1706.08945].

[119] B. Grzadkowski, M. Iskrzynski, M. Misiak and J. Rosiek, *Dimension-Six Terms in the Standard Model Lagrangian*, *JHEP* **10** (2010) 085 [1008.4884].

[120] S. Das Bakshi, J. Chakrabortty and S.K. Patra, *CoDEx: Wilson coefficient calculator connecting SMEFT to UV theory*, *Eur. Phys. J. C* **79** (2019) 21 [1808.04403].

[121] J. Fuentes-Martín, M. König, J. Pagès, A.E. Thomsen and F. Wilsch, *A proof of concept for matchete: an automated tool for matching effective theories*, *Eur. Phys. J. C* **83** (2023) 662 [2212.04510].

[122] A. Carmona, A. Lazopoulos, P. Olgoso and J. Santiago, *Matchmakereft: automated tree-level and one-loop matching*, *SciPost Phys.* **12** (2022) 198 [2112.10787].

[123] M. Chala, J. López Miras, J. Santiago and F. Vilches, *Efficient on-shell matching*, *SciPost Phys.* **18** (2025) 185 [2411.12798].

[124] E.E. Jenkins, A.V. Manohar and M. Trott, *Renormalization Group Evolution of the Standard Model Dimension Six Operators I: Formalism and lambda Dependence*, *JHEP*

10 (2013) 087 [1308.2627].

[125] E.E. Jenkins, A.V. Manohar and M. Trott, *Renormalization Group Evolution of the Standard Model Dimension Six Operators II: Yukawa Dependence*, *JHEP* **01** (2014) 035 [1310.4838].

[126] R. Alonso, E.E. Jenkins, A.V. Manohar and M. Trott, *Renormalization Group Evolution of the Standard Model Dimension Six Operators III: Gauge Coupling Dependence and Phenomenology*, *JHEP* **04** (2014) 159 [1312.2014].

[127] R. Alonso, H.-M. Chang, E.E. Jenkins, A.V. Manohar and B. Shotwell, *Renormalization group evolution of dimension-six baryon number violating operators*, *Phys. Lett. B* **734** (2014) 302 [1405.0486].

[128] E. Celada, T. Giani, J. ter Hoeve, L. Mantani, J. Rojo, A.N. Rossia et al., *Mapping the SMEFT at high-energy colliders: from LEP and the (HL-)LHC to the FCC-ee*, *JHEP* **09** (2024) 091 [2404.12809].

[129] R. Alonso, E.E. Jenkins and A.V. Manohar, *A Geometric Formulation of Higgs Effective Field Theory: Measuring the Curvature of Scalar Field Space*, *Phys. Lett. B* **754** (2016) 335 [1511.00724].

[130] T. Cohen, N. Craig, X. Lu and D. Sutherland, *Is SMEFT Enough?*, *JHEP* **03** (2021) 237 [2008.08597].

[131] I. Banta, T. Cohen, N. Craig, X. Lu and D. Sutherland, *Non-decoupling new particles*, *JHEP* **02** (2022) 029 [2110.02967].

[132] G. Crawford and D. Sutherland, *Scalars with non-decoupling phenomenology at future colliders*, *JHEP* **04** (2025) 197 [2409.18177].

[133] I. Brivio, T. Corbett, O.J.P. Éboli, M.B. Gavela, J. Gonzalez-Fraile, M.C. Gonzalez-Garcia et al., *Disentangling a dynamical Higgs*, *JHEP* **03** (2014) 024 [1311.1823].

[134] M.J. Herrero and R.A. Morales, *One-loop corrections for WW to HH in Higgs EFT with the electroweak chiral Lagrangian*, *Phys. Rev. D* **106** (2022) 073008 [2208.05900].

[135] T. Plehn, A. Butter, B. Dillon, T. Heimel, C. Krause and R. Winterhalder, *Modern Machine Learning for LHC Physicists*, 2211.01421.

[136] HEP ML Community, "A Living Review of Machine Learning for Particle Physics."

[137] ATLAS collaboration, *Search for nonresonant pair production of Higgs bosons in the $b\bar{b}b\bar{b}$ final state in pp collisions at $\sqrt{s} = 13$ TeV with the ATLAS detector*, 2301.03212.

[138] M. McCullough, *An Indirect Model-Dependent Probe of the Higgs Self-Coupling*, *Phys. Rev. D* **90** (2014) 015001 [1312.3322].

[139] G. Degrassi, P.P. Giardino, F. Maltoni and D. Pagani, *Probing the Higgs self coupling via single Higgs production at the LHC*, *JHEP* **12** (2016) 080 [1607.04251].

[140] M. Gorbahn and U. Haisch, *Indirect probes of the trilinear Higgs coupling: $gg \to h$ and $h \to \gamma\gamma$*, *JHEP* **10** (2016) 094 [1607.03773].

[141] G.D. Kribs, A. Maier, H. Rzehak, M. Spannowsky and P. Waite, *Electroweak oblique parameters as a probe of the trilinear Higgs boson self-interaction*, *Phys. Rev. D* **95** (2017) 093004 [1702.07678].

[142] Anisha, O. Atkinson, A. Bhardwaj, C. Englert and P. Stylianou, *Quartic Gauge-Higgs couplings: constraints and future directions*, *JHEP* **10** (2022) 172 [2208.09334].

[143] K. Agashe, R. Contino and A. Pomarol, *The Minimal composite Higgs model*, *Nucl. Phys. B* **719** (2005) 165 [hep-ph/0412089].

[144] R. Contino, L. Da Rold and A. Pomarol, *Light custodians in natural composite Higgs models*, *Phys. Rev. D* **75** (2007) 055014 [hep-ph/0612048].

[145] S. Dawson, *The Effective W Approximation*, *Nucl. Phys. B* **249** (1985) 42.

[146] R. Contino, C. Grojean, M. Moretti, F. Piccinini and R. Rattazzi, *Strong Double Higgs Production at the LHC*, *JHEP* **05** (2010) 089 [1002.1011].

[147] T. Hahn, *Generating Feynman diagrams and amplitudes with FeynArts 3*, *Comput. Phys. Commun.* **140** (2001) 418 [hep-ph/0012260].

[148] T. Hahn and M. Perez-Victoria, *Automatized one loop calculations in four-dimensions and D-dimensions*, *Comput. Phys. Commun.* **118** (1999) 153 [hep-ph/9807565].

[149] L. Di Luzio, R. Gröber and M. Spannowsky, *Maxi-sizing the trilinear Higgs*

self-coupling: how large could it be?, *Eur. Phys. J. C* **77** (2017) 788 [1704.02311].

[150] F. Arco, S. Heinemeyer and M.J. Herrero, *Exploring sizable triple Higgs couplings in the 2HDM*, *Eur. Phys. J. C* **80** (2020) 884 [2005.10576].

[151] F. Arco, S. Heinemeyer, M. Mühlleitner and K. Radchenko, *Sensitivity to Triple Higgs Couplings via Di-Higgs Production in the 2HDM at the (HL-)LHC*, 2212.11242.

[152] R.N. Cahn and S. Dawson, *Production of Very Massive Higgs Bosons*, *Phys. Lett. B* **136** (1984) 196.

[153] D.L. Rainwater, D. Zeppenfeld and K. Hagiwara, *Searching for $H \to \tau^+\tau^-$ in weak boson fusion at the CERN LHC*, *Phys. Rev. D* **59** (1998) 014037 [hep-ph/9808468].

[154] D. Zeppenfeld, R. Kinnunen, A. Nikitenko and E. Richter-Was, *Measuring Higgs boson couplings at the CERN LHC*, *Phys. Rev. D* **62** (2000) 013009 [hep-ph/0002036].

[155] T. Figy, C. Oleari and D. Zeppenfeld, *Next-to-leading order jet distributions for Higgs boson production via weak boson fusion*, *Phys. Rev. D* **68** (2003) 073005 [hep-ph/0306109].

[156] T. Figy, *Next-to-leading order QCD corrections to light Higgs Pair production via vector boson fusion*, *Mod. Phys. Lett. A* **23** (2008) 1961 [0806.2200].

[157] F.A. Dreyer and A. Karlberg, *Vector-Boson Fusion Higgs Pair Production at N^3LO*, *Phys. Rev. D* **98** (2018) 114016 [1811.07906].

[158] K. Arnold et al., *VBFNLO: A Parton level Monte Carlo for processes with electroweak bosons*, *Comput. Phys. Commun.* **180** (2009) 1661 [0811.4559].

[159] J. Baglio, A. Djouadi, R. Gröber, M.M. Mühlleitner, J. Quevillon and M. Spira, *The measurement of the Higgs self-coupling at the LHC: theoretical status*, *JHEP* **04** (2013) 151 [1212.5581].

[160] J. Alwall, M. Herquet, F. Maltoni, O. Mattelaer and T. Stelzer, *MadGraph 5: Going Beyond*, *JHEP* **06** (2011) 128 [1106.0522].

[161] R. Frederix, S. Frixione, V. Hirschi, F. Maltoni, O. Mattelaer, P. Torrielli et al., *Higgs pair production at the LHC with NLO and parton-shower effects*, *Phys. Lett. B*

732 (2014) 142 [1401.7340].

[162] FCC collaboration, *FCC-hh: The Hadron Collider: Future Circular Collider Conceptual Design Report Volume 3*, *Eur. Phys. J. ST* **228** (2019) 755.

[163] ATLAS collaboration, *Search for pair production of Higgs bosons in the $b\bar{b}b\bar{b}$ final state using proton-proton collisions at $\sqrt{s} = 13$ TeV with the ATLAS detector*, *JHEP* **01** (2019) 030 [1804.06174].

[164] ATLAS collaboration, *Search for the $HH \to b\bar{b}b\bar{b}$ process via vector-boson fusion production using proton-proton collisions at $\sqrt{s} = 13$ TeV with the ATLAS detector*, *JHEP* **07** (2020) 108 [2001.05178].

[165] CMS collaboration, *Search for Higgs Boson Pair Production in the Four b Quark Final State in Proton-Proton Collisions at $\sqrt{s}$ = 13 TeV*, *Phys. Rev. Lett.* **129** (2022) 081802 [2202.09617].

[166] CMS collaboration, *Search for nonresonant pair production of highly energetic Higgs bosons decaying to bottom quarks*, 2205.06667.

[167] ATLAS collaboration, *Search for resonant and non-resonant Higgs boson pair production in the $b\bar{b}\tau^+\tau^-$ decay channel using 13 TeV pp collision data from the ATLAS detector*, 2209.10910.

[168] CMS collaboration, *Search for Higgs boson pair production in events with two bottom quarks and two tau leptons in proton–proton collisions at $\sqrt{s}$ =13TeV*, *Phys. Lett. B* **778** (2018) 101 [1707.02909].

[169] CMS collaboration, *Search for Higgs boson pair production in the $bb\tau\tau$ final state in proton-proton collisions at $\sqrt{s}$ = 8 TeV*, *Phys. Rev. D* **96** (2017) 072004 [1707.00350].

[170] CMS collaboration, *Search for nonresonant Higgs boson pair production in final state with two bottom quarks and two tau leptons in proton-proton collisions at $\sqrt{s}$ = 13 TeV*, 2206.09401.

[171] ATLAS collaboration, *Searches for Higgs boson pair production in the $hh \to bb\tau\tau, \gamma\gamma WW^*, \gamma\gamma bb, bbbb$ channels with the ATLAS detector*, *Phys. Rev. D* **92** (2015) 092004 [1509.04670].

[172] ATLAS collaboration, *Search for Higgs boson pair production in the two bottom quarks plus two photons final state in pp collisions at $\sqrt{s}$ = 13 TeV with the ATLAS detector*, *Phys. Rev. D* **106** (2022) 052001 [2112.11876].

[173] CMS collaboration, *Search for nonresonant Higgs boson pair production in final states with two bottom quarks and two photons in proton-proton collisions at $\sqrt{s} = 13$ TeV*, *JHEP* **03** (2021) 257 [2011.12373].

[174] C. Bierlich et al., *A comprehensive guide to the physics and usage of PYTHIA 8.3*, 2203.11601.

[175] E. Conte, B. Fuks and G. Serret, *MadAnalysis 5, A User-Friendly Framework for Collider Phenomenology*, *Comput. Phys. Commun.* **184** (2013) 222 [1206.1599].

[176] M. Cacciari, G.P. Salam and G. Soyez, *FastJet User Manual*, *Eur. Phys. J. C* **72** (2012) 1896 [1111.6097].

[177] M. Cacciari and G.P. Salam, *Dispelling the N^3 myth for the k_t jet-finder*, *Phys. Lett. B* **641** (2006) 57 [hep-ph/0512210].

[178] M.J. Dolan, C. Englert, N. Greiner and M. Spannowsky, *Further on up the road: hhjj production at the LHC*, *Phys. Rev. Lett.* **112** (2014) 101802 [1310.1084].

[179] M.J. Dolan, C. Englert, N. Greiner, K. Nordstrom and M. Spannowsky, *hhjj production at the LHC*, *Eur. Phys. J. C* **75** (2015) 387 [1506.08008].

[180] F. Bishara, R. Contino and J. Rojo, *Higgs pair production in vector-boson fusion at the LHC and beyond*, *Eur. Phys. J. C* **77** (2017) 481 [1611.03860].

[181] Z. Chacko, C. Kilic, S. Najjari and C.B. Verhaaren, *Testing the Scalar Sector of the Twin Higgs Model at Colliders*, *Phys. Rev. D* **97** (2018) 055031 [1711.05300].

[182] S. Di Vita, G. Durieux, C. Grojean, J. Gu, Z. Liu, G. Panico et al., *A global view on the Higgs self-coupling at lepton colliders*, *JHEP* **02** (2018) 178 [1711.03978].

[183] B. Li, Z.-L. Han and Y. Liao, *Higgs production at future e^+e^- colliders in the Georgi-Machacek model*, *JHEP* **02** (2018) 007 [1710.00184].

[184] H. Abramowicz et al., *Higgs physics at the CLIC electron–positron linear collider*, *Eur. Phys. J. C* **77** (2017) 475 [1608.07538].

[185] D. Domenech, M.J. Herrero, R.A. Morales and M. Ramos, *Double Higgs boson production at TeV e+e- colliders with effective field theories: Sensitivity to BSM Higgs couplings*, *Phys. Rev. D* **106** (2022) 115027 [2208.05452].

[186] M. Gonzalez-Lopez, M.J. Herrero and P. Martinez-Suarez, *Testing anomalous $H - W$ couplings and Higgs self-couplings via double and triple Higgs production at*

e^+e^- *colliders*, *Eur. Phys. J. C* **81** (2021) 260 [2011.13915].

[187] CLICDP collaboration, *Double Higgs boson production and Higgs self-coupling extraction at CLIC*, *Eur. Phys. J. C* **80** (2020) 1010 [1901.05897].

[188] INTERNATIONAL MUON COLLIDER collaboration, *The Muon Collider*, 2504.21417.

[189] J. de Blas et al., *Higgs Boson Studies at Future Particle Colliders*, *JHEP* **01** (2020) 139 [1905.03764].

[190] M. Cepeda et al., *Report from Working Group 2: Higgs Physics at the HL-LHC and HE-LHC*, *CERN Yellow Rep. Monogr.* **7** (2019) 221 [1902.00134].

[191] R. Contino et al., *Physics at a 100 TeV pp collider: Higgs and EW symmetry breaking studies*, 1606.09408.

[192] ILC collaboration, *The International Linear Collider. A Global Project*, 1901.09829.

[193] U. Baur, T. Plehn and D.L. Rainwater, *Measuring the Higgs Boson Self Coupling at the LHC and Finite Top Mass Matrix Elements*, *Phys. Rev. Lett.* **89** (2002) 151801 [hep-ph/0206024].

[194] M.J. Dolan, C. Englert and M. Spannowsky, *Higgs self-coupling measurements at the LHC*, *JHEP* **10** (2012) 112 [1206.5001].

[195] R. Alonso and M. West, *Roads to the Standard Model*, *Phys. Rev. D* **105** (2022) 096028 [2109.13290].

[196] J.F. Gunion, R. Vega and J. Wudka, *Higgs triplets in the standard model*, *Phys. Rev. D* **42** (1990) 1673.

[197] K. Hartling, K. Kumar and H.E. Logan, *The decoupling limit in the Georgi-Machacek model*, *Phys. Rev. D* **90** (2014) 015007 [1404.2640].

[198] C. Englert, E. Re and M. Spannowsky, *Pinning down Higgs triplets at the LHC*, *Phys. Rev. D* **88** (2013) 035024 [1306.6228].

[199] CMS collaboration, *Search for charged Higgs bosons produced in vector boson fusion processes and decaying into vector boson pairs in proton–proton collisions at* $\sqrt{s} = 13$ *TeV*, *Eur. Phys. J. C* **81** (2021) 723 [2104.04762].

[200] A. Ismail, H.E. Logan and Y. Wu, *Updated constraints on the Georgi-Machacek*

model from LHC Run 2, 2003.02272.

[201] D. Egana-Ugrinovic and S. Thomas, *Effective Theory of Higgs Sector Vacuum States*, 1512.00144.

[202] I. Banta, *A strongly first-order electroweak phase transition from Loryons*, *JHEP* **06** (2022) 099 [2202.04608].

[203] D.A. Ross and J.C. Taylor, *Renormalization of a unified theory of weak and electromagnetic interactions*, *Nucl. Phys. B* **51** (1973) 125.

[204] A. Denner, S. Dittmaier and J.-N. Lang, *Renormalization of mixing angles*, *JHEP* **11** (2018) 104 [1808.03466].

[205] A. Sirlin, *Radiative Corrections in the SU(2)-L x U(1) Theory: A Simple Renormalization Framework*, *Phys. Rev. D* **22** (1980) 971.

[206] G. Passarino and M.J.G. Veltman, *One Loop Corrections for e^+e^- Annihilation Into $\mu^+\mu^-$ in the Weinberg Model*, *Nucl. Phys. B* **160** (1979) 151.

[207] A. Djouadi, *The Anatomy of electro-weak symmetry breaking. I: The Higgs boson in the standard model*, *Phys. Rept.* **457** (2008) 1 [hep-ph/0503172].

[208] D. Carmi, A. Falkowski, E. Kuflik, T. Volansky and J. Zupan, *Higgs After the Discovery: A Status Report*, *JHEP* **10** (2012) 196 [1207.1718].

[209] R. Contino, Y. Nomura and A. Pomarol, *Higgs as a holographic pseudoGoldstone boson*, *Nucl. Phys. B* **671** (2003) 148 [hep-ph/0306259].

[210] R. Alonso, E.E. Jenkins and A.V. Manohar, *Sigma Models with Negative Curvature*, *Phys. Lett. B* **756** (2016) 358 [1602.00706].

[211] R. Alonso, E.E. Jenkins and A.V. Manohar, *Geometry of the Scalar Sector*, *JHEP* **08** (2016) 101 [1605.03602].

[212] G. Ferretti, *UV Completions of Partial Compositeness: The Case for a SU(4) Gauge Group*, *JHEP* **06** (2014) 142 [1404.7137].

[213] R. Contino, *The Higgs as a Composite Nambu-Goldstone Boson*, in *Theoretical Advanced Study Institute in Elementary Particle Physics: Physics of the Large and the Small*, pp. 235–306, 2011, DOI [1005.4269].

[214] M. Golterman and Y. Shamir, *Top quark induced effective potential in a composite*

Higgs model, *Phys. Rev. D* **91** (2015) 094506 [1502.00390].

[215] L. Del Debbio, C. Englert and R. Zwicky, *A UV Complete Compositeness Scenario: LHC Constraints Meet The Lattice*, *JHEP* **08** (2017) 142 [1703.06064].

[216] V. Ayyar, T. DeGrand, D.C. Hackett, W.I. Jay, E.T. Neil, Y. Shamir et al., *Partial compositeness and baryon matrix elements on the lattice*, *Phys. Rev. D* **99** (2019) 094502 [1812.02727].

[217] L. Del Debbio, A. Lupo, M. Panero and N. Tantalo, *Multi-representation dynamics of SU(4) composite Higgs models: chiral limit and spectral reconstructions*, *Eur. Phys. J. C* **83** (2023) 220 [2211.09581].

[218] R. Grober and M. Muhlleitner, *Composite Higgs Boson Pair Production at the LHC*, *JHEP* **06** (2011) 020 [1012.1562].

[219] G. Durieux, M. McCullough and E. Salvioni, *Gegenbauer Goldstones*, *JHEP* **01** (2022) 076 [2110.06941].

[220] J.A. Wolf, *Spaces of constant curvature*, AMS Chelsea Pub., Providence, R.I, 6th ed. ed. (2011).

[221] J.D. Bekenstein, *The Relation between physical and gravitational geometry*, *Phys. Rev. D* **48** (1993) 3641 [gr-qc/9211017].

[222] S. Bruggisser, B. von Harling, O. Matsedonskyi and G. Servant, *Dilaton at the LHC: Complementary Probe of Composite Higgs*, 2212.00056.

[223] W.D. Goldberger, B. Grinstein and W. Skiba, *Distinguishing the Higgs boson from the dilaton at the Large Hadron Collider*, *Phys. Rev. Lett.* **100** (2008) 111802 [0708.1463].

[224] A. Dedes, W. Materkowska, M. Paraskevas, J. Rosiek and K. Suxho, *Feynman rules for the Standard Model Effective Field Theory in R_ξ -gauges*, *JHEP* **06** (2017) 143 [1704.03888].

[225] M.J. Herrero and R.A. Morales, *One-loop renormalization of vector boson scattering with the electroweak chiral Lagrangian in covariant gauges*, *Phys. Rev. D* **104** (2021) 075013 [2107.07890].

[226] R. Rattazzi and A. Zaffaroni, *Comments on the holographic picture of the Randall-Sundrum model*, *JHEP* **04** (2001) 021 [hep-th/0012248].

[227] Z. Komargodski and A. Schwimmer, *On Renormalization Group Flows in Four Dimensions*, *JHEP* **12** (2011) 099 [1107.3987].

[228] M.J. Dolan, C. Englert and M. Spannowsky, *New Physics in LHC Higgs boson pair production*, *Phys. Rev. D* **87** (2013) 055002 [1210.8166].

[229] R.L. Delgado, A. Dobado and F.J. Llanes-Estrada, *One-loop $W_L W_L$ and $Z_L Z_L$ scattering from the electroweak Chiral Lagrangian with a light Higgs-like scalar*, *JHEP* **02** (2014) 121 [1311.5993].

[230] M.B. Gavela, K. Kanshin, P.A.N. Machado and S. Saa, *On the renormalization of the electroweak chiral Lagrangian with a Higgs*, *JHEP* **03** (2015) 043 [1409.1571].

[231] I.n. Asiáin, D. Espriu and F. Mescia, *Introducing tools to test Higgs boson interactions via WW scattering: One-loop calculations and renormalization in the Higgs effective field theory*, *Phys. Rev. D* **105** (2022) 015009 [2109.02673].

[232] R. Gómez-Ambrosio, F.J. Llanes-Estrada, A. Salas-Bernárdez and J.J. Sanz-Cillero, *SMEFT is falsifiable through multi-Higgs measurements (even in the absence of new light particles)*, *Commun. Theor. Phys.* **75** (2023) 095202 [2207.09848].

[233] R. Gómez-Ambrosio, F.J. Llanes-Estrada, A. Salas-Bernárdez and J.J. Sanz-Cillero, *Distinguishing electroweak EFTs with WLWLnh*, *Phys. Rev. D* **106** (2022) 053004 [2204.01763].

[234] Anisha, D. Domenech, C. Englert, M.J. Herrero and R.A. Morales, *Bosonic multi-Higgs correlations beyond leading order*, 2405.05385.

[235] D. de Florian, I. Fabre and J. Mazzitelli, *Triple Higgs production at hadron colliders at NNLO in QCD*, *JHEP* **03** (2020) 155 [1912.02760].

[236] P. Basler, S. Dawson, C. Englert and M. Mühlleitner, *Showcasing HH production: Benchmarks for the LHC and HL-LHC*, *Phys. Rev. D* **99** (2019) 055048 [1812.03542].

[237] P. Stylianou and G. Weiglein, *Constraints on the trilinear and quartic Higgs couplings from triple Higgs production at the LHC and beyond*, 2312.04646.

[238] M.J. Ramsey-Musolf, *The electroweak phase transition: a collider target*, *JHEP* **09** (2020) 179 [1912.07189].

[239] O. Karkout, A. Papaefstathiou, M. Postma, G. Tetlalmatzi-Xolocotzi, J. van de

Vis and T. du Pree, *Triple Higgs boson production and electroweak phase transition in the two-real-singlet model*, 2404.12425.

[240] M. Muhlleitner, M.O.P. Sampaio, R. Santos and J. Wittbrodt, *The N2HDM under Theoretical and Experimental Scrutiny*, *JHEP* **03** (2017) 094 [1612.01309].

[241] S.L. Glashow and S. Weinberg, *Natural Conservation Laws for Neutral Currents*, *Phys. Rev. D* **15** (1977) 1958.

[242] G.C. Branco, P.M. Ferreira, L. Lavoura, M.N. Rebelo, M. Sher and J.P. Silva, *Theory and phenomenology of two-Higgs-doublet models*, *Phys. Rept.* **516** (2012) 1 [1106.0034].

[243] P. Basler, M. Krause, M. Muhlleitner, J. Wittbrodt and A. Wlotzka, *Strong First Order Electroweak Phase Transition in the CP-Conserving 2HDM Revisited*, *JHEP* **02** (2017) 121 [1612.04086].

[244] O. Atkinson, M. Black, A. Lenz, A. Rusov and J. Wynne, *Cornering the Two Higgs Doublet Model Type II*, *JHEP* **04** (2022) 172 [2107.05650].

[245] O. Atkinson, M. Black, C. Englert, A. Lenz, A. Rusov and J. Wynne, *The flavourful present and future of 2HDMs at the collider energy frontier*, *JHEP* **11** (2022) 139 [2202.08807].

[246] R.A. Battye, G.D. Brawn and A. Pilaftsis, *Vacuum Topology of the Two Higgs Doublet Model*, *JHEP* **08** (2011) 020 [1106.3482].

[247] A. Pilaftsis, *On the Classification of Accidental Symmetries of the Two Higgs Doublet Model Potential*, *Phys. Lett. B* **706** (2012) 465 [1109.3787].

[248] P.S.B. Dev and A. Pilaftsis, *Natural Standard Model Alignment in the Two Higgs Doublet Model*, *J. Phys. Conf. Ser.* **631** (2015) 012030 [1503.09140].

[249] R. Coimbra, M.O.P. Sampaio and R. Santos, *ScannerS: Constraining the phase diagram of a complex scalar singlet at the LHC*, *Eur. Phys. J. C* **73** (2013) 2428 [1301.2599].

[250] M. Mühlleitner, M.O.P. Sampaio, R. Santos and J. Wittbrodt, *ScannerS: parameter scans in extended scalar sectors*, *Eur. Phys. J. C* **82** (2022) 198 [2007.02985].

[251] P. Bechtle, D. Dercks, S. Heinemeyer, T. Klingl, T. Stefaniak, G. Weiglein et al., *HiggsBounds-5: Testing Higgs Sectors in the LHC 13 TeV Era*, *Eur. Phys. J. C* **80**

(2020) 1211 [2006.06007].

[252] P. Bechtle, S. Heinemeyer, T. Klingl, T. Stefaniak, G. Weiglein and J. Wittbrodt, *HiggsSignals-2: Probing new physics with precision Higgs measurements in the LHC 13 TeV era*, *Eur. Phys. J. C* **81** (2021) 145 [2012.09197].

[253] H. Bahl, T. Biekötter, S. Heinemeyer, C. Li, S. Paasch, G. Weiglein et al., *HiggsTools: BSM scalar phenomenology with new versions of HiggsBounds and HiggsSignals*, *Comput. Phys. Commun.* **291** (2023) 108803 [2210.09332].

[254] H.E. Haber and H.E. Logan, *Radiative corrections to the Z b anti-b vertex and constraints on extended Higgs sectors*, *Phys. Rev. D* **62** (2000) 015011 [hep-ph/9909335].

[255] O. Deschamps, S. Descotes-Genon, S. Monteil, V. Niess, S. T'Jampens and V. Tisserand, *The Two Higgs Doublet of Type II facing flavour physics data*, *Phys. Rev. D* **82** (2010) 073012 [0907.5135].

[256] F. Mahmoudi and O. Stal, *Flavor constraints on the two-Higgs-doublet model with general Yukawa couplings*, *Phys. Rev. D* **81** (2010) 035016 [0907.1791].

[257] T. Hermann, M. Misiak and M. Steinhauser, *$\bar{B} \to X_s\gamma$ in the Two Higgs Doublet Model up to Next-to-Next-to-Leading Order in QCD*, *JHEP* **11** (2012) 036 [1208.2788].

[258] M. Misiak et al., *Updated NNLO QCD predictions for the weak radiative B-meson decays*, *Phys. Rev. Lett.* **114** (2015) 221801 [1503.01789].

[259] M. Misiak and M. Steinhauser, *Weak radiative decays of the B meson and bounds on $M_{H^\pm}$ in the Two-Higgs-Doublet Model*, *Eur. Phys. J. C* **77** (2017) 201 [1702.04571].

[260] M. Misiak, A. Rehman and M. Steinhauser, *Towards $\overline{B} \to X_s\gamma$ at the NNLO in QCD without interpolation in m_c*, *JHEP* **06** (2020) 175 [2002.01548].

[261] P. Basler, L. Biermann, M. Mühlleitner, J. Müller, R. Santos and J.a. Viana, *BSMPT v3 A Tool for Phase Transitions and Primordial Gravitational Waves in Extended Higgs Sectors*, 2404.19037.

[262] P. Basler, M. Mühlleitner and J. Müller, *BSMPT v2 a tool for the electroweak phase transition and the baryon asymmetry of the universe in extended Higgs Sectors*, *Comput. Phys. Commun.* **269** (2021) 108124 [2007.01725].

[263] P. Basler and M. Mühlleitner, *BSMPT (Beyond the Standard Model Phase Transitions): A tool for the electroweak phase transition in extended Higgs sectors*, *Comput. Phys. Commun.* **237** (2019) 62 [1803.02846].

[264] J.R. Espinosa, G.F. Giudice, E. Morgante, A. Riotto, L. Senatore, A. Strumia et al., *The cosmological Higgstory of the vacuum instability*, *JHEP* **09** (2015) 174 [1505.04825].

[265] H.H. Patel and M.J. Ramsey-Musolf, *Baryon Washout, Electroweak Phase Transition, and Perturbation Theory*, *JHEP* **07** (2011) 029 [1101.4665].

[266] M. Quiros, *Field theory at finite temperature and phase transitions*, *Helv. Phys. Acta* **67** (1994) 451.

[267] M. Quiros, *Finite temperature field theory and phase transitions*, in *ICTP Summer School in High-Energy Physics and Cosmology*, pp. 187–259, 1, 1999 [hep-ph/9901312].

[268] D.E. Morrissey and M.J. Ramsey-Musolf, *Electroweak baryogenesis*, *New J. Phys.* **14** (2012) 125003 [1206.2942].

[269] P.B. Arnold and O. Espinosa, *The Effective potential and first order phase transitions: Beyond leading-order*, *Phys. Rev. D* **47** (1993) 3546 [hep-ph/9212235].

[270] P. Basler, M. Mühlleitner and J. Müller, *Electroweak Phase Transition in Non-Minimal Higgs Sectors*, *JHEP* **05** (2020) 016 [1912.10477].

[271] P. Basler, L. Biermann, M. Mühlleitner and J. Müller, *Electroweak baryogenesis in the CP-violating two-Higgs doublet model*, *Eur. Phys. J. C* **83** (2023) 57 [2108.03580].

[272] C. Degrande, *Automatic evaluation of UV and R2 terms for beyond the Standard Model Lagrangians: a proof-of-principle*, *Comput. Phys. Commun.* **197** (2015) 239 [1406.3030].

[273] C. Degrande, C. Duhr, B. Fuks, D. Grellscheid, O. Mattelaer and T. Reiter, *UFO - The Universal FeynRules Output*, *Comput. Phys. Commun.* **183** (2012) 1201 [1108.2040].

[274] A. Djouadi, M. Spira and P.M. Zerwas, *Production of Higgs bosons in proton colliders: QCD corrections*, *Phys. Lett. B* **264** (1991) 440.

[275] CMS collaboration, *A portrait of the Higgs boson by the CMS experiment ten years*

after the discovery., *Nature* **607** (2022) 60 [2207.00043].

[276] T. Plehn, M. Spira and P.M. Zerwas, *Pair production of neutral Higgs particles in gluon-gluon collisions*, *Nucl. Phys. B* **479** (1996) 46 [hep-ph/9603205].

[277] S. Dawson, S. Dittmaier and M. Spira, *Neutral Higgs boson pair production at hadron colliders: QCD corrections*, *Phys. Rev. D* **58** (1998) 115012 [hep-ph/9805244].

[278] S. Borowka, N. Greiner, G. Heinrich, S.P. Jones, M. Kerner, J. Schlenk et al., *Full top quark mass dependence in Higgs boson pair production at NLO*, *JHEP* **10** (2016) 107 [1608.04798].

[279] J. Baglio, F. Campanario, S. Glaus, M. Mühlleitner, J. Ronca, M. Spira et al., *Higgs-Pair Production via Gluon Fusion at Hadron Colliders: NLO QCD Corrections*, *JHEP* **04** (2020) 181 [2003.03227].

[280] S. Heinemeyer, M. Mühlleitner, K. Radchenko and G. Weiglein, *Higgs Pair Production in the 2HDM: Impact of Loop Corrections to the Trilinear Higgs Couplings and Interference Effects on Experimental Limits*, 2403.14776.

[281] J. Ellis, M. Lewicki and J.M. No, *On the Maximal Strength of a First-Order Electroweak Phase Transition and its Gravitational Wave Signal*, *JCAP* **04** (2019) 003 [1809.08242].

[282] P. Athron, L. Morris and Z. Xu, *How robust are gravitational wave predictions from cosmological phase transitions?*, *JCAP* **05** (2024) 075 [2309.05474].

[283] T.S. Roussy et al., *An improved bound on the electron's electric dipole moment*, *Science* **381** (2023) adg4084 [2212.11841].

[284] D. Fontes, M. Mühlleitner, J.C. Romão, R. Santos, J.a.P. Silva and J. Wittbrodt, *The C2HDM revisited*, *JHEP* **02** (2018) 073 [1711.09419].

[285] T. Biekötter, D. Fontes, M. Mühlleitner, J.C. Romão, R. Santos and J.a.P. Silva, *Impact of new experimental data on the C2HDM: the strong interdependence between LHC Higgs data and the electron EDM*, *JHEP* **05** (2024) 127 [2403.02425].

[286] M. Mühlleitner, M.O.P. Sampaio, R. Santos and J. Wittbrodt, *Phenomenological Comparison of Models with Extended Higgs Sectors*, *JHEP* **08** (2017) 132 [1703.07750].

[287] FCC collaboration, *Higgs and Electro-weak symmetry breaking at the FCC-hh*, .

[288] A. Papaefstathiou, G. Tetlalmatzi-Xolocotzi and M. Zaro, *Triple Higgs boson production to six b-jets at a 100 TeV proton collider*, *Eur. Phys. J. C* **79** (2019) 947 [1909.09166].

[289] S. Kanemura, M. Kikuchi and K. Yagyu, *One-loop corrections to the Higgs self-couplings in the singlet extension*, *Nucl. Phys. B* **917** (2017) 154 [1608.01582].

[290] J. Braathen and S. Kanemura, *Leading two-loop corrections to the Higgs boson self-couplings in models with extended scalar sectors*, *Eur. Phys. J. C* **80** (2020) 227 [1911.11507].

[291] H. Bahl, J. Braathen, M. Gabelmann and G. Weiglein, *anyH3: precise predictions for the trilinear Higgs coupling in the Standard Model and beyond*, *Eur. Phys. J. C* **83** (2023) 1156 [2305.03015].

[292] T. Kajita, *Nobel Lecture: Discovery of atmospheric neutrino oscillations*, *Rev. Mod. Phys.* **88** (2016) 030501.

[293] A.B. McDonald, *Nobel Lecture: The Sudbury Neutrino Observatory: Observation of flavor change for solar neutrinos*, *Rev. Mod. Phys.* **88** (2016) 030502.

[294] KamLAND collaboration, *First results from KamLAND: Evidence for reactor anti-neutrino disappearance*, *Phys. Rev. Lett.* **90** (2003) 021802 [hep-ex/0212021].

[295] K2K collaboration, *Indications of neutrino oscillation in a 250 km long baseline experiment*, *Phys. Rev. Lett.* **90** (2003) 041801 [hep-ex/0212007].

[296] W. Konetschny and W. Kummer, *Nonconservation of Total Lepton Number with Scalar Bosons*, *Phys. Lett. B* **70** (1977) 433.

[297] M. Magg and C. Wetterich, *Neutrino Mass Problem and Gauge Hierarchy*, *Phys. Lett. B* **94** (1980) 61.

[298] J. Schechter and J.W.F. Valle, *Neutrino Masses in SU(2) x U(1) Theories*, *Phys. Rev. D* **22** (1980) 2227.

[299] T.P. Cheng and L.-F. Li, *Neutrino Masses, Mixings and Oscillations in SU(2) x U(1) Models of Electroweak Interactions*, *Phys. Rev. D* **22** (1980) 2860.

[300] R.N. Mohapatra and G. Senjanovic, *Neutrino Masses and Mixings in Gauge Models with Spontaneous Parity Violation*, *Phys. Rev. D* **23** (1981) 165.

[301] G. Lazarides, Q. Shafi and C. Wetterich, *Proton Lifetime and Fermion Masses in an SO(10) Model*, *Nucl. Phys. B* **181** (1981) 287.

[302] A. Zee, *Quantum Numbers of Majorana Neutrino Masses*, *Nucl. Phys. B* **264** (1986) 99.

[303] K.S. Babu, *Model of 'Calculable' Majorana Neutrino Masses*, *Phys. Lett. B* **203** (1988) 132.

[304] T. Han, B. Mukhopadhyaya, Z. Si and K. Wang, *Pair production of doubly-charged scalars: Neutrino mass constraints and signals at the LHC*, *Phys. Rev. D* **76** (2007) 075013 [0706.0441].

[305] Anisha, U. Banerjee, J. Chakrabortty, C. Englert, M. Spannowsky and P. Stylianou, *Effective connections of aμ, Higgs physics, and the collider frontier*, *Phys. Rev. D* **105** (2022) 016019 [2108.07683].

[306] CMS collaboration, *A search for doubly-charged Higgs boson production in three and four lepton final states at* $\sqrt{s} = 13$ TeV, .

[307] ATLAS collaboration, *Search for doubly charged Higgs boson production in multi-lepton final states with the ATLAS detector using proton–proton collisions at* $\sqrt{s} = 13\,TeV$, *Eur. Phys. J. C* **78** (2018) 199 [1710.09748].

[308] ATLAS collaboration, *Search for doubly charged scalar bosons decaying into same-sign W boson pairs with the ATLAS detector*, *Eur. Phys. J. C* **79** (2019) 58 [1808.01899].

[309] ATLAS collaboration, *Search for doubly charged Higgs boson production in multi-lepton final states using 139* fb^{-1} *of proton–proton collisions at* $\sqrt{s} = 13$ *TeV with the ATLAS detector*, *Eur. Phys. J. C* **83** (2023) 605 [2211.07505].

[310] G. Bambhaniya, J. Chakrabortty and S.K. Dagaonkar, *Rare meson decay through off-shell doubly charged scalars*, *Phys. Rev. D* **91** (2015) 055020.

[311] T. Wang, Y. Jiang, Z.-H. Wang and G.-L. Wang, *Doubly-charged scalar in rare decays of the* B_c *meson*, *Phys. Rev. D* **97** (2018) 115031 [1802.03120].

[312] J. Chakrabortty, P. Ghosh, S. Mondal and T. Srivastava, *Reconciling* $(g\text{-}2)_\mu$ *and charged lepton flavor violating processes through a doubly charged scalar*, *Phys. Rev. D* **93** (2016) 115004 [1512.03581].

[313] R. Primulando, J. Julio and P. Uttayarat, *Scalar phenomenology in type-II seesaw model*, *JHEP* **08** (2019) 024 [1903.02493].

[314] B. Fuks, M. Nemevšek and R. Ruiz, *Doubly Charged Higgs Boson Production at Hadron Colliders*, *Phys. Rev. D* **101** (2020) 075022 [1912.08975].

[315] Y. Cai, T. Han, T. Li and R. Ruiz, *Lepton Number Violation: Seesaw Models and Their Collider Tests*, *Front. in Phys.* **6** (2018) 40 [1711.02180].

[316] S. Antusch, O. Fischer, A. Hammad and C. Scherb, *Low scale type II seesaw: Present constraints and prospects for displaced vertex searches*, *JHEP* **02** (2019) 157 [1811.03476].

[317] P.S. Bhupal Dev and Y. Zhang, *Displaced vertex signatures of doubly charged scalars in the type-II seesaw and its left-right extensions*, *JHEP* **10** (2018) 199 [1808.00943].

[318] F. del Águila and M. Chala, *LHC bounds on Lepton Number Violation mediated by doubly and singly-charged scalars*, *JHEP* **03** (2014) 027 [1311.1510].

[319] CMS collaboration, *Prospects for a Search for Doubly Charged Higgs Bosons at the HL-LHC*, .

[320] Z. Maki, M. Nakagawa and S. Sakata, *Remarks on the unified model of elementary particles*, *Prog. Theor. Phys.* **28** (1962) 870.

[321] B. Pontecorvo, *Neutrino Experiments and the Problem of Conservation of Leptonic Charge*, *Zh. Eksp. Teor. Fiz.* **53** (1967) 1717.

[322] P.F. de Salas, D.V. Forero, C.A. Ternes, M. Tortola and J.W.F. Valle, *Status of neutrino oscillations 2018: 3σ hint for normal mass ordering and improved CP sensitivity*, *Phys. Lett. B* **782** (2018) 633 [1708.01186].

[323] D.N. Dinh, A. Ibarra, E. Molinaro and S.T. Petcov, *The $\mu - e$ Conversion in Nuclei, $\mu \to e\gamma$, $\mu \to 3e$ Decays and TeV Scale See-Saw Scenarios of Neutrino Mass Generation*, *JHEP* **08** (2012) 125 [1205.4671].

[324] J. Chakrabortty, P. Ghosh and W. Rodejohann, *Lower Limits on $\mu \to e\gamma$ from New Measurements on U_{e3}*, *Phys. Rev. D* **86** (2012) 075020 [1204.1000].

[325] N.D. Barrie and S.T. Petcov, *Lepton Flavour Violation tests of Type II Seesaw Leptogenesis*, *JHEP* **01** (2023) 001 [2210.02110].

[326] T. Li, *Type II Seesaw and tau lepton at the HL-LHC, HE-LHC and FCC-hh*, *JHEP* **09**

(2018) 079 [1802.00945].

[327] M. Williams, M. Bellis and C.A. Meyer, *Multivariate side-band subtraction using probabilistic event weights*, *JINST* **4** (2009) P10003 [0809.2548].

[328] ATLAS collaboration, *Search for new phenomena in events containing a same-flavour opposite-sign dilepton pair, jets, and large missing transverse momentum in $\sqrt{s} = 13$ pp collisions with the ATLAS detector*, *Eur. Phys. J. C* **77** (2017) 144 [1611.05791].

[329] ATLAS collaboration, *Higgs boson production cross-section measurements and their EFT interpretation in the 4ℓ decay channel at $\sqrt{s}$ =13 TeV with the ATLAS detector*, *Eur. Phys. J. C* **80** (2020) 957 [2004.03447].

[330] ATLAS collaboration, *Measurement of the total and differential cross-sections of $t\bar{t}W$ production in pp collisions at $\sqrt{s} = 13$ TeV with the ATLAS detector*, 2401.05299.

[331] M.D. Schwartz, *TASI Lectures on Collider Physics*, in *Proceedings, Theoretical Advanced Study Institute in Elementary Particle Physics : Anticipating the Next Discoveries in Particle Physics (TASI 2016): Boulder, CO, USA, June 6-July 1, 2016*, R. Essig and I. Low, eds., pp. 65–100 (2018), DOI [1709.04533].

[332] Y. Cheng, X.-G. He, F. Huang, J. Sun and Z.-P. Xing, *Electroweak precision tests for triplet scalars*, *Nucl. Phys. B* **989** (2023) 116118 [2208.06760].

[333] J. Haller, A. Hoecker, R. Kogler, K. Mönig, T. Peiffer and J. Stelzer, *Update of the global electroweak fit and constraints on two-Higgs-doublet models*, *Eur. Phys. J. C* **78** (2018) 675 [1803.01853].

[334] J. Fan, M. Reece and L.-T. Wang, *Possible Futures of Electroweak Precision: ILC, FCC-ee, and CEPC*, *JHEP* **09** (2015) 196 [1411.1054].

[335] M. Gorbahn, J.M. No and V. Sanz, *Benchmarks for Higgs Effective Theory: Extended Higgs Sectors*, *JHEP* **10** (2015) 036 [1502.07352].

[336] TLEP Design Study Working Group collaboration, *First Look at the Physics Case of TLEP*, *JHEP* **01** (2014) 164 [1308.6176].

[337] D.M. Asner et al., *ILC Higgs White Paper*, in *Snowmass 2013: Snowmass on the Mississippi*, 10, 2013 [1310.0763].

[338] P.D. Bolton and S.T. Petcov, *Measurements of $\mu \to 3e$ decay with polarised muons as a probe of new physics*, *Phys. Lett. B* **833** (2022) 137296 [2204.03468].

[339] A.G. Akeroyd, M. Aoki and H. Sugiyama, *Lepton Flavour Violating Decays tau —> anti-l ll and mu —> e gamma in the Higgs Triplet Model*, *Phys. Rev. D* **79** (2009) 113010 [0904.3640].

[340] M.M. Ferreira, T.B. de Melo, S. Kovalenko, P.R.D. Pinheiro and F.S. Queiroz, *Lepton Flavor Violation and Collider Searches in a Type I + II Seesaw Model*, *Eur. Phys. J. C* **79** (2019) 955 [1903.07634].

[341] MEG II collaboration, *A search for $\mu^+ \to e^+\gamma$ with the first dataset of the MEG II experiment*, *Eur. Phys. J. C* **84** (2024) 216 [2310.12614].

[342] MEG II collaboration, *New limit on the μ+->e+γ decay with the MEG II experiment*, 2504.15711.

[343] SINDRUM collaboration, *Search for the Decay $\mu^+ \to e^+e^+e^-$*, *Nucl. Phys. B* **299** (1988) 1.

[344] MEG collaboration, *Search for the lepton flavour violating decay $\mu^+ \to e^+\gamma$ with the full dataset of the MEG experiment*, *Eur. Phys. J. C* **76** (2016) 434 [1605.05081].

[345] I. Zurbano Fernandez et al., *High-Luminosity Large Hadron Collider (HL-LHC): Technical design report*, *CERN-2020-010* **10/2020** (2020) .

[346] V. Barger, P. Langacker, M. McCaskey, M. Ramsey-Musolf and G. Shaughnessy, *Complex Singlet Extension of the Standard Model*, *Phys. Rev. D* **79** (2009) 015018 [0811.0393].

[347] G.-C. Cho, C. Idegawa and E. Senaha, *Electroweak phase transition in a complex singlet extension of the Standard Model with degenerate scalars*, *Phys. Lett. B* **823** (2021) 136787 [2105.11830].

[348] N. Chen, T. Li, Y. Wu and L. Bian, *Complementarity of the future e^+e^- colliders and gravitational waves in the probe of complex singlet extension to the standard model*, *Phys. Rev. D* **101** (2020) 075047 [1911.05579].

[349] G.-C. Cho, C. Idegawa and R. Inumiya, *A complex singlet extension of the Standard Model with a singlet fermion dark matter*, 2312.05776.

[350] V.K. Oikonomou and A. Giovanakis, *Electroweak phase transition in singlet extensions of the standard model with dimension-six operators*, *Phys. Rev. D* **109** (2024) 055044 [2403.01591].

[351] A. Crivellin, M. Ghezzi and M. Procura, *Effective Field Theory with Two Higgs Doublets*, *JHEP* **09** (2016) 160 [1608.00975].

[352] C. Birch-Sykes, N. Darvishi, Y. Peters and A. Pilaftsis, *Accidental symmetries in the 2HDMEFT*, *Nucl. Phys. B* **960** (2020) 115171 [2007.15599].

[353] Anisha, L. Biermann, C. Englert and M. Mühlleitner, *Two Higgs doublets, effective interactions and a strong first-order electroweak phase transition*, *JHEP* **08** (2022) 091 [2204.06966].

[354] Anisha, D. Azevedo, L. Biermann, C. Englert and M. Mühlleitner, *Effective 2HDM Yukawa Interactions and a Strong First-Order Electroweak Phase Transition*, 2311.06353.

[355] B.A. Ouazghour, A. Arhrib, K. Cheung, E.-s. Ghourmin and L. Rahili, *Charged Higgs production at the Muon Collider in the 2HDM*, 2308.15664.

[356] S. Ashanujjaman, K. Ghosh and K. Huitu, *Type-II see-saw: searching the LHC elusive low-mass triplet-like Higgses at e^-e^+ colliders*, *Phys. Rev. D* **106** (2022) 075028 [2205.14983].

[357] S. Ashanujjaman and K. Ghosh, *Revisiting type-II see-saw: present limits and future prospects at LHC*, *JHEP* **03** (2022) 195 [2108.10952].

[358] R. Padhan, D. Das, M. Mitra and A. Kumar Nayak, *Probing Doubly and Singly Charged Higgs at pp Collider HE-LHC*, *Springer Proc. Phys.* **277** (2022) 209.

[359] J. Das and N. Kumar, *Veltman criteria in the beyond standard model effective field theory of a complex scalar triplet*, *Phys. Rev. D* **108** (2023) 035048 [2301.05524].

[360] Anisha, U. Banerjee, J. Chakrabortty, C. Englert and M. Spannowsky, *Extended Higgs boson sectors, effective field theory, and Higgs boson phenomenology*, *Phys. Rev. D* **103** (2021) 096009 [2103.01810].

[361] U. Banerjee, J. Chakrabortty, S. Prakash, S.U. Rahaman and M. Spannowsky, *Effective Operator Bases for Beyond Standard Model Scenarios: An EFT compendium for discoveries*, *JHEP* **01** (2021) 028 [2008.11512].

[362] X. Li, D. Zhang and S. Zhou, *One-loop matching of the type-II seesaw model onto the Standard Model effective field theory*, *JHEP* **04** (2022) 038 [2201.05082].

[363] M. Ardu and S. Davidson, *What is Leading Order for LFV in SMEFT?*, *JHEP* **08**

(2021) 002 [2103.07212].

[364] G. Abbiendi, *Status of the MUonE experiment*, *Phys. Scripta* **97** (2022) 054007 [2201.13177].

[365] MUONE collaboration, *MUonE Experiment at SPS*, *Acta Phys. Polon. Supp.* **16** (2023) 7.

[366] J. de Blas, Y. Du, C. Grojean, J. Gu, V. Miralles, M.E. Peskin et al., *Global SMEFT Fits at Future Colliders*, in *Snowmass 2021*, 6, 2022 [2206.08326].

[367] A. Celis, J. Fuentes-Martin, A. Vicente and J. Virto, *DsixTools: The Standard Model Effective Field Theory Toolkit*, *Eur. Phys. J. C* **77** (2017) 405 [1704.04504].

[368] J. Fuentes-Martin, P. Ruiz-Femenia, A. Vicente and J. Virto, *DsixTools 2.0: The Effective Field Theory Toolkit*, *Eur. Phys. J. C* **81** (2021) 167 [2010.16341].

[369] J. Aebischer, J. Kumar and D.M. Straub, *Wilson: a Python package for the running and matching of Wilson coefficients above and below the electroweak scale*, *Eur. Phys. J. C* **78** (2018) 1026 [1804.05033].

[370] M. Nowakowski and A. Pilaftsis, *On gauge invariance of Breit-Wigner propagators*, *Z. Phys. C* **60** (1993) 121 [hep-ph/9305321].

[371] A. Denner and S. Dittmaier, *Electroweak Radiative Corrections for Collider Physics*, *Phys. Rept.* **864** (2020) 1 [1912.06823].

[372] R.E. Cutkosky, *Singularities and discontinuities of Feynman amplitudes*, *J. Math. Phys.* **1** (1960) 429.

[373] M.J.G. Veltman, *Unitarity and causality in a renormalizable field theory with unstable particles*, *Physica* **29** (1963) 186.

[374] G. Passarino, C. Sturm and S. Uccirati, *Higgs Pseudo-Observables, Second Riemann Sheet and All That*, *Nucl. Phys. B* **834** (2010) 77 [1001.3360].

[375] H.A. Weldon, *The Description of Unstable Particles in Quantum Field Theory*, *Phys. Rev. D* **14** (1976) 2030.

[376] N.K. Nielsen, *On the Gauge Dependence of Spontaneous Symmetry Breaking in Gauge Theories*, *Nucl. Phys. B* **101** (1975) 173.

[377] P. Gambino and P.A. Grassi, *The Nielsen identities of the SM and the definition of*

mass, *Phys. Rev. D* **62** (2000) 076002 [hep-ph/9907254].

[378] P.A. Grassi, B.A. Kniehl and A. Sirlin, *Width and partial widths of unstable particles in the light of the Nielsen identities*, *Phys. Rev. D* **65** (2002) 085001 [hep-ph/0109228].

[379] A. Denner and S. Dittmaier, *The complex-mass scheme for perturbative calculations with unstable particles*, *Nucl. Phys. B Proc. Suppl.* **160** (2006) 22 [hep-ph/0605312].

[380] S. Actis and G. Passarino, *Two-Loop Renormalization in the Standard Model Part III: Renormalization Equations and their Solutions*, *Nucl. Phys. B* **777** (2007) 100 [hep-ph/0612124].

[381] A. Denner and J.-N. Lang, *The Complex-Mass Scheme and Unitarity in perturbative Quantum Field Theory*, *Eur. Phys. J. C* **75** (2015) 377 [1406.6280].

[382] F. Maltoni, M.K. Mandal and X. Zhao, *Top-quark effects in diphoton production through gluon fusion at next-to-leading order in QCD*, *Phys. Rev. D* **100** (2019) 071501 [1812.08703].

[383] S. Dittmaier and M. Huber, *Radiative corrections to the neutral-current Drell-Yan process in the Standard Model and its minimal supersymmetric extension*, *JHEP* **01** (2010) 060 [0911.2329].

[384] N. Kauer, *Top pair production beyond double pole approximation: $pp, p\bar{p} \to$ six fermions and zero, one or two additional partons*, *Phys. Rev. D* **67** (2003) 054013 [hep-ph/0212091].

[385] A. Denner, *Techniques for calculation of electroweak radiative corrections at the one loop level and results for W physics at LEP-200*, *Fortsch. Phys.* **41** (1993) 307 [0709.1075].

[386] C. Englert, I. Low and M. Spannowsky, *On-shell interference effects in Higgs boson final states*, *Phys. Rev. D* **91** (2015) 074029 [1502.04678].

[387] N. Kauer and C. O'Brien, *Heavy Higgs signal–background interference in $gg \to VV$ in the Standard Model plus real singlet*, *Eur. Phys. J. C* **75** (2015) 374 [1502.04113].

[388] S. Goria, G. Passarino and D. Rosco, *The Higgs Boson Lineshape*, *Nucl. Phys. B* **864** (2012) 530 [1112.5517].

[389] S. Dawson et al., *Report of the Topical Group on Higgs Physics for Snowmass 2021:*

The Case for Precision Higgs Physics, in *Snowmass 2021*, 9, 2022 [2209.07510].

[390] D.-M. Zeng, S.-Q. Wang, X.-G. Wu and J.-M. Shen, *The Higgs-boson decay $H \to gg$ up to α_s^5-order under the minimal momentum space subtraction scheme*, *J. Phys. G* **43** (2016) 075001 [1507.03222].

[391] J. Zeng, X.-G. Wu, X.-C. Zheng and J.-M. Shen, *Gauge dependence of the perturbative QCD predictions under the momentum space subtraction scheme*, *Chin. Phys. C* **44** (2020) 113102 [2004.12068].

[392] C. Englert and M. Spannowsky, *Limitations and Opportunities of Off-Shell Coupling Measurements*, *Phys. Rev. D* **90** (2014) 053003 [1405.0285].

[393] C. Englert, Y. Soreq and M. Spannowsky, *Off-Shell Higgs Coupling Measurements in BSM scenarios*, *JHEP* **05** (2015) 145 [1410.5440].

[394] T. Kugo and I. Ojima, *Local Covariant Operator Formalism of Nonabelian Gauge Theories and Quark Confinement Problem*, *Prog. Theor. Phys. Suppl.* **66** (1979) 1.

[395] CDF collaboration, *High-precision measurement of the W boson mass with the CDF II detector*, *Science* **376** (2022) 170.

[396] ATLAS collaboration, *Measurement of the W-boson mass and width with the ATLAS detector using proton-proton collisions at $\sqrt{s} = 7$ TeV*, 2403.15085.

[397] CMS collaboration, *Measurement of the W boson mass in proton-proton collisions at $\sqrt{s} = 13$ TeV*, Tech. Rep. CMS-PAS-SMP-23-002, CERN, Geneva (2024).

[398] S. Banerjee, D. Reichelt and M. Spannowsky, *Electroweak corrections and EFT operators in W+W- production at the LHC*, *Phys. Rev. D* **110** (2024) 115012 [2406.15640].

[399] ATLAS collaboration, *Inclusive and differential cross-sections for dilepton $t\bar{t}$ production measured in $\sqrt{s} = 13$ TeV pp collisions with the ATLAS detector*, *JHEP* **07** (2023) 141 [2303.15340].

[400] A. Buckley, C. Englert, J. Ferrando, D.J. Miller, L. Moore, M. Russell et al., *Constraining top quark effective theory in the LHC Run II era*, *JHEP* **04** (2016) 015 [1512.03360].

[401] N.P. Hartland, F. Maltoni, E.R. Nocera, J. Rojo, E. Slade, E. Vryonidou et al., *A Monte Carlo global analysis of the Standard Model Effective Field Theory: the top quark*

sector, *JHEP* **04** (2019) 100 [1901.05965].

[402] I. Brivio, S. Bruggisser, F. Maltoni, R. Moutafis, T. Plehn, E. Vryonidou et al., *O new physics, where art thou? A global search in the top sector*, *JHEP* **02** (2020) 131 [1910.03606].

[403] S. Bißmann, C. Grunwald, G. Hiller and K. Kröninger, *Top and Beauty synergies in SMEFT-fits at present and future colliders*, *JHEP* **06** (2021) 010 [2012.10456].

[404] SMEFiT collaboration, *Combined SMEFT interpretation of Higgs, diboson, and top quark data from the LHC*, *JHEP* **11** (2021) 089 [2105.00006].

[405] F. Garosi, D. Marzocca, A.R. Sánchez and A. Stanzione, *Indirect constraints on top quark operators from a global SMEFT analysis*, *JHEP* **12** (2023) 129 [2310.00047].

[406] O. Atkinson, C. Englert, M. Kirk and G. Tetlalmatzi-Xolocotzi, *Collider-Flavour Complementarity from the bottom to the top*, 2411.00940.

[407] J.A. Aguilar-Saavedra, *Toponium hunter's guide*, *Phys. Rev. D* **110** (2024) 054032 [2407.20330].

[408] B. Fuks, K. Hagiwara, K. Ma and Y.-J. Zheng, *Simulating toponium formation signals at the LHC*, 2411.18962.

[409] M.V. Garzelli, G. Limatola, S.O. Moch, M. Steinhauser and O. Zenaiev, *Updated predictions for toponium production at the LHC*, 2412.16685.

[410] H.K. Dreiner, H.E. Haber and S.P. Martin, *Two-component spinor techniques and Feynman rules for quantum field theory and supersymmetry*, *Phys. Rept.* **494** (2010) 1 [0812.1594].

[411] S. Dittmaier, A. Huss and C. Schwinn, *Mixed QCD-electroweak $\mathcal{O}(\alpha_s\alpha)$ corrections to Drell-Yan processes in the resonance region: pole approximation and non-factorizable corrections*, *Nucl. Phys. B* **885** (2014) 318 [1403.3216].

[412] C. Englert, M. Russell and C.D. White, *Effective Field Theory in the top sector: do multijets help?*, *Phys. Rev. D* **99** (2019) 035019 [1809.09744].

[413] ATLAS collaboration, *Measurement of the top-quark decay width in top-quark pair events in the dilepton channel at $\sqrt{s} = 13$ TeV with the ATLAS detector*, ATLAS-CONF-2019-038, ATLAS-CONF-2019-038.

[414] ILC collaboration, H. Baer et al., eds., *The International Linear Collider Technical*

Design Report - Volume 2: Physics, 1306.6352.

[415] P. Lebrun, L. Linssen, A. Lucaci-Timoce, D. Schulte, F. Simon, S. Stapnes et al., *The CLIC Programme: Towards a Staged e+e- Linear Collider Exploring the Terascale : CLIC Conceptual Design Report*, 1209.2543.

[416] CLICDP, CLIC collaboration, *The Compact Linear Collider (CLIC) - 2018 Summary Report*, 1812.06018.

[417] E. Manosperti, R. Tomas and A. Pastushenko, *Design of CLIC beam delivery system at 7 TeV*, *JACoW* **IPAC2023** (2023) MOPL113.

[418] H. Al Ali et al., *The muon Smasher's guide*, *Rept. Prog. Phys.* **85** (2022) 084201 [2103.14043].

[419] M. Chiesa, F. Maltoni, L. Mantani, B. Mele, F. Piccinini and X. Zhao, *Measuring the quartic Higgs self-coupling at a multi-TeV muon collider*, *JHEP* **09** (2020) 098 [2003.13628].

[420] A. Costantini, F. De Lillo, F. Maltoni, L. Mantani, O. Mattelaer, R. Ruiz et al., *Vector boson fusion at multi-TeV muon colliders*, *JHEP* **09** (2020) 080 [2005.10289].

[421] E. Celada, T. Han, W. Kilian, N. Kreher, Y. Ma, F. Maltoni et al., *Probing Higgs-muon interactions at a multi-TeV muon collider*, *JHEP* **08** (2024) 021 [2312.13082].

[422] A. Dedes, M. Paraskevas, J. Rosiek, K. Suxho and L. Trifyllis, *SmeftFR – Feynman rules generator for the Standard Model Effective Field Theory*, *Comput. Phys. Commun.* **247** (2020) 106931 [1904.03204].

[423] A. Dedes, J. Rosiek, M. Ryczkowski, K. Suxho and L. Trifyllis, *SmeftFR v3 – Feynman rules generator for the Standard Model Effective Field Theory*, *Comput. Phys. Commun.* **294** (2024) 108943 [2302.01353].

[424] H. Murayama, I. Watanabe and K. Hagiwara, *HELAS: HELicity amplitude subroutines for Feynman diagram evaluations*, .

[425] K. Seidel, F. Simon, M. Tesar and S. Poss, *Top quark mass measurements at and above threshold at CLIC*, *Eur. Phys. J. C* **73** (2013) 2530 [1303.3758].

[426] S. Chekanov, M. Demarteau, A. Fischer and J. Zhang, *Effect of PYTHIA8 tunes on event shapes and top-quark reconstruction in e^+e^- annihilation at CLIC*, 1710.07713.

[427] Z. Li, X. Sun, Y. Fang, G. Li, S. Xin, S. Wang et al., *Top quark mass measurements at the $t\bar{t}$ threshold with CEPC*, *Eur. Phys. J. C* **83** (2023) 269 [2207.12177].

[428] G. Durieux, M. Perelló, M. Vos and C. Zhang, *Global and optimal probes for the top-quark effective field theory at future lepton colliders*, *JHEP* **10** (2018) 168 [1807.02121].

[429] CLICDP collaboration, *Top-Quark Physics at the CLIC Electron-Positron Linear Collider*, *JHEP* **11** (2019) 003 [1807.02441].

[430] C. Englert and M. Russell, *Top quark electroweak couplings at future lepton colliders*, *Eur. Phys. J. C* **77** (2017) 535 [1704.01782].

[431] CMS collaboration, *Search for production of four top quarks in final states with same-sign or multiple leptons in proton-proton collisions at $\sqrt{s} = 13$ TeV*, *Eur. Phys. J. C* **80** (2020) 75 [1908.06463].

[432] ATLAS collaboration, *Evidence for $t\bar{t}t\bar{t}$ production in the multilepton final state in proton–proton collisions at $\sqrt{s} = 13$ TeV with the ATLAS detector*, *Eur. Phys. J. C* **80** (2020) 1085 [2007.14858].

[433] ATLAS collaboration, *Measurement of the $t\bar{t}t\bar{t}$ production cross section in pp collisions at $\sqrt{s} = 13$ TeV with the ATLAS detector*, *JHEP* **11** (2021) 118 [2106.11683].

[434] CMS collaboration, *Evidence for the simultaneous production of four top quarks in proton-proton collisions at $\sqrt{s} = 13$ TeV*, Tech. Rep. (2022).

[435] CMS collaboration, *Search for the production of four top quarks in the single-lepton and opposite-sign dilepton final states in proton-proton collisions at $\sqrt{s} = 13$ TeV*, *JHEP* **11** (2019) 082 [1906.02805].

[436] ATLAS collaboration, *Search for four-top-quark production in the single-lepton and opposite-sign dilepton final states in pp collisions at $\sqrt{s} = 13$ TeV with the ATLAS detector*, *Phys. Rev. D* **99** (2019) 052009 [1811.02305].

[437] C. Zhang, *Constraining qqtt operators from four-top production: a case for enhanced EFT sensitivity*, *Chin. Phys. C* **42** (2018) 023104 [1708.05928].

[438] G. Banelli, E. Salvioni, J. Serra, T. Theil and A. Weiler, *The Present and Future of Four Top Operators*, *JHEP* **02** (2021) 043 [2010.05915].

[439] R. Aoude, H. El Faham, F. Maltoni and E. Vryonidou, *Complete SMEFT predictions for four top quark production at hadron colliders*, *JHEP* **10** (2022) 163 [2208.04962].

[440] C. Englert, G.F. Giudice, A. Greljo and M. McCullough, *The $\hat{H}$-Parameter: An Oblique Higgs View*, *JHEP* **09** (2019) 041 [1903.07725].

[441] E. Alvarez, B.M. Dillon, D.A. Faroughy, J.F. Kamenik, F. Lamagna and M. Szewc, *Bayesian probabilistic modeling for four-top production at the LHC*, *Phys. Rev. D* **105** (2022) 092001 [2107.00668].

[442] L. Builtjes, S. Caron, P. Moskvitina, C. Nellist, R.R. de Austri, R. Verheyen et al., *Climbing four tops with graph networks, transformers and pairwise features*, 2211.05143.

[443] K.J.F. Gaemers and F. Hoogeveen, *Higgs Production and Decay Into Heavy Flavors With the Gluon Fusion Mechanism*, *Phys. Lett. B* **146** (1984) 347.

[444] D. Dicus, A. Stange and S. Willenbrock, *Higgs decay to top quarks at hadron colliders*, *Phys. Lett. B* **333** (1994) 126 [hep-ph/9404359].

[445] S. Jung, J. Song and Y.W. Yoon, *Dip or nothingness of a Higgs resonance from the interference with a complex phase*, *Phys. Rev. D* **92** (2015) 055009 [1505.00291].

[446] R. Frederix and F. Maltoni, *Top pair invariant mass distribution: A Window on new physics*, *JHEP* **01** (2009) 047 [0712.2355].

[447] M. Carena and Z. Liu, *Challenges and opportunities for heavy scalar searches in the $t\bar{t}$ channel at the LHC*, *JHEP* **11** (2016) 159 [1608.07282].

[448] B. Hespel, F. Maltoni and E. Vryonidou, *Signal background interference effects in heavy scalar production and decay to a top-anti-top pair*, *JHEP* **10** (2016) 016 [1606.04149].

[449] A. Djouadi, J. Ellis, A. Popov and J. Quevillon, *Interference effects in $t\bar{t}$ production at the LHC as a window on new physics*, *JHEP* **03** (2019) 119 [1901.03417].

[450] ATLAS collaboration, *Search for Heavy Higgs Bosons A/H Decaying to a Top Quark Pair in pp Collisions at $\sqrt{s} = 8$ TeV with the ATLAS Detector*, *Phys. Rev. Lett.* **119** (2017) 191803 [1707.06025].

[451] CMS collaboration, *Search for heavy Higgs bosons decaying to a top quark pair in*

proton-proton collisions at $\sqrt{s} = 13$ *TeV*, *JHEP* **04** (2020) 171 [1908.01115].

[452] G. Bevilacqua and M. Worek, *Constraining BSM Physics at the LHC: Four top final states with NLO accuracy in perturbative QCD*, *JHEP* **07** (2012) 111 [1206.3064].

[453] F. Maltoni, D. Pagani and I. Tsinikos, *Associated production of a top-quark pair with vector bosons at NLO in QCD: impact on* $t\bar{t}H$ *searches at the LHC*, *JHEP* **02** (2016) 113 [1507.05640].

[454] R. Frederix, D. Pagani and M. Zaro, *Large NLO corrections in* $t\bar{t}W^{\pm}$ *and* $t\bar{t}t\bar{t}$ *hadroproduction from supposedly subleading EW contributions*, *JHEP* **02** (2018) 031 [1711.02116].

[455] ATLAS collaboration, G. Aad et al., *Measurement of the b-tag Efficiency in a Sample of Jets Containing Muons with 5* fb^{-1} *of Data from the ATLAS Detector*, 3, 2012.

[456] E. Bols, J. Kieseler, M. Verzetti, M. Stoye and A. Stakia, *Jet Flavour Classification Using DeepJet*, *JINST* **15** (2020) P12012 [2008.10519].

[457] A. Blance and M. Spannowsky, *Unsupervised event classification with graphs on classical and photonic quantum computers*, *JHEP* **21** (2020) 170 [2103.03897].

[458] O. Atkinson, A. Bhardwaj, C. Englert, P. Konar, V.S. Ngairangbam and M. Spannowsky, *IRC-Safe Graph Autoencoder for Unsupervised Anomaly Detection*, *Front. Artif. Intell.* **5** (2022) 943135 [2204.12231].

[459] O. Atkinson, A. Bhardwaj, C. Englert, V.S. Ngairangbam and M. Spannowsky, *Anomaly detection with convolutional Graph Neural Networks*, *JHEP* **08** (2021) 080 [2105.07988].

[460] F.A. Dreyer and H. Qu, *Jet tagging in the Lund plane with graph networks*, *JHEP* **03** (2021) 052 [2012.08526].

[461] O. Atkinson, A. Bhardwaj, S. Brown, C. Englert, D.J. Miller and P. Stylianou, *Improved constraints on effective top quark interactions using edge convolution networks*, *JHEP* **04** (2022) 137 [2111.01838].

[462] M. Wang, D. Zheng, Z. Ye, Q. Gan, M. Li, X. Song et al., *Deep Graph Library: A Graph-Centric, Highly-Performant Package for Graph Neural Networks*, *arXiv e-prints* (2019) arXiv:1909.01315 [1909.01315].

[463] A. Paszke, S. Gross, F. Massa, A. Lerer, J. Bradbury, G. Chanan et al., *Pytorch: An*

imperative style, high-performance deep learning library, in *Advances in Neural Information Processing Systems 32*, pp. 8024–8035, Curran Associates, Inc. (2019), http://papers.neurips.cc/paper/9015-pytorch-an-imperative-style-high-performance-deep-learning-library.pdf.

[464] L. Heinrich, M. Feickert and E. Rodrigues, "pylhe: v0.5.0." 10.5281/zenodo.1217031.

[465] D.P. Kingma and J. Ba, *Adam: A Method for Stochastic Optimization*, *arXiv e-prints* (2014) arXiv:1412.6980 [1412.6980].

[466] H. Qu and L. Gouskos, *ParticleNet: Jet Tagging via Particle Clouds*, *Phys. Rev. D* **101** (2020) 056019 [1902.08570].

[467] R. Barbieri, A. Pomarol, R. Rattazzi and A. Strumia, *Electroweak symmetry breaking after LEP-1 and LEP-2*, *Nucl. Phys. B* **703** (2004) 127 [hep-ph/0405040].

[468] ATLAS collaboration, G. Aad et al., *Search for $t\bar{t}H/A \to t\bar{t}t\bar{t}$ production in the multilepton final state in proton-proton collisions at $\sqrt{s} = 13$ TeV with the ATLAS detector*, 2022.

[469] F. Blekman, F. Déliot, V. Dutta and E. Usai, *Four-top quark physics at the LHC*, *Universe* **8** (2022) 638 [2208.04085].

[470] E. Alvarez, A. Juste and R.M.S. Seoane, *Four-top as probe of light top-philic New Physics*, *JHEP* **12** (2019) 080 [1910.09581].

[471] E. Alvarez, D.A. Faroughy, J.F. Kamenik, R. Morales and A. Szynkman, *Four tops for LHC*, *Nucl. Phys. B* **915** (2017) 19 [1611.05032].

[472] S. Kanemura, H. Yokoya and Y.-J. Zheng, *Searches for additional Higgs bosons in multi-top-quarks events at the LHC and the International Linear Collider*, *Nucl. Phys. B* **898** (2015) 286 [1505.01089].

[473] L. Darmé, B. Fuks and F. Maltoni, *Top-philic heavy resonances in four-top final states and their EFT interpretation*, *JHEP* **09** (2021) 143 [2104.09512].

[474] L. Darmé, B. Fuks and M. Goodsell, *Cornering sgluons with four-top-quark events*, *Phys. Lett. B* **784** (2018) 223 [1805.10835].

[475] P.S. Bhupal Dev and A. Pilaftsis, *Maximally Symmetric Two Higgs Doublet Model with Natural Standard Model Alignment*, *JHEP* **12** (2014) 024 [1408.3405].

[476] Q.-H. Cao, J.-N. Fu, Y. Liu, X.-H. Wang and R. Zhang, *Probing top-philic new physics via four-top-quark production*, *Chin. Phys. C* **45** (2021) 093107 [2105.03372].

[477] A. Butter, G. Kasieczka, T. Plehn and M. Russell, *Deep-learned Top Tagging with a Lorentz Layer*, *SciPost Phys.* **5** (2018) 028 [1707.08966].

[478] J.H. Collins, K. Howe and B. Nachman, *Extending the search for new resonances with machine learning*, *Phys. Rev. D* **99** (2019) 014038 [1902.02634].

[479] O. Atkinson, C. Englert and P. Stylianou, *On interference effects in top-philic decay chains*, *Phys. Lett. B* **821** (2021) 136618 [2012.07424].

[480] F.F. Freitas, J.a. Gonçalves, A.P. Morais and R. Pasechnik, *Phenomenology of vector-like leptons with Deep Learning at the Large Hadron Collider*, *JHEP* **01** (2021) 076 [2010.01307].

[481] J. Hollingsworth and D. Whiteson, *Resonance Searches with Machine Learned Likelihood Ratios*, 2002.04699.

[482] O. Kitouni, B. Nachman, C. Weisser and M. Williams, *Enhancing searches for resonances with machine learning and moment decomposition*, *JHEP* **21** (2020) 070 [2010.09745].

[483] S. Frixione, E. Laenen, P. Motylinski and B.R. Webber, *Angular correlations of lepton pairs from vector boson and top quark decays in Monte Carlo simulations*, *JHEP* **04** (2007) 081 [hep-ph/0702198].

[484] P. Artoisenet, R. Frederix, O. Mattelaer and R. Rietkerk, *Automatic spin-entangled decays of heavy resonances in Monte Carlo simulations*, *JHEP* **03** (2013) 015 [1212.3460].

[485] F. Kling, J.M. No and S. Su, *Anatomy of Exotic Higgs Decays in 2HDM*, *JHEP* **09** (2016) 093 [1604.01406].

[486] P. Arnan, D. Bečirević, F. Mescia and O. Sumensari, *Two Higgs doublet models and $b \to s$ exclusive decays*, *Eur. Phys. J. C* **77** (2017) 796 [1703.03426].

[487] A. Crivellin, D. Müller and C. Wiegand, *$b \to s\ell^+\ell^-$ transitions in two-Higgs-doublet models*, *JHEP* **06** (2019) 119 [1903.10440].

[488] X.-F. Han and H.-X. Wang, *Revisiting wrong sign Yukawa coupling of type II two-Higgs-doublet model in light of recent LHC data*, *Chin. Phys. C* **44** (2020) 073101

[2003.06170].

[489] T. Biekötter, S. Heinemeyer, J.M. No, M.O. Olea-Romacho and G. Weiglein, *The trap in the early Universe: impact on the interplay between gravitational waves and LHC physics in the 2HDM*, 2208.14466.

[490] S. Dawson, D. Fontes, S. Homiller and M. Sullivan, *Role of dimension-eight operators in an EFT for the 2HDM*, *Phys. Rev. D* **106** (2022) 055012 [2205.01561].

[491] M. Krause, M. Mühlleitner and M. Spira, *2HDECAY —A program for the calculation of electroweak one-loop corrections to Higgs decays in the Two-Higgs-Doublet Model including state-of-the-art QCD corrections*, *Comput. Phys. Commun.* **246** (2020) 106852 [1810.00768].

[492] A. Djouadi, J. Kalinowski and M. Spira, *HDECAY: A Program for Higgs boson decays in the standard model and its supersymmetric extension*, *Comput. Phys. Commun.* **108** (1998) 56 [hep-ph/9704448].

[493] A. Djouadi, J. Kalinowski, M. Muehlleitner and M. Spira, *HDECAY: Twenty$_{++}$ years after*, *Comput. Phys. Commun.* **238** (2019) 214 [1801.09506].

[494] M. Krause, M. Muhlleitner, R. Santos and H. Ziesche, *Higgs-to-Higgs boson decays in a 2HDM at next-to-leading order*, *Phys. Rev. D* **95** (2017) 075019 [1609.04185].

[495] P. Bechtle, O. Brein, S. Heinemeyer, G. Weiglein and K.E. Williams, *HiggsBounds: Confronting Arbitrary Higgs Sectors with Exclusion Bounds from LEP and the Tevatron*, *Comput. Phys. Commun.* **181** (2010) 138 [0811.4169].

[496] P. Bechtle, O. Brein, S. Heinemeyer, G. Weiglein and K.E. Williams, *HiggsBounds 2.0.0: Confronting Neutral and Charged Higgs Sector Predictions with Exclusion Bounds from LEP and the Tevatron*, *Comput. Phys. Commun.* **182** (2011) 2605 [1102.1898].

[497] P. Bechtle, O. Brein, S. Heinemeyer, O. Stal, T. Stefaniak, G. Weiglein et al., *Recent Developments in HiggsBounds and a Preview of HiggsSignals*, *PoS* **CHARGED2012** (2012) 024 [1301.2345].

[498] P. Bechtle, O. Brein, S. Heinemeyer, O. Stål, T. Stefaniak, G. Weiglein et al., HiggsBounds – 4*: Improved Tests of Extended Higgs Sectors against Exclusion Bounds from LEP, the Tevatron and the LHC*, *Eur. Phys. J. C* **74** (2014) 2693 [1311.0055].

[499] P. Bechtle, S. Heinemeyer, O. Stal, T. Stefaniak and G. Weiglein, *Applying*

Exclusion Likelihoods from LHC Searches to Extended Higgs Sectors, Eur. Phys. J. C **75** (2015) 421 [1507.06706].

[500] H. Bahl, V.M. Lozano, T. Stefaniak and J. Wittbrodt, *Testing exotic scalars with HiggsBounds*, Eur. Phys. J. C **82** (2022) 584 [2109.10366].

[501] CMS collaboration, *Search for charged Higgs bosons decaying into a top and a bottom quark in the all-jet final state of pp collisions at* $\sqrt{s} = 13$ *TeV*, JHEP **07** (2020) 126 [2001.07763].

[502] ATLAS collaboration, *Search for heavy Higgs bosons decaying into two tau leptons with the ATLAS detector using pp collisions at* $\sqrt{s} = 13$ *TeV*, Phys. Rev. Lett. **125** (2020) 051801 [2002.12223].

List of figures

List of tables